The Use of Hyperspectral Imaging for Remote Sensing, and the Development of a Novel Hyperspectral Imager

NANDI, DAVID,ANIL

The Use of Hyperspectral Imaging for Remote Sensing, and the Development of a Novel Hyperspectral Imager

David Nandi

October 27, 2016

Abstract

This thesis determines the potential uses of a novel technology in hyperspectral remote sensing, by testing the capabilities of a prototype imaging spectrometer that was built using microslice technology. These capabilities are compared to those of current hyperspectral remote sensing instruments in the context of the requirements for various remote sensing applications. Due to the wide variety of potential applications for hyperspectral imaging, any unique capability of a new instrument is likely to improve a current application, or even develop a new one.

The use of microslice technology allows a 2-dimensional field of view (FoV) to be imaged simultaneously with a wide spectral range. Modelling of the remote sensing performance of the spectrometer shows that this enables it to achieve a signal to noise ratio (SNR) an order of magnitude higher than conventional hyperspectral instruments. The prototype microslice spectrometer images in the 475-650 nm wavelength range at 7 nm spectral resolution. It also images an instantaneous field of view (IFoV) of 260 x 52 mrad, at a spatial resolution of 2.6 mrad. Classification techniques are used on ground based laboratory and field test data from the instrument to demonstrate that it can accurately identify some mineral, vegetation, and water pollutant samples.

Various trade-offs can theoretically be performed on the prototype specifications to develop an instrument with particular capabilities for a specific application. This novel design means that a greater detector area is required than for conventional designs; but the 2-dimentsional FoV gives greater trade-off flexibility, in particular allowing the SNR to enter into the trade-off equation. This unique capability was found to lend itself to two applications in particular: detecting water pollutants in rivers, and detecting hydrocarbons contamination of ecosystems.

PhD Thesis - Department of Physics and Department of Geography, Durham University

Acknowledgments

I would like to thank my two supervisors, Professor Ray Sharples and Professor Danny Donoghue for their support and guidance throughout my research.

I would like to thank Robert Content for designing and overseeing the production of the instrument on which this research is based; and Colin Dunlop for his technical assistance during integration and laboratory testing.

I would like to thank Christopher Wheatley of the British Geological Survey (BGS) for his assistance in providing mineral samples for testing; and Amy Woodget of the University of Worcester for providing a site for conducting field tests.

I would like to thank Patrice Carbonneau Avi Baruch of Durham University, as well as Suresh Gurjar and Haridas Mohanta of IIT Kanpur for their assistance in conducting field tests on the River Ganges, and the subsequent laboratory tests.

Contents

List of Tables

List of Figures

Chapter 1

Introduction

1.1 What is Remote Sensing?

Remote Sensing is the process of gathering data from a distance; typically in the form of Earth Observation (EO), i.e. a using satellite, aircraft or unmanned aerial vehicle (UAV) to image the Earth. This data can be gathered using *active* remote sensors, or *passive* remote sensors. Active remote sensors emit their own signal to be reflected by a target and measured on its return to the sensor, such as SONAR (SOund Navigation And Ranging) and LIDAR (LIght Detection And Ranging) [1]. Passive remote sensors are much more common than active remote sensors, however, and use naturally reflected solar radiation, or naturally emitted thermal radiation. Remote sensing EO can be used to obtain many different types of data, such as water depth [2], air quality [3], land use [4], and topography [].

The first recorded airborne remote sensing survey was performed in 1858, when balloonist Gaspard-Félix Tournachon took aerial photographs of Paris, but it was not until aerial photography was used for military surveillance during World War I that the use of systematic remote sensing began [5]. As imaging technology became more advanced, the potential uses of remote sensing became apparent in many other areas, such as agriculture, archeology, forestry, and urban mapping. Multispectral imagery, which gathers information from several different broad wavelength ranges (known as *bands*) in the electromagnetic spectrum was developed around 1970 and became a particularly useful tool for remote sensing [6].

Further technological advances led to the advent of hyperspectral remote sensing [7, 8]. Hyperspectral imaging differs from multispectral imaging in that it gathers data from many narrow, contiguous spectral bands. Hyperspectral remote sensing generates 3-dimensional data, which is presented as a *datacube* (see Figure 1.1). The three dimensions of the datacube consist two spatial dimensions showing a spatial image of the target area, and one spectral dimension. This means that for every wavelength band a spatial image can be constructed, and for every spatial pixel a spectrum can be

extracted. Figure 1.2 shows how hyperspectral data provides a lot more spectral information than multispectral data, which can be useful for remote sensing applications. This thesis focuses on the use of passive remote sensing to gather hyperspectral image data from the Earth's surface.

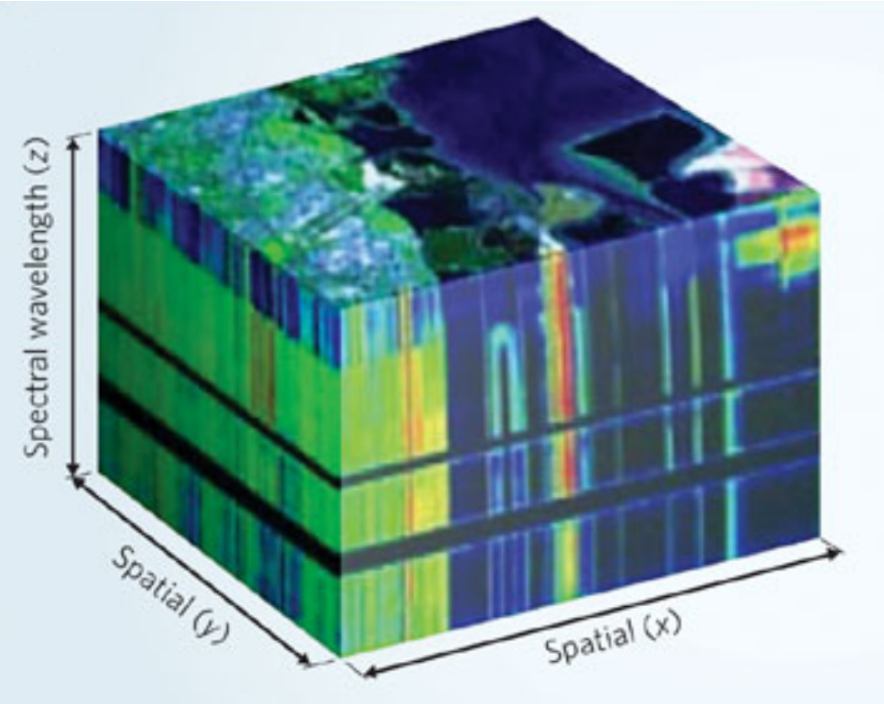

Figure 1.1: This image shows a visual representation of a hyperspectral datacube. A datacube is a standard way to store hyperspectral image data, and consists of a 3-dimensional array with two spatial dimensions and one spectral dimension. This image was taken from [9].

The first hyperspectral remote sensing instruments were airborne spectrometers mounted on small aircrafts (later supplemented by UAVs), which were used to image specific areas of ground at a spatial resolution of about 5 m. Most current hyperspectral remote sensing instruments, however, are space-borne spectrometers, which are mounted on satellites and used to obtain full spatial coverage of the Earth with a regular temporal coverage (i.e. a short revisit time) at a spatial resolution of about 30 m.

Airborne remote sensing instruments generally operate at altitudes of about 1-5 km. A remote sensing aircraft typically travels at speeds of about 100 $m\,s^{-1}$, which allows for typical integration times (*dwell times*) of over 10 ms [11]. Spaceborne hyperspectral instruments generally operate in low Earth orbit (LEO), around 700 km, at orbital velocities of about 7.5 $km\,s^{-1}$, which allows for typical dwell times of under 10 ms (see Table 1.1). Geostationary satellites are much less common, but can be used to image a fixed wide field of view (FoV). These are positioned at an altitude of about 35,000 km, which only allows for a spatial resolution of the order of kilometers. More details about different hyperspectral

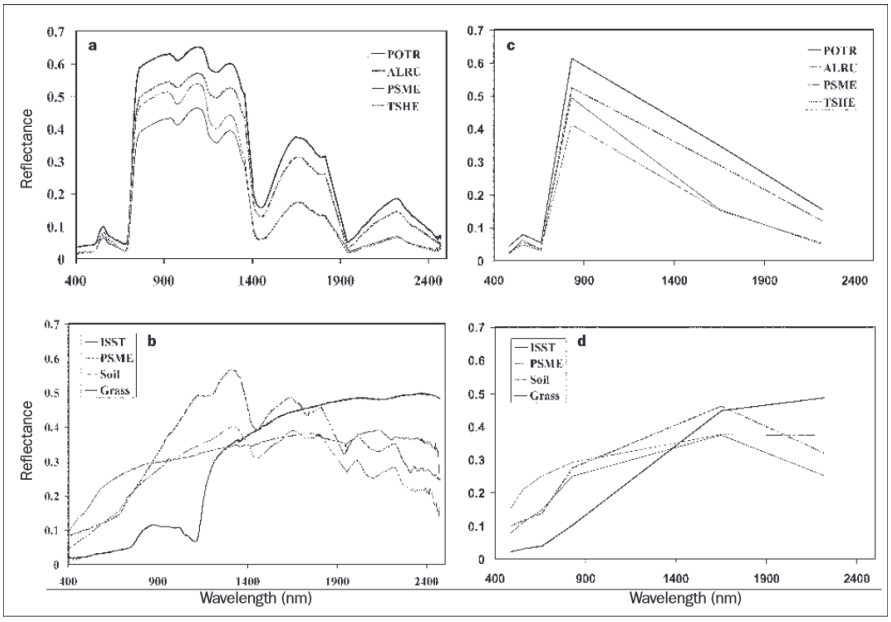

Figure 1.2: These graphs shows the spectral reflectance of various different targets as measured by a hyperspectral imager (left), and a multi-spectral imager (right). It can be seen that the hyperspectral imagery provides much more detailed spectra than the multispectral imagery, allowing the spectra from different targets to be distinguished more easily. This figure was taken from [10].

remote sensing systems are give in Table 1.1, and discussed throughout the thesis.

1.2 Remote Sensing Aims and Objectives

Remote sensing is used to gather information that it is too time consuming, difficult, costly, or dangerous to gather directly. This can include recording data of the tops of mountains, the beds of rivers, or the canopies of forests. The main advantage of gathering data using remote sensing is that data can be gathered over a large spatial area in a short period of time. Remote sensing data has been used for a wide range of applications spanning environmental, commercial, and military; and can be expected to have many more to come. Current applications of hyperspectral remote sensing data are presented in Chapter 2.

The demand for remote sensing data is increasing all the time. In this modern information age it is imperative for scientific, commercial and political enterprises to have the highest quality and most up-to-date information available. Also, as humanity's effect on the global environment comes increasingly under scrutiny, it is vital that environmental scientists have the best possible quality and coverage of spectral data of the Earth that they possibly can. As a result of these factors, the last 15 years have shown an increase in the development rate of hyperspectral remote sensing instruments (see Table 1.1).

The development of specific new applications for hyperspectral data, with different requirements, drives

the need for improved instruments with better specifications. The push towards more spaceborne instruments signifies a joint effort among members of the scientific remote sensing community towards the ultimate goal of achieving full coverage of the Earth with high spectral resolution, spatial resolution, temporal resolution, and signal to noise ratio (SNR) over a complete spectral range. The development of a spectral instrument always involves a trade-off between all of these desirable characteristics, and therefore achieving this goal will require multiple spectral instruments working simultaneously.

1.3 Scanning Techniques and Multiplexing

Hyperspectral remote sensing imagery is generally gathered using a pushbroom or whiskbroom scanning method. A pushbroom scanner images a line of pixels that is perpendicular to the direction of flight, meaning that as the airborne platform moves forwards the area of ground that is imaged by the pixels changes. The imaged area is known as a swath, with the swath width being determined by the length of the line of pixels, and the swath length being determined by distance travelled by the platform. A whiskbroom sensor works in a similar way, but with only one pixel in the swath width being imaged at a time. The angle of imaging oscillates rapidly across the swath width to allow the entire swath to be imaged. Figure 1.3 demonstrates these two imaging techniques.

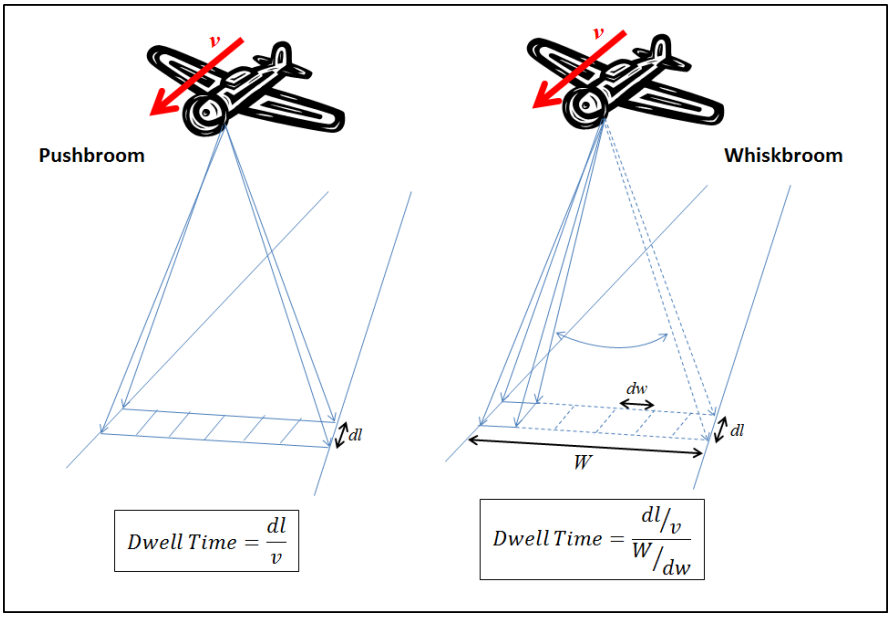

Figure 1.3: This image shows the mode of operation of a typical pushbroom remote sensing instrument (left), and a typical whiskbroom remote sensing instrument (right). The different scanning techniques lead to different dwell times, as indicated in the image, where v is the ground velocity of the platform, and w is the swath width. The size of the spatial elements along and across the the swath are typically the same, and are denoted by dl and dw respectively.

The main difference between different scanning techniques is the level of spatial multiplexing attained. Multiplexing refers to simultaneous data capture. A pushbroom scanner provides 1-dimensional spatial

multiplexing, while a whiskbroom scanner does not provide any spatial multiplexing. The higher the level of spatial multiplexing used, the higher the dwell time of the instrument. The dwell times of conventional pushbroom and whiskbroom sensors are given in Figure 1.3. The dwell time and the level of spectral multiplexing determine the length of time that data is gathered for a particular point in the datacube. This is an important factor, as the longer data are gathered for, the higher the SNR that can be achieved is. Therefore, in theory, the higher the level of multiplexing of an instrument, the higher the SNR that it can achieve. High levels of multiplexing do, however, require a larger detector space to record the data received.

The novel hyperspectral instrument presented in this thesis has the unique capability of being able to perform simultaneous spectral and 2-dimensional spatial multiplexing. The 2-dimensional instantaneous field of view (IFoV) produced by this instrument leads to a larger dwell time, as the multiple pixels are simultaneously imaged along, as well as across, the flight path. This thesis will determine if the high SNR achievable with the high level of multiplexing provided by the novel hyperspectral instrument can improve the potential capabilities of hyperspectral remote sensing.

This 2-dimensional spatial multiplexing also provides the possibility of using an alternative scanning method. This scanning method would involve varying the angle of imaging slightly along the swath during flight, to enable each area of ground to be imaged by the same area of detector for an elongated period of time. Figure 1.4 displays this concept, and shows the dwell time of such a scanning method. This method is known as step-and-stare, or framing. Using step-and-stare together with spectral multiplexing and has been proposed previously, but has not yet been put into practice [12].

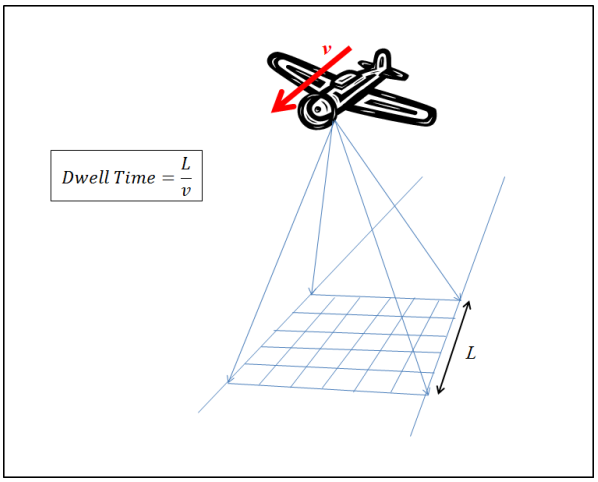

Figure 1.4: This image shows the novel scanning method proposed to accommodate the 2-dimentional instantaneous field of view (IFoV) of a new hyperspectral instrument for remote sensing. This scanning method works by varying the angle of imaging along the swath slightly during flight so that an area of ground can be imaged for an elongated period of time. The dwell time achieved is also shown, where L represents the number of along swath spatial elements multiplied by the length of each element. This method is known as step-and-stare or framing.

1.4 The Technology Behind Hyperspectral Imaging

1.4.1 An Imaging Spectrograph

The core part of a hyperspectral imaging instrument (or *spectrometer*), is an imaging spectrograph. An imaging spectrograph is an optical system that is used to record an image containing both spatial and spectral information. The basic optical design of an imaging spectrograph consists of five components: an entrance slit, a collimator, a diffraction element, a camera, and a detector (see Figure 1.5).

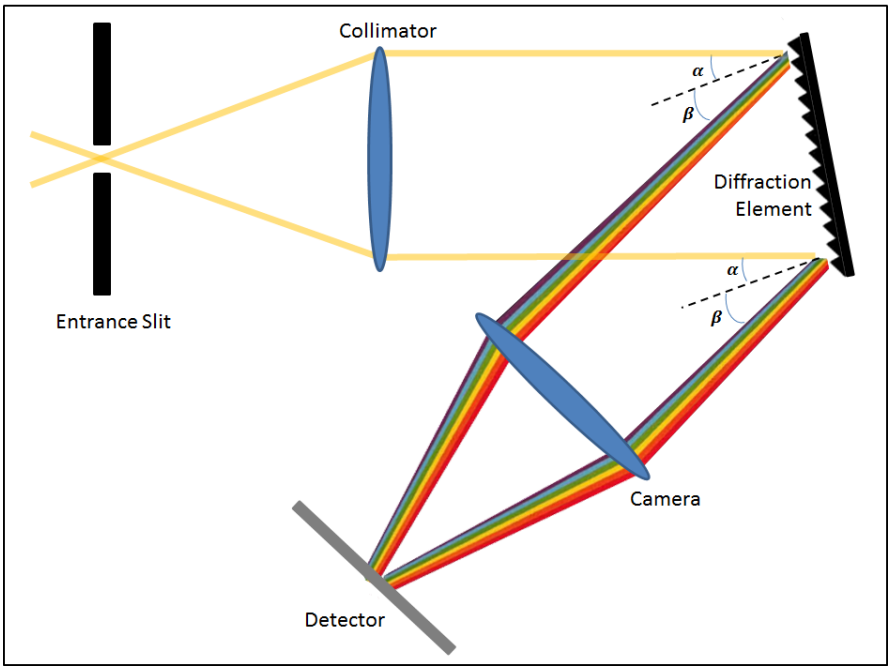

Figure 1.5: This image shows a typical design of an imaging spectrograph. The five key components are labelled. The dispersing element used can be either a grating or a prism, or a combination of both (a *grism*). The collimator and camera can be made up of either lenses or mirrors. α and β represent the angle of incidence and dispersion of the diffraction element respectively.

The entrance slit (or slits) is placed at the focal point of incoming light, and controls the light field that enters the spectrograph, which is ultimately what is imaged on the detector. The collimator is a lens or mirror, which refracts or reflects the light (respectively) so that the light rays are traveling parallel to each other. The dispersion element is the part of the spectrograph that disperses the light into its constituent wavelengths. It is generally a grating, but can be a prism or *grism* (a transmissive grating and prism combined).

There are several different types of gratings that can be used as the dispersive element of a spectrograph, and they can be split into two distinct types: transmissive gratings (which diffract light as it passes through) and reflective gratings (which diffract light through reflection). The most common grating used in a spectrograph is a plane ruled reflection grating, as these can be manufactured to have high

efficiency around a specified wavelength. This specified wavelength is determined by *blaze angle* of the grating, i.e. the angle at which the grooves are ruled into the reflective surface.

A plane transmission grating could be used instead, which diffracts the light by refracting it through a similarly ruled transparent surface. As with the reflection grating, the blaze angle is set to maximise the efficiency for the central wavelength. There are other types of gratings available, such as volume phase holographic (VPH) gratings (which use glass with a variable refractive index instead of rulings to create dispersion), and Echelle gratings (which use a very low ruling density and use high incidence angles and diffraction orders) [13].

In a standard plane grating, the spacing of the grooves determines the angle of dispersion, and therefore impacts on the wavelength coverage that can be achieved. The dispersion relation is shown in Equation 1.1, where d is the grove spacing, α is the angle of incidence, β is the angle of diffraction, m is the integer order of diffraction, and λ is the wavelength of light. This equation indicates that the frequency of grooves determines the angle of diffraction for a given wavelength, providing a trade-off between the spectral coverage over a given detector area, and the spectral resolution. The order of diffraction indicates that the light of the same wavelength will be dispersed at different angles for each integer value of m. The grating is usually blazed so that the first order of diffraction is diffracted at the appropriate angle to be used by the spectrograph. Light from the other orders of diffraction should therefore be blocked to avoid contaminating the signal.

$$d\,(sin\alpha + sin\beta) = m\lambda \tag{1.1}$$

The camera of the spectrograph uses either a lens or a mirror to focus the dispersed light onto the detector. The detector is generally CCD (charge coupled device) array in the optical region, but CMOS (complimentary metal-oxide semiconductor) or other detector types can be used [14]. The size of the detector is an important factor in remote sensing, as it determines the amount of information that can be detected by the instrument.

1.4.2 A Fourier Transform Spectrometer (FTS)

A Fourier transform spectrometer (FTS) is a spectrometer that uses light interference, rather than dispersion, to obtain spectral data. A typical FTS is effectively a Michelson interferometer with a moveable mirror (see Figure 1.6). This uses a beam splitter, a fixed mirror, and a translating mirror to generate interference for different path lengths. By adjusting the position of the translating mirror, an interference pattern is created that is a Fourier transform of the source spectrum.

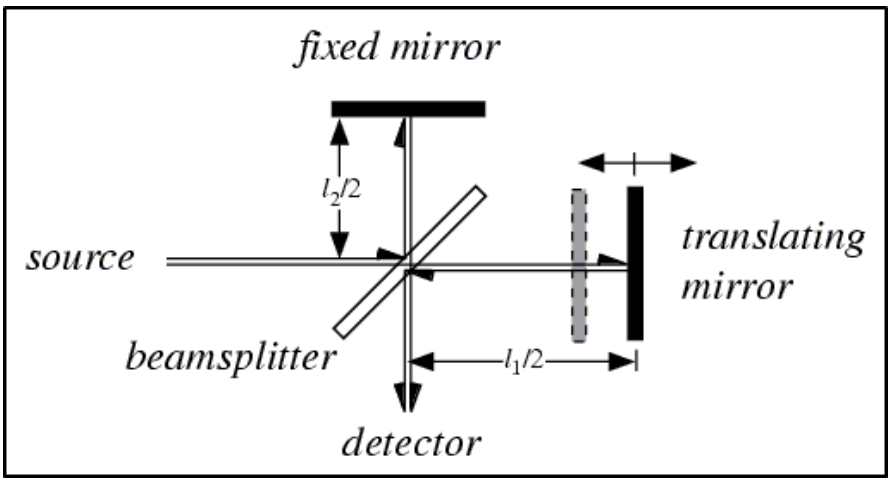

Figure 1.6: This diagram shows the design of a typical Fourier transform spectrometer (FTS). The beam splitter sends the source light along two different paths of lengths l_1 and l_2. The path difference ($\mid l_1 - l_2 \mid$) determines what interference occurs at the detector, and can be varied by changing the position of the translating mirror. The interference pattern created by scanning the translating mirror is a Fourier transform of the source spectrum. This image was taken from [15].

In this spectrometer design the translating mirror must scan to achieve full spectral coverage, meaning that a standard FTS does not provide spectral multiplexing. This means that the SNR achieved is not merely dependent of the dwell time of the instrument, but also the wavelength range and scanning rate used. It is possible, however, for a hyperspectral remote sensing FTS to capture a 2-dimensional IFoV while also spectrally multiplexing. In order to achieve this, a specific type of FTS must be used, which is known as a lateral sharing interferometer (LSI), and can detect multiple interference patters for different spectral bands simultaneously [16].

1.4.3 Atmospheric Effects

When analysing data from hyperspectral remote sensing, the effects of the atmosphere on the propagating light must be considered. When solar radiation travels through the Earth's atmosphere, molecules scatter and absorb some of the light (see Figure 1.7). Air molecules provide Rayleigh scattering, while aerosol molecules provide Mie scattering []. This means that the light detected by the sensor is not merely a product of the solar radiation and the reflectance of the target; it also incorporates the composition of the atmosphere, and the path length of the light. The atmosphere particularly affects spaceborne remote sensing, as the light will have to travel through the entire atmosphere before being imaged as opposed to the shorter distance travelled for airborne imaging. In order to get reliable data from a remote sensing spectrometer, the raw data must therefore be processed to account for such interference. This processing is known as atmospheric correction, and is discussed in further in Section 7.1.

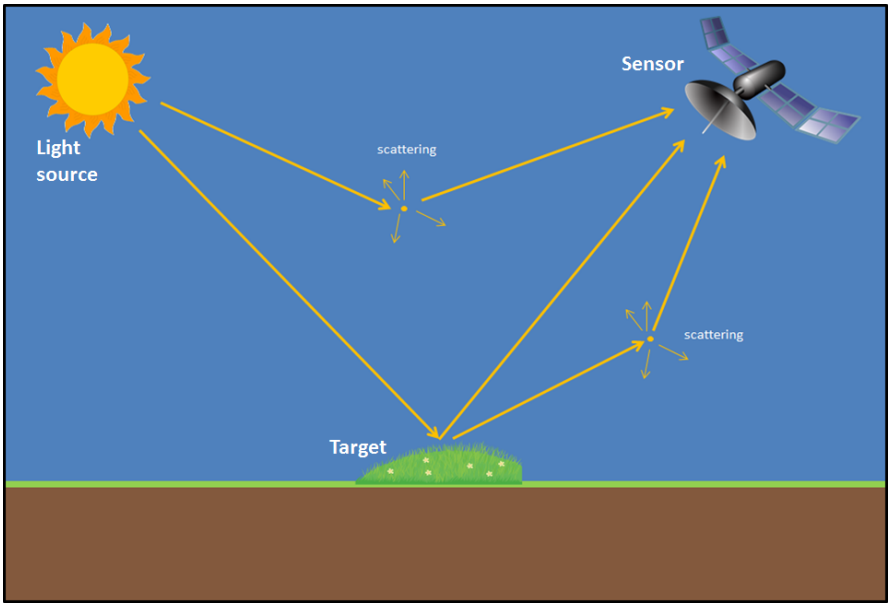

Figure 1.7: This image shows how the the light detected by a remote sensing instrument not only comes from reflectance of the target, but also from atmospheric scattering. The light is also affected by atmospheric absorption on both the downward and upward paths.

1.5 The History of Hyperspectral Remote Sensing

The LANDSAT program is an Earth observation (EO) program that has been collecting spectral data continuously since 1972, and has formed the basis of modern EO [17]. It has comprised 8 satellite deployments to date, with the latest deployment (Landsat 8) imaging the Earth at a spatial resolution of 30 m (in the near and short-wave infrared) and a temporal resolution of 16 days. Since LANDSAT images a maximum of 9 non-contiguous spectral bands, it is considered to provide multispectral data, rather than hyperspectral data.

The use of hyperspectral imagers for remote sensing began in the 1980s, when remote sensing applications such as vegetation monitoring began to develop more demanding spectral requirements of their instruments [18]. The Airborne Imaging Spectrometer (AIS) became the first remote sensing hyperspectral imaging system in 1983, but it had limited capabilities [7]. In 1989, however, AVIRIS (the Airborne Visible and Infra-Red Imaging Spectrometer) became the first fully functional airborne hyperspectral imaging instrument to image reflected solar radiation across the $0.4 - 2.5\mu m$ wavelength range (which has become the standard wavelength range for visible and short-wave infrared sensors) [8]. It was developed by the Jet Propulsion Laboratory (JPL), managed by the California Institute of Technology (CIT), for the National Aeronautics and Space Administration (NASA), to follow on from AIS, and thanks to continual improvements it is still operational today. Since the conception of AVIRIS, the development of hyperspectral remote sensing instruments, and the demand for hyperspectral remote sensing data has grown. Table 1.1 details the specifications of the major hyperspectral remote sensing instruments that have since been deployed.

Instrument	Deployment	Developed by/for	Platform	Spectral Range / nm	No. of Bands	Spectral Resolution / nm	Spatial Resolution / m	IFoV / km	Dwell Time / ms	SNR (approximate maximum)	Size /cm	Weight /kg
AIS [7]	1983	NASA	airborne	1200 - 2400	128	9.6	1.9 mrad	3.7 deg	n/k	100	n/k	n/k
AVIRIS[8]	1989	JPL (NASA)	airborne	400 - 2500	224	10	20	0.02 x 13.5 @ 20	100	100 - 600	n/k	n/k
CASI [19]	1989	n/k	airborne	400-950	288	3	6	0.006 x 3 @ 3	n/k	400	n/k	55
AISA [20]	1993	Finland and NASA	airborne	450 - 900	286	1.6 - 9.4	1	0.001 x 0.384 @ 1	> 4	n/k	n/k	n/k
HYDICE [21]	1994	Naval Research Laboratory	airborne	400 - 2500	210	7.5 - 20	4	0.004 x 12 1.15 @ 7.5	32	200	30x30x30	200
Probe-1 [22]	1997	Earth Search Systems	airborne	400 - 2500	128	20	1	n/k	n/k	n/k	n/k	n/k
MODIS [23]	1998	NASA	spaceborne (EOS-AM1)	620 - 14385	36	multi-spectral	250	10 x 0.25 @ 705	0.1	100-1400	160x100x100	250
ASTER [24]	1998	NASA	spaceborne (EOS-AM1)	520 - 11650	15	multi-spectral	15	0.015 x 60 @ 705	2	n/k	n/k	406
AVIS [25]	1999	Ludwig-Maximilians-University	airborne	400 - 900	64	8	3 mrad	n/k	n/k	n/k	n/k	n/k
HyMap[26]	1999	Integrated Spectronics/HyVista	airborne	450 - 2500	100 - 200	10 - 20	2 - 10	0.01 x 2.3 @ 5	180	200 - 1700	n/k	n/k
MERIS [27]	1999	ESA	spaceborne (Envisat)	390 -1040	15	1.7 - 30	300	0.3 x 1.1 @ 800	45	n/k	180x100x90	200
Hyperion [28]	2000	NASA	spaceborne (EO-1)	400 - 2500	242	10	30	0.03 x 7.7 @ 705	4	150	75x65x39	49
CHRIS[29]	2001	ESA	spaceborne (PROBA)	400 - 1050	18 or 62	1.3 - 12	20 or 40	0.02 x 15 @ 670	15	100	79x26x20	14
HySI [30]	2008	ISRO	spaceborne	400 - 920	64	15	80	0.08 x 20 @ 100	11	100	n/k	3
HISCO [31]	2009	Naval Research Laboratory	spaceborne	400 - 900	n/k	5.7	90	0.083 x 42 @ 350	12	100 - 500	89x53x43	41
EAGLE [32]	n/k	AISA Specim	airborne	400 -970	488	3.3	0.5	0.0005 x 0.5 @ 1	5	1250	35x15x15	6.5
HAWK [32]	n/k	AISA Specim	airborne	970 - 2500	254	12	1	0.001 x 0.3 @ 1	10	800	47x28x22	18
OWL [32]	n/k	AISA Specim	airborne	7700 - 12000	100	100	1.1	0.001 x 0.43 @ 1	11	500	29x20x19	13

Table 1.1: This table shows the full range of specifications of many of the hyperspectral remote sensing instruments that have been deployed since AIS in 1983. 'n/k' is entered where a specification is not known.

Although most hyperspectral remote sensing instruments image in the $0.4 - 2.5\mu m$ wavelength range (as can be seen from Table 1.1), instruments imaging in the thermal infrared spectral region ($8 - 15\,\mu m$) are also useful for many remote sensing applications. The Advanced Spaceborne Thermal Emission and Reflection Radiometer (ASTER) is an example of such an instrument that captures spectral imagery in the thermal infra-red bands for a variety of applications [24]. Although the demand for thermal spectral data is lower than for shorter wavelengths, such data has the advantage of providing radiative data as well as reflectance data.

Early remote sensing hyperspectral instruments were used to image from airborne platforms, but in the past 15 years the emphasis of hyperspectral remote sensing technology has been on developing spaceborne instruments. The deployment of the Hyperion instrument in 2000 represented the birth of high resolution spaceborne hyperspectral remote sensing [28]. While airborne instruments are good for mapping specific areas of ground at high spatial resolution, spaceborne instruments have the advantage of being able to provide full Earth coverage with a reasonable temporal resolution.

The information obtainable by an instrument is limited by the number of detector pixels available. This creates a trade-off between specifications in the instrument design for a given detector size. Due to the multitude of specifications required for different applications that cannot all be satisfied at once, different instruments are being developed for specific applications. Some instruments try to account for these limitations by operating in different modes, allowing trade-off to be performed during operation; for example, the CHRIS instrument can operate imaging 18 spectral bands at 20 m spatial resolution, or 62 bands at 40 m spatial resolution (see Table 1.1). With the appropriate amount of collaboration, however, a set of optimal spaceborne instruments can be developed that provide full coverage of the Earth's surface with high spectral resolution, spatial resolution, temporal resolution, and signal to noise ratio (SNR) over a complete spectral range.

1.6 The Contribution of this Thesis

The main aim of this thesis is to assess the degree to which the capabilities of currently available hyperspectral remote sensing instruments suit the current and potential application requirements, so that the potential remote sensing applications of a novel type of hyperspectral imaging instrument can be determined. This thesis begins with a review of current and potential applications of hyperspectral remote sensing data; and analyses to what extent currently available hyperspectral imaging instrument capabilities are optimal for these applications. Various processing and interpretation techniques are also analysed, which are used to convert raw instrument data into hyperspectral data, and convert hyperspectral data into quantitative scientific data.

The main contribution of this thesis lies in the analysis of the potential capabilities and applications

of microslice technology in hyperspectral remote sensing. A prototype hyperspectral imager with a novel optical design that uses microslice technology was built at Durham University for the purpose of this research, and as a proof-of-concept instrument. The unique capability of the microslice system design lies in its capacity to allow a 2-dimensional spatial area to be imaged simultaneously with relatively broad hyperspectral coverage. Laboratory and field tests were conducted using the prototype instrument, and the results were used in conjunction with data from modelling the remote sensing performance of the instrument to support an analysis of the advantages and disadvantages of using this novel approach to hyperspectral remote sensing.

Chapter 2 discusses the main applications of hyperspectral imaging in remote sensing, and the instrument requirements associated with these applications. It highlights the range of applications for hyperspectral remote sensing and the diversity of hyperspectral instruments required to meet these different requirements.

Chapter 3 looks at the data processing required to obtain fully calibrated hyperspectral data, and the analysis techniques available for deriving useful information from this data. A practical demonstration is presented of these techniques being performed on data from a current airborne hyperspectral remote sensing instrument.

Chapter 4 details the development of the prototype microslice hyperspectral imaging system that is the focus of the thesis. The optical design, initial testing and development of data processing software are the main focus areas of this chapter.

Chapter 5 presents laboratory tests that were performed using the prototype microslice spectrometer to determine its specifications and capabilities as a hyperspectral imaging system.

Chapter 6 documents field experiments that were conducted using the prototype microslice spectrometer to determine the capabilities of the instrument when imaging targets in their natural environment. This chapter also documents a field and laboratory spectroscopy experiment that was carried out to determine if hyperspectral remote sensing could be used to detect river pollutants.

Chapter 7 presents results from modelling the potential capabilities of a future microslice spectrometer deployed on a remote sensing platform, and compares this to the modeled performance of a conventional pushbroom hyperspectral remote sensing imager.

Chapter 8 presents the conclusions of this thesis.

Chapter 2

Environmental Applications of Hyperspectral Imaging in Remote Sensing

Hyperspectral imaging is a technique that was developed specifically for remote sensing of the Earth, but now has a wide variety of applications, both inside and outside of Earth Observation (EO). Aside from EO, hyperspectral imaging has been used in food quality control [33, 34], face recognition [35], and medicine [36, 37]. The main uses of hyperspectral imaging technology however are in EO remote sensing, and it is these applications that will be focused on in this chapter. Hyperspectral remote sensing data is used for a wide variety of applications, most of which fit into two categories: environmental and military. Military applications include surveillance and detection [38, 39]. There is not a lot of information freely available about these applications, however, so this chapter will focus on the environmental applications. Environmental applications can be split into many different categories, but predominately feature agricultural [40, 41, 42, 43, 44, 45], water quality [46, 47], forestry [48, 49, 50, 22], and geological [51, 52, 53] applications. Atmospheric imaging is also a common use of hyperspectral imaging , but this thesis will largely focus on ground imaging applications. In this chapter several examples of important hyperspectral remote sensing studies are provided for each of these key environmental application areas. These case studies are selected to give an idea of the variety of applications in each area, and provide examples of the methodologies used in such studies. These examples also will demonstrate the specific benefits that hyperspectral imaging brings to different applications of remote sensing, and the capabilities required of the instruments to gather the appropriate data.

2.1 Hyperspectral Remote Sensing for the Environment

The focus of the vast majority of scientific research in hyperspectral imaging deals with environmental remote sensing because the status of the environment is becoming an increasingly important issue, as the effects of humanity on nature become more significant. In particular, issues such as global climate change and the depletion of fossil fuels are recognised as requiring urgent attention. In this section the use of hyperspectral remote sensing in four main environmental areas is documented. These areas are: agriculture, water quality, forestry, and geology.

2.1.1 Agricultural Remote Sensing

As the population of the Earth is expanding at an ever increasing rate, the efficiency of food production is becoming increasingly important. As a result of this farmers are always looking for new techniques and technologies to improve production, and remote sensing is the latest addition to the technological advancement of agriculture. Remotely sensed data can provide a lot of useful information to farmers; for example, it can be used to determine the amount of fertilizer required in different areas of the farm, or to detect areas of drought or disease [].

When analysing hyperspectral imaging data of vegetation, certain key absorption features are used for characterization that are caused by specific biological parameters, such as the level of water, chlorophyll or minerals present within the plant. These absorption features occur in the visible and near-infrared parts of the spectrum (400-1500 nm). An example of one very prominent spectral feature present in vegetation spectra is the *red edge* (see Figure 2.1). This is a sharp increase in reflectance that occurs between the red and near-infrared parts of the spectrum (around 680-740 nm). This feature is a result of a combination of chlorophyll-a having a high absorption in the red end of the visible spectrum, and plant cell scattering in the near infra-red [54].

Various spectral parameters of vegetation spectra can be used to determine certain biological parameters of the vegetation being imaged. One such spectral parameter is the position of the red edge, which is measured by the *red edge inflection point* (REIP). The REIP is defined as the point of maximum slope of the reflectance, and is an indicator of chlorophyll content of vegetation [55]. A high chlorophyll content broadens the chlorophyll-a absorption feature leading to a shift of the red edge to higher wavelengths. Similarly a low chlorophyll content narrows the chlorophyll-a absorption feature, shifting the red edge to shorter wavelengths. The REIP is also an indicator of nitrogen concentration [56], and leaf area index (LAI) [42], which is a parameter that is defined in Chapter 3. Techniques for determining the position of the REIP are also presented in Chapter 3

Case Study I: The Effects of Weed Infestations and Nitrogen Deficiency on Corn Crops

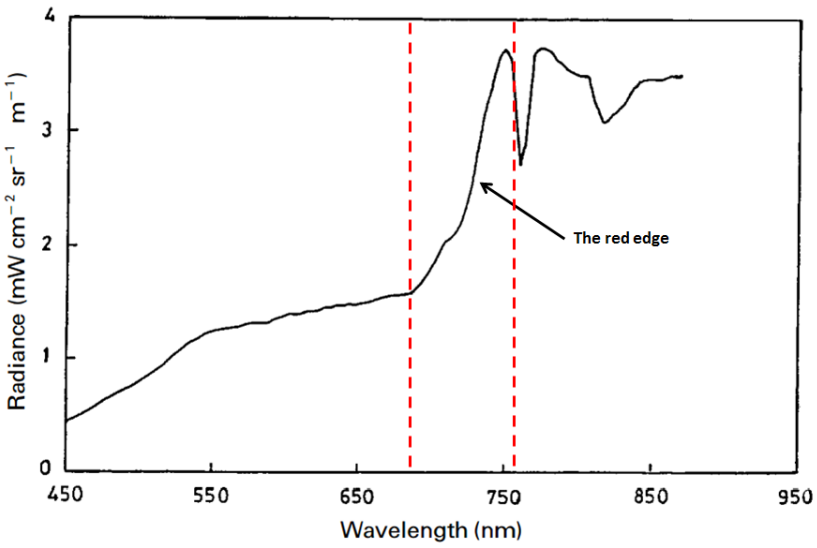

Figure 2.1: This graph shows a typical reflectance spectrum of a wheat plant. The position of the red edge is the part of the spectrum between the two red dotted lines. This is a prominent feature in all vegetation reflectance spectra, and the spectral parameters of the red edge can be used to determine biological parameters of the vegetation. The peak at about 550 nm is due to the presence of chlorophyll, and the sharp dips at 765 and 830 nm are due to atmospheric oxygen absorption. This image was taken from [41].

Since the advent of hyperspectral remote sensing, much research has been conducted to assess its potential applications in agriculture. There have been many studies that have sucessfully used hyperspectral remote sensing to determine various health parameters of crops [ ]. Key factors affecting the health of agricultural crops include the plant Nitrogen content and level of weed infestation. One particular study conducted in 2000, shows the capabilities of using remote sensing to detect nitrogen deficiencies and weed infestations in corn crops [19]. This study was chosen as it clearly shows the methodology, rsults, and implications of the study. The airborne hyperspectral instrument CASI (see Table 1.1) was used to image a test area of corn crops at a 2 m spatial resolution with 288 spectral bands in the 400-950 nm wavelength range. Four corn plots of 80 x 20 m were created as test areas, each with a different level of weed control. Each plot was split into three 20 x 20 m sub-plots, each of which had different rates of nitrogen (fertiliser) application. All plots were imaged at three different stages of growth using the CASI instrument from an aircraft that was flown at an altitude of around 1100 m.

This study showed that a higher level of weed control corresponded to a lower reflectance intensity in the near-infrared region of the spectrum (see Figure 2.2). It was also shown that higher nitrogen application rates were also linked to higher reflectance intensities in the near-infrared region of the spectrum. These trends are caused by the increase in biomass that is expected as a result of the presence of weeds or higher levels of fertilisation. Calculations were carried out to determine if there

were statistically significant differences between the data from the different plots, for detection of weeds and nitrogen levels. Only at the medium and high nitrogen application rates was there no significant difference between some weed control and full weed control. It was found that between all other combinations of parameters there were significant differences between the results at the 2σ level. This study has therefore shown that it is possible to use hyperspectral remote sensing data to detect weed infestations and nitrogen levels in corn crops at different stages of growth.

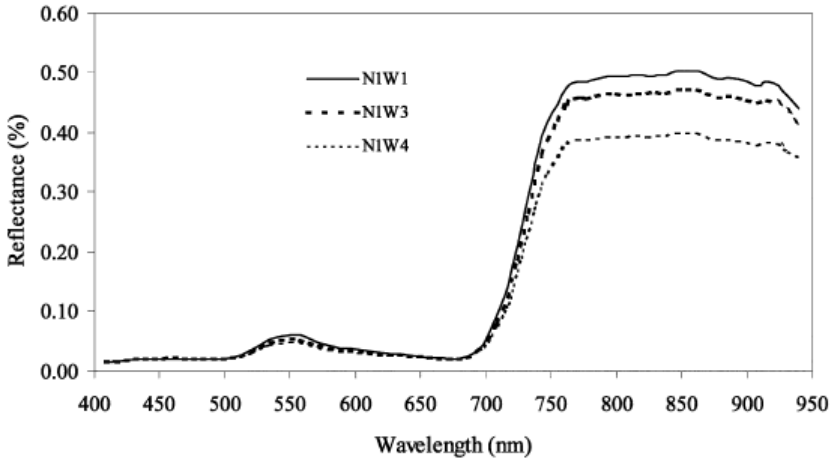

Figure 2.2: This graph shows the reflectance of corn crops that have been subject to different levels of weed control, as measured by the airborne CASI spectrometer operating in 288 band mode [19]. In the legend N1W$\boldsymbol{x}$ refers to a normal level of nitrogen application and weed control of level $\boldsymbol{x}$, where a higher value of $\boldsymbol{x}$ represents more stringent weed control This figure was taken from [19].

Case Study II: Measuring Soil Salinity Using Hyperspectral Data

The salinisation of soil can be natural or human-induced, and is a major environmental hazard. It has been estimated that 1 billion hectares of land is naturally salt-affected, with a further 77 million salinised by human activity [57]. Studies have been carried out to determine the potentials and constraints of detecting soil salinisation using hyperspectral remote sensing [ ]. In 1999 a study was carried out in the Murray-Darling Basin, Australia with two aims: to assess the ability of spectral imagery to measure soil salinity, and to determine if irrigation induced soil salinisation can be detected using hyperspectral remote sensing [58].

This study is used in this thesis to highlight the importance of gathering ground truth data when performing hyperspectral remote sensing. Ground truth measurements are important as they provide a benchmark by which to assess remotely sensed data. There are two types of ground truth measurements. The first type are spectral readings taken at ground level with a high resolution field spectrometer; these are used to assess the accuracy of the remote sensing spectral readings, and are particularly important when testing a new remote sensing instrument. The second type are physical samples taken from the target areas that are used to determine a particular physical or chemical char-

acteristic of the target, which can be compared to the remote sensing data. The first type are used for validation of the remote sensing instrument, and the second type are used to determine if remote sensing data can be used to measure a particular ground parameter.

In this study both types of ground truth data were acquired to satisfy the two aims of the field work. Physical samples of soil were taken to provide ground truth data about the salinity of the soil, and a FieldSpec FR field spectrometer was used to take spectral ground truth measurements of soils of different salinity. The FieldSpec FR provided 1 nm spectral resolution over the 350-2500 nm wavelength range. The results obtained from these ground truth measurements are shown in Figure 2.3, and show that the level of salinity of soil has an impact on its reflectance.

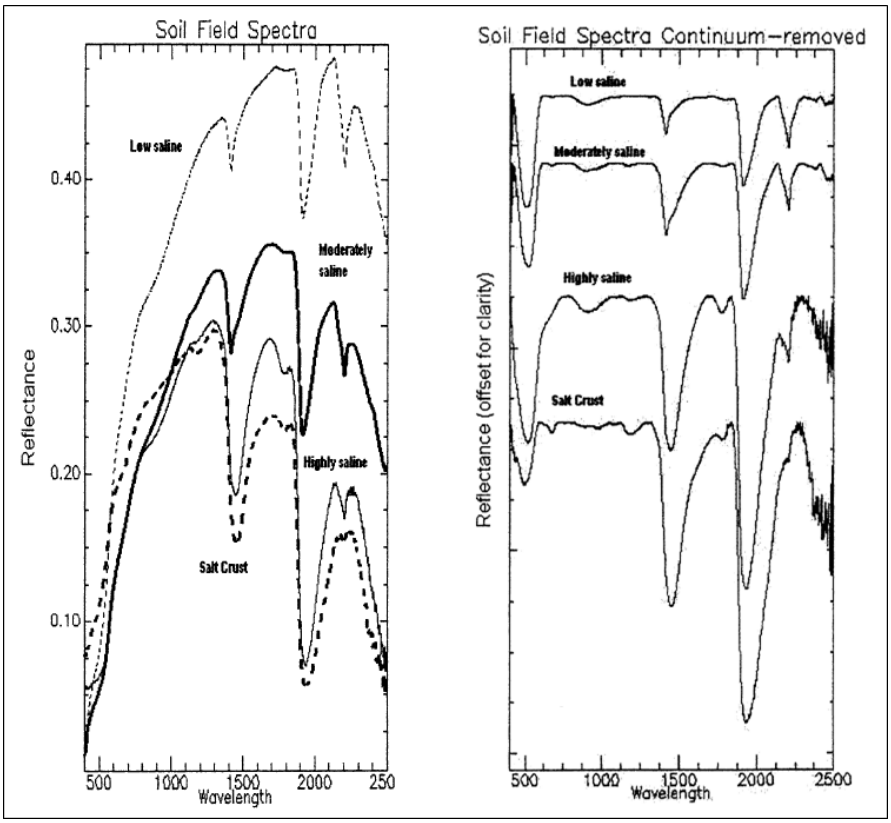

Figure 2.3: This figure shows the reflectance spectra of soils of different salinity. The graph on the left shows the relative reflectance of each soil type, while the graph on the right shows the continuum removed spectrum of each soil type. See Section 3.1.3 for details on continuum removal. This figure was taken from [58].

The HyMap spectrometer was used to obtain a remotely sensed hyperspectral image of the test area with 128 bands of approximately 20 nm width in the 400–2500 nm spectral range, at approximately 5 m spatial resolution. Spectral unmixing was performed on this data (see Section 3.1.6) to create a map of salinisation in the area (see Figure 2.4). This gave an accurate indication of salt-affected areas, showing that highly saline soil and salt crusts generally occur around the edges of drainage channels.

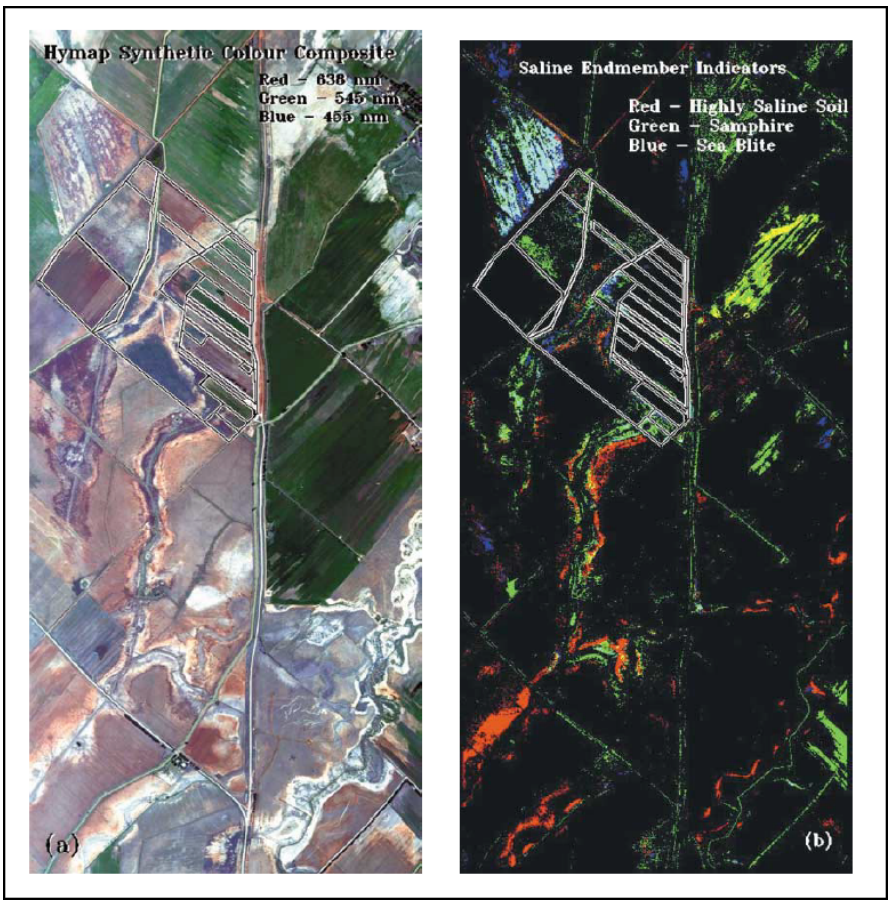

Figure 2.4: This figure shows two maps of an agricultural test area produced from HyMap hyperspectral data. The map on the left uses standard RGB bands to create synthetic true-colour image of the test area. The map on the right uses three derived endmember spectra as RGB bands to highlight the presence of salinisation (highly saline soil in red, samphire in green, and sea blite in blue). This figure was taken from [58].

Case Study III: Detecting Variations in Wheat Crop Growth Parameters

Due to the large amount of information provided by hyperspectral remote sensing, it can be used to assess multiple plant growth parameters [ ]. A study was conducted in 1997 to examine the ability of airborne hyperspectral imagery to detect variations in crop growth parameters. This study examined two of the most important parameters, leaf area index (see Section 3.1.2), and total chlorophyll content [41]. Information about these parameters has been linked to the position of the REIP .

The spectrometer used in this study was the Airborne Imaging Spectrometer for Applications (AISA) (see Table 1.1), which gathered data at 2 m and 10 nm spatial and spectral resolution respectively. The instrument was flown at an altitude of 3 km to image an area of approximately 10 x 2 km. This area contained 17 wheat plots, each of which was at a different stage of growth. Physical samples of the crops were also taken at random from each plot in order to provide ground truth data of the leaf area index (LAI) and chlorophyll content of the plants.

The ground truth measurements found that in general, more mature wheat crops had a lower LAI and a lower chlorophyll content than younger crops, particularly those that were flowering. This implies that being able to determine the LAI and chlorophyll content of a plot area can give a good indication of the stage of growth of the crops. The hyperspectral remote sensing results found that there was a loose linear relationship between the position of the red edge inflection and LAI, as well as chlorophyll content (see Figure 2.5). For a LAI ranging from 0.08 to 3.16 and a chlorophyll content ranging from 2 to 39 gm^{-2}, the REIP wavelength was shown vary from 713 to 723 nm.

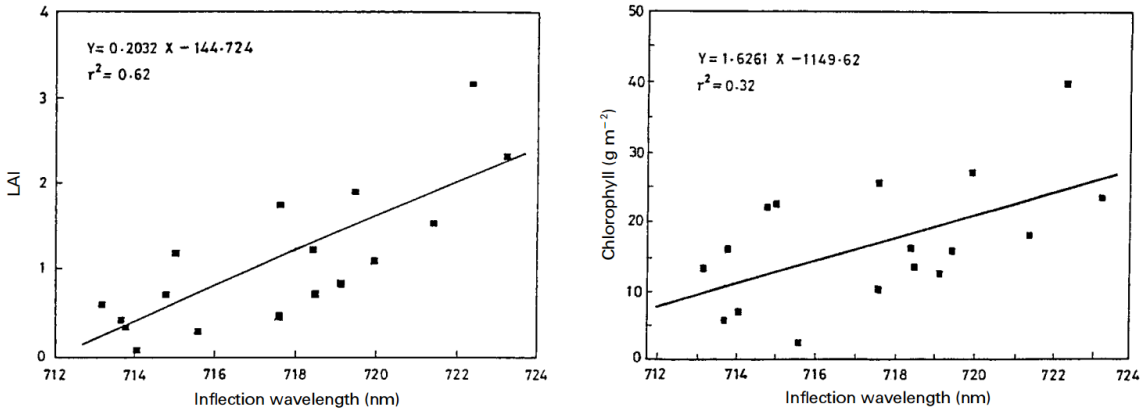

Figure 2.5: These graphs show the correlation of the LAI and chlorophyll content of wheat crops with the wavelength of the inflection of the red edge in their reflectance spectra. These graphs were taken from [41].

This study has shown that hyperspectral remote sensing can be used to determine the growth stage of wheat crops, and to do so requires a spectrometer with spectral resolution of under 2 nm in the 670-780 nm spectral range. This information can be used by farmers to determine the productivity of different areas of land, as well as the most appropriate time to harvest.

2.1.2 Water Quality Remote Sensing

Maintaining a high standard of water quality in rivers, lakes, reservoirs and coastal areas is very important, as these provide habitats for thousands of animal species, as well as drinking water for communities. It is therefore important to monitor the quality of such waters to check if they are becoming polluted, and to take measures to combat any pollution that is occurring. Remote sensing has been proven to be a key tool in monitoring water quality, and this section details two studies that have used hyperspectral remote sensing data in this way.

Case Study I: The Monitoring of Coastal Water Pollution

There are many different parrameters affecting water quality that can be imaged using remote sensing [ ]. This case study looks at mapping three of the main parameters in the coastal area of Moreton Bay, Australia [46]. Data from six passes of the Hyperion sensor (see Table 1.1) in 2000/2001 were used as test data. Data was gathered with 30 m spatial resolution, and 10 nm spectral resolution across the 400-2500 nm wavelength range. In-situ ground truth reflectance measurements were also collected at the same time as these passes. Figure 2.6 shows a comparison between the in-situ reflectance and the remotely sensed reflectance of the coastal area.

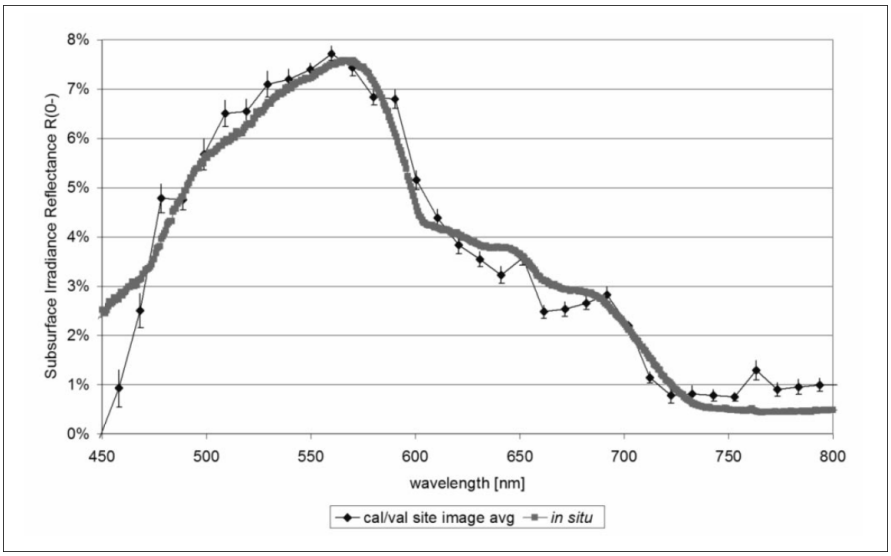

Figure 2.6: This graph compares the spectral reflectance of the coastal area of Moreton Bay, Australia as measured by Hyperion to the reflectance measured by in-situ spectral measurements. This graph therefore represents a validation of the atmospheric correction used, and was taken from [46].

The spectral imagery was used to make maps of the chlorophyll, coloured dissolved organic matter (CDOM), and the total suspended matter (*tripton*) of the coastal area (see Figure 2.7).

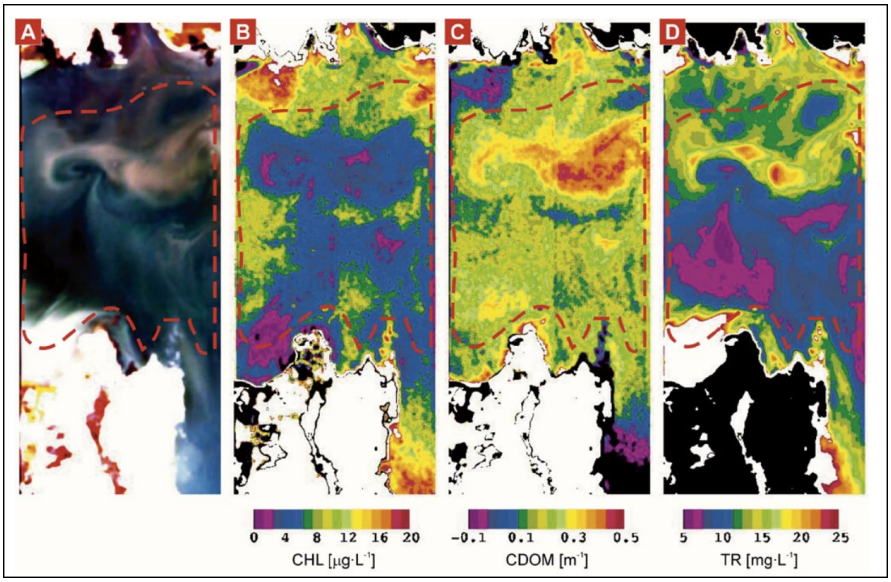

Figure 2.7: This figure shows four maps of the coastal area of Moreton Bay, Australia generated using data from the spaceborne Hyperion imager. The four maps show: A - low-pass filtered subsurface irradiance reflectance from Hyperion imagery, B - chlorophyll content (CHL), C - coloured dissolved organic matter (CDOM), and D - tripton (TR). The dashed red line defines the cloud-free and optically deep water region. This figure was taken from [46].

Case Study II: Measuring the Water Quality of Lakes in Finland

One of the tasks of the Finish Environmental Administration is to monitor and classify the quality of the lake water in Finland. Prior to April 2001 this was done by obtaining and testing water samples taken from many of the largest lakes across Finland. Although this provided a reasonable assessment of the general quality of lake water, the data obtained was very limited. This method only covered 79% of the total lake surface area in Finland. It also provided no measure of the spatial variation of water quality within lakes, and the temporal resolution of the data was fairly poor (one measurement every 4 years) [47].

This case study shows how using remote sensing to classify the water quality in the lakes improves upon the current limitations. It also shows the diversity of hyperspectral imagery, with two of the three water quality parametersbeing distinct from Case Study I. An experiment was carried out to assess the potential of using hyperspectral remote sensing to classify the water quality of lakes using the Airborne Imaging Spectrometer for Applications (AISA) (see Table 1.1). This instrument was used to obtain data from 11 lakes over 8 non-consecutive days over the 450-900 nm spectral region, at a resolution of 1.6-9.4 nm. The hyperspectral data obtained had a spatial resolution of about 1 m, and was used to classify three variables: the turbidity, the chlorophyll-a content, and the Secchi depth. These variables all have threshold levels for acceptable water quality, which depend on what the lake is used for.

The turbidity of a lake is a measure of the cloudiness of the water, which is caused by suspended particles. For a high quality lake the turbidity of the water is expected to be low, as this means that there will be less particulate matter contaminating the water. An increase in turbidity in the water is revealed by a general increase in radiance across the spectrum due to scattering from the suspended matter. In order to make an accurate measure of the increase in reflectance due to turbidity, an area of the spectrum with minimal absorption from other substances is chosen. In this experiment the peak at 710 nm was chosen to be most appropriate spectral region (see Figure 2.8).

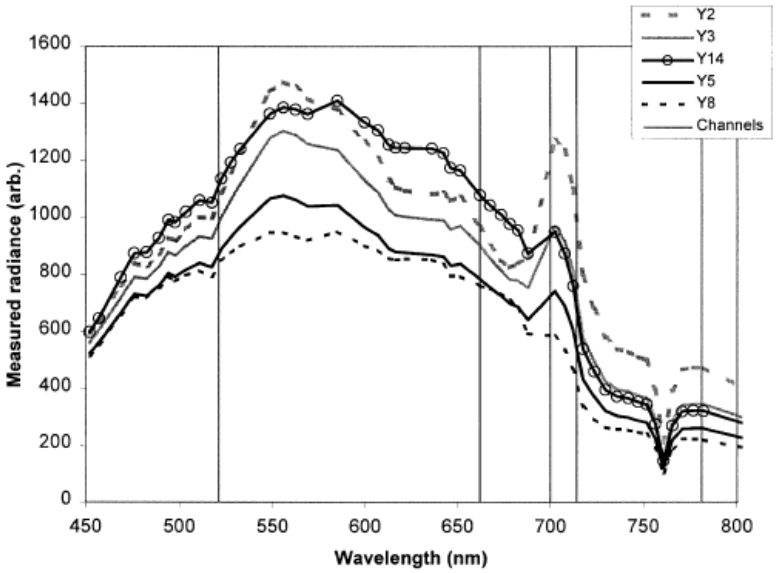

Figure 2.8: This graph shows the radiance of lake water in Finland measured by the AISA spectrometer. The different spectra show the radiance at different ground truth data points. The intensity of radiance peaks at about 710 nm are used to provide an estimate of the turbidity and chlorophyll-a content of the water at these points. This graph is taken from [47].

Chlorophyll-a is predominately found in plant life, and therefore provides a measure of the vegetation present in the lake. For a high quality lake the chlorophyll-a content is expected to be low, as this is an indication of low levels of algae and phytoplankton. A higher concentration of chlorophyll-a is linked directly to a higher spectral peak at around 700 nm (see Figure 2.8). This has been explained by the absorption caused by phytoplankton (660-670 nm), as well as the chlorophyll-a fluorescence, which has a peak at about 685 nm [59]. The variation in intensity of radiance peaks at 700 nm in Figure 2.8 represents a chlorophyll-a variation of $7.5 - 70\,\mu g\,l^{-1}$, with the extremes being for points Y8 and Y2 respectively.

The Secchi depth is a measure of the clarity of the water. It is not a very well defined parameter, generally given by the depth to which a metal disk (know as a Secchi disk) can be lowered into the

water while still being visible. It is therefore not an independent variable, and is inversely related to both the chlorophyll-a content and the turbidity, as shown in Figure 2.9.

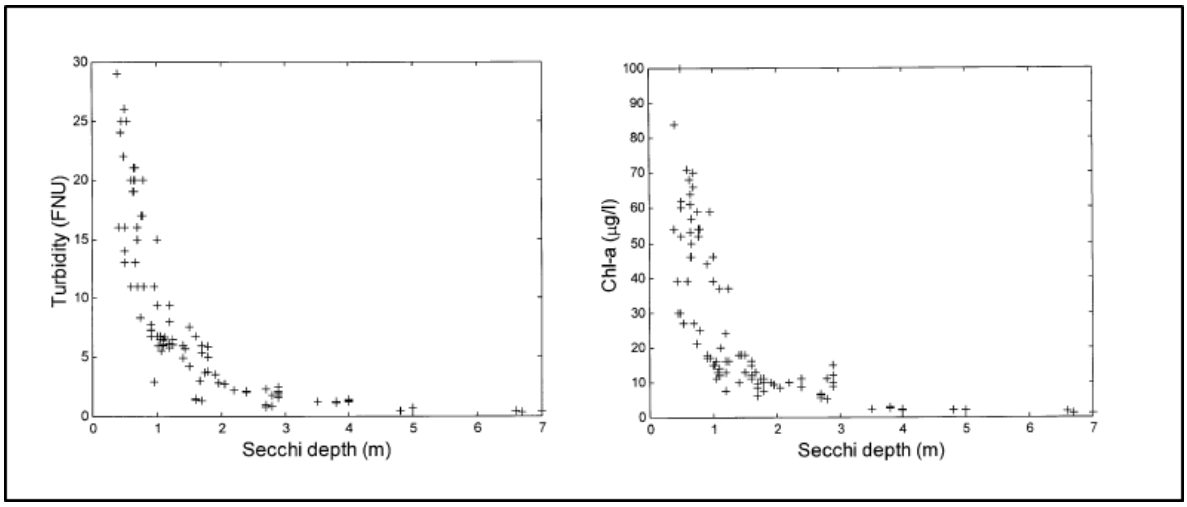

Figure 2.9: These graphs show how the Secchi depth of the water in Finish lakes is correlated with the turbidity and the chlorophyll-a content. FNU stands for Formazin Nephelometric Units. The graphs are taken from [47].

The spectral characteristics of the AISA data were used to classify the levels of the three water quality parameters. These classifications were compared to the ground truth data obtained at the same time. It was found that the Secchi depth could be classified by hyperspectral remote sensing with an accuracy of 88%, the turbidity with a accuracy of 76%, and the chlorophyll-a with an accuracy of 81%. These results, however, were achieved for complete classification, and hence lead to false positive rates of 12%, 24%,and 19% respectively.

The main advantage of using remote sensing data to monitor lake water quality is the high spatial and temporal resolution that can be attained. Remote sensing monitoring means that lake quality can be assessed several times a year, rather than only once every four years. Also 100% of the lake area can be covered, and any variations of quality across the lake can be detected. On top of this, the time and manpower required to obtain a full set of data is much lower when using remote sensing.

This study shows that reasonably accurate measurements of lake water quality can be taken using hyperspectral remote sensing. This method of assessing the water quality is faster, cheaper, has greater coverage, and can be done more often than traditional in-situ measurements of water quality. This technique requires data with a spectral resolution of about 5 nm in the 660-720 nm spectral region, and a spatial resolution of better than 50 m to measure the smallest lakes. The information can be used by the Finish Environmental Administration to keep track of the water quality of lakes in Finland.

2.1.3 Forestry Remote Sensing

Forests play an extremely important role in maintaining the health of the planet, as they are a key part of the carbon and water cycles. Forests also provide habitats for millions of insect species as well as thousands of species of other animals and plants. With deforestation destroying approximately 8 million hectares of forest per year [60], it is important that deforestation is monitored closely and that forests are protected from disease, forest fires and illegal logging. These are just some of the problems facing forests, which are very difficult to monitor on the ground, but are much easier to monitor with aerial imaging. Studies have shown that hyperspectral remote sensing has great potential in the monitoring of forests to deal with such issues.

Case Study I: Estimating Forest Productivity Through Remote Sensing of Canopy Nitrogen

The nitrogen content in foliage is related to the rate of photosynthesis, and can thus be related to the level of carbon dioxide in the atmosphere. This has already been done for various separate plant species over small areas [61]. If this could also be done for a large diverse forest, however, then the rate of growth of the forest could be estimated, and the nitrogen and carbon cycles of a whole ecosystem could be linked. Remote sensing therefore has the potential to be of great use in estimating forest productivity, as it is able to image a large area in a relatively short time frame. Several studies have attempted to use of hyperspectral imaging for this purpose with varying degrees of success [ ].

A study carried out in the White Mountain National Forest, USA in the late 1990s with the airborne AVIRIS spectrometer (see Table 1.1) demonstrated that hyperspectral remote sensing can be used to estimate the canopy level nitrogen concentration; and therefore can be used to estimate overall forest productivity [48]. This study used a total of 85 plots of varying sizes (0.09-0.64 km^2) that contained a variety of species as test areas within the forest. The AVIRIS data used had a spatial resolution of 20 m and a spectral resolution of 10 nm across the 400-2500 nm wavelength range. Ground truth data was also obtained by taking in-situ samples of the trees to determine the nitrogen concentration and wood biomass of the canopy. The samples were taken in mid-summer to coincide with the peak growing season and the over flight of AVIRIS. Partial least square (PLS) regression analysis was performed on the spectral data to produce a map of nitrogen concentration across the test areas (see Figure 2.10). PLS analysis is a type of dimensionality reduction algorithm that uses eigenvector analysis. Dimensionality reduction methods will be discussed in more detail in Chapter 3.

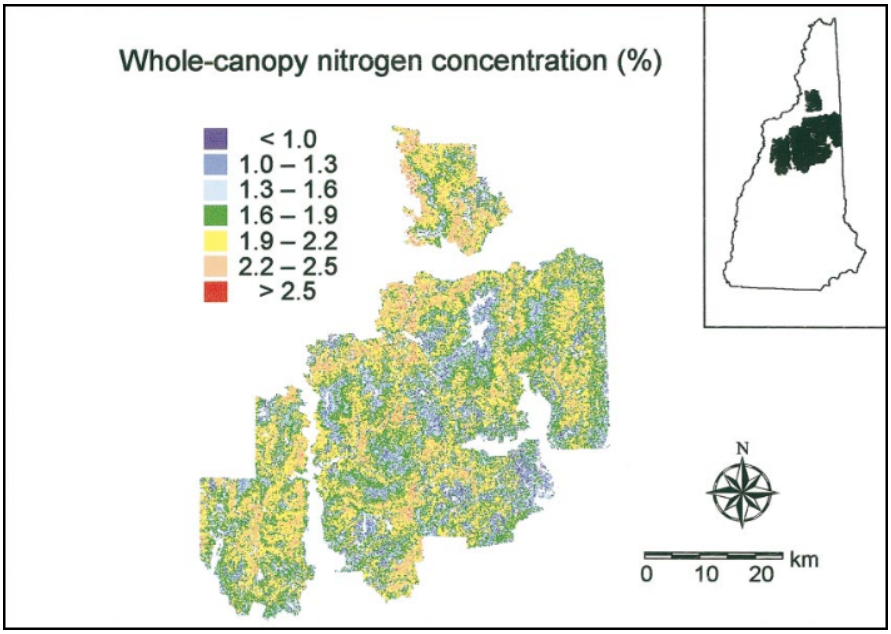

Figure 2.10: This image shows a map of the canopy nitrogen concentration across an area of the White Mountain National Forest. This map was generated using hyperspectral remote sensing data from the airborne AVIRIS spectrometer. This image was taken from [48].

Case Study II: The Mapping and Classification of Mangrove Ecosystems

Mangrove forests provide unique ecosystems that protect coastlines from high tides as well as support many food chains [62]. They are, however, in serious decline around the world, causing sedimentation problems and a shortage of fish supplies [50]. Tree type classification is a common use for hyperspectral remote sensing, and many studies have shown it's appropriateness for this task [ ]. The case study in this section shows a directly practical application of such classifications, and introduces a number of classification methods. The study was carried out using the CASI spectrometer (see Table 1.1) in conjunction with the Airborne National Aeronautics & Space Administration's Radar (AIRSAR) to remotely map and monitor mangrove forests. The test area used was the estuary of the Daintree River in Australia, because this area displays a large diversity of mangrove species.

The data gathered was in fourteen 10 nm bands in the 400-1000 nm spectral region with a spatial resolution of 2.5 m. Various classification techniques, including spectral angle mapper (SAM) and maximum likelihood (which will be presented in detail in Section 3.1.5), were applied to the spectral data to classify different mangrove types (see Figure 2.11). When applied to the CASI and AIRSAR data these methods were able to produce classification accuracies of up to 80%. This study showed that there is considerable scope in the use of hyperspectral and/or radar data, for mapping and monitoring mangroves for mangrove diversity or ecological studies

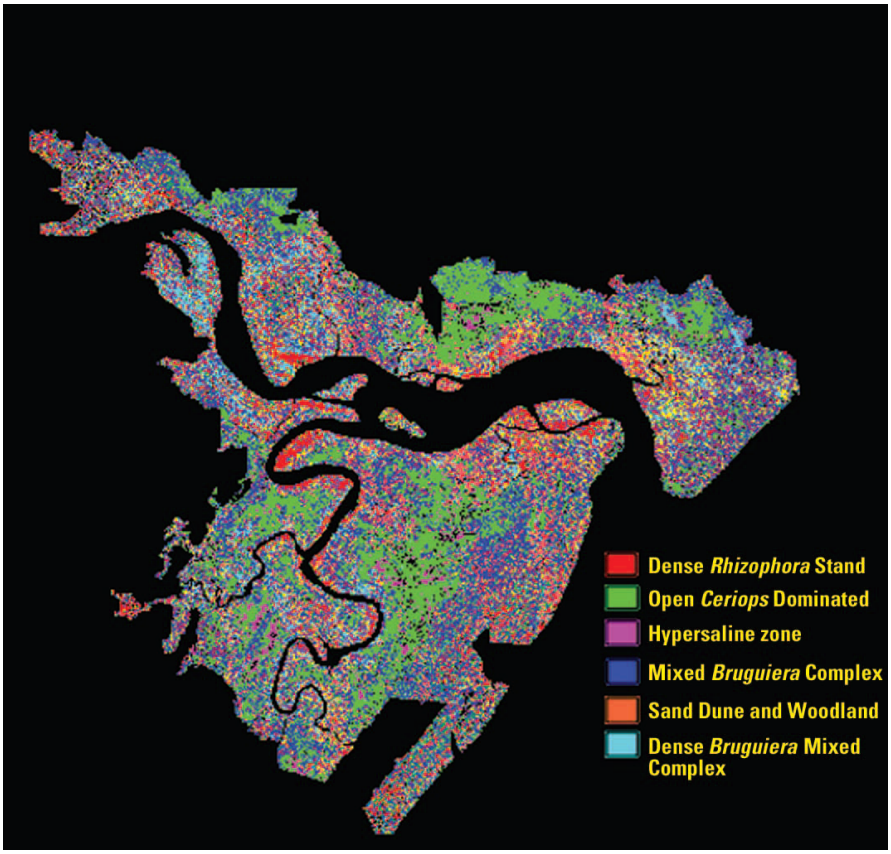

Figure 2.11: This image shows a classification map of mangrove tree types at the estuary of the Daintree River. The spectral angle mapper (SAM) classification technique was used on spectral data obtained from the CASI hyperspectral imager. This image was taken from [50].

Case Study III: Early Detection of Douglas-Fir Beetle Infestations

One common cause of poor health in forests is insect infestations. Infestation caused by Douglas-fir beetles are an issue throughout the western side of North America, attacking and killing small groups of trees (see Figure 2.12). Detecting and eradicating such infestations early is of great importance to foresters, who want to minimise economic loss due to spoilt timber. It has been asserted that multi-spectral remote sensing imagery had previously been used to map areas that have been infested [22]. To detect infestations early enough to prevent long term damage, however, higher spectral resolution is required.

The insect infestation causes changes in the leaf physiology, chemistry, and photosynthetic efficiency; which in turn affects the reflectance of the tree canopy. Various changes in reflectance spectra signify canopy stresses; in particular the width, depth, skewness and symmetry of absorption features can be analysed. This is another case study that highlights the usefullness of the large amount of data gathered by hyperspectral imagery for a specific application.

Figure 2.12: This image shows a typical group of trees that has been attacked and killed by a Douglas-fir beetle infestation. The characteristic red foliage occurs when a tree is already dead. This image was taken from [63].

A study was carried out in 1999 to test the potential use of hyperspectral imagery in early detection of Douglas-fir beetle infestations. A test area of Douglas-fir trees in Yellowstone National Park that had known occurrence of Douglas-fir beetle infestations was used [22]. Ground truth data was gathered by using field observations to classify the trees into three classes: *healthy*, *attacked* and *dead*. The Probe-1 hyperspectral sensor (see Table 1.1) was used from a helicopter to image the test area at a spatial resolution of 1 m, and a spectral resolution of 20 nm across the 400-2500 nm wavelength range.

Figure 2.13 shows the spectra retrieved from the Probe-1 sensor for different targets, including the three classes of trees. It can be seen that the overall shapes of the spectra are very similar, but specific features vary between classes. In such situations it is most appropriate to use CART (Classification And Regression Tree) analysis (which will be presented in detail in Section 3.1.5) to discriminate between classes, as this technique examines specific spectral features rather than the overall spectral shape.

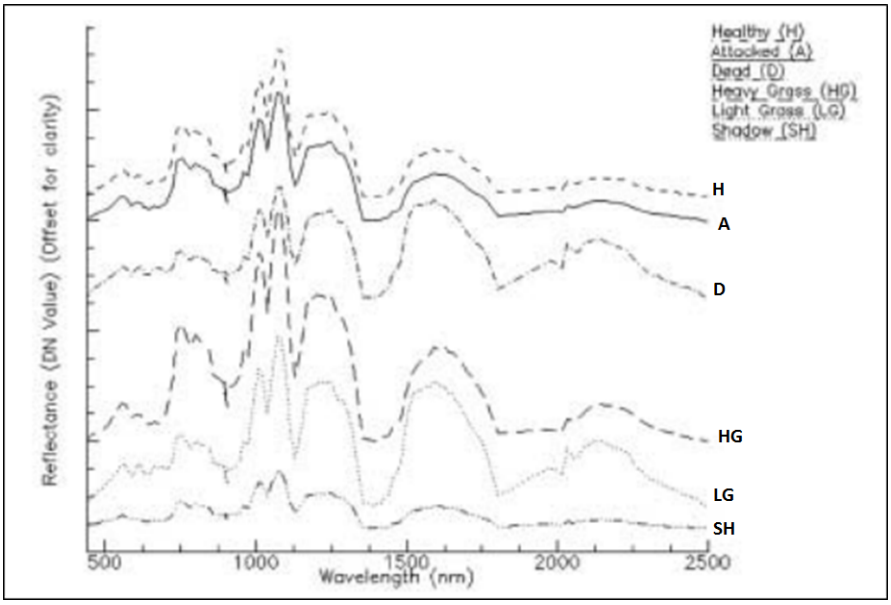

Figure 2.13: This graph shows the reflectance spectra of Douglas-fir trees in different states of health, as well as spectra of surrounding vegetation. The data was remotely sensed using the Probe-1 hyperspectral remote sensor, and was be used to determine discriminating features between classes. This graph was taken from [22].

Using CART an overall accuracy of 92.5% was achieved, with 100% accuracy in the attacked class. This study shows that hyperspectral imaging is able to detect all trees that are under attack from Douglas-fir beetle infestations. There will be false-positive detections, with some healthy and dead trees being incorrectly classified, but the most important detection trait for minimising damage to the forests is that no attacked tree goes undetected. This means that the false-positive results are not much of an issue, so long as there are not too many of them.

This study has shown that accurate early detection of Douglas-fir beetle infestations is possible, through the use of CART classification on remotely sensed hyperspectral data. This requires a spectrometer with a spatial resolution smaller than a tree canopy (about 5 m), and a spectral resolution of about 20 nm in the near and short-wave infrared spectral region. This identification can help forest owners to monitor infestations and to prevent them spreading, thus preventing timber from becoming spoilt.

2.1.4 Geological Remote Sensing

There are several different aspects to geological hyperspectral remote sensing. Hyperspectral remote sensing has been used for mineral mapping [64, 51], but environmental applications are primarily concerned with detecting natural and anthropogenic pollutants, as well as volcanic activity. This section details case studies of two such applications.

Case Study I: Detecting Hydrocarbons Using Remote Sensing

Hydrocarbon pollution of land is an issue due to its widespread occurrence and the risks that it poses to the health of ecosystems [65]. It is important to detect hydrocarbon contamination early, so as to reduce the potential ecological damage. The detection of hydrocarbons on the ground could also be a method of finding the remainder of the Earth's fossil fuels, which will extend the time available for transition into new energy sources. Hyperspectral remote sensing has previously been used to determine the mineral composition of large areas of land, making it a plausible method for providing a quick survey of large areas for the presence of hydrocarbons [51].

In 1998 a project named the Pro Smart Experiment began, which was organised by the German Aerospace Center [53]. This project is discussed here becuase the results have since been referenced in multiple studies [ ], and due to the dual purpose of the experiment: to develop a methodology for the detection and mapping of hydrocarbons, and to improve knowledge of the spectral properties of hydrocarbons. This involved carrying out an experiment to determine if hydrocarbon-bearing substances could be detected directly using the airborne hyperspectral scanner HyMap (see Table 1.1). The HyMap instrument provided data with a spatial resolution of about 5 m and spectral resolution of 10-20 nm across the 450-2500 nm wavelength range.

A test area was artificially constructed, containing small target areas with known chemical properties (see Figure 2.14). Some of the target areas contained hydrocarbons (contaminated sand, and plastic), while others did not. Spectral ground truth measurements were taken of the reference targets with a GER Mark V IRIS field spectrometer to determine the real spectral reflectance properties of the target areas. The known concentrations of hydrocarbons, and the spectra from the GER provided the two types of ground truth data required to satisfy the two aims of the study.

The reference area was imaged by the airborne HyMap instrument to determine if remote sensing could detect the same spectral features as the GER spectrometer. The HyMap instrument was used to image the reference area at two different altitudes (2200 m and 1137 m) to produce data with different spatial resolutions. The reference images created by HyMap were also used to determine the effects of under-sampling for small targets, as well as determining the limits of the method for levels of contamination in targets.

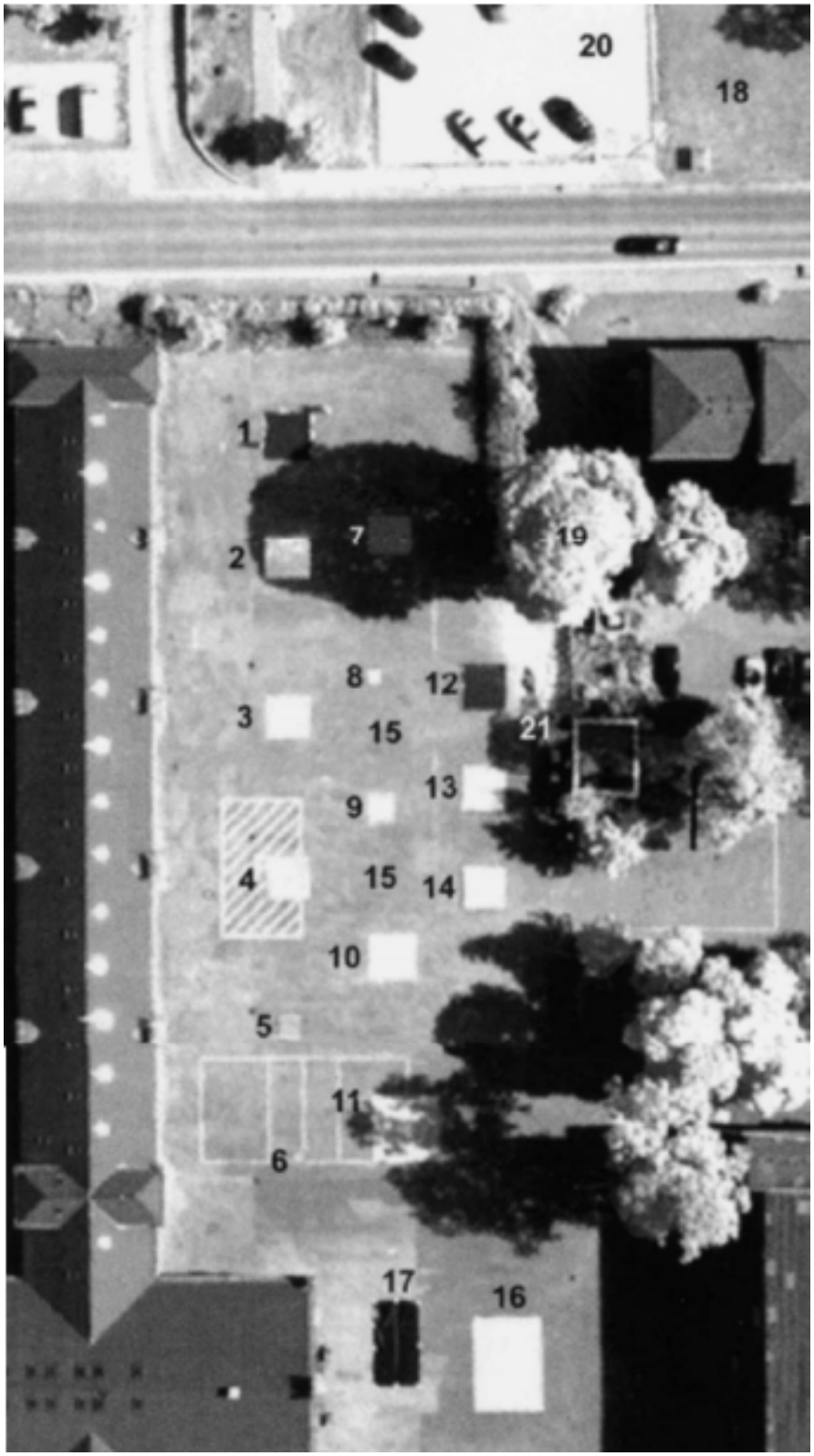

Figure 2.14: This image shows a plan view of a test target region that was used to test the potential of hyperspectral remote sensing for detecting hydrocarbons. Each numbered rectangle represents a separate especially constructed target of known composition. The image was taken with an airborne high resolution stereo camera at the same time as spectral data was recorded with the HyMap instrument. This image was taken from [53].

It had already been previously demonstrated that objects bearing hydrocarbons are characterized by absorption maxima at 1730 and 2310 nm [66]. The GER field spectrometer results show clear absorptions in the reflectance spectra of targets containing hydrocarbons at these two wavelengths (see Figure 2.15). The spectra from the HyMap data show the same features but less prominently than in the GER spectra. The 1730 nm feature is more prominent than the 2310 nm feature in the spectra from both instruments, and therefore the detection of this feature was deemed to be the most useful hydrocarbon indicator. Even the 1730 nm absorption spectral feature was not very prominent in the remotely sensed spectra, despite the superior signal to noise ratio (SNR) of the HyMap sensor compared to most other instruments (about 800 at 1730 nm, see Table 1.1). A remote sensing instrument with an even higher SNR would therefore be useful to detect this feature more distinctly.

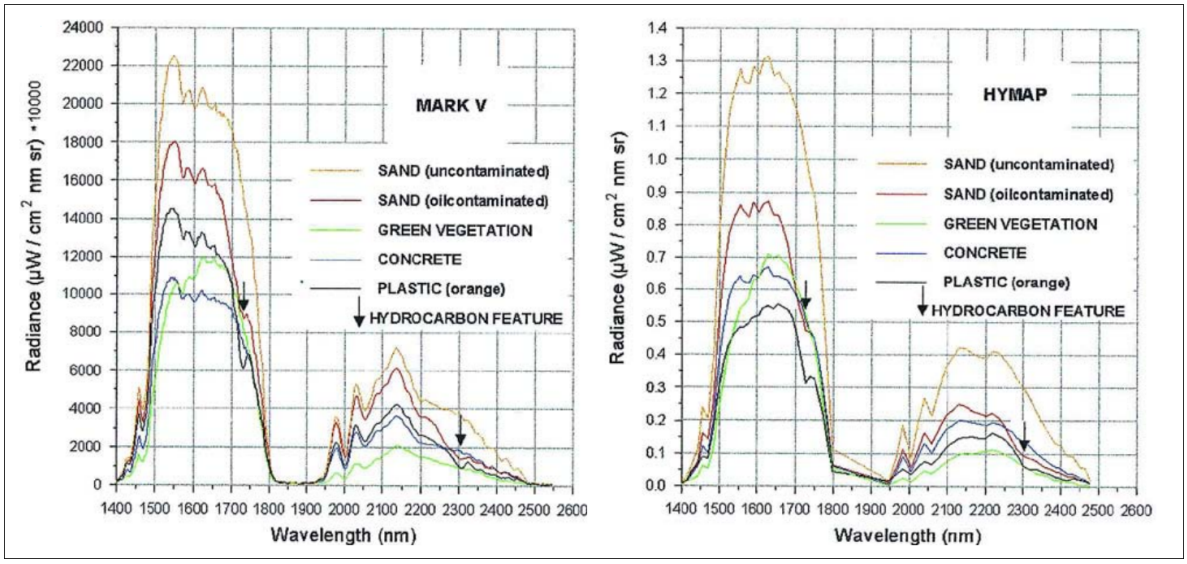

Figure 2.15: These graphs show the the reflectance spectra of various artificially created imaging targets, some of which contained hydrocarbons. The graph on the left shows the reflectance spectra of the targets when measured at close range with a GER Mark V IRIS field spectrometer. The graph of the right shows the reflectance spectra of the same targets measured with the HyMap hyperspectral imager from an altitude of about 1100m. The absorption features relating to the presence of hydrocarbons are indicated with arrows, and are visible on the appropriate spectra from both instruments, but can be seen much more prominently on the GER spectra. These graphs were taken from [53].

This study has shown that hyperspectral remote sensing can successfully be used to detect hydrocarbon contamination in sand. It is expected that this could be extended to contamination of other substances, such as soil, grass, and potentially water. A spectrometer with an SNR of at least 800 at 1730 nm is required, with a spectral resolution of about 10 nm in the short-wave infrared spectral region.

Case Study II: Assessing the Sulfur Dioxide Emissions from volcanoes

Assessment of the sulfur dioxide (SO_2) emission from volcanoes is important for two reasons. Firstly, SO_2 is a major pollutant to the atmosphere, causing acid rain and having significant impact on human health [67]. Secondly, the amount of SO_2 emitted from a volcano is a key parameter in understanding and anticipating volcano activity [68]. Monitoring SO_2 emissions from in-situ measurements is a logistically difficult, and dangerous task. Using remote sensing provides an easier, safer, and more accurate method of SO_2 monitoring.

The detection of atmospheric pollutants is also important for assessing urban air quality, and so several instruments that have previously been developed to measure atmospheric composition [ ]. These instruments are generally point-based spectrometers, rather than imaging spectrometers. This example is included here, however, to show the diversity of applications and requirements of hyperspectral remote sensing instruments, and also to highlight the possibility of developing an imaging spectrometer for SO_2 monitoring.

The point-based hyperspectral correlation spectrometer (COSPEC) was developed in the 1960s for measuring emissions from industrial plants, but its potential for monitoring volcanic emissions was quickly recognised [69]. The COSPEC spectrometer imaged at 2 nm resolution in the ultraviolet (UV) spectral region, and could be mounted on a moving platform, such as a car or aircraft to obtain total integrated concentration cross-sections of SO_2. In the early 1970s a study was carried out, which used COSPEC to measure the SO_2 emissions of Central American volcanoes [70]. Multiple COSPEC instruments have since been deployed, and have played a major role in many volcanic crises and eruptions [71, 72, 73].

Maintaining and replacing COSPEC instruments became very costly, however, with regular replacements costing $60,000 each. More recently a low-cost, miniature, ultraviolet fiber-optic differential optical absorption spectrometer (mini-DOAS) has been developed, as an up-to-date alternative to COSPEC [74]. The mini-DOAS detects spectra in the 245–380 nm range at 0.6 nm resolution, at a cost of less than $6,000 for all of the individual components. The performance of mini-DOAS spectrometer was assessed by performing a series of field experiments at the Masaya (Nicaragua) and Soufriere Hills (Montserrat) volcanoes in 2001. These experiments showed that this low-cost point based hyperspectral remote sensing instrument could be used to accurately measure the SO_2 flux emitted from a volcano. Figure 2.16 compares the SO_2 flux as measured by mini-DOAS and COSPEC of the Soufriere Hills volcano.

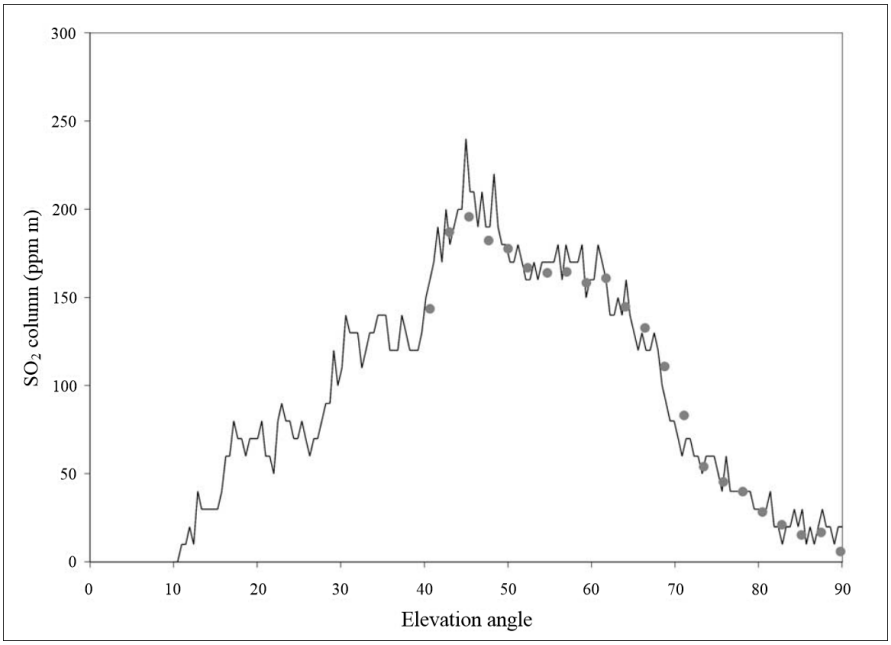

Figure 2.16: This plot shows the SO_2 flux released by the Soufriere Hills volcano measured at different elevation angles, from $\phi = 10°$ (i.e. close to horizon) up to $\phi = 90°$ (zenith). The graph compares COSPEC data (continuous line) to mini-DOAS data (circles). This graph was taken from [74].

2.2 Instrument Requirements for Remote Sensing Applications

This chapter has so far presented multiple applications for hyperspectral remote sensing technologies, which have mostly involved environmental monitoring. Due to the large amount of information contained within hyperspectral imaging data, each application uses different parameters of the data, and applies different processes to obtain their results. As a result of this, the different applications have different requirements for the capabilities of the instruments used. For example, when looking for a sharp spectral absorption feature over a large homogeneous area, an instrument with a high spectral resolution is needed; but when looking for variations in broad absorption features over a small spatial area, having an instrument with a high spatial resolution is more crucial.

The wavelength ranges required for spectral remote sensing instruments vary, but are almost always in the visible/near-infrared region of the spectrum (400-2500 nm), as this is where the significant spectral features of natural targets occur. The point based SO_2 spectrometer mini-DOAS, and multi-spectral instruments ASTER and MODIS are notable exceptions (see Table 1.1). Table 2.1 details the instrument specifications required for each of the applications discussed in this chapter, showing that different applications require a variety different specification. Developing a hyperspectral instrument always involves compromising the quality of various specifications of the instrument, and so different instruments are most appropriate for different applications. The development of new hyperspectral imagers with unique capabilities is therefore key to the progression of hyperspectral remote sensing

applications.

2.2.1 Driving Requirements for Applications

All of the applications described in this chapter have basic requirements of the spectral coverage, the spectral resolution, the spatial resolution, and the SNR of the instruments used. Some of these requirements can be matched by the majority of remote sensing hyperspectral instruments. Others, however, push the boundaries of what can be achieved by remote sensing spectrometry, and it is these that are the driving requirements. The aim of this section is to highlight the key driving requirements for the spectral instruments for each application. In this section, the details that are presented about the capabilities of current hyperspectral instruments are taken from Table 2.1.

I. Agriculture

The case studies in this chapter have shown that agricultural remote sensing is largely focused on the spectral signatures of crops, and the reflectance of soil. The imaging is largely done by aircraft remote sensing, as it is more suitable than satellite imaging for examining a relatively small specific area (such as a farm) at a variable temporal resolution.

The near-infrared part of the spectrum contains the most relevant crop parameters, in particular the red edge inflection point (REIP). The red edge presents a large intensity variation, meaning that the SNR of the data is not so important. Most airborne spectrometers provide a spatial resolution of less than 10 m, which is good enough for assessing the variation of crop properties. The spectral range required for detecting features on and around the red edge is 650-800 nm, which is within the range of most hyperspectral imaging spectrometers.

The driving requirement for detection of the REIP is therefore the spectral resolution. In agricultural Case Study III, changes in the chlorophyll content and LAI of wheat crops were shown to be determined to a greater degree of accuracy by detecting of the REIP more accurately, down to sub-nanometer resolution. This means that when looking for a suitable instrument for detecting the red edge one would look for an instrument with a high spectral resolution that can be used to image from an aircraft.

Application Type	Application	Spectral Range / nm	Spectral Resolution / nm	Spatial Resolution / m	SNR	Sensor used
Agricultural	Estimating LAI and chlorophyll-a content [41]	670 - 760	3	2	n/k	AISA
	Detecting Nitrogen deficiencies and weed infestations in crops [19]	400 - 950	7.5	3	n/k	CASI
Water Quality	Lake water monitoring [47]	660 - 720	2	100	n/k	MERIS
	Determining coastal water quality [46]	400 - 900	10	30	100	Hyperion
Forestry	Detecting Douglas-fir beetle infestations [22]	700 - 2500	~ 20	1	n/k	Probe-1
	Classification of a Mangrove forest [50]	400-1000	7.5	3	n/k	CASI
Geological	Detecting hydrocarbons in rocks/soil [53]	1600 - 2400	~10	< 10	800	HyMap
	Monitoring SO_2 emissions from volcanoes [74]	245 - 380	0.6	N/A	n/k	mini-DOAS

Table 2.1: This table shows the typical specifications required of hyperspectral imaging instruments for the various remote sensing applications that have been presented in this chapter. These specifications give an indication of the variety of hyperspectral instruments that are used for hyperspectral remote sensing. 'n/k' = not known.

II. Water Quality

The case studies in this chapter have shown that using spectral imaging to assess water quality generally requires the reflectance intensity of certain spectral features to be determined. These spectral features are reasonably narrow, requiring a spectral resolution of about 5 nm, but this is achievable for many hyperspectral instruments. The spectral features are generally related to vegetation absorption or scattering, which occurs in the visible and near-infrared range, and is covered by the majority of hyperspectral instruments.

The spatial resolution required for water monitoring is variable, with the size and shape of targets varying from large coastal areas to small rivers. The detection of small scale spatial variations in water quality are generally not required, however. For large areas, spatial resolutions of about 30 m are sufficient, which is within the capabilities of most spaceborne hyperspectral instruments. Imaging smaller water targets may require a smaller spatial resolution, and are also best monitored using airborne imaging, which is generally able to achieve a spatial resolution of less than 10 m. The spatial resolution is therefore only a driving requirement for providing precise spatial coverage over a very large spatial area.

The reflectance of water targets is generally low (see Figure 2.6), and the variations in reflectance intensity that must be measured are often quite small (see Figure 2.8). The key driving factor when assessing lake quality is therefore the SNR. Data with a high SNR will be able to detect variations in reflected radiance more accurately. Current instruments detect with a SNR of about 100-200, but it can be beneficial to have data with a much higher SNR [75].

III. Forestry

The case studies in this chapter have shown that the remote sensing of forests is purely concerned with detecting the reflectance features of tree canopies, most of which are found in the visible to near-infrared region of the spectrum (400-2500 nm). This full spectral range is covered by a several hyperspectral instruments (See Table 1.1). The spectral features are generally fairly prominent and broad (see Figure 2.13) meaning that neither a high spectral resolution nor a high SNR are necessary.

The spatial coverage required varies (from about 1 hectare to 1000s of hectares) depending on the area being surveyed. It is often beneficial to be able to classify individual trees, and so a spatial resolution of under 5 m is required for providing accurate mapping. For mapping large areas of forest at a high temporal resolution, it can be costly and time consuming to use airborne imaging, so spaceborne

imaging would be more suitable. No spaceborne hyperspectral imager is able to achieve a 5 m spatial resolution, however, and so the spaceborne spatial resolution is therefore the driving requirement for forest mapping. It would, be very challenging to develop an instrument that could achieve a 5 m spatial resolution and a full 400-2500 nm spectral range. One solution to this issue would be to image only the specifically required parts of the 400-2500 nm spectral range to reduce the amount of information required to be recorded by the detector.

IV. Geology

The case studies in this chapter have shown two very distinct geological remote sensing applications. The first was concerned with detecting hydrocarbons in the Earth's surface, where having a low spatial resolution has the advantage of more precise detection and mapping, but is not generally a requirement. The second was concerned with detecting atmospheric pollutants, and gathered spectral data but not spatial data.

The detection of hydrocarbons was shown to involve detecting two specific spectral absorption features at 1730 nm and 2310 nm. A spatial resolution of about 10 nm is therefore required over the 1600-2400 nm wavelength range. Such instruments are available (e.g. Hyperion (spaceborne) and AVIRIS (airborne)), but 10 nm is the limit of the currently available spectral resolution at these wavelengths. The two spectral features are very shallow, meaning that they will only be detectable if the SNR of the sensor is high enough. A SNR of about 800 is required, but an even higher SNR would be beneficial for detecting lower concentrations of hydrocarbons. Only the HyMap and HAWK sensors have a high enough SNR across the wavelength range. The driving factor in hydrocarbon detection is therefore being able to simultaneously achieve a SNR of over 800 with less than 10 nm spectral resolution.

The detection of atmospheric SO_2 was shown to require sub-nanometer spectral resolution in the ultraviolet (UV) wavelength range (245-380 nm). This wavelength range also requires high sensitivity, as there is strong atmospheric absorption of UV light, particularly below 300 nm [76]. These requirements are quire distinct from the capabilities of any current remote sensing imaging system. Since precise spatial information is not a requirement for SO_2 detection, especially designed point based spectrometers are used, which are tailored to the spectral requirements. Due to the small wavelength range required, it could be possible to develop a remote sensing hyperspectral imager with the necessary spectral resolution. Although this would provide more information about the spatial variation in SO_2 pollution, it would be much more costly than the current point based instruments. It would therefore be essential that a specific application of this spatial data is found, and/or additional applications of a sub-nanometer ultraviolet hyperspectral imager are found, to make it viable to develop such an instrument.

2.2.2 Summary

This chapter has demonstrated that different applications of hyperspectral remote sensing require different instrument specifications, and that each application has its own driving requirements, which is the current limit on instrument capabilities in that area. The spatial resolution, spectral resolution, and SNR have all been shown to be driving requirements for different hyperspectral remote sensing applications. The spatial coverage required of each application is dependent on the specific targets being imaged, while the temporal resolution required is dependent on the specific application of the data.

In the development of a hyperspectral instrument the amount of data that can be gathered is limited by the number of detector pixels available. Instrument design therefore involves a trade-off between the instrument specifications, as improving one of the instrument driving requirements will limit the other capabilities of the instrument. Different instruments, with different designs are therefore required to address each of these driving requirements individually.

The potential applications of hyperspectral data is not only dependent on the specifications of the instrument, but also the processing and interpretation techniques employed. Choosing the optimal way to process and interpret hyperspectral data is important, as it makes the best use of the data available. The driving requirements for applications are therefore not purely determined by the specifications of the instrument used, but are also affected by the the quality of interpretation techniques available. The next chapter presents and applies various different interpretation techniques that can be applied to hyperspectral data.

Chapter 3

Processing and Interpretation of Hyperspectral Remote Sensing Data

Chapter 2 provided examples of the most common hyperspectral remote sensing applications, and presented the methods and findings of the various remote sensing studies. Some of the methods of data interpretation used in these studies were mentioned, but they were not discussed in detail. The quality of the data interpretation techniques employed can determine the capabilities of the data. The first two sections of this chapter present some of the processing and interpretation methods that are commonly used when dealing with hyperspectral data. Hyperspectral data processing is used to convert raw sensor data into the form of a calibrated datacube, while hyperspectral data interpretation consists of analysing the spectral data with various mathematical techniques to obtain quantitative results. The third section of this chapter analyses the results obtained when specific classification methods were applied to hyperspectral data gathered from an airborne instrument.

3.1 Hyperspectral Data Interpretation Techniques

Due to the spectrally contiguous nature of hyperspectral data, it contains vast amounts of information, which is one reason that there are so many applications for hyperspectral imaging spectrometers. Due to the large amount of information available, there are also many potential analytical techniques that can be applied to hyperspectral data, and many different types of information that can be derived. The case studies in Chapter 2 mentioned some of the methods of interpreting hyperspectral data used to obtain quantitative results. These included comparing the shape or spectral position of spectral features (Section *2.1.2, Case Study II*), comparing mathematically defined parameters of spectra (Section 2.1.1, *Case Study III*) [41], and comparing the full spectral range for classification (Section 2.1.3, *Case Study II*). In this section the theory behind some of the key methods of hyperspectral data interpretation are presented. These methods can be split into three distinct categories:

1. Calculation of parameters: the red edge inflection point (Section 3.1.1), leaf area index and the

normalised vegetation index (Section 3.1.2).

2. Pre-interpretation algorithms: continuum removal (Section 3.1.3), dimensionality reduction algorithms (Section 3.1.4), and spectral unmixing (Section 3.1.6).

3. Classification techniques: minimum distance, maximum likelihood and spectral angle mapper classifications (Section 3.1.5), and regression tree classification (Section 3.1.7).

3.1.1 The Red Edge Inflection Point (REIP)

The position of the red edge is defined by the red edge inflection point (REIP), which is defined as the wavelength at the point of maximum slope of the reflectance spectrum around the 700 nm wavelength. The red edge is a relatively broad spectral feature (about 680-740 nm), but the shift in the red edge position between different levels of chlorophyll can be relatively small. Generally shifts of less than 10 nm need to be detected, and for some applications sub-nanometer detection can be useful. It is therefore important to be able to measure the REIP to a high degree of accuracy. Two key parameters that are used when locating the REIP are the minimum reflectance (R_0), which is minimum reflectance in the red part of the spectrum (about 670 nm), and the shoulder reflectance (R_s), which is the maximum reflectance at the near-infrared plateau (about 780 nm). There have been many different proposed methods for determining the exact position of the REIP from spectral data, each of which involves fitting a curve to the spectral response, or a derivative of the spectral response. The five main methods for calculating the REIP are discussed here: linear interpolation, inverted Gaussian modelling, maximum first derivative, polynomial fitting, and linear extrapolation.

The linear interpolation method is the most simple way of determining the REIP, and is based on the assumption that the reflectance at the REIP is halfway between the minimum reflectance and the shoulder reflectance. This is shown by Equation 3.1, where R_{REIP} is the reflectance at the REIP. Data from bands either side of the red edge are used for linear interpolation to determine the wavelength at which this reflectance is achieved, as in Equation 3.2, where λ represents wavelength, i pertains to the band before the REIP, and j pertains to the band after the REIP [77].

$$R_{REIP} = \frac{R_0 + R_s}{2} + R_0 \tag{3.1}$$

$$\lambda_{REIP} = \lambda_i + \frac{R_{REIP} - R_i}{R_j - R_i}(\lambda_j - \lambda_i) \tag{3.2}$$

The linear interpolation method works reasonably well for spectrally accurate data, but more complex methods can provide a more precise measure of the REIP, particularly for less accurate spectral data.

The inverted Gaussian modelling method fits a Gaussian distribution function to the reflectance around the red edge. Equation 3.3 is used to model the reflectance, where R_{est} is the modeled reflectance, λ_0 is the wavelength at the minimum reflectance, and σ is the Gaussian shape parameter with units of nm. The values of R_0, R_s, λ_0 and σ are adjusted to minimise the root mean square error (RMSE) between R_{est} and the actual data points. Once these parameters have been calculated the REIP is defined as $(\lambda_0 + \sigma)$ [78].

$$R_{est}(\lambda) = R_s - (R_s - R_0) \exp\left(\frac{(\lambda - \lambda_0)^2}{2\sigma^2}\right) \tag{3.3}$$

The maximum first derivative method calculates the first derivative of the reflectance spectrum using a first derivative transform. The position of the first derivative maximum over the 680-740 nm range is taken to be the REIP [55].

The polynomial fitting technique is similar to the maximum first derivative method. It generally works by fitting a fifth degree polynomial to the reflectance spectrum over the 680-740 nm range, before calculating the first derivative of this curve. The position of the first derivative maximum is again taken to be the REIP [79].

One of the problems of methods that use the first derivative of the reflectance, is that the derivative curve often produces two peaks (due to the nitrogen content), making it ambiguous as to where to define the maximum. The linear extrapolation method was developed to mitigate this double peak by extrapolating from points around the minimum reflectance and two points around the shoulder reflectance on the first derivative curve [80]. The intersection of these points is taken to be the REIP (see Figure 3.1).

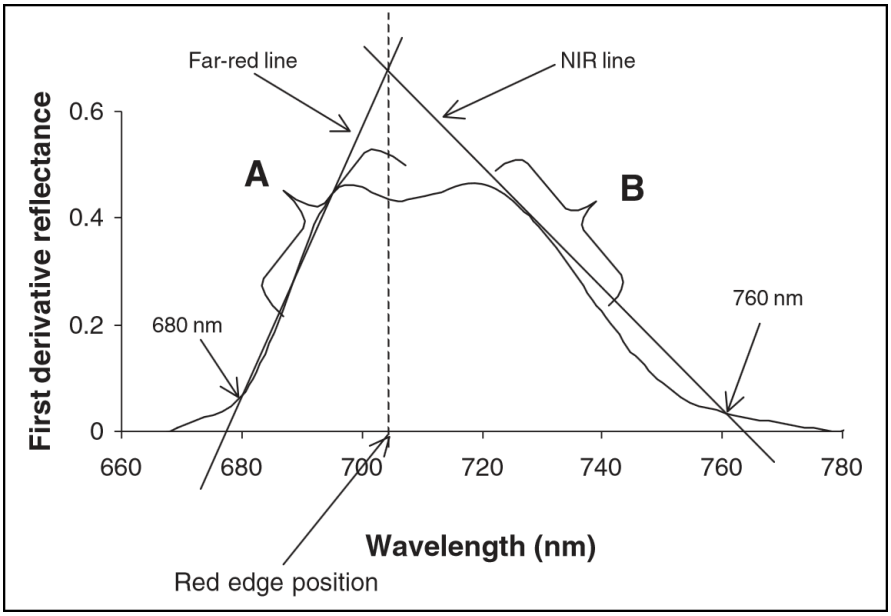

Figure 3.1: This graph demonstrates how linear extrapolation can be used to find the red edge inflection point for vegetation spectra that contain a double slope maximum due to nitrogen content. This figure was taken from [80].

A study was conducted to determine how accurately the REIP definition of each of these five methods could be used to determine nitrogen concentration in vegetation [80]. The data used was from a GER 3700 spectrometer, re-sampled at 10 nm resolution. A straight line was fitted for regression between nitrogen concentration and REIP. This was done for three different vegetation types, and the coefficient of determination (R^2) was calculated for each method (see Figure 3.2). It can be seen that the linear extrapolation method gives the highest R^2 value for each vegetation type, and is therefore the best REIP method for estimating the nitrogen concentration of vegetation using 10 nm resolution spectral data.

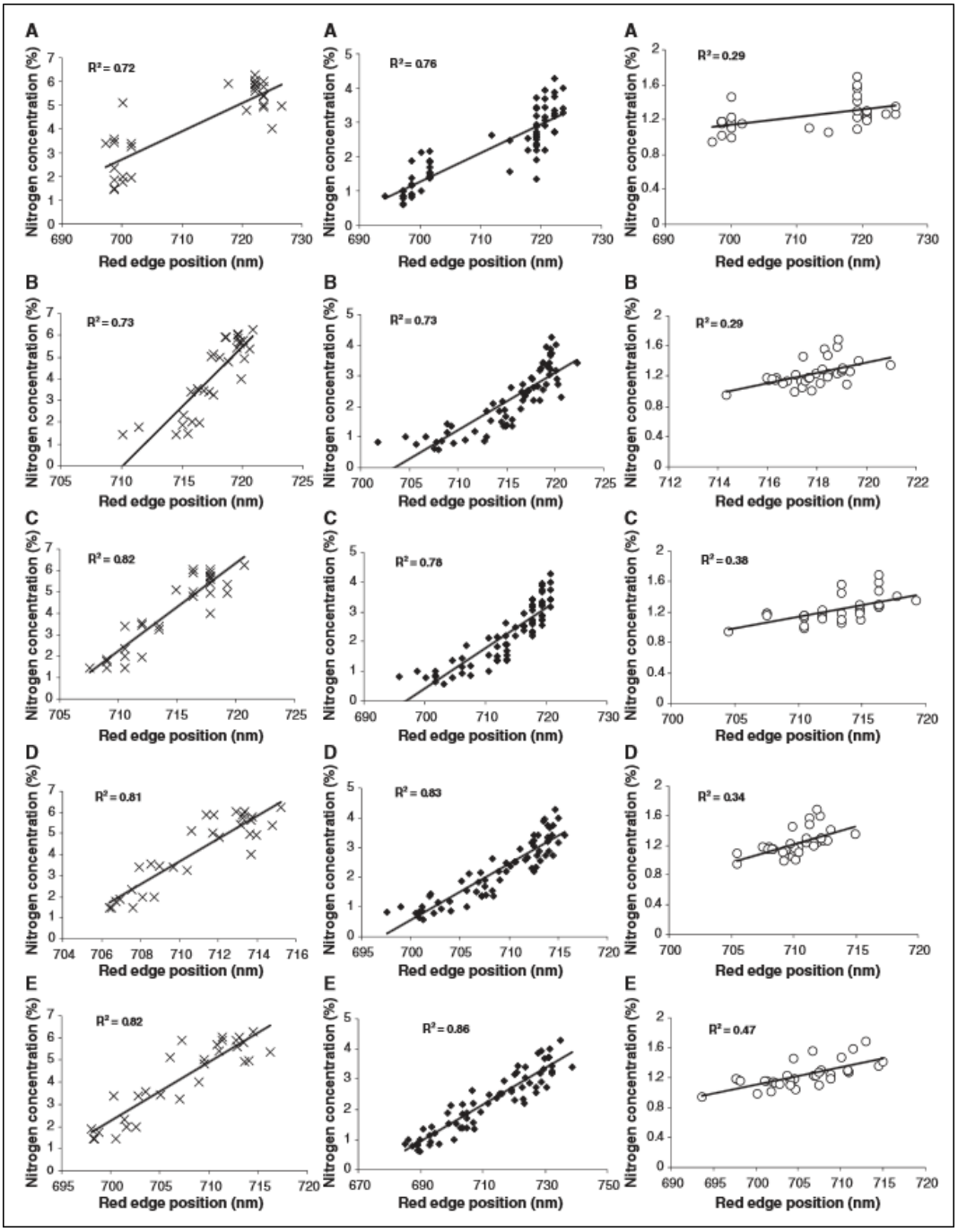

Figure 3.2: This figure compares how useful the five main methods of determining the red edge inflection point (REIP) are for determining the nitrogen concentration of vegetation. The method are: A - maximum first derivative, B - linear interpolation, C - polynomial fitting, D - inverted Gaussian modelling, and E - linear extrapolation. The vegetation samples used were: x = rye canopy, ♦ = maize leaves, and ○ = mixed grass/herb leaf. Straight lines are fitted for regression between nitrogen concentration and REIP for the three vegetation types. Regression fits with a high coefficient of determination (R^2) imply an accurate method for determining nitrogen concentration. This figure was taken from [80].

3.1.2 Leaf Area Index (LAI)

Leaf area index (LAI) is a vegetation parameter that is commonly used when interpreting remote sensing data from crops and forests [81, 82, 41]. LAI is defined as the total area of all leaves (on one side) per area of ground, and is therefore a dimensionless quantity that gives a measure of the canopy coverage given by the plants over a certain area. The LAI value can range from 0 (for bare ground) to over 10 for densely packed forests, with most canopies somewhere towards the middle of that range [83]. It is unclear when the concept of LAI was first developed, but the earliest publication relating to LAI was by Stern and Donald in 1961 [84].

LAI is an important vegetation parameter for assessing many physical quantities, as it has a large effect on the interaction between the vegetation and the atmosphere. This is because leaf surface area is a strong indicator of the amount of solar radiation received by the plant, the amount of precipitation that the plant intercepts, and the amount of gas that it can exchange with the atmosphere [85]. LAI can therefore been used to measure crop growth as well as model the precipitation interception, atmospheric carbon dioxide levels, and atmospheric water vapour levels [41]. In Section 2.1.1 LAI was used in agricultural *Case Study III* to determine the stage of growth of wheat crops.

LAI can be calculated from ground based measurements or using remote sensing data. Ground based measurements can give more accurate results for complex canopies, but are extremely time consuming, particularly when analysing large areas [86]. Remote sensing measurements of LAI are calculated using the normalised vegetation index (NDVI), which is defined by Equation 3.4, where R_{NIR} is the average reflectance in the near-infrared wavelength range (around 800 nm), and R_{VIS} is the average reflectance in the red part of visible wavelength range (around 600 nm). The precise wavelength ranges used for averaging vary between applications.

$$NDVI = \frac{R_{NIR} - R_{VIS}}{R_{NIR} + R_{VIS}} \tag{3.4}$$

NDVI is a parameter that provides a measure of the density of vegetation in a canopy. Leaves reflect more light in the near-infrared range (650-1100 nm) than in the visible range (400-650 nm) due to scattering of near-infrared light by the mesophyll leaf tissue [87]. While other vegetation indices exist, NDVI is the most commonly used, as it is very useful and easy to calculate. NDVI has been used to calculate the annual production of vegetation, the speed of greening (plant growth), the speed of senescence (plant aging), and the proportion of the year that vegetation is present in a particular area [88]. The most accurate measure of vegetation density is obtained when imaging canopies of average density. If the canopy is too sparse, the non-canopy reflectance (i.e. reflectance from the ground) can have a significant impact, and if the canopy is too dense the near-infrared reflectance continues to increase with density, but the visible reflectance does not.

NDVI is a mathematical construct, not a physical quantity, but it can be related to the physical quantity of LAI. The relation between NDVI and LAI has been explored by various studies, in particular by Carlson and Ripley in 1997 [83]. Their results are shown in Figure 3.3, which demonstrates that NDVI increases linearly with increasing LAI for low LAI, but the increase slows asymptotically at higher LAI. For deciduous trees the LAI of a particular area is heavily dependent on the time of year. Generally measurements are taken in the summer, when the LAI is expected to be at its peak value.

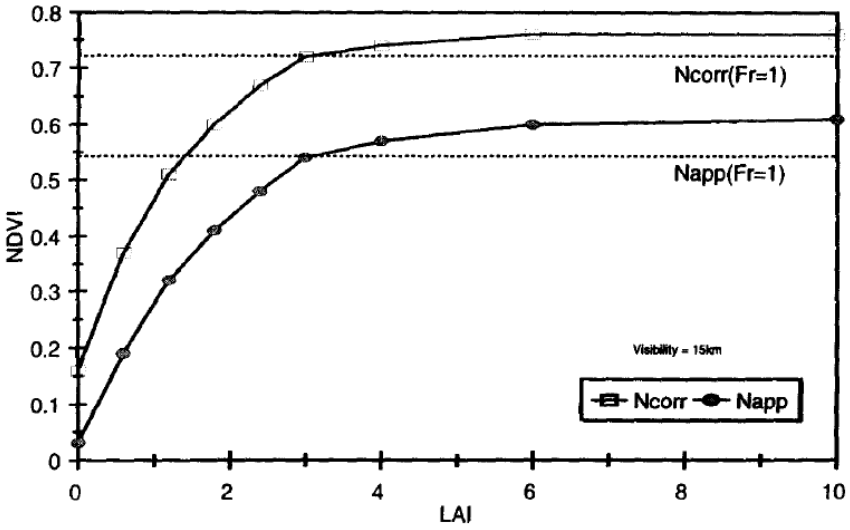

Figure 3.3: This graph shows the relationship between the normalised vegetation index (NDVI) and the leaf area index (LAI). The increase in NDVI with LAI is approximately linear for low LAI, but tails off asymptotically for high LAI. When the LAI increases above 3 (about the point at which there is 100% vegetation cover) the true asymptotic regime starts. The two separate lines show the remotely sensed NDVI (N_{app}) and the ground measurements of the NDVI (N_{corr}). The dotted lines show the NDVI value at which the asymptotic regime begins. This graph was taken from [83].

The following calculations show how the NDVI can be used to obtain an estimate for the LAI. Assuming the ground coverage below the vegetation is soil, the fraction of soil visible from above is defined using LAI by Equation 3.5, where κ is the extinction coefficient ($\kappa \leq 0$). The extinction coefficient is a measure of the absorption of light by the canopy.

$$F_{soil} = e^{\kappa * LAI} \tag{3.5}$$

Using the fact that that $F_{leaf} = 1 - F_{soil}$ we can obtain Equation 3.6, where $NDVI_{soil}$ and $NDVI_{leaf}$ are the NDVI values of pure soil or pure leaves and $NDVI$ is the overall NDVI of the area.

$$NDVI = (F_{soil} * NDVI_{soil}) + (F_{leaf} * NDVI_{leaf}) \tag{3.6}$$

Substituting 3.5 into 3.6 gives Equation 3.7.

$$\kappa * LAI = ln\left[\frac{(NDVI_{leaf} - NDVI)}{(NDVI_{leaf} - NDVI_{soil})}\right] \tag{3.7}$$

If the overall NDVI of the area is calculated from remote sensing measurements, and the NDVI of the leaves and soil are known (or measured) one can calculate $\kappa * LAI$. If κ is also known, then LAI can be calculated, but often $\kappa * LAI$ is more useful than just LAI.

3.1.3 Continuum Removal

Continuum removal is a simple, yet very useful pre-interpretation technique for hyperspectral data. It is a method that is used to emphasise the positions and shapes of specific spectral features. This is done by defining a line connecting the maxima along the spectral curve as a reference, and plotting the spectral intensity relative to this line [89]. Continuum removal works best for predominantly smooth reflectance targets that have specific spectral absorption features, which is why it is often used for mineral classification. It is less useful on spectra that have many overlapping absorption features, however, such those obtained form atmospheric targets. Figure 3.4 shows how continuum removal affects a typical vegetation reflectance spectrum. In this particular example the continuum removed spectra were used to help estimate the nitrogen concentration in foliage [90]. Different maxima can be chosen to produce the continuum line, depending on which features are required to be emphasised.

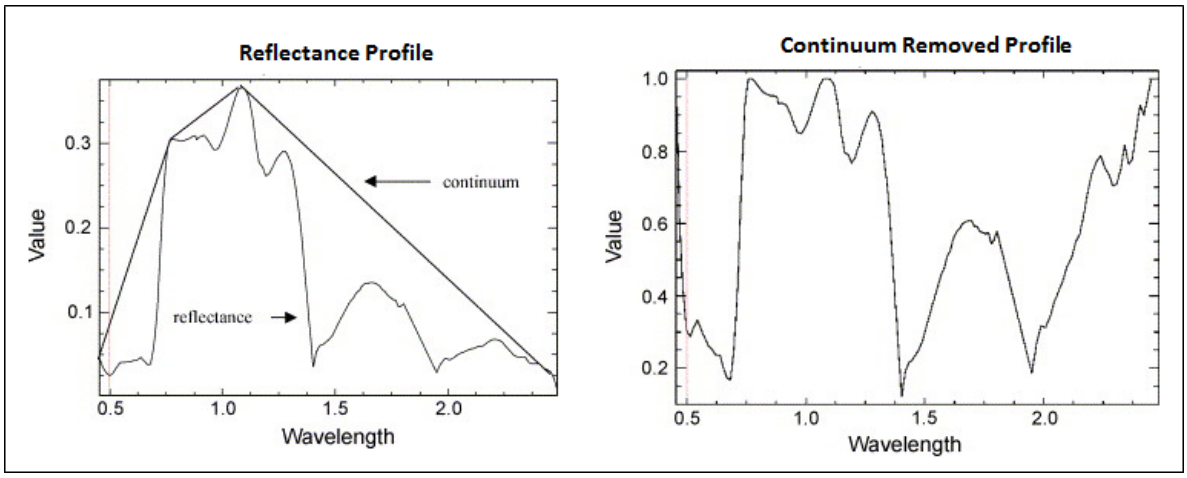

Figure 3.4: These graphs show the reflectance spectrum of a vegetation target before (left), and after (right) continuum removal has been applied. The continuum line used is displayed in the left figure. These graphs were taken from [90].

3.1.4 Dimensionality Reduction Algorithms

The main benefit of hyperspectral data lies in the large amount of information that it contains. Some applications only use specific features within the data, but others use techniques that require all of

the data. The latter techniques therefore require more complicated methods of interpretation. Dimensionality reduction algorithms are techniques that simplify the large multi-dimensional datasets by extracting the most important information and representing it in fewer dimensions. These techniques are used to represent data in terms of its defining features, while ignoring other irrelevant features. There are many slightly different dimensionality reduction algorithms, such as principal component analysis, independent component analysis, and linear discriminant analysis [91]. All of these different algorithms follow similar principles, which involve treating data as vectors in a multi-dimensional space, and performing eigen-decomposition.

The most common example of dimensionality reduction is principal component analysis (PCA). PCA is a very common and very powerful technique that is used to analyse many different types of data, including spectral data [92, 93, 94]. When applying PCA to hyperspectral data the reflectance spectra of different targets are defined as vectors, with each band representing a different dimension. Initial training data is used to define a multidimensional *eigenspace*, with the basis vectors defined by a set of orthogonal eigenvectors, which are a linear combination of bands. These eigenvectors can be used to define any reflectance spectrum that belongs to the same eigenspace. Each eigenvector has an associated weight defined by the corresponding eigenvalue, which determines the significance of each component. The eigenvectors with the highest significance represent the key features of the eigenspace, and are known as the *principal components*, while the less significant eigenvectors contain less relevant or irrelevant information, such as noise. The principal components can therefore used to define a lower dimensional eigenspace.

PCA can be applied to a hyperspectral data set using five mathematical steps:

1. Subtract the mean spectrum from the data by the following equation:

$$\boldsymbol{\nu_0} = \boldsymbol{\nu} - < \boldsymbol{\nu} > \tag{3.8}$$

   where $\boldsymbol{\nu}$ is the matrix of data with the training spectra as columns.

2. Calculate the covariance matrix of the data in $\boldsymbol{\nu_0}$. Covariance is a measure of the level of correlation between two random variables. Equation 3.9 shows the definition of the covariance, σ, between two variables, x and y, where $E[x_i]$ is the expectation value of x_i. If the covariance is positive, there is positive correlation; if it is negative, there is negative correlation, and if it is zero, then there is no correlation.

$$\sigma(x, y) = E[(x - E[x])(y - E[y])] \tag{3.9}$$

   A covariance matrix is a square n x n matrix of all the covariances between pairs of n random variables, which are generally in the form of a set of vectors of length n. For example, $\mathbf{C}_{ij}$ would represent the covariance between the i^{th} entries of the n vectors and the j^{th}entries of the vectors.

The covariance matrix can therefore be defined as in Equation 3.10.

$$\mathbf{C}_{ij} = \sigma(x_i, x_j) = E[(x_i - E[x_i])(x_j - E[x_j])] \tag{3.10}$$

3. Calculate the eigenvalues and unit eigenvectors of the covariance matrix. These are defined as λ and $\mathbf{u}$ respectively in the following equation:

$$\mathbf{C}\mathbf{u_i} = \lambda_i \mathbf{u_i} \tag{3.11}$$

4. Determine the principal components. The higher the eigenvalue is, the more significant the information is that is contained in the corresponding eigenvector. The principal components are defined as the unit eigenvectors corresponding to the highest eigenvalues. The number of principal components can be chosen arbitrarily, but typically about the top 5% of eigenvectors contain the key information.

5. Re-write the data in terms of the principal components. Equation 3.12 rewrites the original data as $\mathbf{\Omega}$ in terms of the new eigenspace, where $\mathbf{U}$ is the matrix made up of rows of the unit principal eigenvectors $\mathbf{u_i}$, and $\boldsymbol{\nu}$ is the matrix of input spectra from Equation 3.8:

$$\mathbf{\Omega} = \mathbf{U}\boldsymbol{\nu} \tag{3.12}$$

These five steps essentially represent the data in far fewer dimensions that include all of the important information, while excluding irrelevant information. This makes categorising the reference data and classifying test data a much more accurate and simple task.

One problem with PCA and most other dimensionality reduction algorithms is that they can be very time consuming and memory heavy processes when applied to large sets of data. This can be an issue when processing hyperspectral data, as the datasets can be incredibly large, and often require real-time or fast processing. Spectral Regression Discriminant Analysis (SRDA) is a new dimensionality reduction algorithm that has been developed specifically for hyperspectral image classification. SRDA has been developed with the aim of reducing the amount of calculation required while still providing the same (or higher) level of accuracy when classifying hyperspectral imagery. For all dimensionality reduction algorithms mentioned previously eigen-decomposition of large matrices is required. For SRDA, however, one only needs to solve a $c-1$ regularized least squares problem, where c is the number of classes. The results of SRDA classification have been compared with those of typical dimensionality reduction methods by performing classification experiments with each method on two different sets of hyperspectral data [95]. For the first set of data SRDA was shown to have a higher classification accuracy than NPE, KPCA and PCA for all chosen training sample sizes, and for the second set SRDA was shown to give much better results that NPE, with similar results to PCA (see

Figure 3.5). These results show SRDA to be the most appropriate dimensionality reduction algorithm to use when dealing with hyperspectral data.

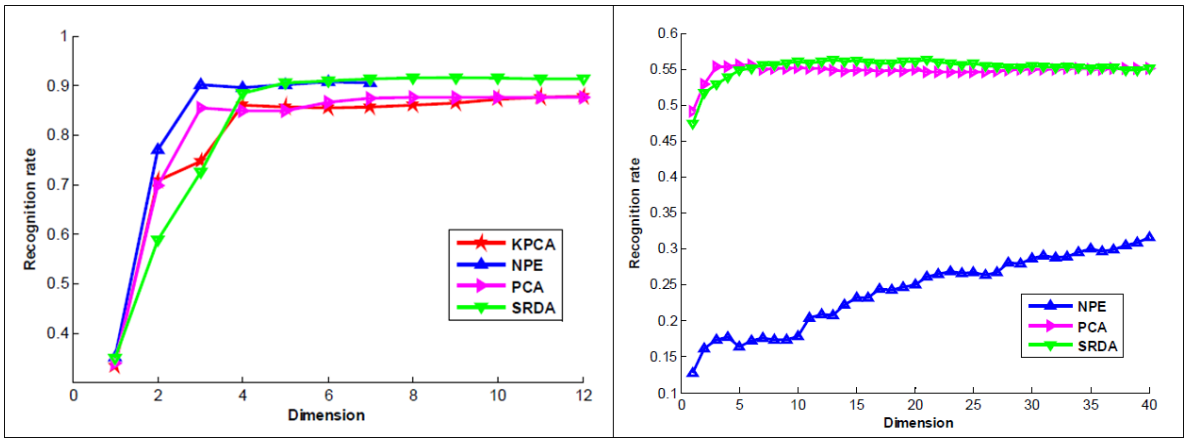

Figure 3.5: These graphs show how the recognition accuracy of SRDA compares to other dimensionality reduction algorithms when using various numbers of dimensions to define the vector space. The two different graphs show results from two different datasets. The graph on the right shows classification results for the 'Washington DC Mall' dataset, which has 11414 samples with 12 bands and containing 9 classes. The graph on the left shows classification results for the 'AVIRIS Indian Pines' dataset, which has 21025 samples with 220 bands and containing 15 classes. These graphs are taken from [95].

3.1.5 Statistical Classification Techniques for Hyperspectral Data in the ENVI software

The classification of a land area into classes, such as land cover types, mineral types or plant species, is an important application of hyperspectral remote sensing data [51, 50]. Various techniques have therefore been developed for classification of hyperspectral data. These methods work under the empirically validated assumption that each land type or species type can be identified by a unique spectral signature. There are several different methods of classification, which can be split into two groups: unsupervised classification, and supervised classification. Unsupervised classification takes the input data and separates it into the classes that are deemed to be most spectrally distinct according to the parameters of the algorithm. Supervised classification methods are processes that require extra input from the user as well as just the raw spectral data, and so are to be used when the classes present in the imaged area are known. Supervised classification has much more practical use for hyperspectral remote sensing data as it provides much more accurate results for predefined classes, and so these methods will be focused on in this thesis.

ENVI (ENvironment for Visualizing Images) is a software application created by Exelis Visual Information Solutions (Exelis VIS) that is used for processing and analysing geographical remote sensing images [96]. Part of the data processing toolbox in the ENVI software contains various classification techniques. Three of these techniques are detailed in this section and applied in Section 3.3. These three methods are:

1. Minimum distance classification

2. Maximum likelihood classification

3. Spectral angle mapper (SAM) classification

To apply these supervised classification techniques the user must define *regions of interest* (ROIs), which are spatial regions within the data that are defined as containing one specific class to be used as reference data. All classes that are to be employed must have at least one defined ROI. The spectra contained within all of the ROIs for a specific class are averaged to produce a reference spectrum for that class. Any form of averaging could be used to obtain a reference spectrum that best represents a specific class. In general, and in this chapter the average spectrum is defined by the mean intensity at each band.

3.1.5.1 Minimum Distance Classification

To perform a minimum distance classification, the spectra for all the spatial pixels in the area to be classified are taken one at a time, and a 'distance' is calculated between this spectrum and each of the reference spectra. The reference spectrum with the smallest distance from the pixel spectrum is found, and the corresponding class becomes the classification for that pixel. A threshold distance can also be defined, above which a pixel is left unclassified. This is useful in situations where classes may be present that have not been predefined. Minimum distance classifications can be split into sub-methods of classification, depending on how the distance is mathematically defined.

Euclidean Distance

The simplest, and probably most natural way to define the distance between two spectra, is the euclidean distance, as defined by Equation 3.13, where d is the distance, E_i is the intensity of the expected spectrum at band i, and x_i is the intensity of the spectrum to be classified at band i. This is equivalent to the method by which physical distance is defined in 3-dimensional space when extended to i dimensions.

$$d = \sqrt{\sum_i (E_i - x_i)^2} \tag{3.13}$$

While the euclidean distance is the most natural way of defining the distance, it is very simplistic, and therefore does not take into account some factors that may be relevant to the classification. One important factor is the amount variation of spectra present within each class. A smaller euclidean distance should be required to classify a pixel as a class with a small variation than a class with a large variation. The variation of spectra within a class can be taken into account by using the standard deviation of the spectra in the corresponding ROIs. If each euclidean distance is normalized by the

corresponding standard deviation, then a more accurate classification may be obtained. This is known as the normalised euclidean distance method.

Mahalanobis Distance

Another type of distance that is commonly used to compare the similarity of an unknown sample to a known sample set is the Mahalanobis distance [97]. This distance classification takes into account more information about the data than the normalised euclidean distance method. The definition of the Mahalanobis distance is given in Equation 3.14, where D is the distance, $\boldsymbol{x}$ is the spectrum to be classified, $\boldsymbol{E}$ is the expected spectrum, and $\boldsymbol{C}$ is the covariance matrix (see equation 3.10) between the bands in that class.

$$D^2 = (\mathbf{x} - \mathbf{E})^T \mathbf{C}^{-1} (\mathbf{x} - \mathbf{E}) \tag{3.14}$$

The incorporation of the covariance matrix in the Mahalanobis distance takes into account any correlation between variables (bands). This means that the Mahalanobis distance measure not only takes into account the spread of the of the data, but also the direction of that spread. This concept is illustrated for two dimensional data in Figure 3.6.

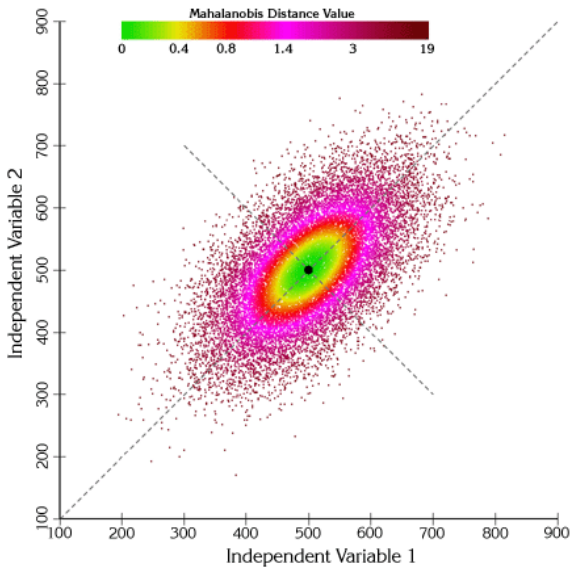

Figure 3.6: This image shows Mahalanobis distance from the center of a set of points governed by two random variables. The shape of the coloured rings demonstrate that this measure of distance takes into account the amount variance in the data, and in what direction the variance occurs. This image was taken from [98].

For hyperspectral data the random variables correspond to the spectral bands, and the vectors correspond to the mean spectra from the ROIs for the relevant land type. The Mahalanobis distance method therefore attempts to make use of any possible correlation between the spectral bands. If such

correlation is present then the Mahalanobis distance uses this extra information present in the data, and could therefore give more accurate results than the normalised euclidean distance would.

3.1.5.2 Spectral Angle Mapper (SAM) Classification

Spectral angle mapper (SAM) classification treats each spectrum as a multi-dimensional vector, as with the minimum distance methods. For SAM, however, the angle between each spatial pixel spectrum and the reference spectra are calculated instead of the distance. The reference spectrum with the smallest angle is found, and the pixel is classified in the corresponding class. The angle between two n-dimensional vectors, s_i and s_j is given by the following formula:

$$\theta\left(s_i, s_j\right) = \cos^{-1}\left(\frac{\sum_{n=1}^{N} s_{in} s_{jn}}{\sqrt{\sum_{n=1}^{N} s_{in}^2}\sqrt{\sum_{n=1}^{N} s_{jn}^2}}\right) \tag{3.15}$$

As with the minimum distance classifications, a threshold (or maximum angle) can be set, above which a pixel is left unclassified. The angle between two spectra is dependent on the spectral shape, but not the spectral intensity. SAM can therefore be a useful classification method when classifying targets with varying illumination.

The angle between two spectra is dependent on the dimensional space within which the spectra are defined. This multi-dimensional space can be chosen in different ways. The most common way is to define a set of *endmember* spectra as the basis vectors. The choice of these endmembers is a very important part of the classification process. One method of defining the endmember spectra is by using a dimensionality reduction algorithm such as PCA. Although PCA is a very effective technique for dealing with a general data set, when dealing with remote sensing data the knowledge of the reflectance spectra of the targets can be taken into account. Using the mean spectra for each class to define the endmembers is more likely to give better results, as, in theory, if these are the only classes within the target area, then homogeneous pixels (where only one ground type is present within the pixel) will be represented by one of these endmember spectra

The idea of defining multiple endmember spectra per class has been tested on a classification of savannah tree species [99]. It was found that using multiple endmember spectra per class produced more accurate SAM classifications. The accuracy was also highly dependent on the training samples used, which implies that it is highly important to select endmembers that represent the diversity within each class.

3.1.5.3 Maximum Likelihood Classification

The maximum likelihood method of classification finds the probability of a pixel belonging to each class. The pixel is then assigned to the class with the highest probability. This technique assumes that all spectra of a specific class are normally distributed around the mean. The parameters of the normal distribution (mean and variance) are determined from the spectra contained within the ROIs. In the most fundamental method, Equation 3.16 is used to calculate the relative probability ($P_k(\mathbf{x})$) of a pixel belonging to a particular class ($\boldsymbol{k}$), where $\boldsymbol{p}$ is the number of bands, $\boldsymbol{x}$ is the spectrum to be classified, E_k is the expected spectrum of class $\boldsymbol{k}$, and $\boldsymbol{C}$ is the covariance matrix [100]. As with the other methods, a threshold probability can be defined for the maximum likelihood classification, below which a pixel would be left unclassified. The maximum likelihood method is in fact very similar to the Mahalanobis distance method, as the probability can be thought of as a distance weighted by the covariance matrix. Indeed the equation for Mahalanobis distance can be seen to be a constituent part of the probability equation.

$$P_k(\mathbf{x}) = \frac{1}{2}pln(2\pi) - \frac{1}{2}ln \mid C \mid -\frac{1}{2}(\mathbf{x}-\mathbf{E_k})^T\mathbf{C}^{-1}(\mathbf{x}-\mathbf{E_k}) \tag{3.16}$$

More complex maximum likelihood methods can be used to take into account prior probabilities, which describe how likely a class is to occur within the data. These prior probabilities adjust the calculated probability to give Equation 3.17, where w_k is any member of class $\boldsymbol{k}$, and $P_k(\mathbf{x})$ the probability from Equation 3.16 [100]. This equation can be used to give improved classification results.

$$P\{w_k|\,\mathbf{x}\} = \frac{P(\mathbf{x})\,P\{w_k\}}{\sum_{k=1}^{K} P_k(\mathbf{x})\,P\{w_k\}} \tag{3.17}$$

3.1.6 Spectral Unmixing

The three statistical classification techniques described above require the area imaged within each spatial pixels to be homogenous for optimal results, so that the pixel spectra are represented by one of the reference spectra. Most airborne remote sensing instruments have 1-10 m spatial resolution, with data from the Eagle and Hawk instruments (which are used as examples in this chapter) having a 1 m spatial resolution at 1 km altitude (see Table 1.1). If the features to be classified are smaller than the spatial resolution then the area imaged by the pixels will be hetrogeneous and would therefore be represented by a linear combination of the endmember spectra.

In order to determine the abundance of each class, spectral unmixing is required. Spectral unmixing uses very similar mathematical techniques to those used in PCA, to define each spectrum as a linear combination of the endmember spectra. The weighting of this linear combination is used to determine

the relative abundance of each class within the spatial pixel [101]. This is a very useful technique, but requires knowledge of all the class spectra that are potentially present in the area.

Spectral unmixing has been used to particularly good effect in characterising surface mineralogy [51]. The technique was tested on 20 m spatial resolution AVIRIS images of the Cuprite area in Nevada, USA. This area has large areas of exposed rock faces, with a high abundance of different minerals that are not all homogeneous over a 20 m area. Knowledge of the spectral signatures of the minerals present in the area was used with spectral unmixing to map the mineralogy of the area (see Figure 3.7).

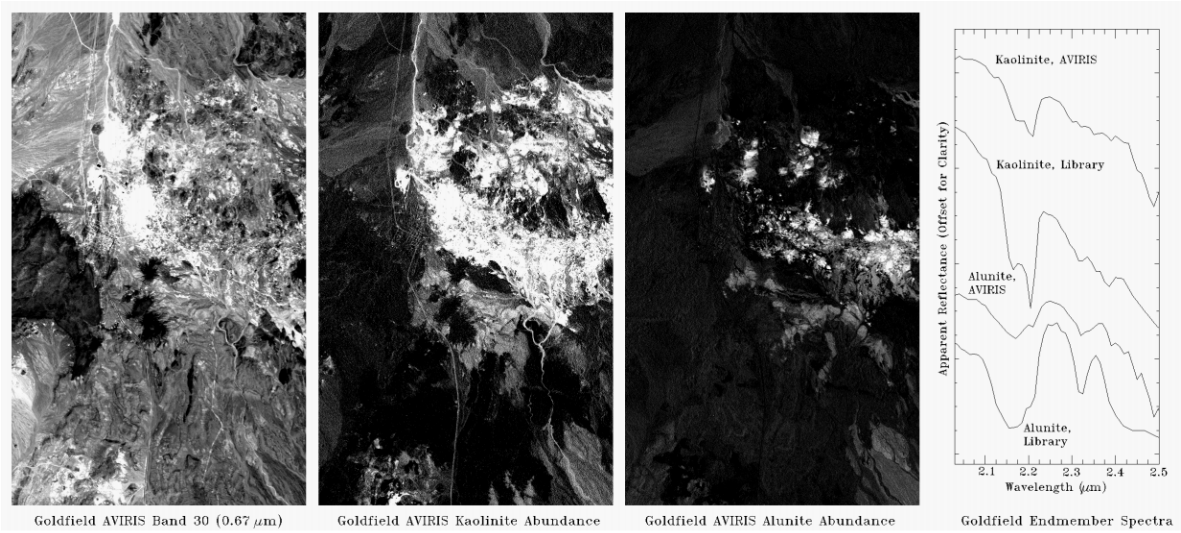

Figure 3.7: This figure shows the results of mineral mapping in the Cuprite area in Nevada, USA using spectral unmixing on AVIRIS data. The area mapped is shown on the far left as a monochromatic 670 nm image, and the endmember spectra used are shown in the plot on the far right. The two central images are maps created of the relative abundance of Kaolinite and Alunite. The abundances range from 0% (black) to 50% (white). These images were taken from [52].

3.1.7 Classification and Regression Tree (CART) Analysis

Classification and regression tree (CART) analysis provides a completely different approach to classification than the ENVI classification techniques (Mahalanobis distance, SAM, and maximum likelihood). The statistical classification techniques provided comparisons using the full spectral range of data to determine the key distinguishing features between each class. CART, however, uses known distinguishing spectral parameters to classify pixels. CART does not necessarily use the full range of information available from hyperspectral data, but does incorporate what are known to be, or expected to be the key distinguishing parameters of the data. CART works by creating a decision tree that asks questions (performs tests) about the input data at the nodes (or splits) of the tree, and uses the responses to generate the outcome at the leaves of the tree (see Figure 3.8). When performing a classification, each data point is passed through the tree to determine its outcome.

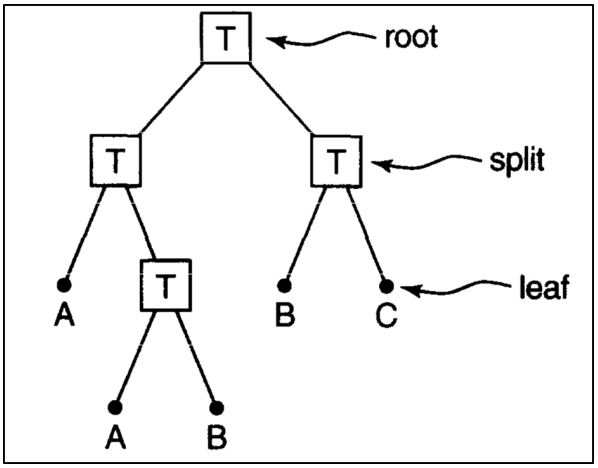

Figure 3.8: This diagram demonstrates the concept of a decision tree by showing how a series of tests can be used to classify data points. The letter Ts represent different tests (each with two outcomes) that are carried out at the nodes of the tree. The letters A, B and C represent different classes at the leaves of the tree. Each data point starts at the root, and is classified into one of the three classes. This image was taken from [102].

Most data sets have a large number of input features that interact in various non-linear ways. To deal with such complicated data the feature space can be divided in smaller regions known as partitions, to which simple models can be applied. This method is known as *recursive partitioning*, and it consists of two parts. First a data point is applied to the global recursive partition decision tree, which determines which partition that data point belongs to. Then the corresponding simple model is used to classify the data point within the partition.

For remote sensing data CART is generally used to classify different types of natural phenomenon imaged on the ground, such as land type or plant species [103, 102]. In such cases the inputs are the characteristics of certain spectral features or parameters, while the outputs would be the classes. Each spatial pixel in a remote sensing image represents a different data point, so the decision tree could be used to classify a whole image pixel by pixel.

In the case studies presented in Chapter 2 decision trees were used in two of the forestry applications: *Case Study II* for classifying mangrove tree types, and *Case Study III* for classifying the damage caused by Douglas-fir beetle infestations. Figure 3.9 shows how choosing appropriate distinguishing factors in the synthetic aperture radar (SAR) reflectance features at the nodes allows the data to be classified into different mangrove species.

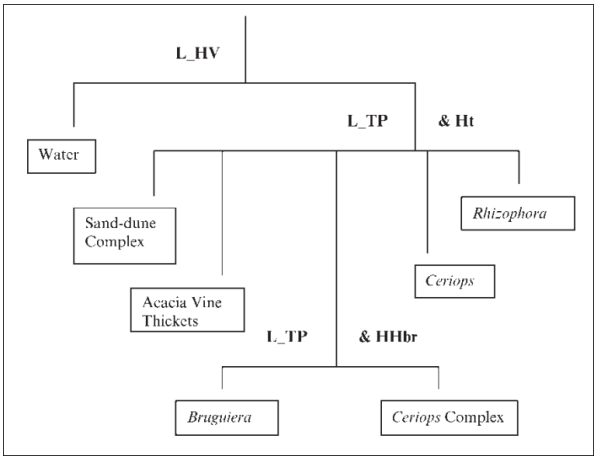

Figure 3.9: This image shows a CART tree for classifying mangrove tree species using synthetic aperture radar (SAR) data. The SAR bands used were L-band HV (L_HV), total power (L_TP), tree height (Ht - derived from the C-band digital elevation model (DEM)), and the percentage of Bragg scattering in the HH component (HHbr). This figure was taken from [50].

3.1.8 Summary of Interpretation Techniques

This section has presented a variety of interpretation techniques that can be applied to hyperspectral data. These techniques can be split into three different types of process, each with a different purpose. The first type of technique simplify and enhance relevant aspects of the hyperspectral data; the second type measure specific spectral features or parameters of the data; and the third type are used to classify the hyperspectral data. Choosing the appropriate interpretation techniques is very important, as this will help make the most of the data received by the instrument. Developing improved processing and interpretation techniques can therefore be equally important as developing instruments with better capabilities.

Relevance to microslice technology.....

3.2 Processing Eagle/Hawk Hyperspectral Data

Data that is gathered from a hyperspectral instrument is in a raw format that requires a certain amount of processing before data interpretation can be performed. In this section the methods involved in processing a raw hyperspectral dataset are investigated. In particular, the processing of a specific test dataset gathered in November 2009 around the River Derwent, near Cockermouth in the UK (see Figure 3.10) is detailed. The data was obtained using the AISA instruments Eagle and Hawk (see Table 1.1).

Figure 3.10: This image shows the approximate location of the test area within the UK ($\sim 30 \times 15$ km), and an image taken of the target area that was later imaged during a survey using the Eagle and Hawk spectrometers. This area was around the River Derwent, from Cockermouth to the mouth. The satellite image was taken from Google Earth.

This dataset was specifically chosen as the Eagle and Hawk instruments represent typical airborne remote sensing instruments, requiring both topographic and radiometric calibration. Also, the target area used contained a variety of targets of interest (including recent flood deposits), and the fact that the survey was conducted in late autumn meant that the light conditions were far from ideal.

3.2.1 The Eagle and Hawk Spectrometers

The Eagle and Hawk spectrometers were developed by the company Specim as part of their AISA instrument suite. The Eagle spectrometer images in the visible and near-infrared spectral region (400-970 nm), while the Hawk spectrometer images in the short-wave infrared spectral region (970-2500 nm). Figure 3.11 shows images and dimensions of the Eagle and Hawk spectrometers.

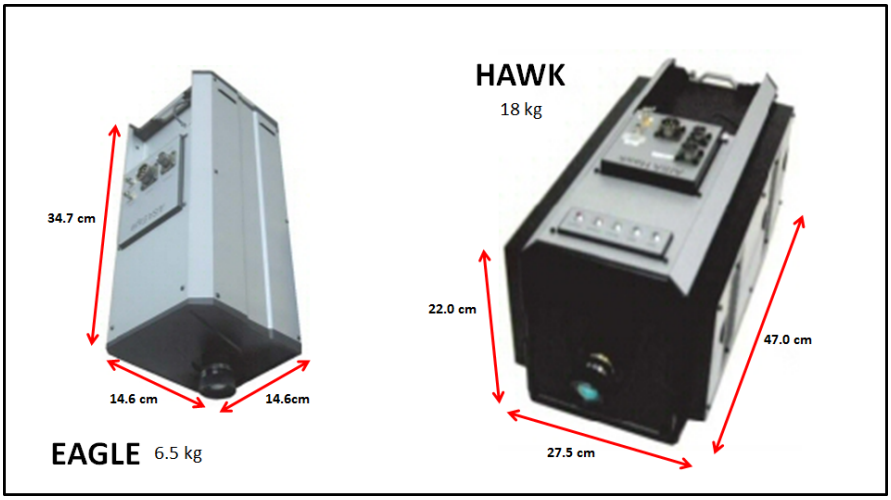

Figure 3.11: This figure shows images of the AISA spectrometers Eagle and Hawk, which are used for airborne imaging. Eagle images the visible and near-infrared spectrum (400-970 nm), while Hawk images the short-wave infrared spectrum (970-2500 nm). They are often used together for simultaneous imaging to provide wide spectral coverage. These images were taken from [32].

The visible and near-infrared spectral region is the most widely used part of the spectrum for remote sensing, as it contains many key vegetation features. These features include the red edge (around 700 nm), and the green peak (around 550 nm) due to chlorophyll absorption [104]. The Eagle instrument is therefore more commonly used for remote sensing than the Hawk instrument. There is, however, useful information that can be obtained from the short-wave infrared region of the spectrum, in particular water absorption features, which are important in the remote sensing of vegetation [104]. The Hawk instrument is therefore often used in conjunction with the Eagle instrument to obtain hyperspectral data over a wider wavelength range. This Eagle/Hawk imaging system has been used to carry out numerous field experiments [105, 106]. More recently a new instrument is being developed (Fenix), which incorporates both the Eagle and Hawk optic into a single instrument with one entrance pupil [32].

Eagle/Hawk data were gathered using a pushbroom scanning technique (see Figure 1.3) from a Dornier 228: G-ENVR aircraft flown at a height of 1000 m. Figure 3.12 shows the optical set-up of a typical pushbroom sensor such as the Eagle/Hawk system.

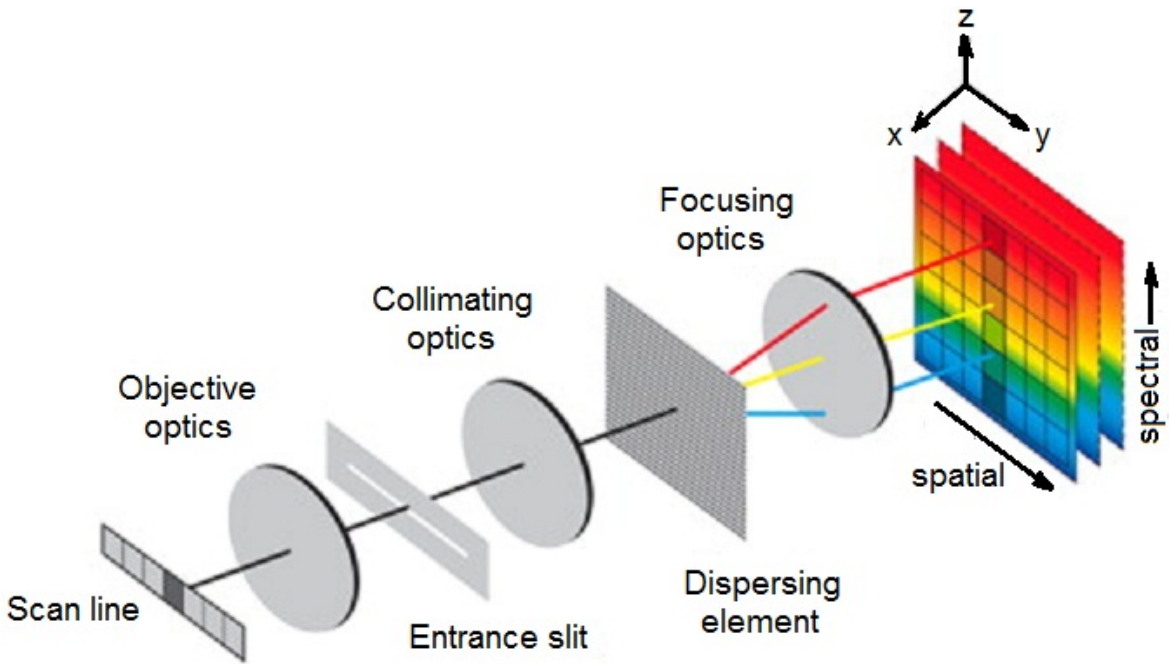

Figure 3.12: This diagram shows the optical set-up of a typical pushbroom spectrometer, such as the Eagle and Hawk instruments. The scan line represents the field of view of the spectrometer, and the objective optics focus the light onto the entrance slit. The entrance slit collimating optics, dispersing element, focusing optics, and detector make up a standard imaging spectrograph, as was described in Section 1.4.1. This image was taken from [107].

The field of view (FoV) of the each instrument depends on the lens used. A typical lens used gives a 36.7° FoV, meaning that in one flight path the aircraft was used to image a swath about 330 m wide at 1 km altitude, which is referred to as one *flightline*. When collecting the data that is processed in this section from the River Derwent area, twelve contiguous flightlines were imaged in total to give data from a wider area (see Figure 3.13). In order to develop an image such as the one in Figure 3.13 various processing steps must be carried out on the raw data obtained from the instrument.

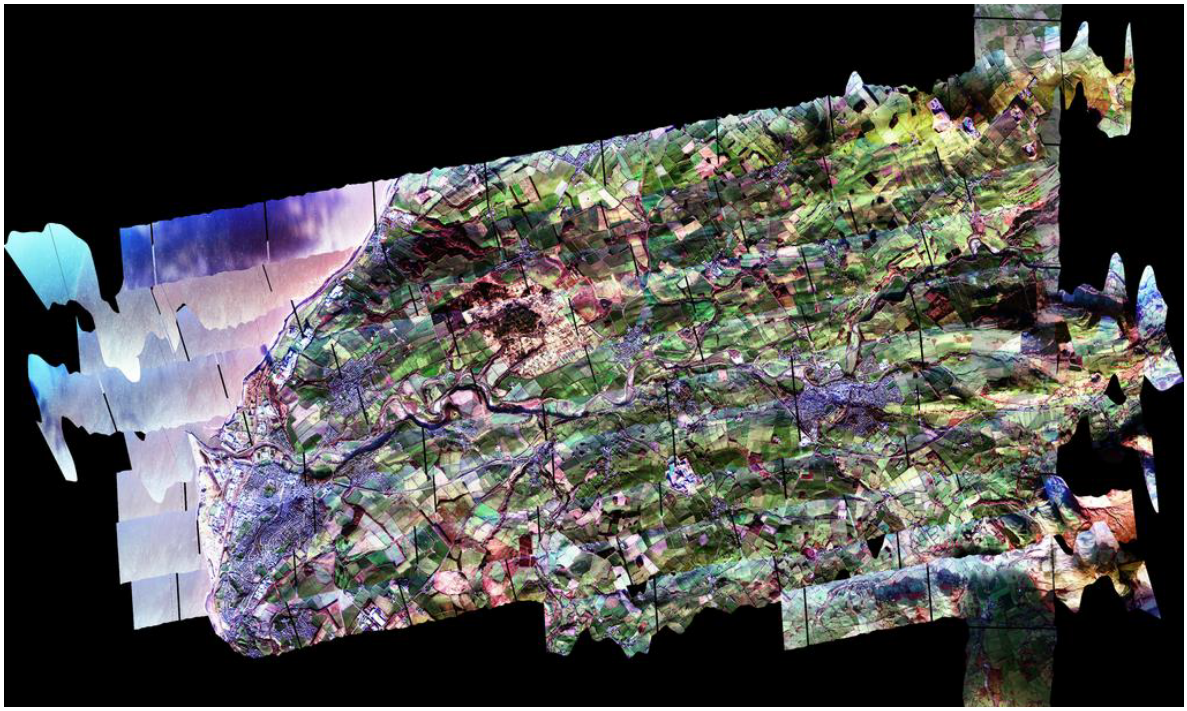

Figure 3.13: This image shows a synthetic true-colour image of a *mosaic* of Eagle data from twelve flightlines imaging the River Derwent area. This mosaic demonstrates that when the data from the flightlines are processed and combined they can be used to produce a complete image of the area. The borders between flightlines are visible in the mosaic due to variations in illumination between imaging times, and the regular black lines on the imagery are due to a technical fault with the instrument timing. Section 3.2.2 details the processing required to obtain this image from the raw instrument data.

3.2.2 Raw Data Processing

This section details the operations performed, and the meta-data required when processing an Eagle/Hawk dataset gathered from a flight over the River Derwent near Cockermouth in November 2009. The dataset was obtained from the Airborne Research and Survey Facility (ARSF). It contains both the raw data and the processing meta-data from the Eagle and Hawk instruments for twelve separate flightlines.

There are seven levels of hyperspectral data. A higher level of data contains more information, in a more usable format. The seven levels are explained below:

1. Level 0 - Raw "sensor format" data at original resolution.
2. Level 1a - Level 0 data reformatted to image files with ancillary files appended.
3. Level 1b - Level 1a data to which radiometric calibration algorithms have been applied, to produce radiance or irradiance, and to which location and navigational information has been appended.
4. Level 2 - Geophysical or environmental parameters derived from Level 1a or 1b data, which may include atmospheric correction.

5. Level 3a - Level 1b or 2 data mapped to a geographic co-ordinate system using on-board attitude and positional information only.

6. Level 3b - Level 1b or 2 data mapped to a geographic co-ordinate system using on-board attitude and positional information with additional ground control points.

7. Level 4 - Multi-temporal/multi-sensor gridded data products.

For any meaningful data interpretation to be applied, data of at least level 3a is required. The Eagle/Hawk data set that was obtained from ARSF contained level 1b image data, and included the additional files required to create level 3b data. The data consisted of five types of data file:

1. A level 1b data file (for each flightline) - this is a *BIL* (Band Interleaved by Line) file containing level 1b spectral data.

2. A navigation data file (for each flightline) - this is a BIL file containing data defining the path of the aircraft.

3. A digital elevation model (DEM) file - this is a file containing details of the shape of the terrain.

4. A sensor field of view (FoV) file (for each sensor) - these are BIL files containing the field of view vectors of the Eagle and Hawk sensors.

5. A grid-shift file - this re-defines the positions of each pixel in each flightline with respect to Ordnance Survey National Grid coordinates.

The APL software package was used in conjunction with the graphical user interface (GUI) 'ARSF Mapper' to process the level 1b data into level 3b. There were three main stages to this process:

1. Use the navigation data file, the DEM file, and the sensor FoV in conjunction with the level 1b data file to create an *IGM* (Input Geometry) file.

2. Use the grid shift file to convert the relative positions in the IGM file to absolute Ordnance Survey positions.

3. Use this IGM file to convert the original level 1b BIL file into a level 3b BIL file.

To produce level 4 data, the area would need to be imaged with different instruments and at regular intervals. That amount of data was not available in this case, so level 3b data was used.

3.2.3 Mosaicking

An extra piece of processing that can be performed on the hyperspectral data is *mosaicking*. When there is more than one geo-referenced hyperspectral datacube of close or overlapping areas it can be helpful for data interpretation if these are stitched together into their relative positions in one datacube. This was done with with the Eagle/Hawk data from the River Derwnet area, as there were twelve spatially contiguous flightlines that could be mosaicked to form a complete image.

The image analysis software ENVI (that contains the classification toolbox discussed earlier) was also used for mosaicking. The resulting datacube that was obtained from the data after mosaicking three of the Derwent Eagle/Hawk flightlines (flightlines 2, 8 and 5) is represented in Figure 3.14. The borders between flightlines are still visible due to variations in illumination between imaging times. This can affect data interpretation, and so applying additional post-processing to calibrate between flightlines could also be helpful, but is not performed here. It can be seen that the are periodic black lines across each flightline. These lines occur where there is missing data due to a technical fault with the instrument timing. Flightlines 2, 8, and 5 were chosen as they are the flightlines that show the path of the River Derwent. The imaging took place soon after a period of flooding, and so using the river as a target area makes it possible to test the potential of classifying different flood deposits using Eagle/Hawk data with different classification techniques.

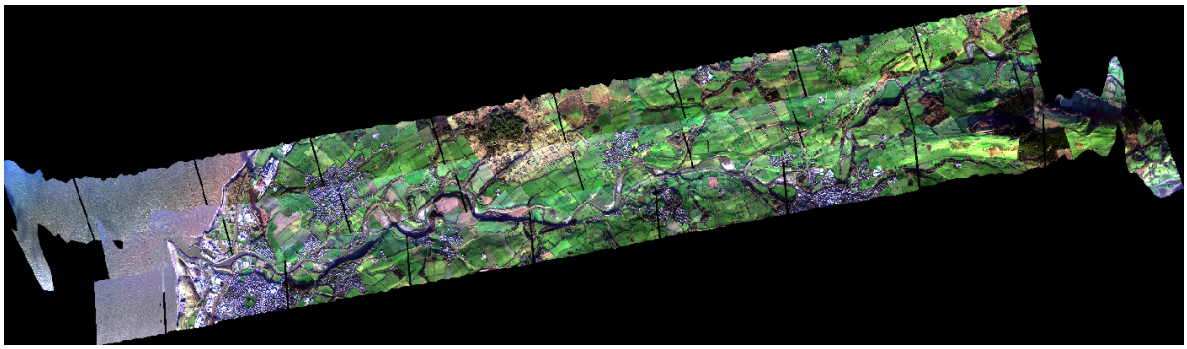

Figure 3.14: This image shows the results of mosaicking the data from three processed Eagle flightlines in ENVI. The three flightlines show the path of the River Derwent, and can now be used for classification as a single datacube. This synthetic true-colour image is made up from three bands - red: band 7, 449 nm; green: band 18, 550 nm; blue: band 29, 654 nm. The regular black lines on the imagery are due to a technical fault with the instrument timing.

3.3 Assessment of Classification Techniques on Eagle Data

Once hyperspectral data has been fully processed into level 3b data, data interpretation can be applied. As mentioned earlier, a standard form of analysis of hyperspectral remote sensing data is land cover classification. This section applies different classification methods to the Eagle dataset from the River Derwent to provide a comparison between the classification techniques, as well as assessing the suitability of using Eagle data for classification. The three classification methods that were discussed in Section 3.1.5 (Mahalanobis distance, Spectral Angle Mapping (SAM), and maximum likelihood) are implemented on the dataset.

When performing classifications it must be decided how many different land cover classes should be used, as this determines what regions of interest (ROIs) need to be defined. For this dataset two sets of target types were defined for two separate classifications. The first set of target types was for a

classification of a variety of the most common land types in the target area. The aim of classification using this set was to determine the ability of the classification methods to distinguish spectra with fundamental differences in shape. The second set of target types focuses on the river area specifically, and uses different river deposits as targets types as well as the targets used for general classification. The dataset had been gathered after recent flooding of the area, and so could be used to determine the capabilities of each method to classify flood deposit types. As well as comparing different classification methods, these classification tests allow the capability of Eagle data to be used for classification to be assessed.

The classification methods described in Section 3.1.5 work best when classifying data with a high SNR. The test area used in this study was imaged at a time of poor illumination. This meant that it could provide a good assesment of the ability of hyperspectral imagery for classification in non-ideal conditions. It is important that hyperspectral data gathered is of sufficient quality for all atmospheric parameters. This study assesses the accuracy to which the Eagle spectrometer, that can capture data at a very high SNR (~1250, see Table 1.1), can classify land cover types under poor illumination conditions.

3.3.1 General Classification

A test area was chosen within the mosaicked dataset for the general classification, and is shown in Figure 3.15. This was deemed an appropriate area for classification tests, as it included a good representation of different land types, as well as the join between two flightlines (flightline 2 and flightline 8).

Figure 3.15: This image shows a test area (about 5 x 3 km, 2500 x 1500 pixels) within the mosaicked Eagle spectrometer data in Figure 3.14. This sub-area of the data is used for classification tests as it includes a good representation of different land types, as well as the join between two flightlines. This colour image was produced in ENVI using three bands - red: band 7, 449 nm; green: band 18, 550 nm; blue: band 29, 654 nm.

Five different types of land cover were chosen for the initial classification, and at least three ROIs were defined for each land cover type. For each class areas of the order of 100s of pixels were chosen to represent the maximum variety of that particular land cover type. The five classes chosen were: grass, deciduous trees, coniferous trees, river water, and gravel deposits.

As there was no ground truth data available of the general land cover types in this area, the ROIs were defined based on the appearance of the image when displayed in ENVI. ROIs were defined in both flightlines, and with different illuminations to help represent the diversity of each target type.

It could be seen from the image construction in ENVI that many areas of grass and water were imaged in shadow (see Figure 3.15). Separate classes were therefore defined for each land cover type in shadow, as the illumination was deemed to have a significant impact on the spectral signature. Figure 3.16 shows the spatial areas that were chosen as ROIs to define the first set of target types. These ROIs were used to classify the test area using the three different classification methods: SAM, maximum likelihood and Mahalanobis distance. The mean spectra of each class within these ROIs was calculated to define the reference spectra for each class, which are shown in Figure 3.17.

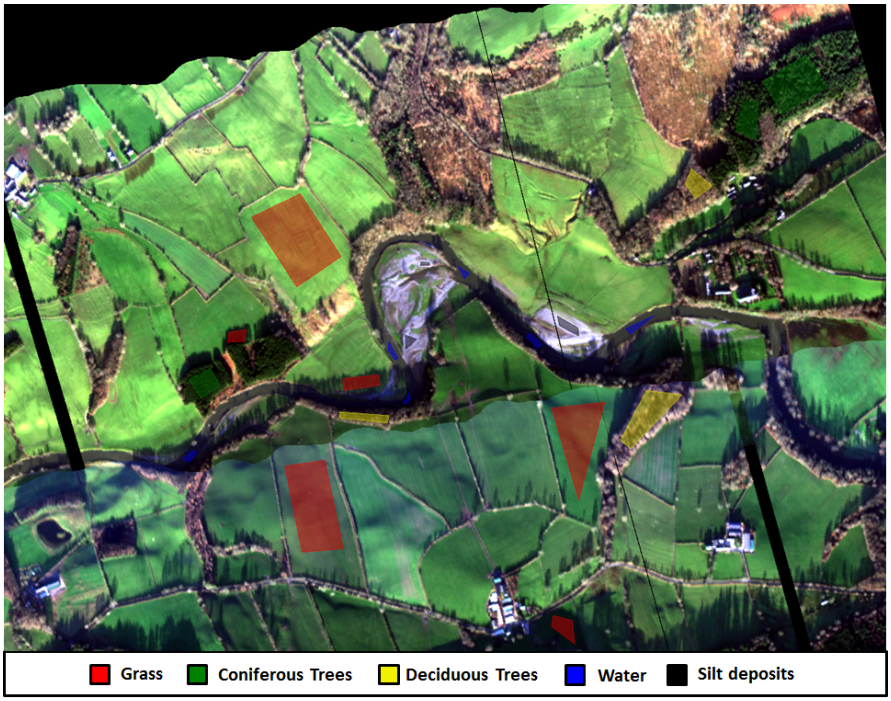

Figure 3.16: This image shows the spatial areas that were chosen as regions of interest (ROIs) within the test area from Figure 3.15 to perform classifications with five land cover types. The semi-transparent coloured boxes show the spatial pixels that were used to define the reference spectra. At least three ROIs were defined for each land type to represent the diversity within that class. Separate classes were defined for shadowed areas to aid classification.

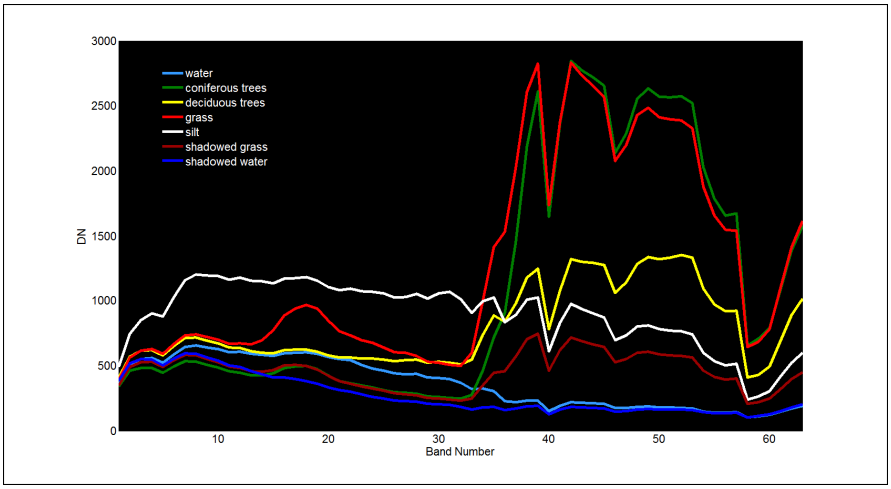

Figure 3.17: This plot shows the reference spectra for each class, defined as the mean spectra of each class in the regions of interest (ROIs) in Figure 3.16. These spectra only include the 63 bands from the Eagle spectrometer data which represent the 400-970 nm wavelength range. These reference spectra are used to perform spectral angle mapper, maximum likelihood and Mahalanobis distance classifications. The Y-axis label DN refers to *data numbers* meaning that the intensity scale is arbitrary.

The *Classification Workflow* tool in ENVI was used to perform SAM, Mahalanobis distance and maximum likelihood classifications on the test area. An important parameter that affects the results of these classifications is the threshold value, as it determines how different a spectrum can be from

the most similar reference spectrum while still being classified. Defining a threshold prevents spectra that differ significantly from the reference spectra from being classified. There are two purposes to this: the first is to allow for the possibility that some pixels contain a different class to those defined by the reference spectra, while the second is to prevent *false-positive* classifications. False-positive classifications occur when pixels are incorrectly classified as the wrong class, due to of unrepresentative reference spectra and/or limitations of the classification technique. Figure 3.18 shows percentage classification of each class within the test area for each classification technique, and how they vary depending on the threshold chosen. It can be seen that the percentage of unclassified pixels decreases, as the threshold increases. It can also be seen that, in general, this reduction in unclassified pixels causes an increase the percentage of pixels classified as grass and deciduous trees.

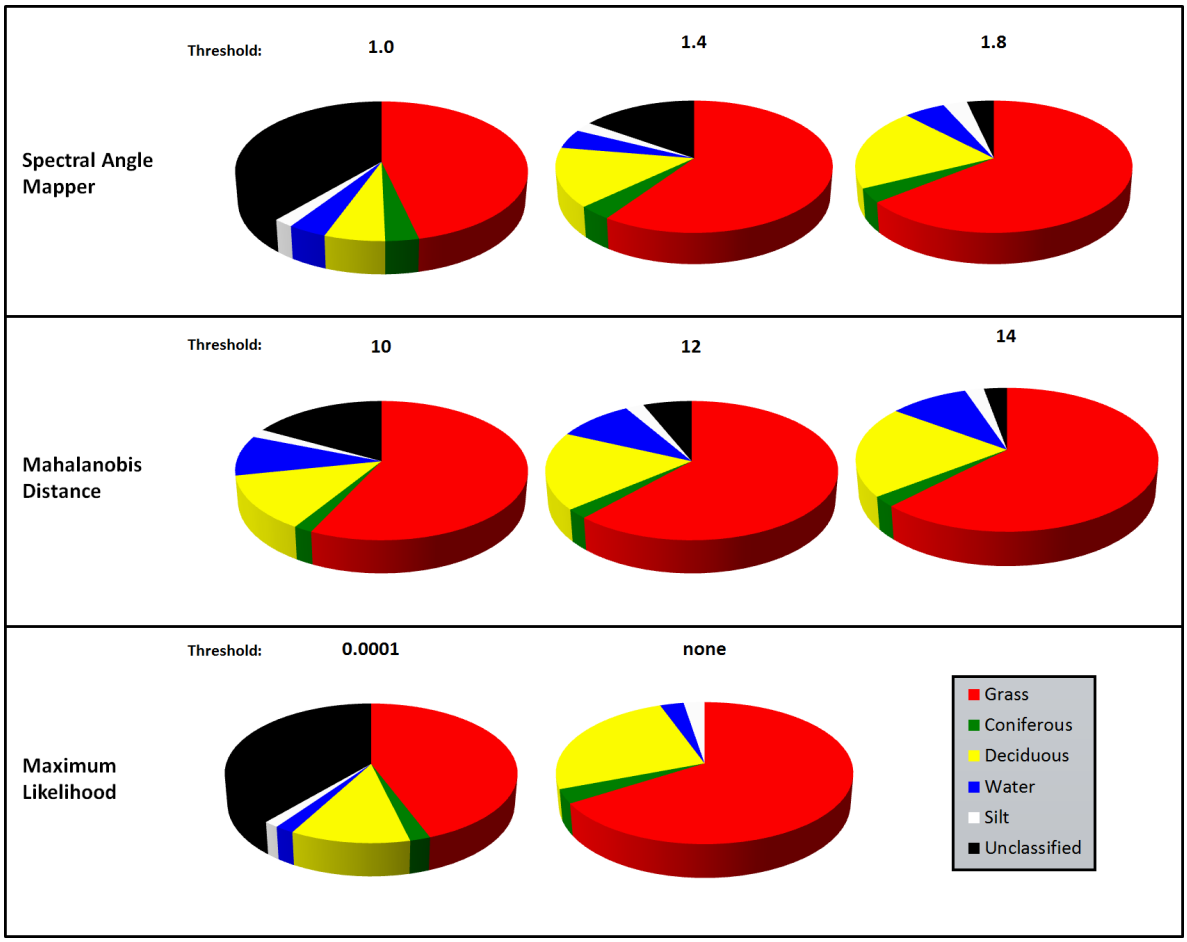

Figure 3.18: This figure shows results from the classification of hyperspectral data gathered around the River Derwent by the Eagle spectrometer. The pie charts show the percentage classification of five different land cover classes. Each row of pie charts shows results from a different classification technique (spectral angle mapper, minimum distance, and Mahalanobis distance), and the pie charts along each row show how the results of each method are affected by the threshold values chosen.

If a threshold is chosen that is too large not all false-positive classifications will be prevented, but if the threshold is too small it would lead pixels being left unclassified that would otherwise have been classified correctly. The optimal choice of threshold depends on the purpose of classification.

A high threshold should be chosen when the aim is to correctly identifying the maximum number of pixels, while a low threshold should be chosen when the aim is to minimise the number of incorrect classifications. This optimal choice for each classification method will also depend on the data that is being classified (i.e. how similar the reference spectra are), and the probability of classes that have not been predefined being present.

Classification tests were carried out to determine the performance of each classification technique at different thresholds. For each class, areas of the order of 100s of test pixels were chosen to extract results from. Ideally these test pixels would be chosen at random, but since ground truth data was not gathered across the entire area only specific test areas could be chosen. These chosen areas were intended to represented the maximum variety of a particular land cover type, while not including any of the pixels defined in the ROIs.

The percentage recognition accuracy and the false-positive rate were calculated in these areas for a range of threshold values, for each classification technique. The results are plotted in Figure 3.19, and show the level of compromise caused by the threshold for each classification technique. These results can therefore be used to obtain an empirical estimate of the optimal threshold values for each classification technique.

It can be seen that to achieve a zero false-positive rate, the total number of pixels classified must be compromised in some methods (to 78% for SAM, 100% for Mahalanobis distance, and 85% for maximum likelihood). When the threshold is increased to a level where 100% of the pixels are classified the false-positive rate remains below 10% for all classification methods, giving a classification accuracy of 98% for SAM, 100% for Mahalanobis distance, and 92% for maximum likelihood. These results suggest that when classifying land cover types with Eagle hyperspectral data the Mahalanobis distance classification method provides the most accurate results. Of the other two methods, the SAM method is able to achieve a higher overall classification accuracy, but maximum likelihood obtains a higher classification accuracy than SAM when classifying at a 0% false-positive threshold.

The classification maps of the test area shown in Figure 3.15 for each classification technique are displayed in Figure 3.20. It can be seen that the main advantage of the Mahalanobis distance method lies in its ability to correctly classify shadowed areas. The maps also show that the SAM technique, appears to have difficulty classifying shadowed grass areas, while the maximum likelihood technique appears to have difficulty classifying shadowed water areas.

Figure 3.20 therefore suggests that the mean accuracy and false-positive rate may vary significantly between classes. The percentage classification accuracies for each class, for each classification method were therefore calculated, and the results are shown in Figure 3.21. This confirms that the main drawback of the maximum likelihood classification is its poor water classification accuracy, and main drawback of the SAM classification is its poor grass classification accuracy. If water classification is

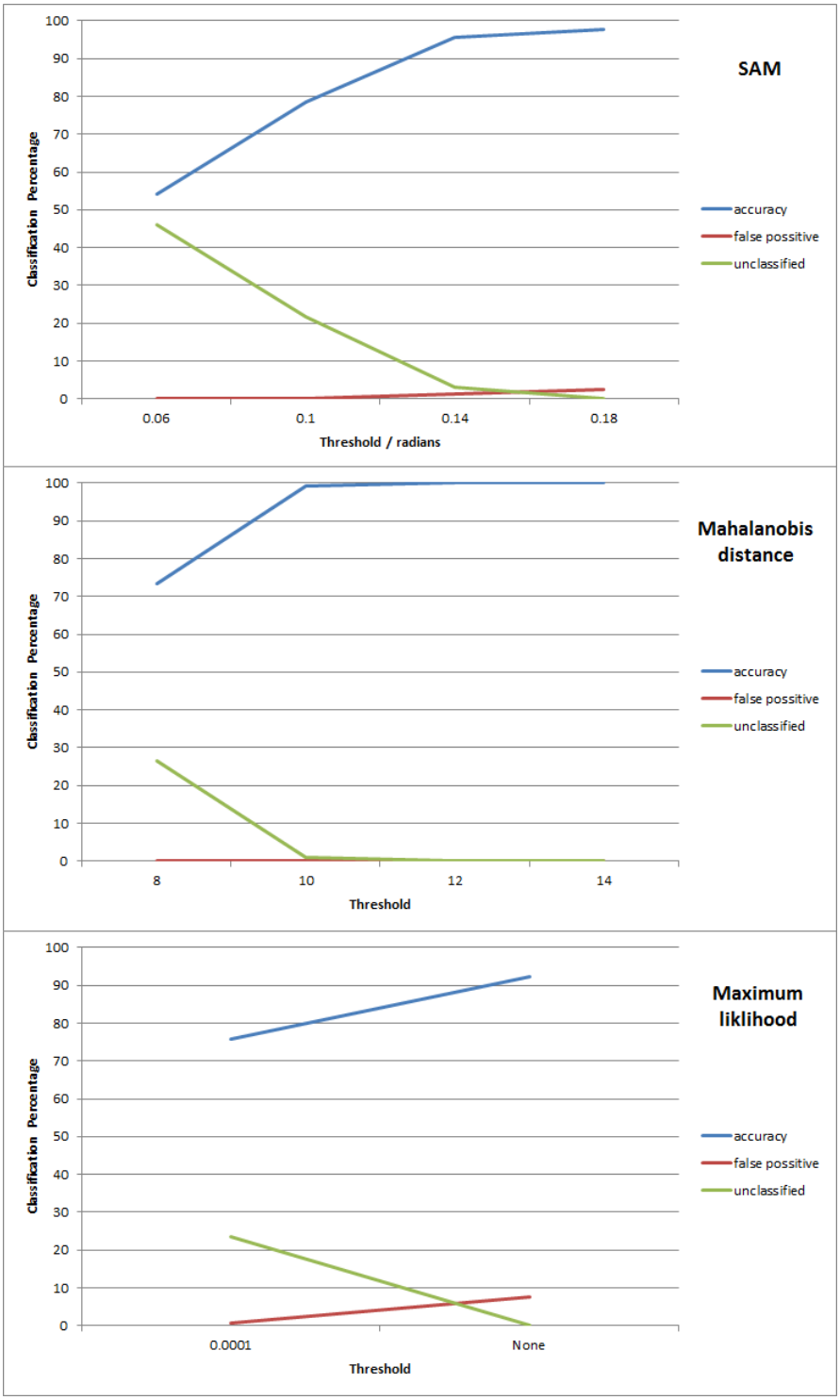

Figure 3.19: This figure compares the accuracy and false-positive rate of three classification techniques (spectral angle mapper, minimum distance, and Mahalanobis distance) when performed on hyperspectral data gathered around the River Derwent by the Eagle spectrometer. They also show how the results for each technique vary as the threshold value is changed.

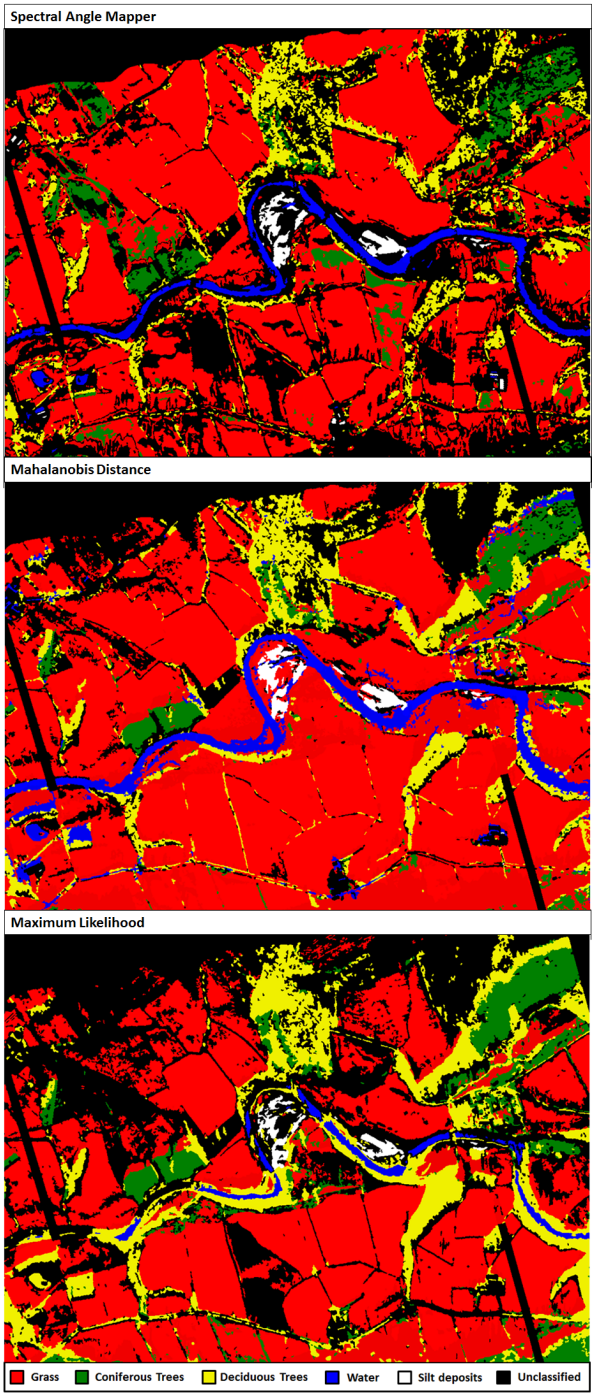

Figure 3.20: This image shows the classification maps of a test area around the river Derwent (shown in Figure 3.15) produced when three different classification methods (spectral angle mapper, Mahalanobis distance, and maximum likelihood) are applied to data from the Eagle spectrometer. These maps can be used to compare and contrast the classification performance of the different techniques over the entire spatial area.

excluded, the maximum likelihood method is able to classify with 100% accuracy, and similarly the SAM method is able to achieve a 100% classification accuracy if grass targets are excluded.

The Mahalanobis distance classification method has been shown to provide the most accurate general land cover classification for Eagle hyperspectral data (100% accuracy), with the SAM and maximum likelihood methods giving equally good results when grass and water targets are not present respectively.

In addition to the targets present, there are other factors that determine the suitability of each classification method for a particular situation. For example, the Mahalanobis distance and the maximum likelihood methods both require multiple input spectra to define the parameters of the reference spectra. Equations 3.14 and 3.16 showed that the covariance matrix of the input spectra must be calculated to define the variation of the spectra in the multi-dimensional space. The SAM classification method, however, only requires one reference spectrum per class. In cases where only one input spectrum is available, the SAM method is therefore the only method of the three that can be applied. Indeed in cases where there are very few input spectra SAM is likely to produce better results as a covariance matrix produced by fewer input spectra is less likely to give an accurate representation of the class variation.

3.3.2 River Deposit Classification

Secondary classification tests were carried out using more specifically defined flood deposit classes. The flood deposit classes were split into four categories, these being clean white gravel, grey gravel, mud and muddy water (see Figure 3.22). This made a total of eight target types: grass, river, coniferous trees, deciduous trees, clean white gravel, grey gravel, mud, and muddy water. These extra classes were used to help determine which of the classification methods could be used to most accurately identify different flood deposit types in the Eagle spectrometer data.

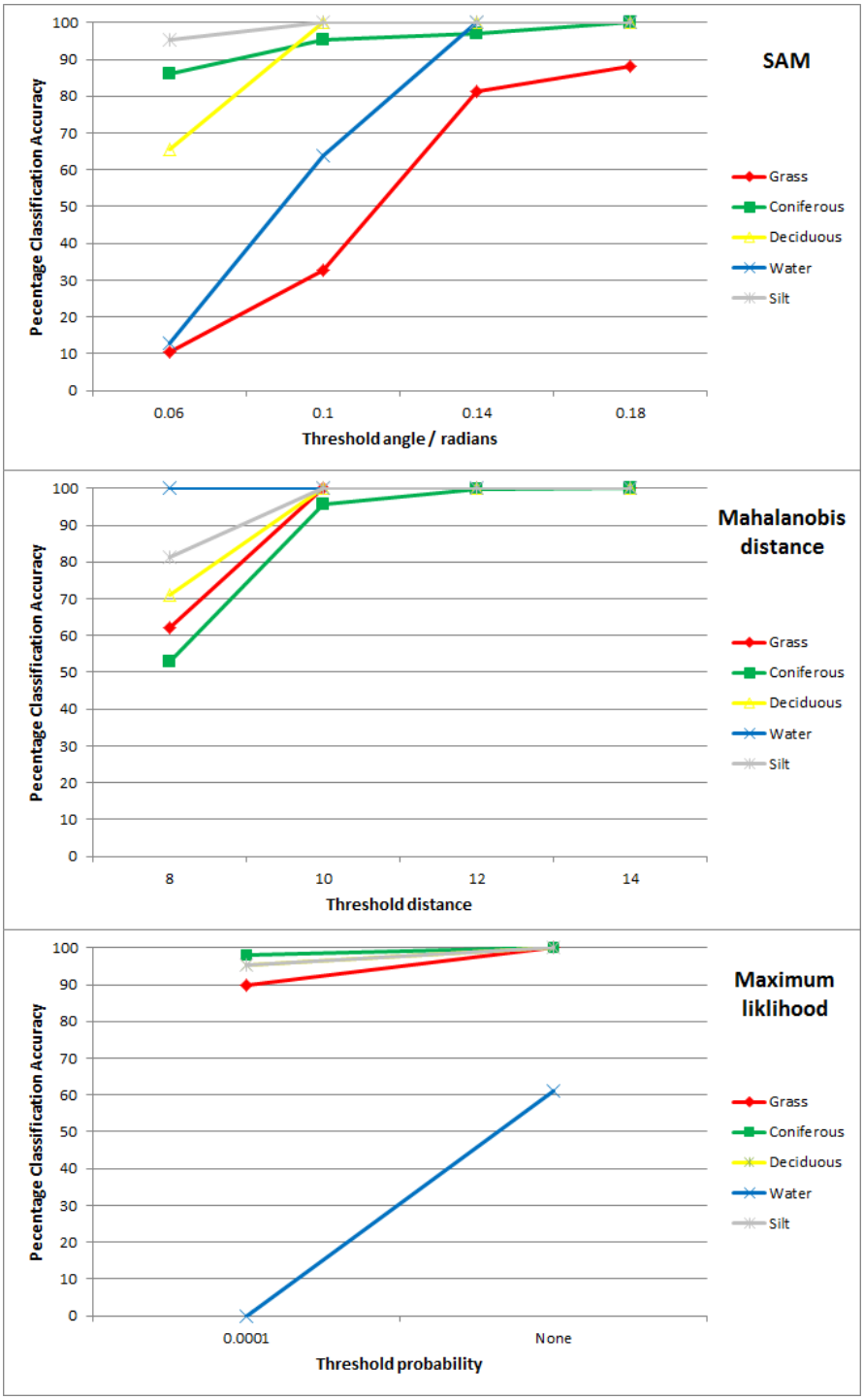

Figure 3.21: This figure shows the percentage classification accuracies achieved by three classification techniques (spectral angle mapper, minimum distance, and Mahalanobis distance) on hyperspectral data gathered around the River Derwent by the Eagle spectrometer. These graphs show how the classification accuracy of each target varies depending on the threshold used.

Figure 3.22: This image shows an area (about 5 x 10 km) around the Derwent river near Cockermouth imaged with the Eagle spectrometer. This is part of the test area that was used for classification of river deposits. The four different types of river deposit to be classified are labelled in the image. The colour image is made up from three bands - red: band 7, 449 nm; green: band 18, 550 nm; blue: band 29, 654 nm.

As the different flood deposit types occur more sparsely than the other land cover types, a larger test area was required. The deposits are only found around the river, so a mask was created that excluded all areas of the mosaic that were not immediately around the river (see Figure 3.24). ROIs were defined along the entire river path across the three flightlines.

Some ground truth data of the river deposits was available for small sections of the imaged flightlines. The little ground truth data that was available was used in conjunction with the appearance of the image when displayed in ENVI (see Figure 3.23), to ensure that the ROIs were defined with a high level of certainty. It was also attempted to include the full diversity of each target type when defining the ROIs, and shadowed areas were defined as different classes (as was done for the earlier classification).

Figure 3.23: This figure shows some of the ground truth photographs that were available for a small area of the Eagle/Hawk dataset gathered around the River Derwent in relation to an aerial image of the area. This data was used in conjunction with the appearance of the image when displayed in ENVI to determine the deposit types that are present in other areas in the flightlines.

Figure 3.24: This image shows part of the Derwent river from Cockermouth to the mouth imaged with the Eagle spectrometer. The image is created by placing a mask over the mosaicked image in Figure 3.14. This allowed a test area to be created that included just the river and its immediate surroundings, which was useful for classifying river deposit types. The colour image is made up from three bands - red: band 7, 449 nm; green: band 18, 550 nm; blue: band 29, 654 nm. The regular black lines on the imagery are due to a technical fault with the instrument timing.

The percentage classification accuracy and false-positive rate were calculated for various thresholds for each classification method. The results are presented in Figure 3.25 to demonstrate the trade-off between a high accuracy and a low false-positive rate.

The compromise required to achieve the minimum false-positive rate when classifying flood deposits,

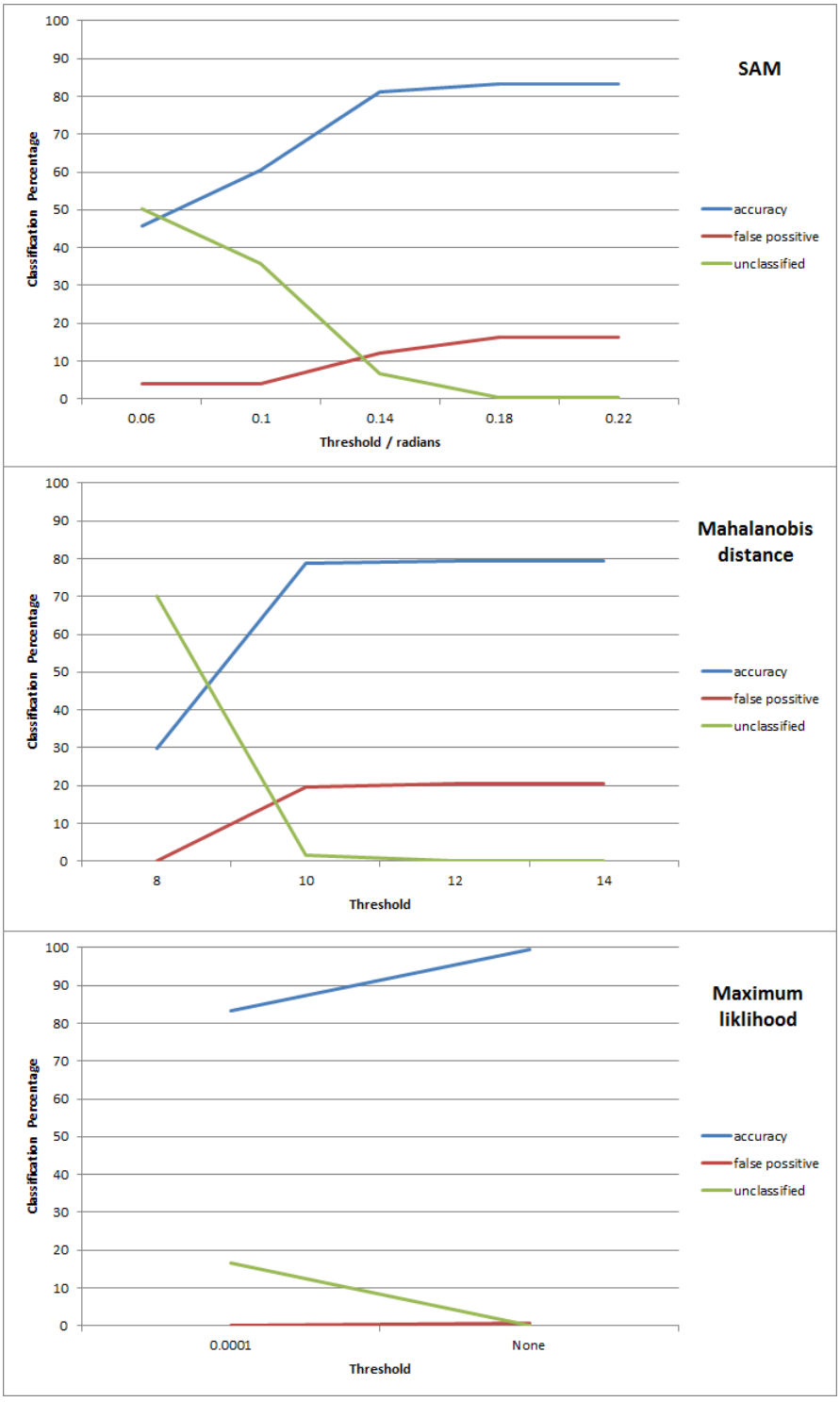

Figure 3.25: This figure compares the accuracy and false-positive rate of three classification techniques (spectral angle mapper, minimum distance, and Mahalanobis distance) to classify flood deposits in hyperspectral data gathered around the River Derwent by the Eagle spectrometer. The graphs show how the results for each technique vary as the threshold value is changed.

limits the total number of pixels classified to 46% for SAM, 30% for Mahalanobis distance, and 83% for maximum likelihood. When the threshold is increased so that 100% of the pixels are classified, the false-positive rates increase, leading to a classification accuracy of 83% for SAM, 80% for Mahalanobis distance, and 99% for maximum likelihood. These results differ from those obtained when performing a general land type classification, with the maximum likelihood method providing by far the most accurate results.

As was the case for the general target classification, the accuracies vary between river deposit targets. Figure 3.26 shows the percentage classification accuracy for each class within each classification method. It can be seen that the downfall of the Mahalanobis distance method when classifying flood deposits lies in the classification of white gravel. Without this class it is able to achieve 100% classification accuracy. False-positive results in the SAM method are shown to be mostly a result of poor white gravel and muddy water classification, with high classification accuracies of grey gravel and mud. The purpose of these methods, however, is to classify between river deposit types, and so classification accuracies of all the deposit types must be taken into account.

The classification tests performed in this section give a good indication of the performance of different classification techniques on Eagle hyperspectral data. The Eagle data used was shown to be of high enough quality to achieve 100% classification accuracy for general target types when using the appropriate method.

These test do, however, have limitations. In particular, because of the very limited ground truth data available about the land cover types, ROIs and test ares had to be largely defined by eye. This meant that only visually identifiable areas in the reconstructed ENVI image were able to be used for obtaining reference spectra and calculating the results. If more extensive ground truth data were available, the pixels used to define ROIs and to gather results from could be selected more randomly, and more extensively.

These classification experiments have highlighted some of the difficulties encountered in classifiying hyperspectral remote sensing data. The poor illumination conditions under which the imagery was taken have shown to have cause classification issues in areas of low reflectivity (i.e. water and shadowed areas). This highlights the potential for improving classification results by using an instrument that can achieve an even higher SNR.

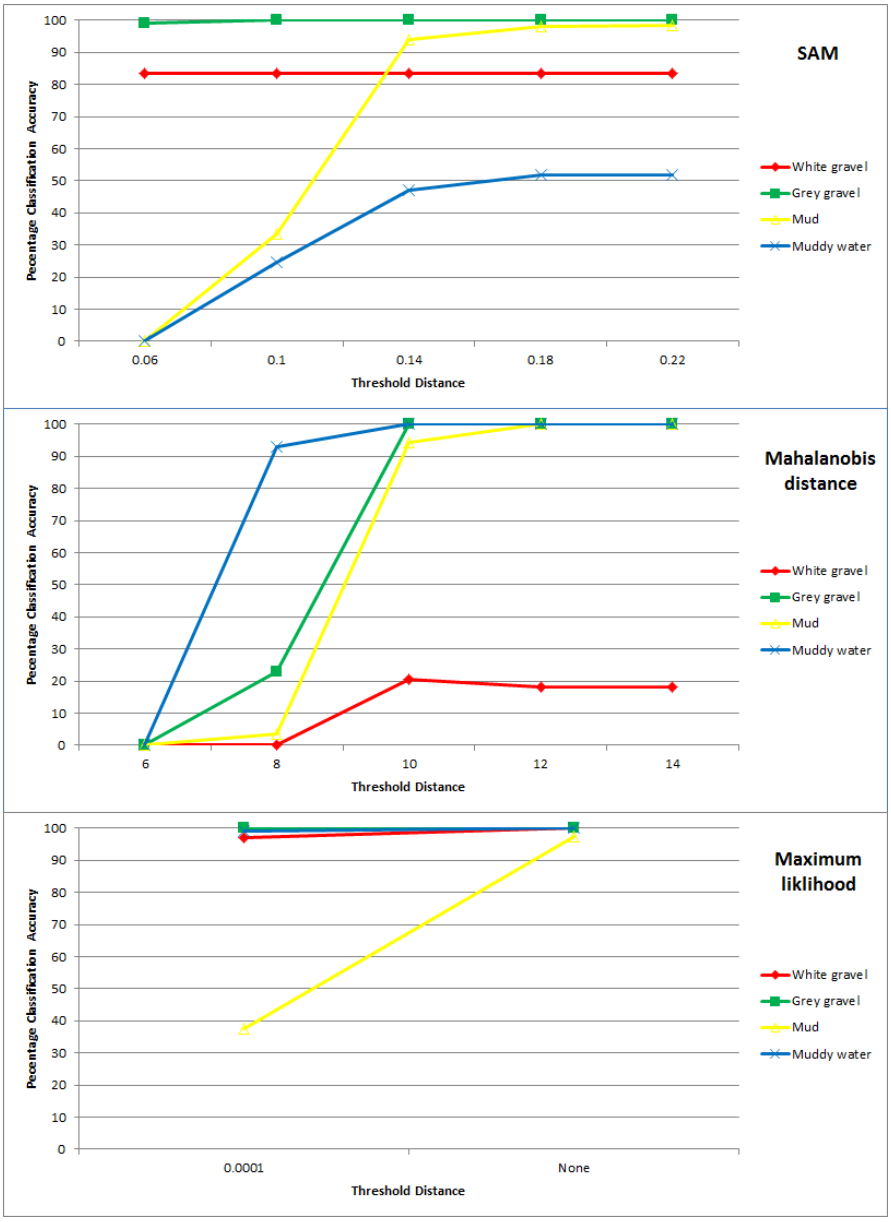

Figure 3.26: This figure shows the percentage classification accuracies achieved by three classification techniques (spectral angle mapper, minimum distance, and Mahalanobis distance) on hyperspectral data gathered around the River Derwent by the Eagle spectrometer. These graphs show how the classification accuracy of different flood deposit targets varies depending on the threshold used.

3.4 Summary

This chapter has consisted of three distinct sections. The first section outlined the ideas behind different methods of hyperspectral data interpretation methods. The second section examined the specifics of processing a hyperspectral dataset gathered using the Eagle and Hawk spectrometers. The third section focused on the quantitative assessment of three different land classification techniques when applied to the Eagle hyperspectral dataset.

The data interpretation section highlighted the fact that, due to the depth of information that hyperspectral data provides, and the variety of applications that it is used for, there are a wide range of hyperspectral data interpretation techniques that can be applied. These included classification techniques, feature detection, and spectrally derived parameter calculations.

The data processing section explained the different levels of hyperspectral data, and described the additional processing meta-data required to obtain fully processed hyperspectral data from raw sensor data.

The ENVI classification section presented some new classification results on Eagle spectrometer data to supplement the data processing and interpretation theory. This study provided a measure of the utility of the Eagle data, as well as the classification techniques used. Classification accuracies of 98%, 100%, and 92% were achieved for SAM, Mahalanobis distance, and maximum likelihood methods respectively when classifying general targets. When classifying flood deposits accuracies of 83%, 80%, and 99% were achieved for SAM, Mahalanobis distance, and maximum likelihood methods respectively. Further to these results it was noted that the classification accuracy was often highly dependent on class, and that a disproportionately high number of false classifications occurred in shadowed areas.

The difficulty of the classification techniques to classify shadowed areas highlights one of the main shortcomings of hyperspectral remote sensing instrument capabilities. Low reflectance intensity targets, such as those in shadow, reduce the signal, and hence the signal to noise ratio (SNR) imaged by a remote sensing instrument. The SNRs of some water target areas within the Eagle dataset were calculated, and are shown in Figure 3.27. These results were obtained by calculating the mean and standard deviation of the signal received over a homogeneous target area. Water targets were used as they are typically dark targets, and they provide very homogeneous areas, meaning that it is appropriate to take the standard deviation of the radiance across multiple pixels as the noise. It can be seen that in shadowed areas the SNR is significantly lower than for target areas with full illumination. An instrument capable of achieving higher overall SNR could therefore be more useful for imaging low reflectance intensity targets.

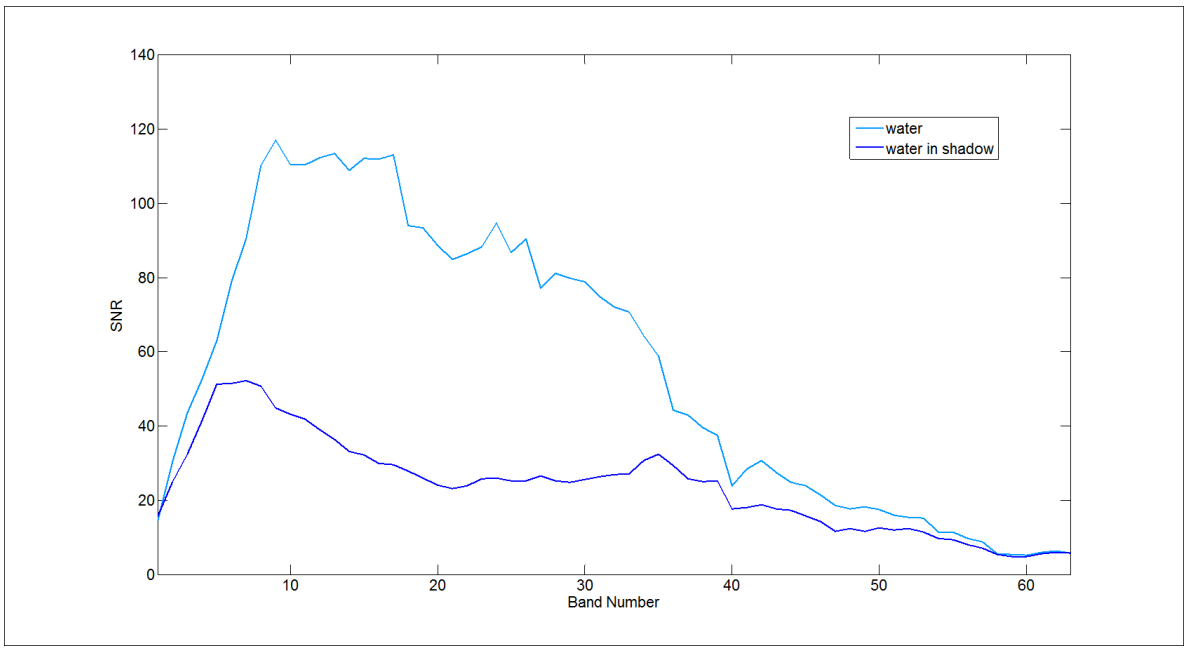

Figure 3.27: This graph shows the signal to noise ratio (SNR) of Eagle data gathered from shadowed and non-shadowed water. This is measured statistically from the processed Eagle data.

Table 1.1 shows that while hyperspectral remote sensing instruments provide a wide range of spatial and spectral resolutions, there is much less variety in the SNR of instruments, with few instruments achieving an SNR of over 500. Chapter 2 showed that some applications are pushing the boundaries of the SNR achievable by remote sensing imaging spectrometers, and so useful data may not be attainable for such applications when imaging targets in sub-optimal illumination conditions. The next chapter details the development of a prototype novel hyperspectral imager that was designed to have the potential to provide a significantly higher SNR than current remote sensing spectrometers.

Chapter 4

The Development of a Prototype Microslice Hyperspectral Imaging System

The key to gathering remote sensing data with a high signal to noise ratio (SNR) lies in maximizing the *dwell time* of the instrument. The dwell time is the length of time that an area of ground is imaged in a single flight pass. A higher dwell time leads to a higher SNR, because the signal gathered increases linearly with exposure time, while the noise increases at a smaller rate (this is explained in more depth in Section 7.1.3). The SNR is also affected by the altitude of the sensor, as light traveling to a higher altitude encounters more interference from the atmosphere, which lowers the signal strength and increases the noise level.

The issue with trying to obtain a high SNR with a standard pushbroom remote sensing instrument is that the sensor only images a single row of pixels that is constantly moving with the airborne platform (see Figure 1.3). This means that the instrument only provides 1-dimensional spatial multiplexing, and is therefore constantly imaging a new area of ground, leading to a short dwell time. For a conventional pushbroom remote sensor there is a minimum speed at which the airborne platform can travel, and therefore a maximum dwell time that can be achieved. Standard airborne pushbroom imagers, such as AVIRIS have typical dwell times of about 100 ms, and standard spaceborne pushbroom imagers, such as Hyperion have typical dwell times of about 3 ms (see Table 1.1).

The Centre for Advanced Instrumentation (CfAI) in the Durham University physics department obtained *seedcorn* funding from the Centre for Earth Observation Instrumentation (CEOI) to develop a prototype hyperspectral imager for remote sensing. This chapter details the design and development of this hyperspectral imaging system, which was designed for ground based laboratory and field testing to

a budget of about £20k. The novelty of the design concept lies in its use of microslicing technology to achieve a 2-dimensional instantaneous field of view (IFoV). Microslicing is a specific method of integral field spectroscopy (IFS), which is a technique currently used in astronomical spectral instruments, but not for Earth observation (EO). The IFS concept and technology was developed at Durham University, and has been implemented in the Gemini near-infrared spectrograph (GNIRS) which was mounted on a telescope at the Gemini observatory for astronomical imaging [108]. The specifics of the microslicing method used will be described in detail later in the chapter along with the rest of the optical design in Section 4.2.1.

In order to best exploit this 2-dimensional IFoV a slightly different scanning technique to a conventional pushbroom is proposed. This technique is known as step-and-stare, and involves changing the angle of the field of view (FoV) slightly during flight so that the same area of ground is imaged for an elongated period of time (see Figure 1.4). This can be achieved by using a de-scan mirror, which would would be a plane mirror used to change the angle of the FoV in a different direction by changing the angle of the mirror.

4.1 Background

As discussed in Chapter 1, different hyperspectral imaging systems use different levels of multiplexing to build the final datacube. A higher level of multiplexing, requires a larger detector, but allows for a greater SNR. Spatial multiplexing methods are useful for monitoring rapidly time-varying phenomena or operating in poor conditions (such as where the spectral transmission of the atmosphere is low and/or varying with time). Each multiplexing method has its own advantages and disadvantages, depending on the final application, but the power of each system is ultimately limited by the total number of detector pixels available.

The most common method of multiplexing is 1-dimensional spatial and spectral multiplexing, which is used in conventional pushbroom systems, such as Hyperion, and Eagle (see Table 1.1). Whiskbroom remote sensors, such as AVIRIS, do not use spatial multiplexing, but do obtain spectrally multiplexed data. Fourier transform spectrometers (see Section 1.4.2) use 2-dimensional spatial multiplexing, but no spectral multiplexing.

The *microslice spectrometer* design presented in this chapter uses spectral multiplexing **and** 2-dimensional spatial multiplexing, potentially making it the first remote sensing instrument to use 3-dimensional multiplexing. The main advantage of this method is that it provides greater opportunity of trade-off between the instruments spatial and spectral specifications. The following design section shows how this 3-dimensional multiplexing is achieved with a compact, high throughput optical system.

4.2 Instrument Design

The principle of operation of the microslice spectrometer is shown in Figure 4.1. The design uses a pair of orthogonal cylindrical microlens arrays to segment the input field into a series of rectangular apertures. These apertures are then reformatted into an array of thin *microslices* by demagnifing them by different amounts in two perpendicular directions (this is known as anamorphic demagnification). The input image is pre-stretched by the anamorphic foreoptics to ensure that the geometrical integrity is preserved in this stage. The microslices form an array of small virtual slits (slitlets), which feed a conventional transmissive spectrograph (see Figure 1.5) with a collimator/camera subsystem and a dispersion element. The dispersed spectra are tilted to make the most effective use of the available detector pixels and avoid spectral overlap. Each dispersed slitlet (spectral slice) contains spatial information along (but not across) the slice.

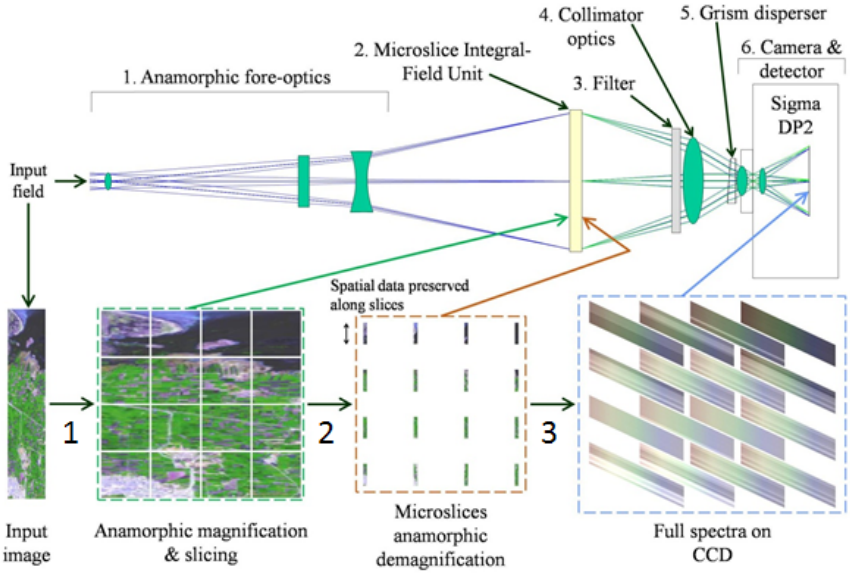

Figure 4.1: The top half of this diagram shows the basic optical design of the prototype microslice spectrometer. The images on the bottom half show how the light in the input image is affected by different parts of the optical set-up. This consists of three main stages: 1) the foreoptics are used to anamorphically stretch the image in both directions, 2) the image is divided into rectangular sections and demagnified to create slices using a microslice integral field unit (IFU), 3) the slices are dispersed across the CCD sensor using a grism.

The number of spatial samples in the final datacube is determined by the number of resolved spatial elements along each microslice (which is determined by the optical point spread function (PSF)) multiplied by the number of microslices. In the case of the prototype system described here, this amounts to approximately 5000 spatial samples, although scaling to much larger sizes is, in principle, possible. The number of spectral samples is determined by the number of resolved spectral elements across each dispersed microslice. This is expected to be about 50 elements, which can be used to give wide spectral coverage at low resolution, or higher spectral resolution over a shorter wavelength range. The following sections describe the optical design in more detail.

4.2.1 Optical Design

A full optical design was completed including a tolerance analysis, which was then iterated with the optics manufacturer (Spanoptic Ltd.) to bring the custom optical components within budget. The detailed optical design of this instrument was created by Robert Content, and has been published in the *Remote Sensing* journal [109]. The optical setup of the microslice hyperspectral imager is composed of five parts:

1. The anamorphic foreoptics
2. The microslice system
3. The collimator
4. The dispersing element
5. The camera (the optics and detector array).

4.2.1.1 Anamorphic foreoptics

The anamorphic foreoptics magnify the light by different amounts in two orthogonal directions. This prepares the light for the image slicer, and ensures that the spatial integrity is preserved when demagnification is performed by the microlenses. The foreoptics consists of three cylindrical lenses and a cylindrical doublet comprising two lens assemblies, one imaging the vertical direction the other in the horizontal. The fore-optic lens assemblies have different powers in the directions parallel and perpendicular to the microslice length, and two different glasses are used to minimise the chromatic aberrations.

In this prototype design the magnification is approximately 5x larger in the direction perpendicular to the slitlet length. The input object field is approximately 10 x 50 cm and is located at a distance of 2 m in front of the first foreoptics lens, giving a total field of view (FoV) of approximately 3^{o} x 15^{o} (as viewed from first lens). The focus of about 2 m is set to facilitate laboratory tests, but the instrument can be refocused to view an object up to infinity. The resulting image on the microslice system is approximately 10 x 10 mm. The vertical and horizontal input planes of the microslice system are not at the same position along the optical axis so the foreoptics were designed accordingly.

4.2.1.2 Microslice system (image slicer)

The image slicer consists of two sets of two microlens arrays (see Figure 4.2). The first pair of microlens arrays demagnify different sections of the image in the two perpendicular directions separately to slice the image up into an array of microslice images. The power of the lenses are set to create enough space between the microslice images to enable the dispersed spectra to be interleaved on the detector (see Figure 4.1). The second pair of microlenses focus the microslice images into slitlets, which prepares them for the imaging spectrograph part of the instrument. The vertical microlens arrays have 33

lenses, and the horizontal arrays have 20 lenses, which have pitches of 330 microns and 500 microns respectively.

To keep the cost of the prototype low, off-the-shelf all-silica microlens arrays were used (from SUSS MicroOptics), which restricted the choices of focal lengths available. With the off-the-shelf optics five arrays were needed instead of four, as two identical arrays were used to replicate a single array of half the focal length. The limitation on the choice of focal lengths also meant that the vertical and horizontal image planes could not be superimposed at both input and output. A choice was made to superimpose the output planes (just inside of the substrate of the final lenslet array) and to have the input focal planes separated by 1.5 mm.

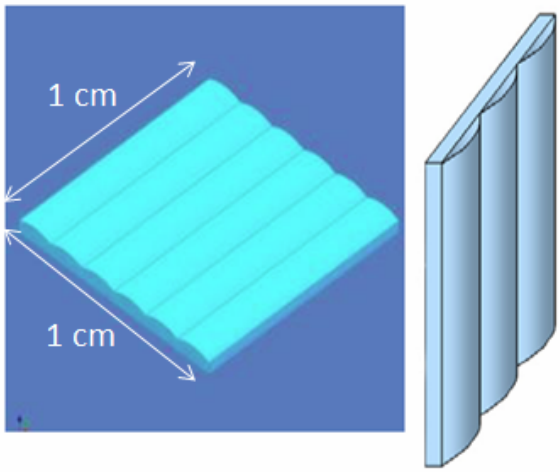

Figure 4.2: This image shows a precision cylindrical microlens array. The arrays used in the prototype microslice spectrometer have lens widths of $500\,\mu m$ in the horizontal direction and $330\,\mu m$ in the vertical direction, with 20 and 33 lenses respectively.

The output achieved by the microslice system is an array of slitlet images each with approximate dimensions of $125 \times 20\,\mu m$ (see step 2 in Figure 4.1). A critical characteristic of this system is that the spatial information is retained along each slitlet. One slitlet contains many individual spectra which are dispersed adjacent to each other on the detector to form a spectral slice (see step 3 in Figure 4.1). With the blurring of the images due to the optical aberrations, there are approximately 9 spatial resolvable elements per slitlet in the preliminary design, giving a total of 180 x 33 spatial elements (and hence independent spectra). This is a very significant improvement on previous lenslet array systems and enables far more spectra to be packed onto the detector [108].

Imperfections in the lenslet arrays meant that the potential for stray light was increased. Small flat areas between the lenslets were covered with opaque strips to minimise stray light.

4.2.1.3 Spectrograph collimator

The collimator is the first component of a compact imaging transmissive spectrograph which also consists of the dispersing element, the camera, and the detector. This transmissive spectrograph is the same as a standard spectrograph (as seen in Figure 1.5), but with lenses being used in place of mirrors, and a grism instead of a grating. Using lenses allows for a linear light path, which is better for producing a compact system. Also imperfections in lenses cause smaller abberations than imperfections in mirrors, and such imperfections have a particularly large impact at short wavelengths, such as the visible wavelength range. Spectrographs that cover a larger wavelength range generally use mirrors as, unlike lenses, they are a-chromatic (i.e. their reflectivity is not wavelength dependent). Also, the smoothness of the surface has less of an impact on longer wavelengths, such as in the infrared.

The slitlet images produced by the microslice lie at the input focal plane of this spectrograph set-up, and act a virtual slits for the spectrograph. The collimator re-images the slitlets close to infinity, and positions the output pupil on the stop of the camera to minimise losses of light by vignetting. This also minimises the effects of higher orders of dispersion from the grism which are cut off, at least in part, by the camera stop.

The dispersive element is not quite in a collimated beam, so that the lens on the camera can be used for fine focus adjustment, and since the input field is approximately 2.6 m in front of the camera the induced aberrations are negligible. A custom optical design (of five elements) was made, since this is the optical system that could best minimise aberrations. Inexpensive glasses were used where possible to keep the cost down. All the custom made optics (together with the microlens arrays) were anti-reflection coated to reduce stray light and ghost reflections.

4.2.1.4 Dispersive element

The dispersing element used in this instrument is a grism (a grating attached to a prism, see Figure 4.3). The grating disperses the light, while the prism maintains the direction of the optical axis for a linear mechanical design. A plane transmissive grating was chosen, so that as much light as possible was directed into the lowest diffraction orders, which also helps maintain a linear mechanical design. The grism used consisted of a custom made 12° prism glued to a plane transmission grating operating over a bandwidth of 400-700 nm. This was attached to the output of the collimator to form one optical element.

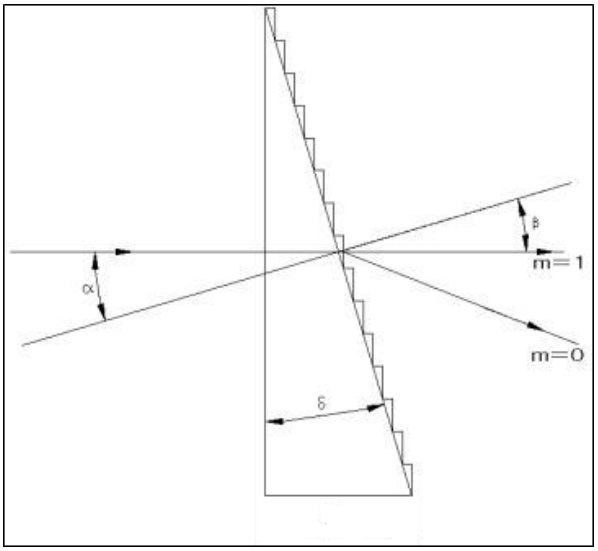

Figure 4.3: This image shows a typical grism dispersing element, as used in the prototype microslice spectrometer. The set-up consists of a plane transmission grating attached to a prism. α and β represent the angle of incidence and dispersion with respect to the normal of the grating. The angle of the prism (δ) is set such that α and β are equal for first order diffraction ($m = 1$), meaning that the light passes through the dispersion element without changing axis. Other dispersion orders propagate in different directions, and should be blocked to avoid contamination. This image was taken from [110].

The grism was placed as near as possible to the camera so that it is close to the stop of the spectrograph. In the prototype design, the off-the-shelf grating used had 200 lines/mm giving 50 spectral elements of approximately 6 nm each sampled by about 4 pixels on the detector. In order to avoid spectrum overlaps the dispersion direction is not exactly in the direction perpendicular to the slitlets, as is the case in a classic spectrograph, but is rotated by 29° to utilize the detector pixels as efficiently as possible (see Figure 4.1).

4.2.1.5 Camera and Detector

For the final design of a fully functional spectrometer, a custom made detector would be used to ensure that all the required capabilities are provided (such as sensitivity and capture software requirements), whilst also optimising the size and weight of the component. For this prototype instrument however, costs were minimised by using a commercially available digital camera, which incorporated the camera optics and detector in the same package.

The digital camera used in the prototype system was changed twice through out the testing process (see Section 4.4). The camera in the initial design was a Sigma DP2 camera, which used a 2640 x 1760 complimentary metal-oxide semiconductor (CMOS) detector with 7.8 μm pixels. The effective spectral length was, in principle, about 25 slitlet widths after leaving a small dead space around each spectrum. The Sigma camera was chosen as it used a novel Foveon® CMOS detector, which is made of three-layer pixels (red, green & blue) to give an equivalent of 14.1 megapixels (see Figure 4.4). It was estimated that this property could be used to increase the length of the spectra by approximately

50% (after extraction) by allowing the blue end of one spectrum to overlap the red end of another on the same spatial pixels. A bandpass filter that limited the wavelength range to 450-675 nm was used to reduce the spectral overlap, and to provide a clearer separation between the first order and zeroth order spectra.

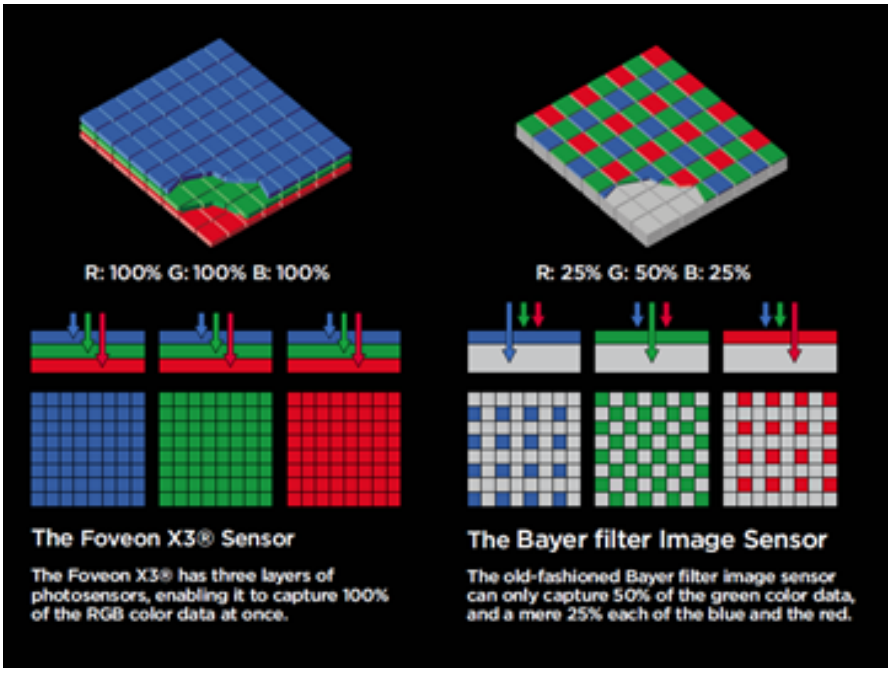

Figure 4.4: This images shows the mode of operation of a Foveon® detector compared to a standard Bayer sensor. The Foveon sensor detects red, green and blue at each spatial pixel, and therefore captures three times as much light for the same detector area. Each spatial pixel on the Bayer sensor detects either red, green or blue, meaning that interpolation is required to create a full RGB image. This image was taken from [111].

A CMOS detector varies from a standard CCD sensor in the way that the data is read from the chip. In a CCD detector the charge for each pixel transported across the chip and read at one corner of the array, and an analog-to-digital converter turns each pixel's value into a digital value [14]. A CMOS sensor uses a transistors at each pixel to amplify and read the charge for that particular pixel. CMOS sensors are cheaper and consume less power than CCDs, but CCD detectors tend to produce higher quality images with lower noise levels.

Both CMOS and CCD detectors use a silicon chip to detect in the visible wavelength range. To detect different wavelength ranges, however, different semiconductor materials would be required; for example, in the AVIRIS sensor (see Table 1.1), silicon (Si) detectors are used for the visible range, indium gallium arsenide (InGaAs) detectors for the near-infrared (NIR), and indium-antimonide (InSb) detectors for the short-wave infrared (SWIR) [112].

4.2.2 Mechanical Design

The purpose of developing this prototype instrument was mainly to investigate the viability of the microslice spectrometer concept, but it was also to explore issues with the assembly and integration. Although the prototype version was not expected to have the level of performance that would be available from an optimised design, the goal was to demonstrate the proof-of-principle, and give some guidance on where improvements in the opto-mechanical design would have the greatest pay-off. The mechanical construction was therefore designed to expedite laboratory tests of performance as benchmarked against conventional spectrometers, and also to be robust enough to enable some measurements to be taken in the field. No particular priority was placed on minimising volume or mass.

The overall mechanical layout of the initial prototype is shown in Figure 4.5. The complete prototype system is contained in a space envelope of approximately $0.008\,m^3$, with optical components and mounts weighing approximately 5 kg. Even though this size and weight could be significantly reduced with an optimal instrument design, it is believed to be unmatched for a system capable of delivering approximately 5000 independent spectra each with about 50 spectral channels. The CHRIS spectrometer (see Table 1.1) is a recent hyperspectral remote sensing imaging system that images 576 independent spectra with 62 spectral bands. It occupies a larger space envelope ($0.04\,m^3$), and weighs more (14 kg) than the prototype microslice spectrometer [29].

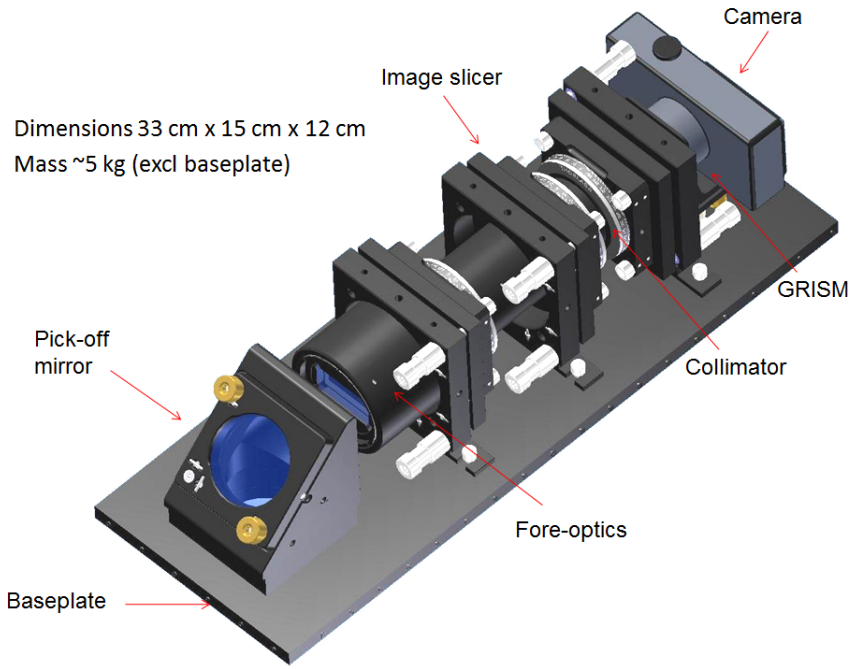

Figure 4.5: This image shows the mechanical design of the prototype microslice hyperspectral imager with the main components labelled. The cover is omitted for clarity.

The mechanical design of the spectrograph consists of four major sub-assemblies: the foreoptics, the microslice system, the collimator, and the camera. These are mounted onto a base plate to form the

core of the instrument.

The foreoptics assembly consists of the optical elements being mounted into a series of lens cells using ultraviolet curing optical adhesive, and then mounted into a cylindrical lens barrel. During instrument assembly the foreoptics lens barrel was inserted into a kinematic rotation mount thereby permitting alignment of the foreoptics to the microslice system. The foreoptics barrel features a series of finely threaded setscrews that engage with flats machined into the periphery of each lens holder. Rotational alignment of the optical elements within the foreoptics barrel was achieved by adjustment of each setscrew pair.

The microslice system comprises the series of five cylindrical microslice arrays arranged sequentially. Each microslice array was retained within a lens cell using ultraviolet curing optical adhesive. Each cell has a series of four precision reamed holes, which precision machined retaining screws pass through. These screws prevent displacement or rotation of the individual lens cells, and also permit clamping together of the lens cells to form the microslice assembly once the individual microlens arrays have been aligned (for shift and rotation) within their cells (further details are provided in Section 4.2.3).

The collimator was procured with all of the collimator optical elements pre-assembled into a lens barrel to form the collimator assembly. At the rear of the collimator assembly an internal screw thread and shoulder face are provided to permit installation of the grism cell. The cell consists of a rectangular aperture, within which the grism was retained using an ultraviolet curing optical adhesive. An external screw thread and shoulder on the grism cell permits installation into the rear of the collimator assembly. Orientation of the grism with respect to the camera was achieved by rotation of the whole collimator assembly within its kinematic rotation mount.

In the original design the spectrograph camera/detector assembly consisted of the Sigma DP2 digital camera on a kinematic mount. The mount was a custom design permitting tip/tilt of the camera and 4 mm of translation in the vertical axis. A mechanical stop was incorporated into the kinematic mount to prevent damage to the grism occurring as a result of inadvertent contact between the camera lens barrel and the grism when the camera is switched on, and is initialising the focus drive.

The full assembly comprises of a base plate onto which the foreoptics, microslicer, collimator and camera assemblies are installed via their respective kinematic mounts. Alignment of each assembly was achieved by manual adjustment of tip/tilt, translation and rotation. For the purposes of alignment, the position of the microslicer was considered to be the fixed reference datum. A fold mirror and corresponding circular aperture in the base plate was also provided to allow the instrument to be maintained in a horizontal orientation when viewing objects below (see Figure 4.6).

All mechanical assemblies were anodised to minimise the effects of stray light in the system. The gap between the back of the grism and the camera was still provided an oppertunity for the entrance of stray light. A two-piece cover was therefore also provided to minimse stray light, as well as to provide some weatherproofing and dust control. This was important of maximising the SNR achievable by the instrument.

The propergation of stray light in the system leads to additional counts on the detector in the presence of illumination. This noise can therefore be present when there is no signal, but also increases in proporton to the signal, and can therfore increases the dark noise and the signal noise (see Section 7.1.3).

Access to the digital camera functions is permitted through apertures in the cover. However, should it be necessary to remove the camera from the spectrograph, the camera cover may be removed by itself without removal of the spectrograph cover. In this way access to the camera may be gained without exposing the spectrograph optics to the ambient environment. The overall space envelope of the spectrograph with the cover fitted is 420 mm (L) x 150 mm (W) x 120 mm (H). The mass of the spectrograph assembly is about 9 kg (including the base plate).

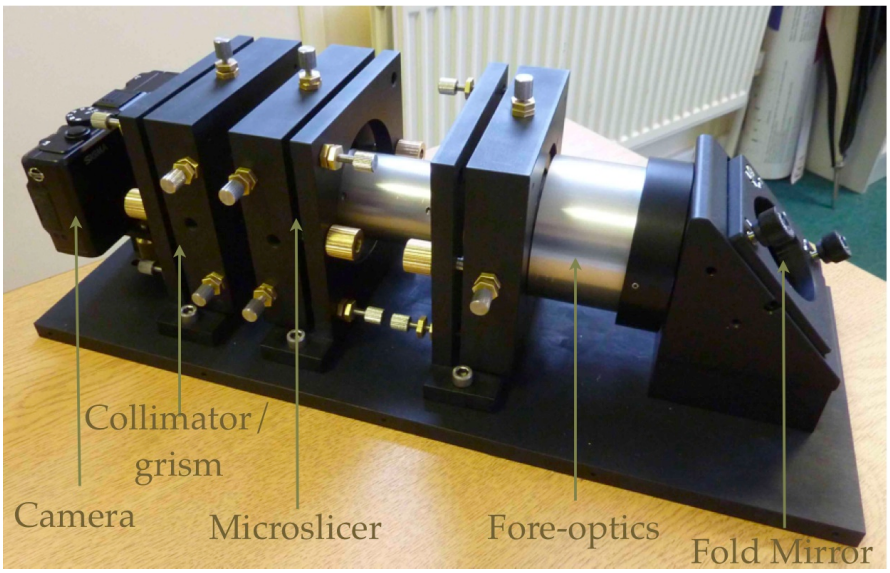

Figure 4.6: This photograph shows the fully assembled prototype microslice hyperspectral imager. The cover is omitted, and each mechanical assembly is labelled for clarity.

4.2.3 Assembly and Integration

The most critical task during assembly and integration (AI) was assembling the microslice system. The 5 arrays had to be aligned with a high precision including their positions along the optical axis. Assembly was done using a custom jig that held each microlens array and permitted it to move and

rotate in the plane of its support (see Figure 4.7). Laser and white light illumination from underneath the nested arrays was used to measure the position and rotation by comparing the spot patterns produced on a target at 2 m distance with simulations made from ray tracing of the optical design. Using this method, displacements of about 1 micron could be detected. Once correctly located, the arrays were fixed using ultraviolet curing adhesive.

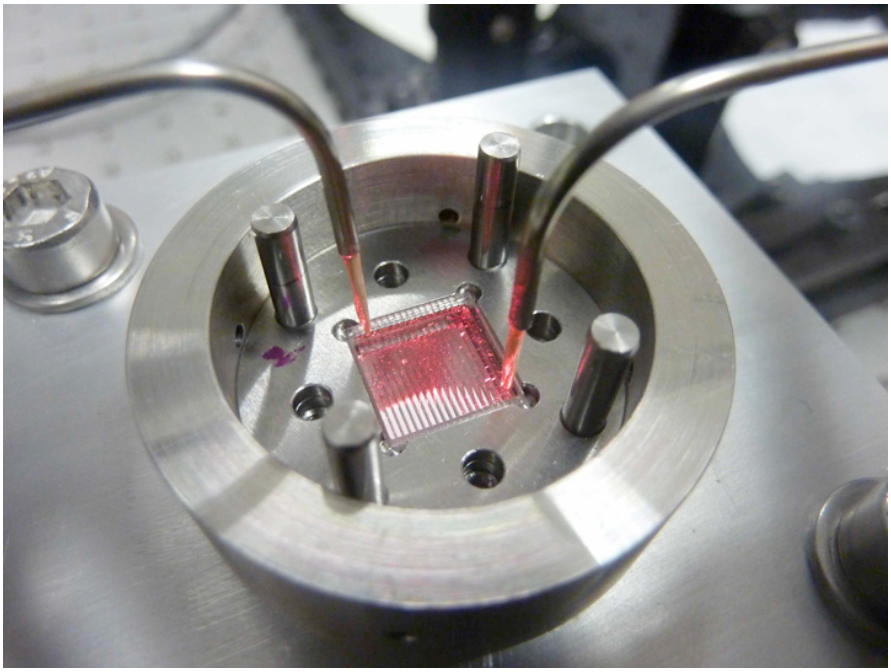

Figure 4.7: This image shows one of the microlens array elements in the image slicer being aligned using a set of micro-manipulators. The array is illuminated from below using a red laser and the spot pattern matched to a printed target produced from ray tracing of the ideal optical design. Each of the arrays are 10 x 10 mm.

An additional problem encountered was that the first array of the stack had a different focal length than was specified by the manufacturer; this had to be compensated for by reversing and displacing one of the arrays by 1.2 mm along the optical axis using shims. A few of the microlenses had become defective as they had been damaged whilst the arrays were being anti-reflection coated by the manufacturer. Also, the microlens arrays were also found to have slight gaps between lenses, which caused parasitic light in the system. Black masks were placed between the microlenses and over the defective microlenses to avoid this problem.

The foreoptics did not require a very high alignment precision and mostly relied on mechanical precision. All of the optical assemblies were then aligned to each other using targets and an alignment telescope, with the microslicer as the reference. These small problems would all be avoided when producing a full function instrument with custom made optics, and less severe constraints on costs.

4.3 Laboratory Performance

During assembly of the instrument, tests were carried out on some of the sub-assemblies of the system. A CCD camera was used to measure the image quality given by the microslice system and by the collimator. Images of spectra were then taken using the fully assembled system illuminated by different continuum and arc lamps. A laser spot was displaced on a white surface on the input focal plane 2 m from the instrument to determine the shape and size of the field of view. Several test patterns were also observed to check the spatial imaging performance of the instrument, although spatial performance of the full system also depends on the quality of datacube reconstruction software (see Section 4.6).

4.3.1 Microslicer Image Quality

The foreoptics were assembled using laboratory mounts and used to test the image quality of the microslice system, which is a crucial parameter for determining the spatial and spectral resolution of the final instrument. The images of the spectral slices at the output were observed with a 10x microscope mounted on a CCD camera imaging the objective (see in Figure 4.8). Each pixel on the CCD corresponded to a width of $0.78\,\mu m$ on the image plane, permitting precise measurement of the aberrations.

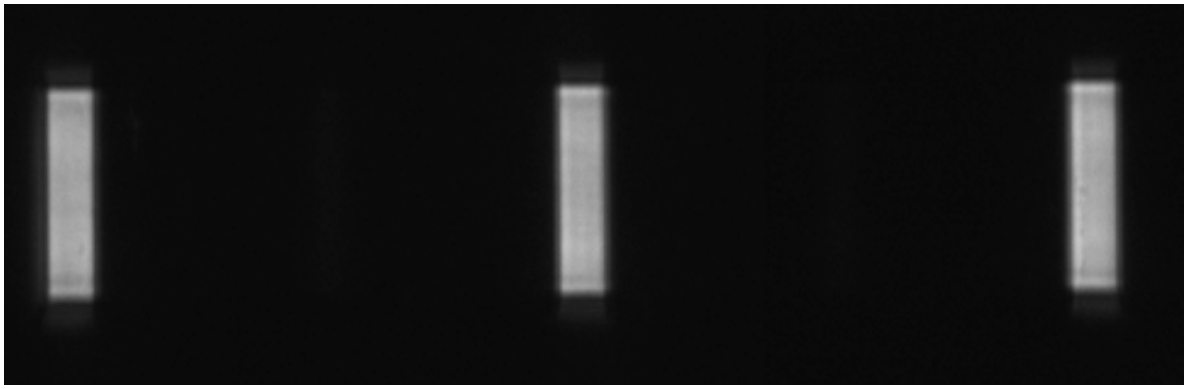

Figure 4.8: This is a 10x magnified image of the output from the microslicer assembly when illuminated with a white light continuum source. These virtual slitlets are used as inputs to the spectrograph, as shown in Figure 4.1. An intensity cross-section through one of these slices is shown in Figure 4.9.

Figure 4.9 shows the intensity distribution and the derivative of the intensity distribution across the width of a microslice. The latter gives a good estimate of the spatial point spread function (PSF) at each side of the slice. The measurements show that the PSF full width at half maximum (FWHM) is smaller than a pixel on the Sigma DP2 camera detector (about $0.3\,\mu m$ compared to $0.8\,\mu m$ on the magnified image plane), which was the design goal.

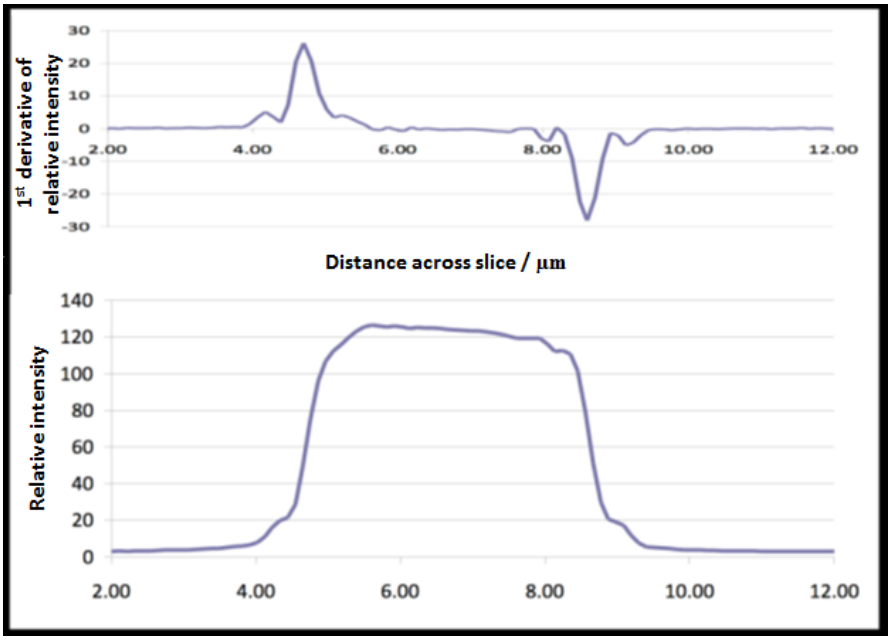

Figure 4.9: The bottom curve shows a cross-section of intensity across one of the slitlet images produced by the microslicer, which were imaged with a 10x microscope aperture (see Figure 4.8). The sharpness of the edges are used to determine the image quality of the microslice system. This sharpness is measured by the upper curve, which shows the derivative of this profile, where the width of the two peaks correspond closely to the spatial point spread function (PSF) of the system, and is less than 1 pixel on the spectrograph detector. The 10x magnification means that each detector pixel corresponds to 0.8 μm on the image plane.

A second test was made by imaging a series of black and white striped targets with stripe widths ranging from 2 pixels to 0.5 pixel. Again this confirmed the image quality of the slicer alone to be smaller than 1 pixel. The difference in position between the the vertical and horizontal foci was precisely measured to be less than 11 microns.

4.3.2 Full Instrument Tests

4.3.2.1 White Light Spectra

The first tests of the fully assembled instrument were performed using a white light continuum source. These showed that the dispersed spectra were well formed on the detector (see Figure 4.10), with sharp edges. The 475-650 nm bandpass filter restricted the overlap between spectra and simplified the problem of dealing with contamination from the zeroth order spectra produced by the grism.

A first (approximate) measurement of the detector response for each layer as a function of wavelength was performed (see Figure 4.11). The blue and red layers are sufficiently well separated to be able to have partially overlapping spectra over the full 400-700 nm range of the system, while still being able to distinguish between different spectra. However a careful study would be necessary to see if it is possible to do this with the high precision required for remote sensing applications.

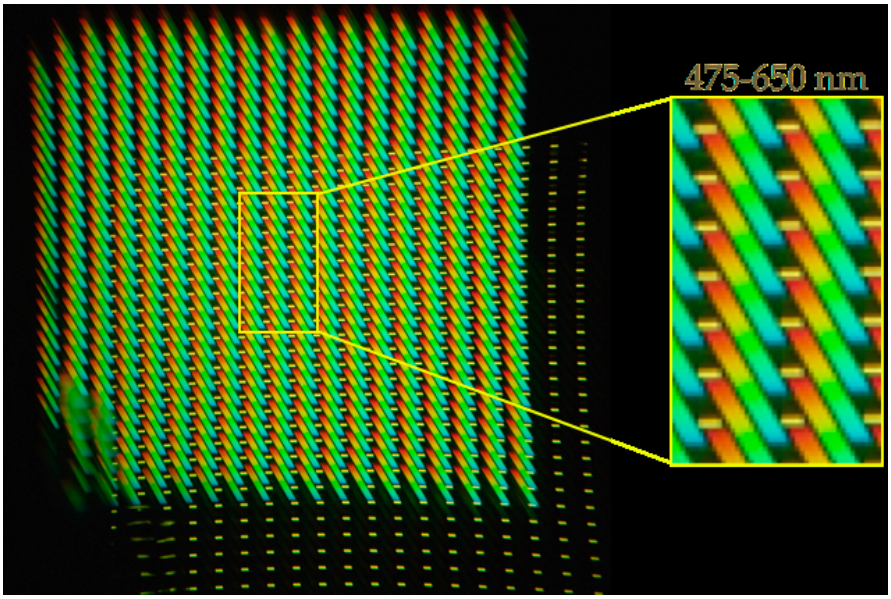

Figure 4.10: This shows an image of white light spectra obtained using the microslice spectrometer with the Sigma DP2 camera. The array of dispersed first order spectra from the 20 x 33 array of horizontal microslices is clearly seen. The displaced array small yellow rectangles are the zeroth order (un-dispersed) spectra, which must be removed as part of the image processing. The zoomed-in section shows that the spectra do not overlap with a 475-650 nm bandpass filter, and that the contamination from the zeroth orders is minimal in this range. The blurred section in the lower left is caused by a defect on one of the lenslet arrays, which occurred during anti-reflection coating.

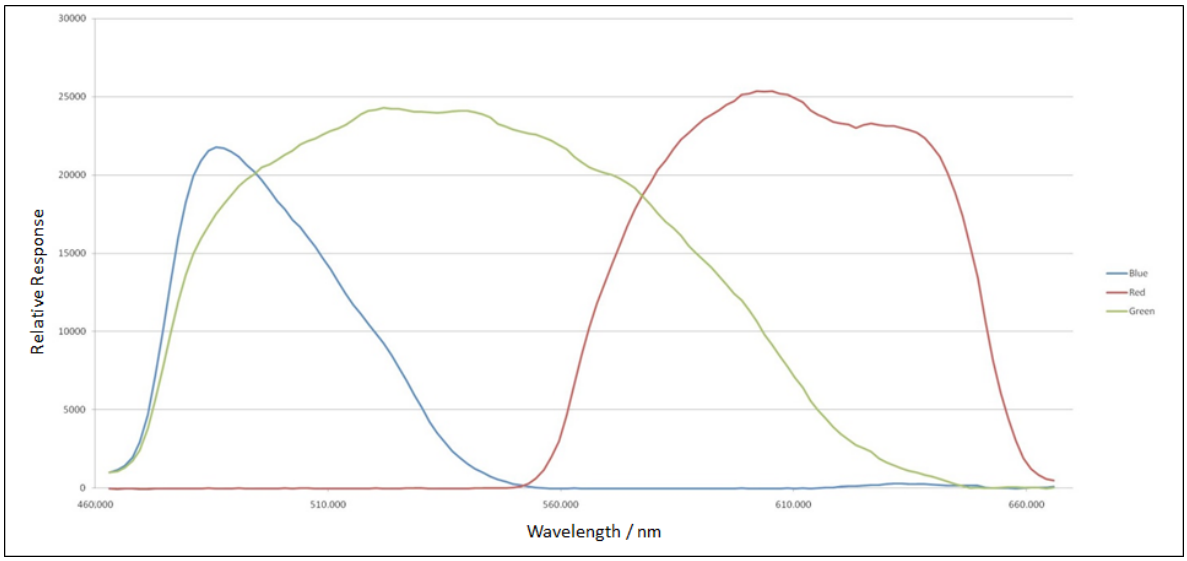

Figure 4.11: This graph shows the relative response of a Foveon detector in a Sigma DP2 camera, measured with white light illumination and a 475-650 nm bandpass filter. The three lines show the detected counts in the three different layers of the sensor at pixels whose position along the spectrum corresponds to the approximate wavelength given on the X-axis.

4.3.2.2 Spatial Line Spectra

To test the overall spatial resolution of the instrument (including the spectrograph and foreoptics), a target of black and white parallel lines with a large middle white stripe was constructed. The images

of the lines were expected to be 1.7 pixels wide on the detector in the absence of aberrations. The pattern can clearly be seen in the dispersed spectral image in Figure 4.12, which shows that the system has good spatial resolution at all wavelengths.

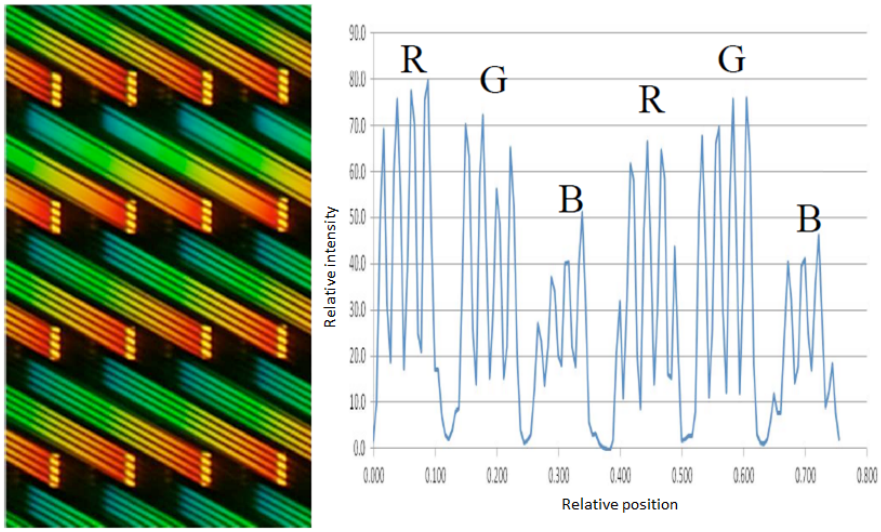

Figure 4.12: The left hand image in this figure is the image produced by the microslice spectrometer when imaging a striped target made up of black and white parallel lines 1.7 pixels wide. The second row of slices reveals the large white stripe in the middle of the target. The right hand graph plots a one pixel wide profile through 6 different spectra showing the contrast in the red at left, then green, blue, red, green, and blue parts of the spectra. The average contrast ratio between minimum and maximum intensity is 0.31.

To make a quantitative estimate of the spatial performance, the contrast between lines at many positions in the field and for wavelengths were measured. Figure 4.12 also shows a profile measured in a single column across 6 different spectra. Because of the stagger in the spectra, the profile is taken at different wavelengths in each spectrum of each slice . Nine of these cuts were used. The average contrast ratio between minimum and maximum intensity was found to be 0.31. Assuming that the PSF is a Gaussian, the FWHM of a point source image giving this contrast value was calculated to be 1.5 pixels, which is better than the goal of 2 pixels FWHM at the detector, and equates to a spatial resolution of 1.1 mrad.

4.3.2.3 Spectral Line Spectra

The spectral resolving power of the spectrometer is another key performance characteristic of the instrument. In order to assess this, a white *spectralon* panel is used, which is a 10 x 10 cm panel with flat spectral reflectance. This panel was illuminated separately with three different spectral lamps: a sodium lamp, a cadmium lamp, and a mercury lamp. These lamps all have narrow emission lines in the 475-650 nm wavelength range. Figure 4.13 shows the spectra obtained from averaging the intensity cross-section from multiple spectral slices. The full widths at half maximum (FWHM) of the peaks were fount to be about 8 bands wide. Since the spectral slices in this plot are 190 bands long, this suggests that each slice contains approximately 24 spectral resolution elements. Since the bandpass

filter limits the spectrometer wavelength range to 475-650 nm (175 nm), 24 spectral resolution elements would equate to a spectral resolution of approximately 7 nm for the instrument, which is close to the design goal of 6 nm.

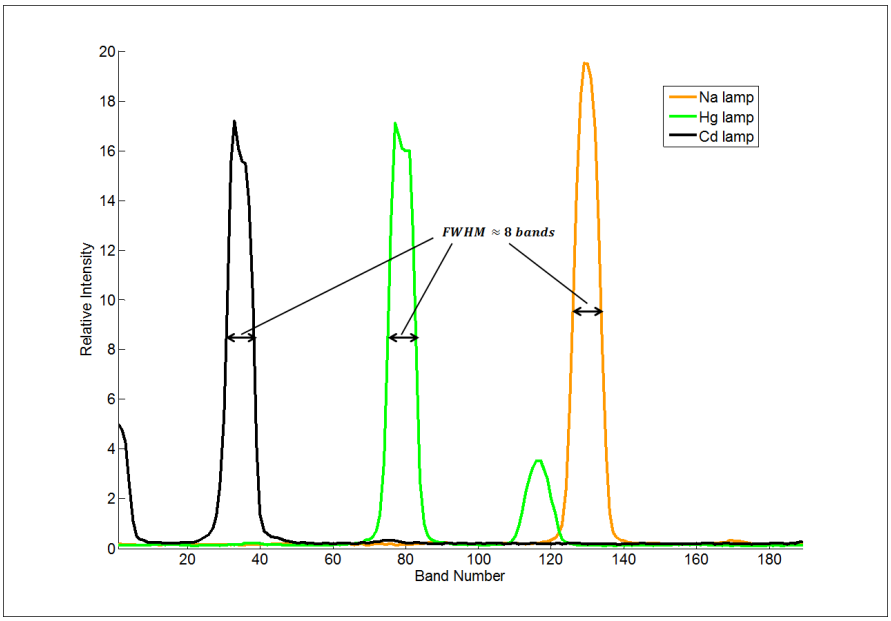

Figure 4.13: This plot shows intensity cross-sections extracted from along the the spectral slices of three microslice spectrometer images of a sodium, a cadmium, and a mercury lamp illuminating a white spectralon panel. The 8 band line widths suggest that the microslice spectrometer can resolve approximately 24 spectral elements across the 475-650 nm range, which equates to a spectral resolution of about 7 nm.

4.4 Camera/Detector Evolution

During initial testing of the system it was found that the Foveon sensor did not allow significant overlap of the spectra without losing data. Since the Foveon detector had some response in most of the 475-650 nm wavelength range range (see Figure 4.11), then overlapping a significant amount of the spectra would mean that the green response of the two spectra could not be distinguished. Moreover, it was found that even when the Sigma camera settings were set to output RAW data, it was apparent that there was still a certain amount of automatic colour balancing performed on the data by the camera, which affected the relative response of the three layers.

The Sigma camera was therefore replaced with a digital single-lens reflex (DSLR) Olympus E-PM1 camera, which used a Bayer CCD 4032 x 3024 detector, with 4.3 μm pixels. A Bayer detector works by detecting different colours at different spatial pixels on the same CCD in a set pattern, as was shown in Figure 4.4. This meant that there were no issues regarding the relative sensitivity of layers, but it did mean interpolation was required to obtain complete spectral coverage at each pixel.

Most importantly however, the Olympus camera allowed the data to be saved into TIFF files using open-source software, rather than saving the data using the camera manufacture software. This ensured

that there was no unwanted pre-processing of the data, and so the images obtained contained the raw data from the detector. The open-source software used was the dcraw package written by Dave Coffin [113].

While the Sigma camera was purchased as a complete camera/detector system, the Olympus camera did not include its own camera lens. This meant that an appropriate lens could be chosen, and focusing could be adjusted manually. The Olympus camera was a miniature digital single-lens reflex (DSLR) camera, meaning that it combined the optics of a standard SLR camera with a digital sensor (see Figure 4.14). The main advantage of using a DSLR camera was that it had an optical view-finder for custom focusing. The camera was bulkier than the Sigma camera due to the inclusion of a mirror and addition of a non-retractable custom lens, but this did not affect the mechanical design of the spectrometer.

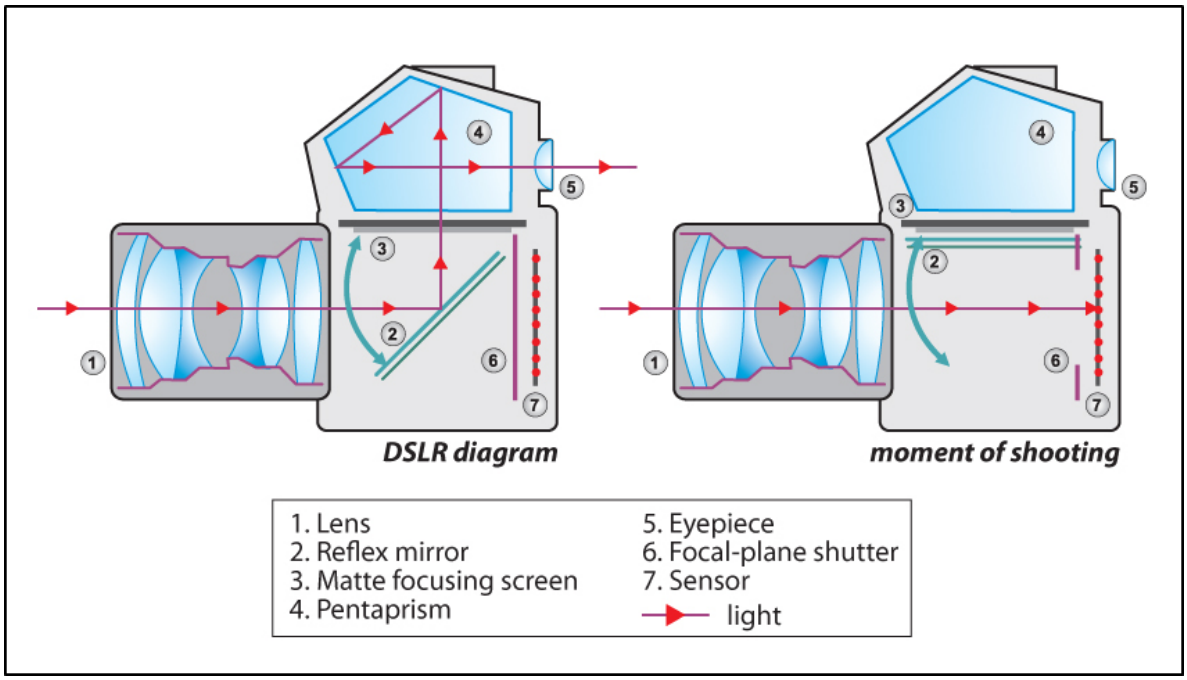

Figure 4.14: This image shows the optical layout of a digital single-lens reflex (DSLR) camera. The mirror allows for an optical view-finder, which is not present in a compact digital camera.

Although the Olympus camera was an improvement on the Sigma camera, it still had some drawbacks. The Bayer sensor meant that a lot of the signal incident on the detector was undetected, as the Bayer filters at each pixel blocks certain wavelengths (see Figure 4.4). This meant that the SNR of the resulting spectra was lower. Also the interpolation required when using the Bayer sensor meant that there were less precise signal measurements at the pixel level on the detector. It was also beneficial to minimise the amount of manual intervention on the instrument. With both the Olympus and Sigma cameras, however, the shutter release was activated by a button on the camera, and the images were stored on a memory card, which had to be removed manually from the camera to access the data. Therefore capturing images and downloading the data required manual intervention, which could affect

the instrument alignment.

The Olympus camera was eventually replaced with an ATIK 383L+ camera, which uses a monochromatic CCD 3362 x 2504 detector with 5.4 μm pixels. The pixel size is larger than that of the Olympus camera, but still smaller than that of the Sigma camera, which was shown to be small enough to sample finer than the spatial and spectral resolution elements. The ATIK camera was designed for scientific astronomical imaging, and is therefore ideal for generating images of raw data with minimal noise and without any Bayer filtering. The same camera lens was used as for the Olympus camera, but an adapter and an extension were required to account for the change in lens attachment and detector position.

The image capture and camera settings for the ATIK camera are controlled by software installed on a laptop computer, which is linked to the camera by USB connection. The data is automatically downloaded to the computer, which means that images can be taken, and the camera settings can be altered without any need to interfere with the instrument itself. The software can be used to set the exposure settings, to automatically save captured images, to view the last image captured, and control the temperature of the detector (which is important for controlling the dark noise, as explained in Section 7.1.3). The ATIK camera was more expensive than the others, costing about £1700 (compared to about £300 for the Olympus and Sigma), but it allows raw data images with low noise to be generated without any complications. For the prototype instrument, the ATIK 383L+ is therefore an ideal compromise between a cheap recreational digital camera and an expensive custom made scientific detector. For performing ground based system testing, the only drawback is that it does not have an in-built battery, meaning that it requires an external power supply to run. This is not a problem for lab testing, but was something that needed to be addressed when testing in the field.

The design of the camera mount was modified throughout the testing process to accommodate the different cameras that were used. This therefore affected the dimensions of the instrument. When the ATIK camera was introduced a large adjustment was required, as it is a much taller camera, with a longer lens, and has a different screw thread attachment. This meant that the base plate of the instrument had to be extended, and a new mount had to be constructed to attach to it. The design of this extension is shown in Figure 4.15, and Figure 4.16 shows an image of the instrument after the attachment has been made. This changed the overall dimensions of the instrument to 54 x 17 x 17 cm, with a mass of 10 kg.

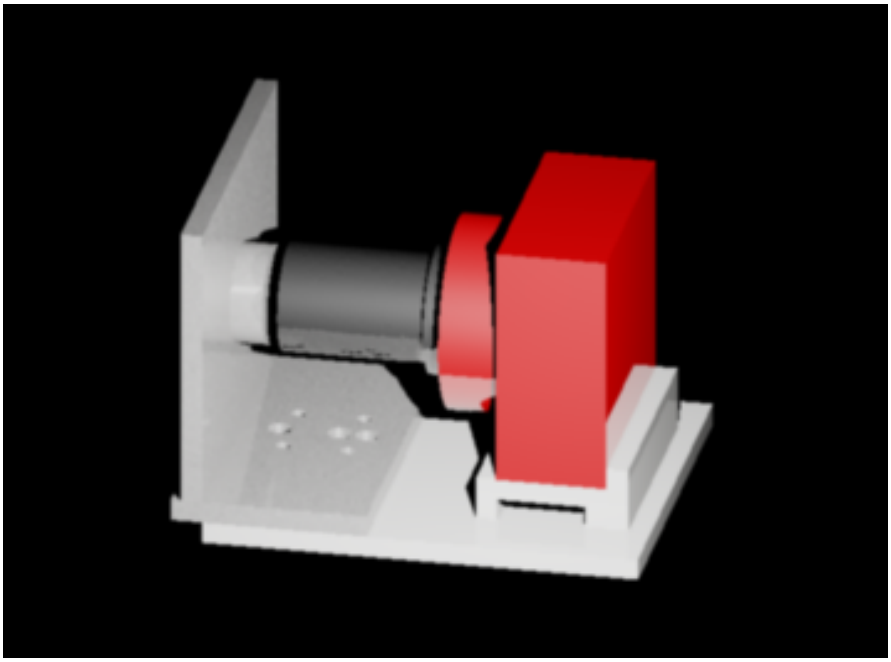

Figure 4.15: This CAD image shows the design of a base plate extension for the microslice imager that was required in order to accommodate for the ATIK 383L+ camera. The dark grey area shows parts of the original instrument design, the light grey area represents the new attachment, the red area represents the new camera, and the black area represents the lens for the new camera. This addition extended the instrument to 54 x 17 x 17 cm in size, and increases its mass to 10 kg.

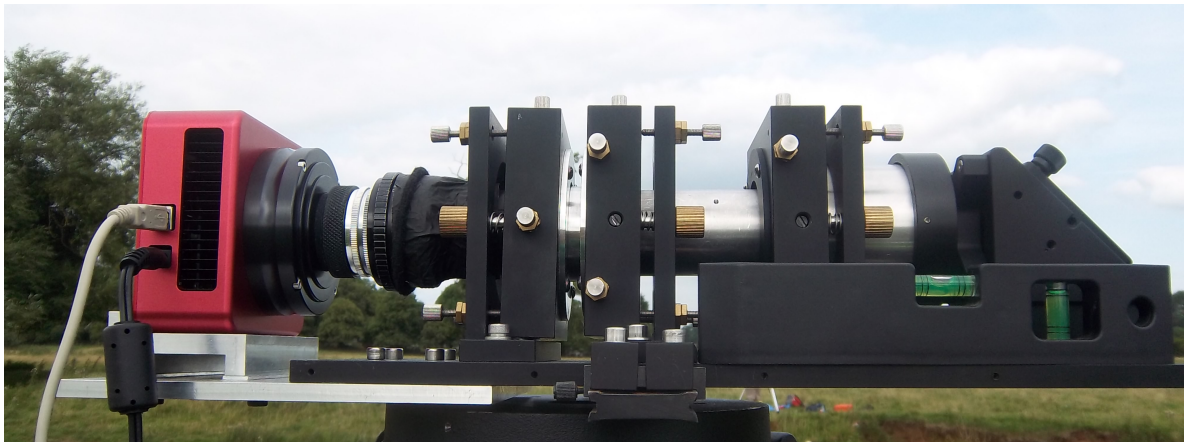

Figure 4.16: This photograph show the microslice instrument being used in the field after the attachment of the ATIK 383L+ camera. A spirit level is being used on the right to check that the instrument is level, but is not part of the instrument itself.

4.5 Software Requirements

In order to develop a complete hyperspectral imaging system, the instrument must be integrated with two software packages: capture software to control the camera, and data processing software to interpret the image. The development of suitable software would create a set-up that allows image capture to be automated by a computer, to which the image is relayed back, and using which a

hyperspectral datacube is generated.

4.5.1 Camera Capture Software

The key features required of the camera capture software include four capabilities:

1. The ability to control the exposure settings;
2. The ability to control the detector temperature;
3. The ability to preset the timings and number of image captures;
4. The ability to communicate wirelessly to the camera through a computer.

The exposure settings of the camera consist of the pupil diameter and the the exposure time. It is important to be able to control these settings, as they determine the amount of light that reaches the detector. More light reaching the detector will increase the signal (and hence SNR), but if there is too much light the detector will become saturated. The optimal setting are therefore those that capture the maximum amount of light while not allowing any saturation. There is not a unique pair of such settings as a low or high exposure time could be counterbalanced by a large or small pupil diameter respectively. Both of these options have their advantages and disadvantages: a large pupil diameter could let in too much stray light, while a long exposure would be more sensitive to change in illumination conditions or vibrations. If the instrument were imaging from a remote sensing platform then the maximum exposure time would be governed by the dwell time of the scanning method used.

CCD detectors are sensitive to the ambient temperature [114]. Signal on CCD is recorded by the incident photons exciting electrons in the sensor. Additional electrons can also be excited by thermal energy in the CCD. The number of additional electrons excited follows a Poisson distribution, which has a higher mean at higher temperatures. These additional excited electrons are known as thermal noise, and can significantly reduce the SNR if the CCD temperature is too high. For this reason it is important that the CCD temperature is kept under control.

The ability to set automatic capture times is a very important capability of the capture software if the instrument is to be used for remote sensing. Whether it is imaging from a satellite or an aircraft, images will need to be taken continually and at very precise times, which is not something that can be managed manually.

Additionally, if the instrument is to be used on a remote sensing platform, then it would be impractical for the instrument to be required to be physically connected to the user interface when acquiring measurements. It would also be impractical to store large amounts of data on the remote sensing platform. It would therefore be essential to download the acquired data by wireless connection as it is

gathered. It is also important that it is saved in a methodical manner, so that it can later be accessed manually.

4.5.2 Data Processing Software

As soon as an image is captured it should be downloaded and saved onto a computer for processing. It could be useful to process the data in real time so that it can be visualised as it is captured, but this is not an essential capability.

There are five main tasks that should be performed by the data processing software:

1. Reading the image file into a program for processing;
2. Defining the positions of the spectral slices;
3. Spectrally calibrating the data in each slice;
4. Rearranging the data in the image into a 3-dimensional datacube;
5. Saving the datacube in an accessible format.

These are the essential processes required to obtain useable data from the system, but there are other processes that can be included in the software that can improve the quality and variety of data obtained. These include: smoothing of the data, to reduce the effects of noise; removing parts of the datacube with missing data, to ensure that full bands are saved; and performing classifications using reference spectra from another instrument.

Detecting the positions of the dispersed slices is a very important part of reconstructing the datacube, as it is the accuracy of this process that determines the quality of the spatial image reconstruction. The method of spectral box detection is something that is constantly being improved in the microslice spectrometer software. The difficulties of detecting the spectral slices, and the latest detection method used for the microslice spectrometer software are discussed in the next section.

Converting the 2-dimensional image into a 3-dimentsional datacube is the is the key outcome of the data processing. The image that comes out of the camera is a 2-dimensional CCD image containing a 20 x 33 grid of 2-dimensional dispersed slices (see Figure 4.17). The main purpose of the data processing software is to automatically extract the 3-dimensional information that is contained within this image, and present it in the form of a datacube. Once the positions of the spectral boxes have been defined the software must map the data present within these boxes to the appropriate place in the datacube, as shown by Figure 4.18. Due to the defects in one of the lenslet arrays, only 16 x 31 spectral slices are actually used in the datacube construction.

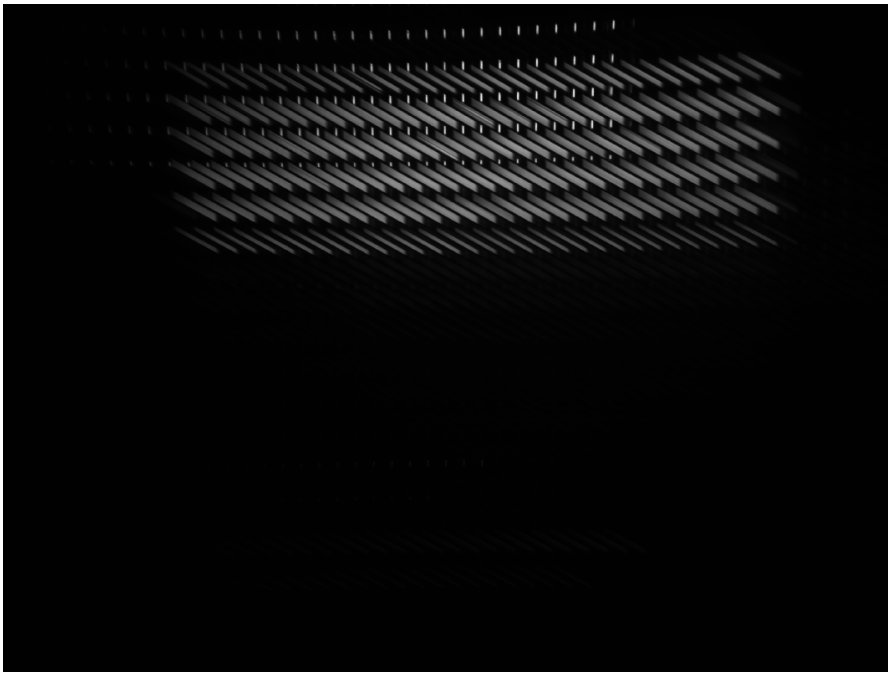

Figure 4.17: This figure shows the raw data captured by the microslice spectrometer, as measured by the ATIK CCD detector, when it is imaging a white target (a spectralon panel illuminated with a quartz halogen lamp). Not all of the spectral slices are visible, as the white target only covers part of the field of view of the instrument.

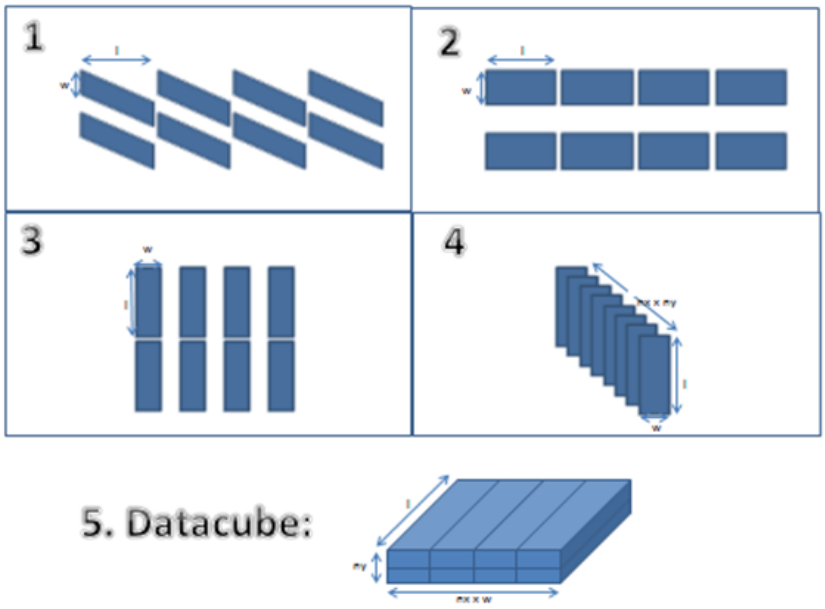

Figure 4.18: This figure provides a visualisation of how the data in the image captured by the instrument is converted into a 3-dimensional datacube. w is the spatial width of each spectrum (28 pixels), l is the spectral length of each spectrum (190 pixels), nx is the number of spectra across the image (16 slices), and ny is the number of spectra down the image (31 slices). The detector image contains 20 x 33 spectral slices, but due to a defect in one of the lenslet array only 16 x 31 are useable. Since spatial information is preserved along, but not across the slice, the total number of spatial elements is 448x31.

When saving the datacube, it is important that it is saved in a format that can be easily accessed and

manipulated by image visualisation software. The software used to visualise datacubes constructed by the microslice spectrometer was ENVI (the classification software used in Chapter 3). In order for ENVI to be able to import the datacube it was saved band sequentially (BSQ), which a useful way of storing hyperspectral image data [115]. A header file must also be created for each datacube, which contains information about the data, such as the number of rows, the number of columns and the number of bands in the datacube. This meta-data allows the ENVI software to decode the data into the appropriate format.

4.6 Software Development

The ready-made ATIK camera capture software was used with the prototype instrument. Since this was a newly developed instrument, there was no such ready-made data processing software. A set of MATLAB scripts were therefore developed to convert the 2-dimensional CCD image into a 3-dimensional datacube. Different MATLAB modules were created to perform different tasks, and integrated into a single data processing MATLAB script. There was no integration of the camera and data processing software, but this could be useful for future system development.

4.6.1 Current Camera Software

The latest camera used on the prototype microslice imager is an ATIK 383L+ camera, which was purchased with its own ready-made capture software. This software can be used to set the exposure time of the camera, as well as control the temperature of the detector. It can also automatically save captured images to a set location. These capabilities were sufficient for testing the prototype instrument.

The ATIK camera would not be suitable for use with the instrument for remote sensing purposes, however, as it connects to a computer with a USB connection, and has no wireless capabilities. Also, although the software can be set to capture images consecutively, it cannot be used to pre-set automatic capture timings.

4.6.2 Development of MATLAB code

The data processing MATLAB software was constantly improved and updated during full system testing. These improvements provided software that required less user input, outputted more accurate results, and presented the data in a clearer fashion. The initial basic version of the data processing software consisted of three modules: one to define the positions of the spectra, one to transform the parallelogram shaped spectra into rectangles, and one to use these rectangles to construct a datacube. Each module had to be run once each to construct a white reference datacube, and then again to construct a target image datacube. Each run would have to be started manually to change various

parameters for each run. This version of the software provided the most basic operations required to construct a datacube, without any calibration, analysis, or thought to ease of use.

The latest version of the software consists of one simple script. Within this script, all of the data parameters are defined, and five different modules automatically run at appropriate times to process the data. The five modules each have well defined tasks, which are detailed in this section. An additional sixth module was created for field testing, which is presented in Chapter 6. The latest major capabilities of the software are as follows:

- provides a spectral calibration of each slice
- generates and saves a normalised datacube with no empty bands
- can deal with repeat images of the white reference and target
- normalises and plots the mean microslice spectrum with an imported reference spectrum
- calculates the *spectral angle* (see Equation 3.15) between those two spectra
- can be run for multiple targets consecutively

The five modules that were developed for use in this software are presented below along with their main processes.

4.6.2.1 The Modules

spectra_posxy

The main purpose of this module is to define the positions of the spectral slices with parallelogram shaped areas (which shall be referred to as spectral boxes) in the detector image (see Figure 4.19). This is a necessary processes as these positions do not always remain constant between images. The reason for this is most likely due to small movements of the mechanical parts through vibrations and flexure.

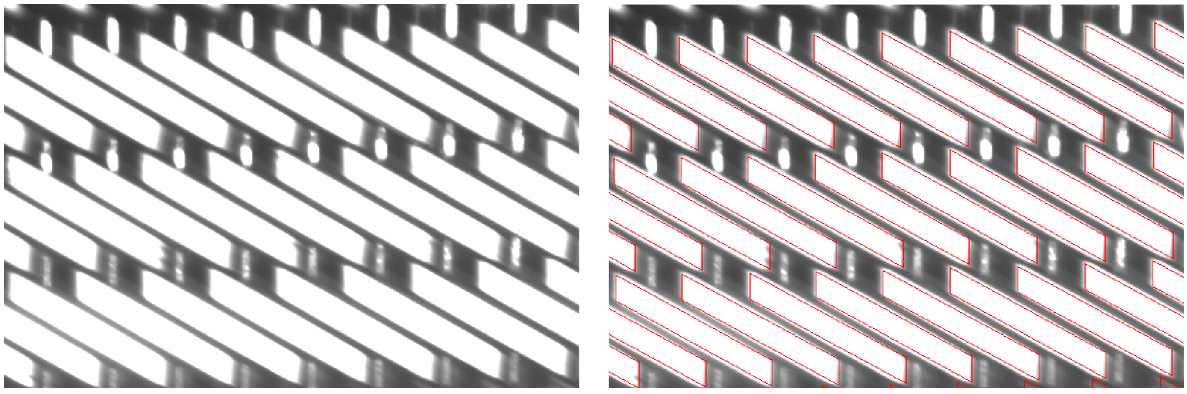

Figure 4.19: This figure shows the positioning of spectral boxes used to define the positions of the spectral slices in an image from the microslice spectrometer. The image on the left shows the raw data obtained from the detector, while the image on the right shows the same data with the defined spectral box overlaid in red.

The spectral box positions are defined from using the white reference image data for each target. The expected positions of the bottom right corners of the spectra are initially defined in a look-up table to give a start location for finding the spectrum. The white reference data is then imported from a TIFF file and thresholded. The threshold is used to distinguish between signal that is part of spectra, and signal from noise or stray light (see Figure 4.20).

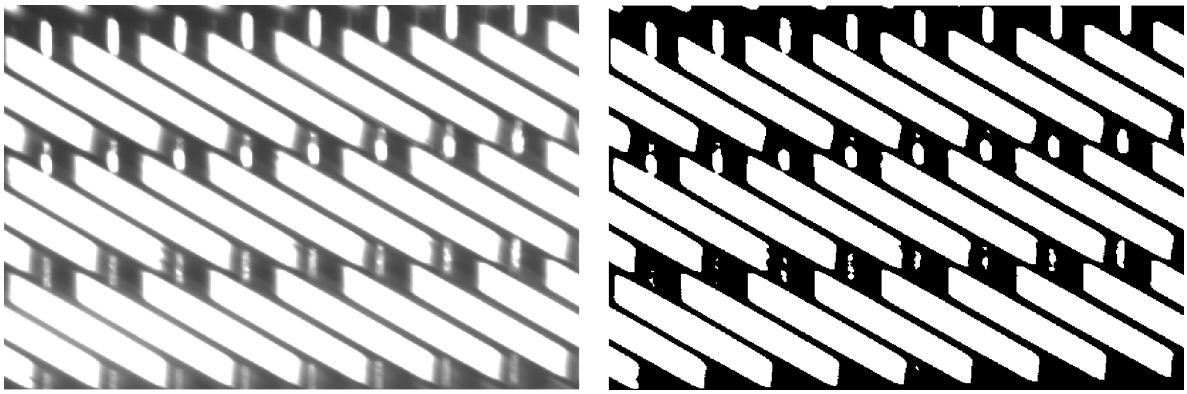

Figure 4.20: This image shows how thresholding can help identify the position of the spectral slices created by the microslice instrument. The image on the left shows the raw data obtained from the detector, while the image on the right shows the same data after a threshold has been applied. The application of a threshold creates a binary image, setting pixels above the threshold value to be one while all other pixels are set to zero. It can be seen that applying the threshold gives much more clearly defined edges to the spectral slices, allowing the perimeter to be identified more easily.

The software defines the area of the slice by finding the top left corner and the bottom right corner of the spectrum. The bottom right corners are found first by using their expected positions along with the thresholded image. The calculated bottom right positions are then used along with a model for expected height and length of the spectra to obtain the expected positions for the top left corners of the spectral slices. The reverse process is then used to find the top left corners from their expected positions. The process used to define the corner positions of the boxes from the expected positions is

shown in Figure 4.21.

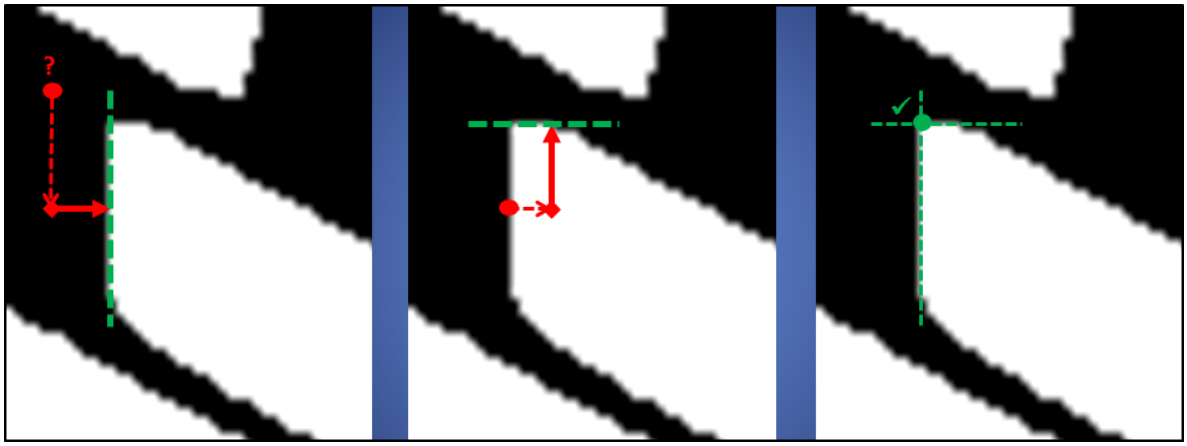

Figure 4.21: This figure shows the logical operations that are used to determine the bottom right corner of the spectral boxes. The left image shows how the expected position of the top left corner of the spectral slice (denoted by *?*) is used to define the left side of the spectral box. The central image shows how this is used to define the top of the spectral box. The right image shows the how the left and top of the spectral box accurate define the corner of the box. The same processes is used in the opposite directions to find the bottom right corner.

The spatial width of each slice is constant at 28 detector pixels. This width can be used, along with the bottom right and top left corner positions, to define a unique spectral box, which is taken to be the area that contains the hyperspectral data for that slice (see Figure 4.22). The positions of the spectral boxes found for a particular white reference image are then used for all target images that use that image as a white reference.

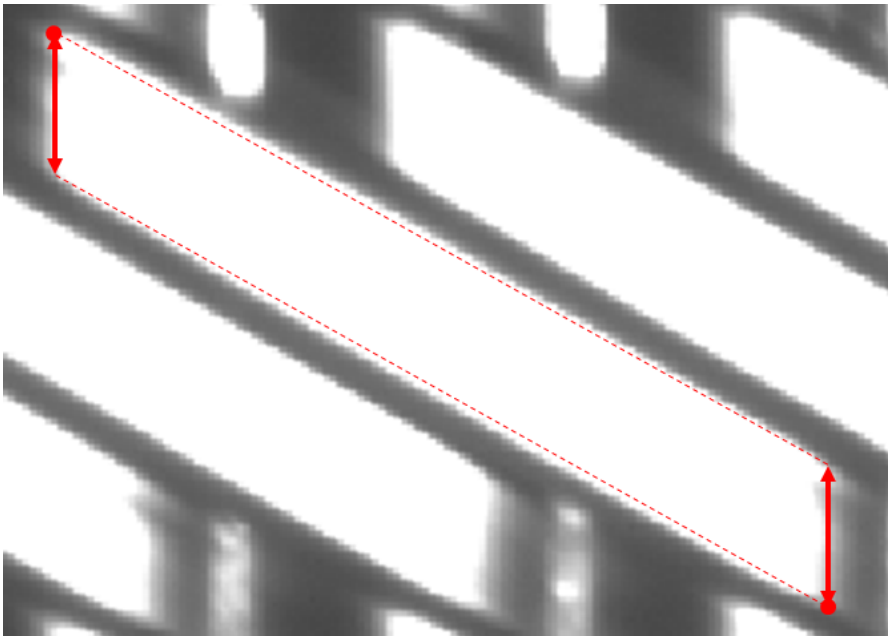

Figure 4.22: This figure shows demonstrates how the positions of the spectral boxes are defined using three parameters: the position of the top left corner, the position of the bottom right corner, and the width of the slice.

When defining the spectral box positions using the process shown in Figure 4.21, it is important that the algorithm is not interfered with by the zeroth order dispersion spectra. The zeroth order spectra occur as a result of using a grism as a dispersing element, and are not part of the spectrograph data. As can be seen from Figure 4.10, some zeroth order spectra are well separated from the dispersed spectra, and so will not interfere, but others are almost overlapping. The complete process of the *spectra_posxy* module is summarised by the flowchart in Figure 4.23. The MATLAB code for this module can be found in Appendix A.1.

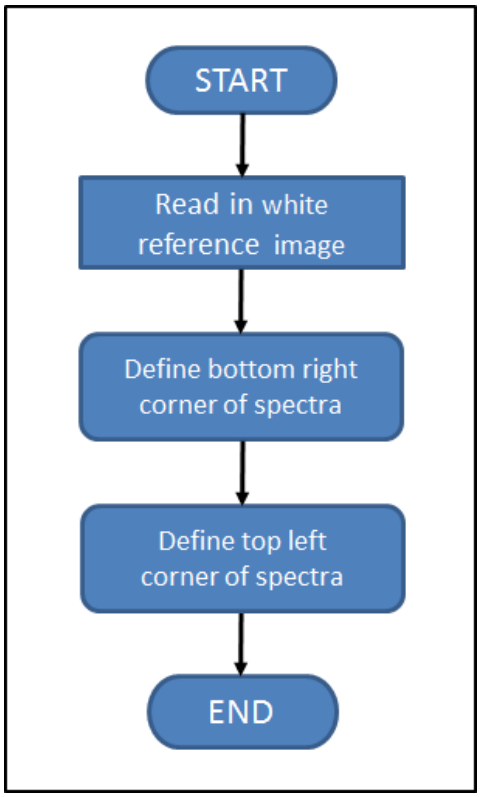

Figure 4.23: This flowchart shows the main operations performed by the *spectra_posxy* MATLAB module. The main purpose of this module is to define the positions of the spectral slices as parallelogram shaped areas in the spectrometer image.

untransform_boxes

The main purpose of this module is to transform the data in each spectral box defined by *spectra_posxy* into a 2-dimensional rectangular array. This is a key part of converting the data from the detector into a 3-dimensional datacube. The image to be processed is imported in the form a TIFF file. An affine transformation of the data in the parallelogram spectral boxes into rectangular arrays is performed, as shown in Figure 4.24. An affine transformation keeps straight lines straight, and parallel lines parallel, but pairs of corner points can move with respect to each other. In this case the number of pixels in the spectral box is preserved.

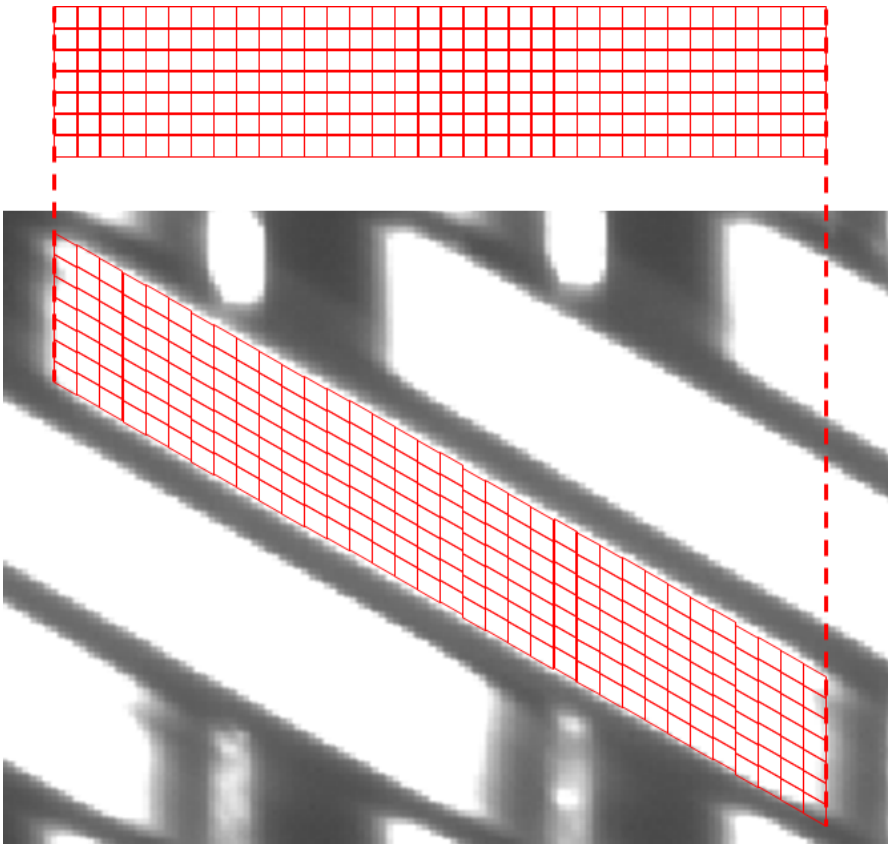

Figure 4.24: This image provides a visual representation of how an affine transformation is used to generate a rectangular array from a parallelogram shaped spectral slice. The small parallelogram shaped areas are not made up of single complete detector pixels, and so interpolation is used to determine the flux present in these areas.

The flux is measured on the detector in square pixels, meaning that the signal received within the small parallelogram shaped sub-areas in Figure 4.24 must be estimated by interpolation. This interpolation is incorporated into the *imtransform* MATLAB function.

The data is then written to a 28 x 190 x 496 array (i.e. slice width x slice length x number of slices). The complete process of the *untransform_boxes* module is summarised by the flowchart in Figure 4.25. The MATLAB code for this module can be found in Appendix A.2.

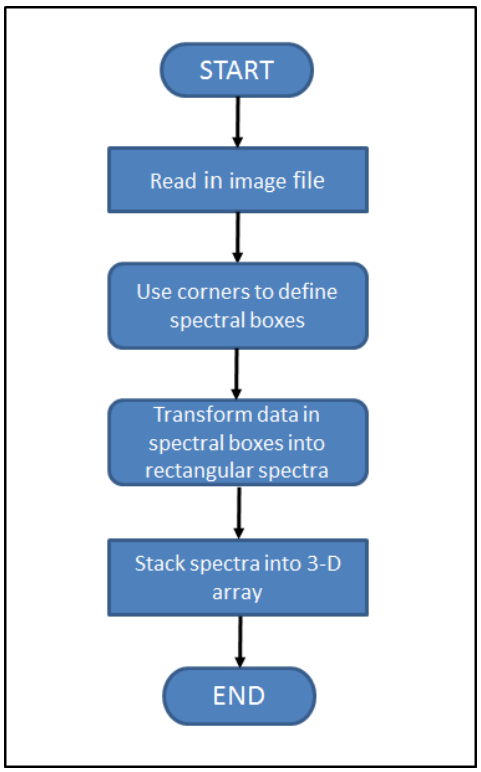

Figure 4.25: This flowchart shows the main operations performed in the *untransform_boxes* MATLAB module. The main purpose of this module is to transform the data in the predefined parallelogram shaped spectral boxes into rectangular arrays.

untransform_speccal

This module performs the same function as *untransform_boxes*, but for a spectral calibration image (Appendix A.3 shows the part of the module code that is different to the *untransform_boxes* module). A different module is required for this as the spectral calibration image is actually a combination of several images. A single calibration image is generated by illuminating a white spectralon panel with a Mercury lamp. This, however, can only illuminate part of the instrument's field of view (FoV) in one image. This module therefore combines two images in which different parts of the FoV illuminated before performing the spectral box transformation (see Figure 4.26). This ensures that all spectral slices are spectrally calibrated. A mercury lamp is used as it has two clear and well spaced spectral peaks in the 475-650 nm range (at 546 nm and at 578 nm), as shown in Figure 4.27 [116].

At least two peaks are necessary to calibrate both the spectral position and the spectral scale. Spectral calibration is performed by using the actual wavelengths of the peaks to interpolate the wavelength of each band. A separate calibration is performed for each slice. It was therefore decided that since the spectral peaks from the mercury spectral lamp were so narrow and consistent, two spectral peaks would be sufficient. Using more than two peaks, however, could lead to a more accurate wavelength calibration. This could be achieved by imaging multiple lamps. In the next chapter multiple spectral lamps are imaged to demonstrate the accuracy of the two peak spectral calibration (see Figure 5.5).

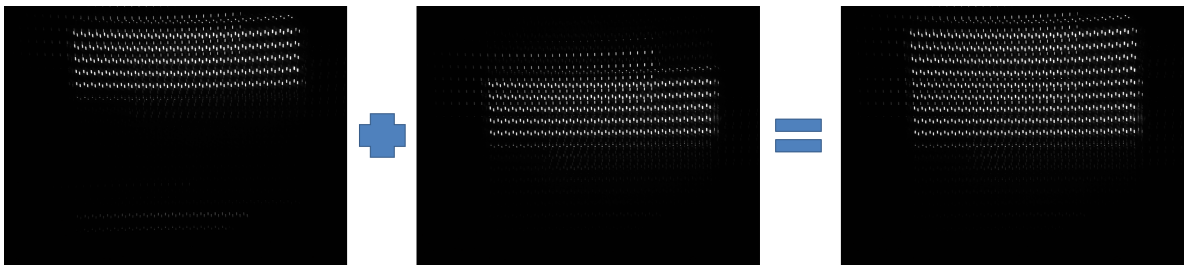

Figure 4.26: These images show how two separate calibration images of separate areas of the field of view (FoV) are combined into a single calibration image of the entire FoV.

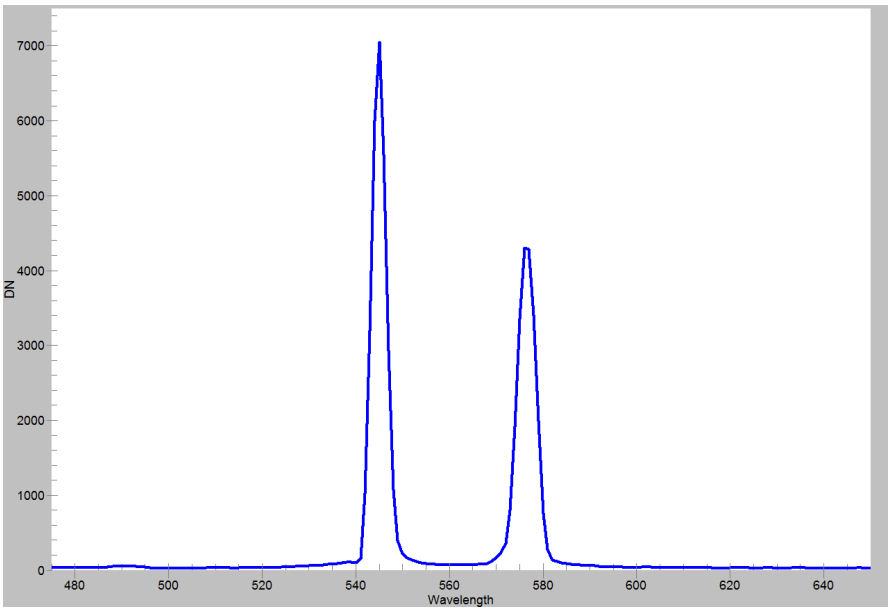

Figure 4.27: This graph shows the spectrum of the light emitted by a Mercury filament lamp, as measured by an ASD FieldSpec 3 spectrometer after reflectance from a white spectralon panel. It clearly shows that there are two sharp emission peaks in the visible wavelength range at about 546 and 578 nm. The ASD spectrometer has a spectral sampling rate of 1.4 nm, and a spectral resolution (FWHM) of about 3 nm (in the 350-1000 nm range).

interpolate

This module has two main functions:

1. to apply the spectral calibration

2. to construct a datacube

In the calibration process each spectral slice is calibrated individually to ensure that any spectral variations between slices are accounted for. The first part of this process is to sum the data in each slice in the spatial dimension to give a single spectrum for each slice. The next step is to locate the position of the spectral peaks in the calibration image spectra. The data around the peaks is centroided to gain a more accurate position of the peak.

A target datacube is constructed by rearranging the data in the 3-dimensional array created in *untransform_boxes* into a 448 x 31 x 190 array with the two spatial dimensions (448 x 31) representing the target area, and one spectral dimension. Each of the 190 pixels in the spectral dimension represents a different spectral band. A white datacube can also be constructed using this script, and used for normalisation.

Due to the optical design of the instrument there is much higher spatial sampling in the along slice direction than the across slice direction. The ratio of the actual FoV in these directions is approximately 5:1, but the ratio of the number of pixels is 448:31 ($\sim 14:1$). The pixels in the across slice direction are therefore increased in length for viewing band images from the datacube. The complete process of the *interpolate* module is summarised by the flowchart in Figure 4.28. The MATLAB code for this module can be found in Appendix A.4.

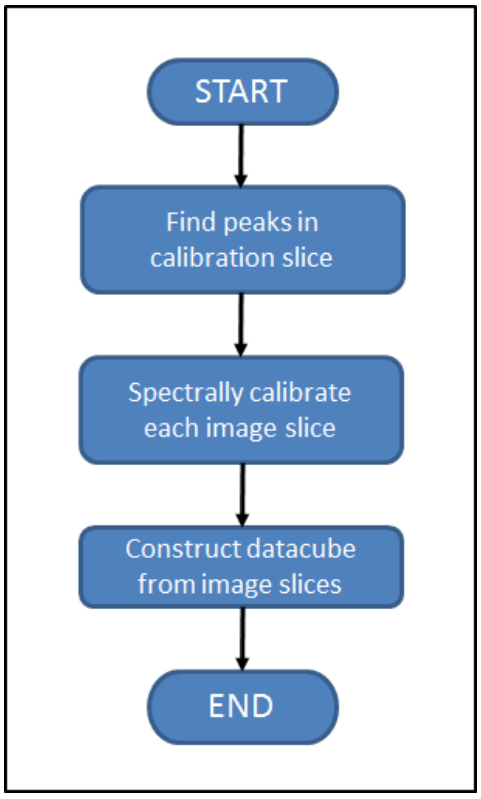

Figure 4.28: This flowchart shows the main operations performed in the *interpolate* MATLAB module. The main purpose of this module is to spectrally calibrate each spectral slice, and to generate a datacube.

asd_comparison

The main purpose of this module is to compare spectra extracted from the microslice spectrometer datacube to spectra from a reference spectrometer. In the laboratory and field tests detailed in the next two chapters an ASD FieldSpec 3 spectrometer is used to gather reference spectral data. This is useful for testing the spectral capabilities of the microslice spectrometer when imaging a homogeneous area.

This module firstly imports all reference spectra of the appropriate target from text files, and calculates the mean spectrum. Then a median spectrum is calculated from a chosen spatial area of the datacube. The median averaging method is used to prevent any pixels with anomalous spectra (possibly due to poor reconstruction) from affecting the data too strongly.

The median microslice spectrum and the the mean reference spectrum are normalized separately to make their minimum value zero and their maximum value one. This ensures that the spectral shape is the main factor affecting the comparison, rather than the relative reflectance intensities. Both spectra are then plotted on the same set of axes, and this graph is saved to provide qualitative comparison between the instruments. A quantitative comparison is provided by calculating the spectral angle between the two spectra using Equation 3.15. The lower the spectral angle is, the more similar the spectral shapes are. The option of producing a 3-dimensional similarity plot is also available, which shows the spectral angle between the reference and the microslice spectrum at each spatial pixel. The complete process of the *asd_comparison* module is summarised by the flowchart in Figure 4.28. The MATLAB code for this module can be found in Appendix A.5.

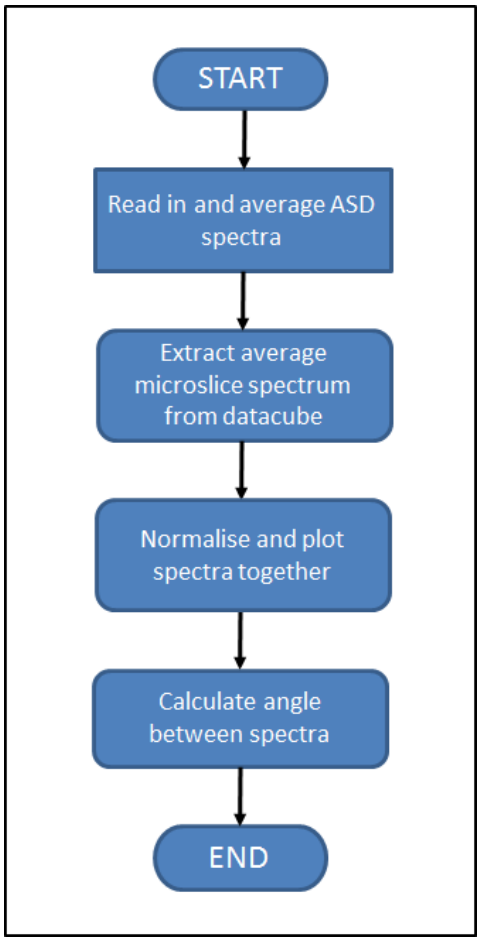

Figure 4.29: This flowchart shows the main operations performed in the *asd_comparison* MATLAB module. The main purpose of this module is to compare spectra extracted from the microslice spectrometer datacube to spectra from a reference spectrometer.

4.6.2.2 Integration of the MATLAB Modules

The five modules detailed above are all used by the main MATLAB processing script to generate a target datacube from multiple white reference and target images. The flowchart in Figure 4.30 provides a visual representation of the order of the processes performed main data processing MATLAB script. The MATLAB code for this script is shown in Appendix A.6. Any spectral bands in the normalised datacube that contain pixels with no data (which may occur as a result of having different spectral calibrations for each slice) are deleted to ensure that the output data is complete. The datacube is then saved band sequentially (BSQ) in a file so that it can be read by image processing software such as ENVI.

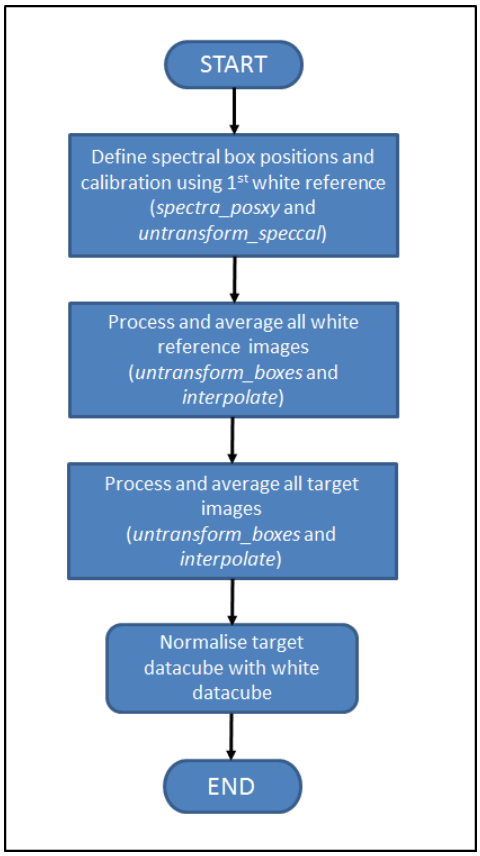

Figure 4.30: This flowchart shows the overall order of operation performed by the main MATLAB script. This script can output a normalised datacube of the target area from multiple input target and reference images.

This section has shown how the current data processing MATLAB modules can be used to generate a 3-dimensional datacube, but there are various ways in which their accuracy could be improved. For example, the spectral boxes in the raw image could be defined as a more complex shape than a parallelogram to account for slight curvature of the spectral slices. This curvature is caused by abberations (geometric distortions), which can be different for different slices. Accounting for this would involve changing the *spec_posxy* module. The slices could also be blended together during reconstruction, instead of simply being tessellated, to produce a smoother spatial image. This would

require changes to the *interpolate* module.

It would also be useful to include a module that removes the zeroth orders from the raw data before the processing is carried out. This would minimise any contamination of the spectral slices from the zeroth order. Also the zeroth order spectra can affect the box positioning algorithm in the *spectra_posxy* module. This would involve creating a new module that would be run on all raw data immediately after being imported. Other improvements that could be made to the code involve extending the capabilities of the software, as discussed in Section 4.5.

4.7 Summary

This chapter has detailed the development of a novel prototype hyperspectral imaging system, from the optical and mechanical design, to the data processing software. The uniqueness of the spectrometer lies in the use of microslice technology to achieve a 2-dimensional instantaneous field of view (IFoV). This, together with the compact nature of the design are the main strengths of the design concept.

The fully constructed instrument measures 54 x 17 x 17 cm, with a mass of 10 kg (including the base plate). The spectral and spatial full widths at half maximum (FWHM) were found to be about 7 nm and 1.1 mrad respectively. These values therefore provide limits on the spectral and spatial resolutions of the hyperspectral imaging system.

The data processing software consists of several modules that were constructed in MATLAB to be combined with the instrument to form a full hyperspectral system. These MATLAB modules are capable of processing multiple white reference and target images into the same datacube, as well as providing a comparison between spectra extracted from the datacube and spectra from a reference spectrometer. The quality of data extraction in the software defines how closely the spectral and spatial resolutions of the system match the 7 nm and 1.1 mrad limits set by the instrument.

Once the system was completed to a working level, full system tests were conducted to give a clear idea of what improvements to the instrument design would have the greatest pay-off. The next two chapters present full system tests, which include laboratory tests (to determine the spatial and spectral resolution), as well as field tests (to compare the spectral response to data from a reference spectrometer, when imaging natural targets).

Chapter 5

Laboratory Spectrometer System Tests

In order to determine the capabilities and level of performance of the complete prototype microslice spectrometer system, a variety of laboratory experiments were carried out. These involved verifying the spatial and spectral resolution of the imaging system, as well as testing its spectral and spatial capabilities when imaging natural targets. The basic set-up for these laboratory tests consisted of the microslice spectrometer mounted on a 1.5 m tripod in a dark room, with a target for imaging on the ground illuminated by a quartz-halogen lamp (see Figure 5.1). For experiments examining the spectral performance of the system, a commercially available point based field spectrometer was also used to provide reference 'truth' spectral data for comparison.

5.1 System Specification Tests

When determining the capabilities of a hyperspectral imaging system, the most important things to investigate are the basic levels of spatial and spectral performance. In Chapter 2 the key requirements of hyperspectral instruments for Earth observation (EO) were shown to be the spectral range, the spectral resolution, the spatial resolution, and the signal to noise ratio (SNR). The spectral range of the prototype instrument is set at 475-650 nm, but different spectral ranges could be achieved by changing the bandpass filter and the grism. The trade-offs required for such changes are discussed in Chapter 8. The instrument is designed to be able to capture a 2-dimensional instantaneous field of view (IFoV) to achieve improved levels of SNR for remote sensing, but the actual SNR achieved is highly dependent on the implementation of the hyperspectral system [117].

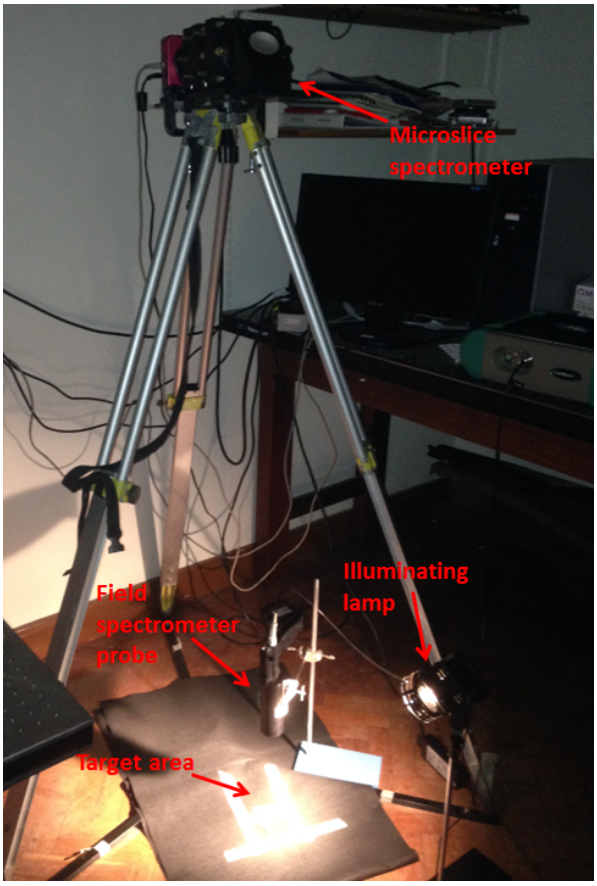

Figure 5.1: This photograph shows the instrument set-up for conducting laboratory tests with the microslice spectrometer system. The instrument was attached to a tripod about 1.5 m above the ground, imaging a target area of about 8 x 40 cm. For experiments examining the systems spectral performance a commercially available point based field spectrometer (an ASD FieldSpec 3) was also used separately to provide reference spectral data for comparison.

The important system capabilities that are dependent on the imaging system itself, rather than its implementation, are therefore the spatial resolution and the spectral resolution. The spatial performance of the prototype microslice spectrometer optical system was tested in Section 4.3.2.2, demonstrating a spatial resolution of 1.1 mrad along the slices. Spectral performance testing demonstrated that approximately 24 spectral elements could be resolved in the 475-650 nm wavelength range, suggesting a potential spectral resolution of about 7 nm for the prototype instrument. Laboratory tests were carried out to determine the spatial and spectral resolution of the complete prototype system, and the results are presented below.

5.1.1 Spatial Resolution Tests

The spatial resolution of an imaging spectrometer is an important specification for determining its remote sensing capabilities. Table 2.1 showed that many current remote sensing applications that involve the imaging of vegetation require a spatial resolution of around 2 m, but for other applications less precise spatial resolutions can be used. Attaining a higher spatial resolution increases the potential

applications of the instrument, and could lead to the development of new applications or methods.

The size of the spatial resolution elements imaged by a spectrometer is fundamentally limited by the number of pixels used. The Nyquist sampling theorem suggests that at least two pixels are required per spatial (or spectral) resolution element for optimal sampling [118]. The limit to the size of the spatial resolution elements is therefore give by Equation 5.1, where $IFoV$ is the instantaneous field of view in the sampling direction, and *pixels* is the number of detector pixels used in the sampling direction. Generally instruments use enough detector pixels to ensure that the spatial (or spectral) sampling is not the limiting factor in the resolution of the instrument.

$$minimum\,spatial\,element\,size = \frac{2 \times IFoV}{pixels} \tag{5.1}$$

The use of image slicing to generate a 2-dimensional field of view (FoV) could potentially lead to different spatial resolutions in the two different dimensions, causing different spatial sampling. Also the datacube reconstruction leads to one spatial dimension consisting of the reconstruction of pixels from different slices, with the other dimension consisting of the reconstruction of contiguous pixels from the same slice (see Figure 4.18). These two dimensions will be referred to as the across field and along field dimensions respectively. For the prototype microslice spectrometer the sampling rate allows for spatial elements as small as 0.9 x 1.6 mrad, but it was determined in Section 4.3.2.2 that the resolving power of the optics provides a limit of 1.1 mrad on the spatial resolution, due to aberrations. This gives a spatial resolution of 1.1 x 1.6 mrad, which is likely to be further limited by the datacube reconstruction software.

An experiment was conducted to determine the delivered spatial resolution of the system. This experiment involved imaging multiple black and white striped targets with different stripe widths in two perpendicular directions (across field and along field). The *contrast transfer function* (CTF) was then calculated across the stripes on each reconstructed image. The CTF is a function that is used to assess the spatial quality of an optical system based on the contrast in the images that it creates [119]. Figure 5.2 shows the CTF definition, and how it provides an assessment of spatial image quality.

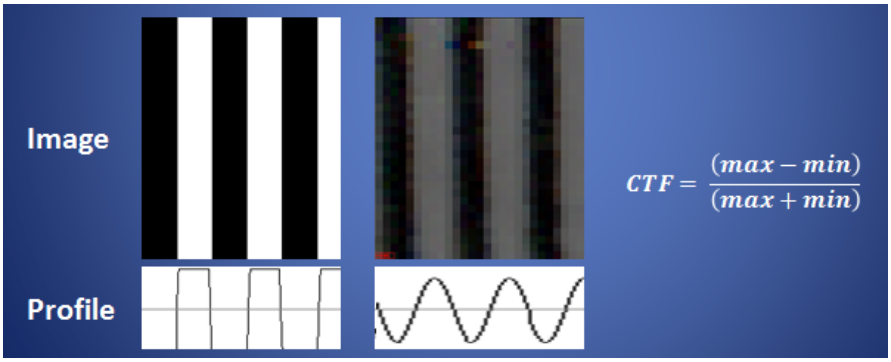

Figure 5.2: This figure shows the definition of the contrast transfer function (CTF) of an image profile, and demonstrates how it determines the spatial quality of a striped target image. For a perfect system the CTF of a perfect target will be 1. If the quality of the imaging system is lower, the contrast between the brightest areas and the darkest areas will be less, and hence the CTF will decrease.

Plotting the calculated contrast against the spatial frequency of the lines imaged gives the CTF, which gives a good indication of the spatial performance of an optical system. The expected form of this graph is roughly a third degree polynomial, with the asymptotes tending towards contrasts of zero and one, and a point of inflection where the contrast is 0.5 (see Figure 5.3). A higher contrast for a given spatial frequency is therefore an indication of a more precise spatial imaging system. Since a contrast of 0.5 represents both the mid-point of the contrast, and the point of inflection of the curve; the line width corresponding to this contrast can therefore be seen as the most appropriate place to define the spatial resolution.

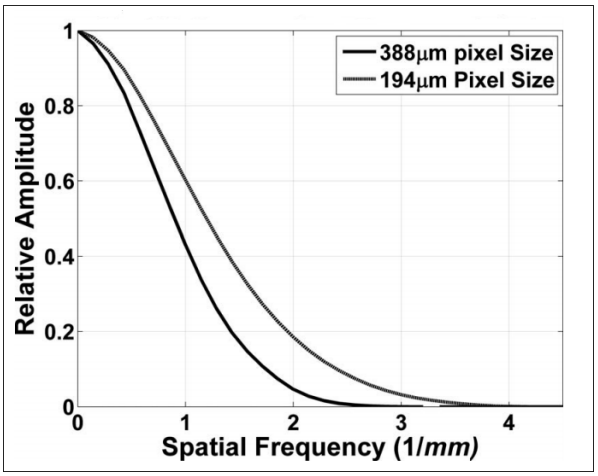

Figure 5.3: This contrast transfer function (CTF) graph plots the contrast against the spatial frequency of images taken with a tomography imaging system. This plot shows the typical shape of a CTF, as well as demonstrating the adverse effect that an increase in pixel size in an instrument can have on image quality. This image was taken from [120].

Ten different black and white striped targets were imaged by the microslice spectrometer with line widths ranging from 2.25 mm to 17.5 mm (i.e. 0.06-0.44 lines/mm). For each target image an average contrast across three parts of the image and for three different spectral bands was calculated. A third degree polynomial was then fitted to the data from both the along and across directions to find the

spatial frequencies at which a contrast of 0.5 was achieved (see Figure 5.4).

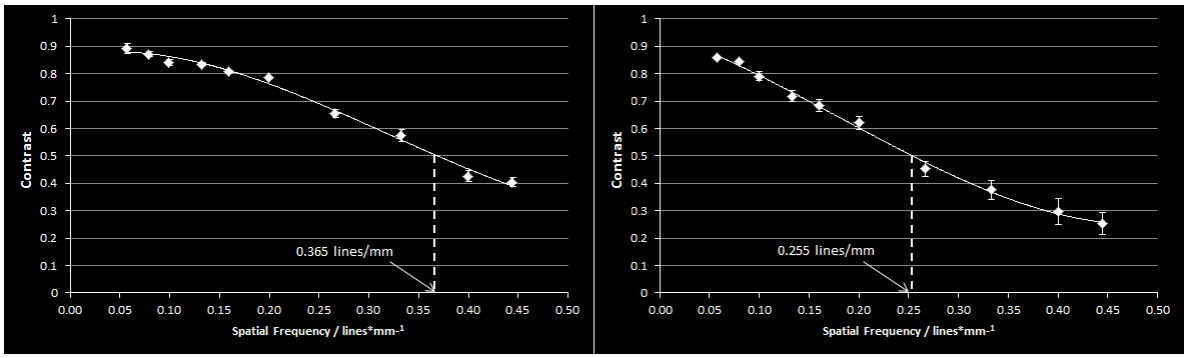

Figure 5.4: These contrast transfer function (CTF) graphs show how the spatial frequency of a striped pattern affects the contrast of the profile of the image obtained when measuring it with the prototype microslice spectrometer. The graph on the left shows the results when the stripes are imaged along the spectral slices, and the image on the right shows the results when the stripes are imaged across the spectral slices. The spatial frequencies for the along and across dimensions at 0.5 CTF are found to be 0.365 and 0.255 lines/mm respectively. These equate to spatial resolutions of 2.7 and 3.9 mm (when imaging from 1.5 m), or more generally, 1.8 and 2.6 mrad.

These plots show the spatial resolution of the system to be 2.7 and 3.9 mm at a target distance of 1.5 m. This equates to angular spatial resolutions of 1.8 and 2.6 mrad in the along and across field spatial directions respectively. These resolution values are significantly larger than the resolving power of the instrument (1.1 x 1.6 mrad), so it can be deduced that the spatial resolution is limited by the accuracy of the reconstruction software.

The spatial resolution values of 1.8 and 2.6 mrad recorded for the prototype microslice system are larger than for most hyperspectral remote sensing instruments (see Table 1.1), but are suitable for ground based laboratory and field testing. This lower spatial resolution is part of the trade-off that allows the microslice design to have a large IFoV, which theoretically leads to a larger SNR. Alterations of the foreoptics of the instrument, can be performed to produce a better spatial resolution, for a smaller IFoV (and hence SNR), or vise-versa.

The larger of the two spatial resolutions (2.6 mrad) can be taken to be the spatial resolution of the system, as it is the finest element size that can be resolved in both dimensions. An angular spatial resolution of 2.6 mrad equates an absolute spatial resolution of 2.6 m at 1 km altitude (a typical altitude for a remote sensing aircraft). For spaceborne imagery, however, the 2.6 mrad spatial resolution equates to a 1.8 km spatial resolution at an altitude of 700 km (a typical altitude for a remote sensing instrument in low Earth orbit). To use a microslice instrument for spaceborne remote sensing, design alterations would therefore be required to optimise the spatial resolution. Deploying the microslice spectrometer as part of a fully operational remote sensing system may also present further issues that could affect the spatial resolution. For example, vibrations caused by the aerial platform could cause blurring, and slight distortions could be caused by the proposed scanning technique (see Figure 1.4). Both of these effects could have an adverse effect on the final spatial resolution of the system.

5.1.2 Spectral Resolution Tests

The spectral resolution of a hyperspectral imager is another important parameter for determining its remote sensing capabilities. It can be seen from Table 2.1 that some current applications require a remote sensing instrument with a spectral resolution of less than 2 nm, but for many current applications 7.5 nm spectral resolution is sufficient. Attaining a higher spectral resolution increases the potential applications of the instrument, and could lead to the development of new applications or methods.

As with the spatial resolution, the spectral resolution is fundamentally limited by the number of pixels used, as shown by Equation 5.2. The spectral sampling rate of the microslice instrument allows for a spectral resolution as low as 1.8 nm, but the spectral resolution is also limited by the optical system. This limit was expected to about 6 nm, but Figure 4.13 suggested a 7 nm resolution is more likely.

$$minimum\,spectral\,element\,size = \frac{2 \times wavelength\,range}{pixels} \tag{5.2}$$

The spectral resolution of the prototype microslice spectrometer system was determined by imaging light from various spectral lamps that had well defined sharp emission peaks in the 475-650 nm wavelength range. The spectral lames used were mercury (Hg), cadmium (Ca), argon (Ar) and sodium (Na). These can be split up into two types of spectral lamp; the mercury and cadmium lamps were filament lamps, while the argon and sodium lamps were gas lamps. The filament lamps produced very bright light which was imaged by reflecting it off a white spectralon panel, which was imaged from the standard distance of 1.5 m. The gas lamps produced much fainter light, which was imaged directly from a distance of about 0.3 m to maximise the signal intensity. The light from the gas lamps was dispersed by covering the lamp with translucent paper (which had a roughly flat spectral transmittance), so that the field of view (FoV) of the instrument was more evenly illuminated. The average spectra measured by the microslice across the illuminated FoV for each spectral lamp are plotted in Figure 5.5.

The light from each lamp was also imaged by a commercial point based hyperspectral field spectrometer. This instrument was an ASD Field Spec 3, which was designed for gathering highly accurate spectral readings from a single point at close range for field spectroscopy. The ASD spectrometer has a spectral resolution (FWHM) of 3 nm and obtains data with a signal to noise ratio (SNR) of $\sim 7 \times 10^8$ (in the 350-1000 nm range) [121]. The spectra obtained from imaging the mercury lamp using the ASD instrument and the microslice spectrometer are plotted in Figure 5.6. For this image both data sets were re-sampled to 1.8 nm spectral elements (95 elements over the 475-650 nm range). The spectral resolutions of the instruments were determined by measuring the full width at half maximum (FWHM) of the spectral peaks. These are shown to be about 7 nm for the microslice spectrometer, and 4 nm for the ASD spectrometer.

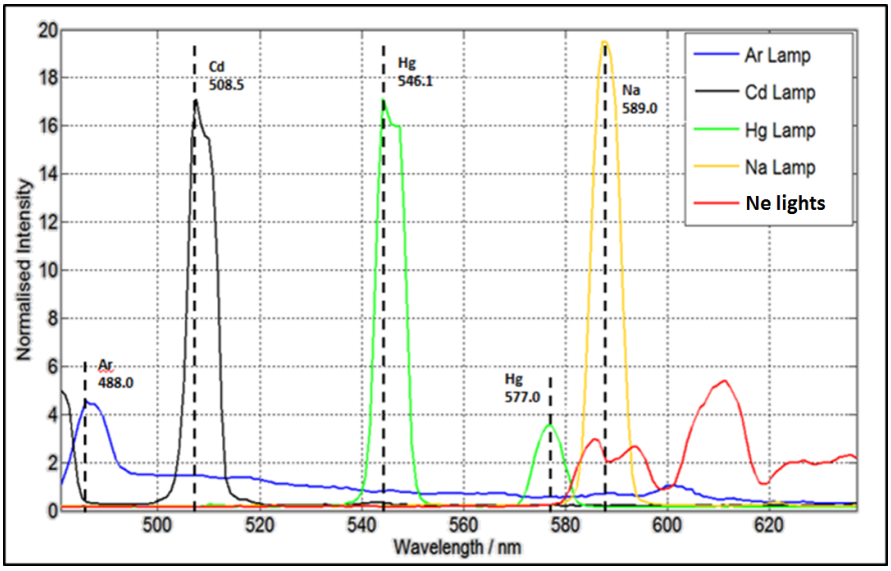

Figure 5.5: This graph shows spectral plots of four different spectral lamps (as well as the spectrum of neon lights, which are included for reference), as measured by the microslice spectrometer. These spectra were used to determine the spectral resolution of the microslice instrument by measuring the full width at half maximum (FWHM) of the spectral peaks. The four lamps used were mercury, cadmium, argon, and sodium, and the theoretically expected wavelengths of the peaks are displayed on the graph. This data could potentially be used to spectrally calibrate the instrument more accurately than with just the mercury spectrum.

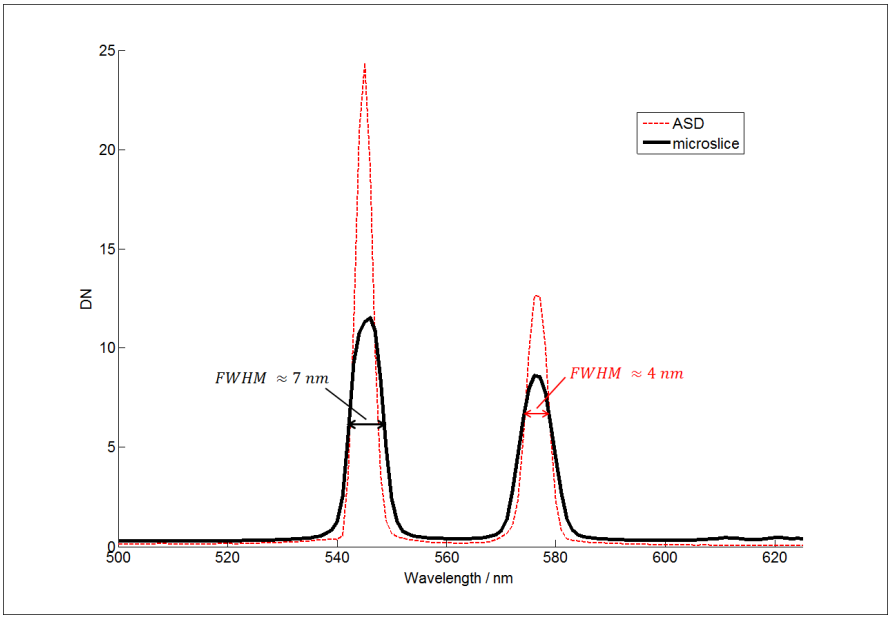

Figure 5.6: This graph plots the spectral peaks of a mercury lamp, as imaged by the microslice spectrometer and the ASD spectrometer. The sharp spectral emission lines allows the spectral resolution of the microslice spectrometer be determined and compared to that of the ASD spectrometer. The microslice spectrometer gives a full width at half maximum (FWHM) of 7 nm, while the ASD spectrometer gives a FWHM of 4 nm. The Y-axis label DN refers to *data numbers* meaning that the intensity scale is arbitrary.

An important characteristic to determine for the laboratory tests is the performance of the quartz-

halogen lamp that is used for illumination. This is expected to be a relatively spectrally flat light source, but spatial and temporal variations can be expected. A spectralon panel is imaged (as a homogeneous, flat reflectance target) for each experiment to provide a *white reference* image to negate systematic spectral and spatial variations, by normalising the target images against the spectralon image. Temporal variations, and changes in the illumination across the FoV may still have an effect, however. To test the effect of these variations two experiments were conducted.

To test for temporal variations, multiple consecutive images were captured of the white reference spectralon panel under constant illumination from the lamp, with consistent instrument exposure settings. The initial image was used as a white reference to the subsequent spectralon images, so that the expected spectrum would be a flat value of 1. The temporal variation was assessed by measuring the amount of variation in the spectrum of a specific pixel between images. The mean and standard deviation spectra were calculated for this pixel.

To test for changes in the illumination across the FoV just one of the white referenced images of the spectralon panel was used. The mean and standard deviation spectra were calculated across all of the pixels in this image. Figure 5.7 plots the results from both of these tests. It can be seen that for a specific white reference image the spectra across the FoV vary uniformly with intensity, with a standard deviation of about 2%. The spectra between images also appear to vary uniformly with intensity, but with a much higher standard deviation (about 20%). These results suggest that using multiple exposures (for example to increase integration time) leads to less precise data than using a single exposure.

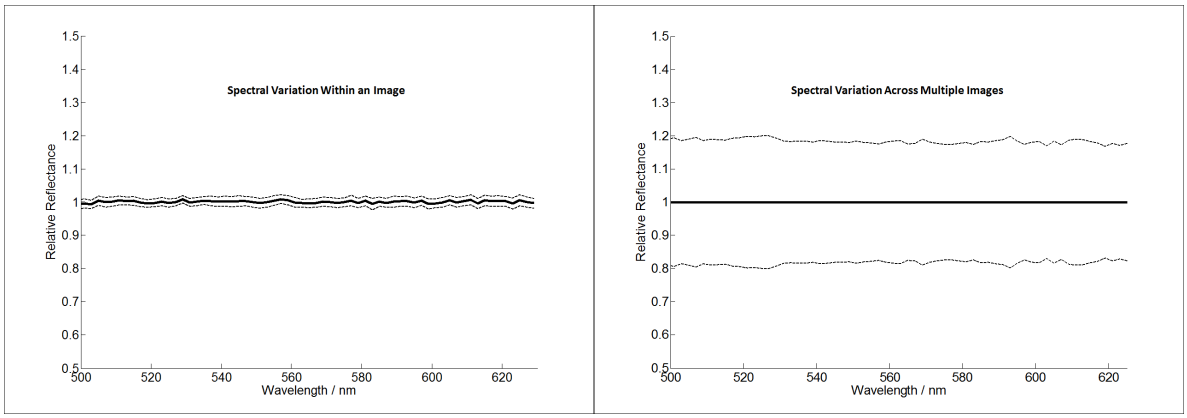

Figure 5.7: These plots show the variation of spectra within a white referenced image of a spectralon panel (left) and the variation for the same spatial pixel between images (right), captured using the prototype microslice spectrometer. The plots show the mean spectrum (solid line), and spectra that represent one standard deviation either side (dotted lines).

5.2 System Performance Tests

Further to the system specification tests, more laboratory tests were carried out using the prototype microslice spectrometer in order to determine its overall performance when imaging natural targets. Targets that would be typically imaged by remote sensing were chosen: firstly leaves, and secondly minerals. An ASD FieldSpec 3 was used in these tests (as with the spectral resolution tests) to provide reference spectral data to compare with that gathered using the microslice spectrometer. Since the ASD spectrometer records the reflectance spectrum from a single point to a high spectral accuracy, it is ideal for assessing the quality of the spectral results of the microslice instrument.

5.2.1 Imaging Leaves

Vegetation targets are amongst the most commonly imaged targets in hyperspectral remote sensing, with five of the ten remote sensing applications detailed in Chapter 2 involving the imaging of vegetation. As the microslice spectrometer is a prototype hyperspectral remote sensing instrument, it is useful to determine the quality of spectral data that it can gather when imaging vegetation targets. Due to the narrow wavelength range of the microslice spectrometer (475-650 nm), many of the prominent vegetation spectral features cannot be detected. For example, the red-edge (680-740 nm) is just outside this wavelength range [54]. The microslice spectrometer is, however, able to detect the green peak at about 550 nm caused by chlorophyll absorption in the red area of the spectrum. Leaves of different health have different levels of chlorophyll, and hence have different reflectance spectra in the 550-750 nm range.

The purpose of the experiment described in this Section was to determine the ability of the microslice spectrometer to distinguish between the reflectance of different natural targets. This provides a general demonstration of the spectral capabilities of the microslice.

5.2.1.1 Method

An experiment was conducted to determine if the variation in spectral reflectance between leaves of different health could be detected by the microslice spectrometer. The experiment was conducted on four separate leaves. Each leaf was in a different state of health, giving it a unique colour (see Figure 5.8). Leaf 1 had been removed from the tree and dried for three weeks. Leaf 2 had just been removed from the tree, but was of distinctly different colour, potentially due to poor health. Leaf 3 had been removed from the tree and dried for six months. Leaf 4 had been removed from the tree and dried for twelve months. Each leaf was imaged with the microslice spectrometer, and an ASD FieldSpec 3 spectrometer for reference, while being illuminated with a quartz-halogen lamp.

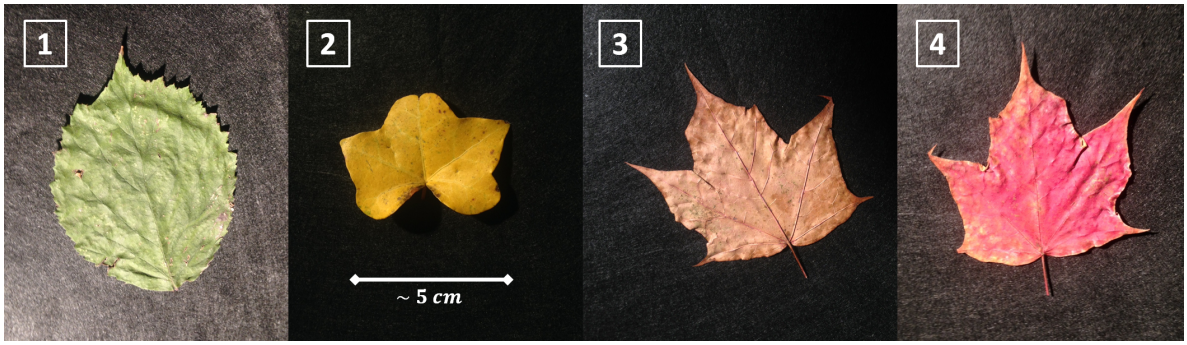

Figure 5.8: These photographs show the appearance of four leaf samples (labelled 1-4) of different states of health. These were imaged with the microslice spectrometer and an ASD spectrometer to determine how accurately the microslice spectrometer could detect the differences in spectral reflectance of the leaves. Samples were selected to be as homogeneous as possible so that the microslice spectrometer spectrum could be averaged over a wider spatial area.

Each leaf was imaged three times with the microslice spectrometer on a background of black cloth. A spatial area of 28 x 10 pixels was averaged in the microslice spectrometer images, as this was determined to be about the largest homogeneous area within each image. This area corresponded to approximately 3 x 3 cm on the physical target. The ASD was used to image with a 1° field of view (FoV) from a distance of 30 cm, equating to a target area of about $0.3\,cm^2$. Three ASD measurements consisting of 25 exposures of 272 ms were averaged for each leaf. A much smaller FoV was used for the ASD than the microslice spectrometer, as the ASD spectrometer required a small imaging distance to avoid doubt about the location of the target area, but the microslice spectrometer need a wider FoV to avoid noisy data.

5.2.1.2 Results and Discussions

The spectral results obtained using the ASD spectrometer clearly showed that there were significant spectral variations between the different leaves (see Figure 5.9). The table in Figure 5.9 provides a quantitative comparison of the spectra in terms of the spectral angle between each leaf in the 475-650 nm wavelength range, calculated using Equation 3.15. The microslice spectrometer operates in the 475-650 nm wavelength range, which is where the most prominent spectral variations occur.

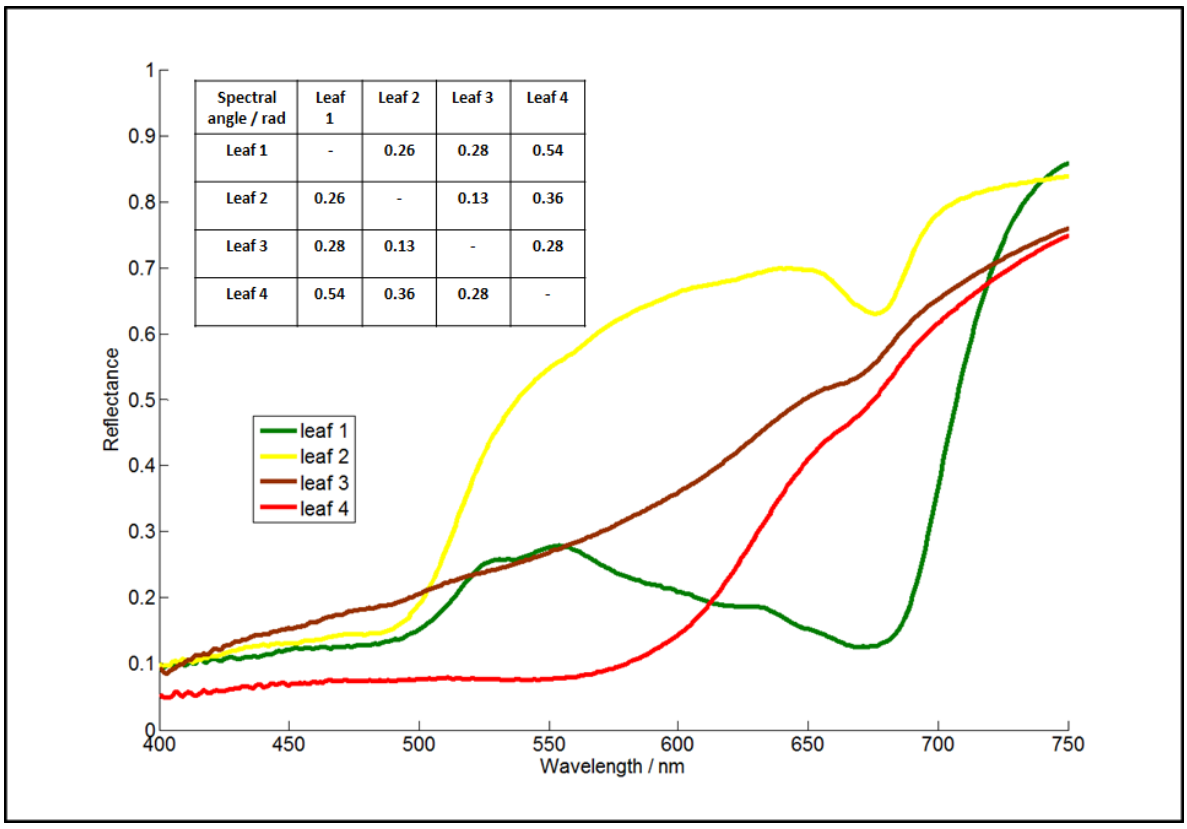

Figure 5.9: This graph shows the reflectance spectra obtained from imaging four leaves of different health using an ASD FieldSpec 3 spectrometer. It can clearly be seen that there are significant differences between the reflectance of the different leaves in the visible wavelength range. The table shows the spectral angle between the reflectance spectra, calculated using Equation 3.15, in the 475-650 nm wavelength range.

Both the ASD and microslice spectra were normalised to give a maximum value of one and a minimum value of zero using Equation 5.3, where $S(\lambda)$ is the original spectrum, and $S(\lambda)_{norm}$ is the normalised spectrum. This normalisation method shall be referred to as *zero-to-one* normalisation. It is applied here as it emphasised the variations in spectral shape while ignoring variations in spectral intensity. The spectral angle was calculated between the spectra obtained from the two instruments for each leaf.

Figure 5.10 provides a comparison between the results obtained from the two instruments. It can be seen that the microslice spectrometer is able to detect the spectra of the different leaves within an accuracy of 0.21 radians. The spectral angle between the instruments for each leaf is lower than the spectral angle between the ASD spectrum for that leaf and any other. It can therefore be concluded that the microslice spectrometer can be used to distinguish between leaves of suitably different health.

$$S(\lambda)_{norm} = \frac{S(\lambda) - min(S(\lambda))}{max(S(\lambda) - min(S(\lambda)))} \tag{5.3}$$

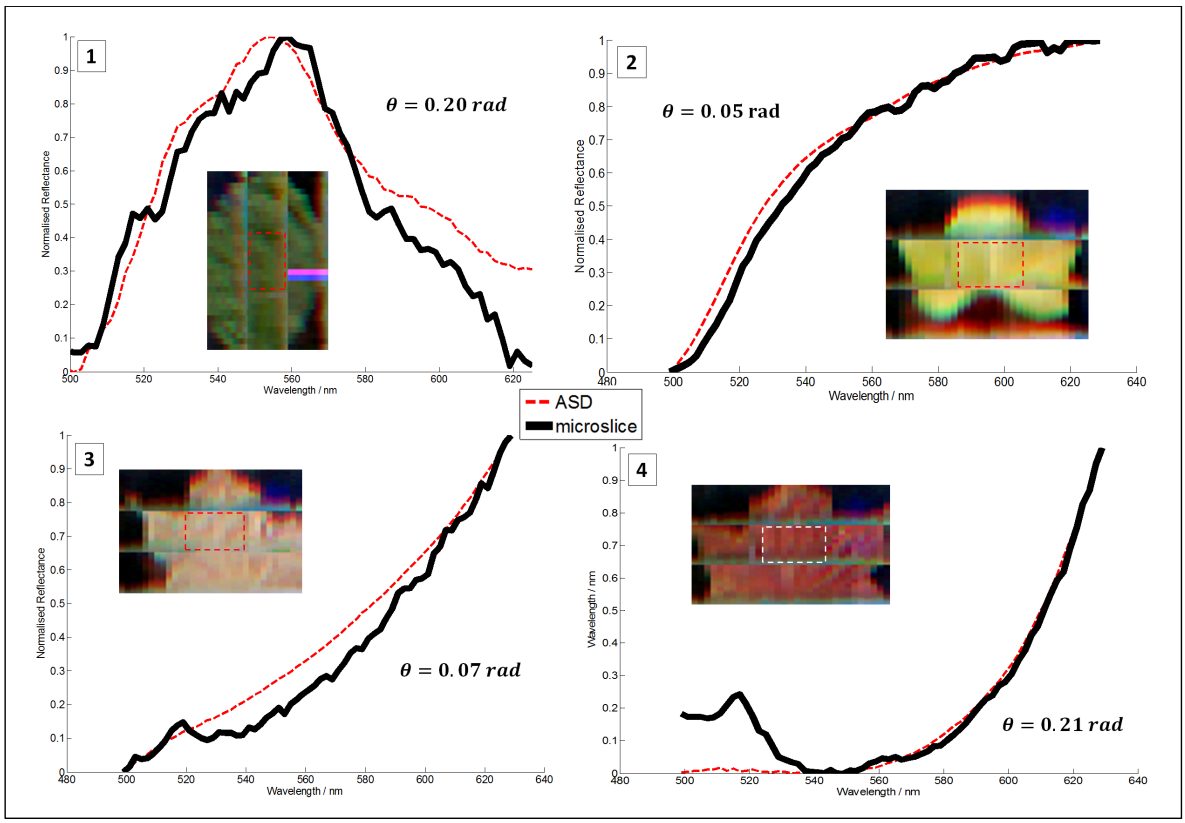

Figure 5.10: This figure compares the reflectance spectra obtained using the microslice spectrometer to those obtained using an ASD field spectrometer when imaging four leaves of different health. The spectra are plotted here after *zero-to-one* normalisation, with the microslice spectra being represented the solid black lines, and the ASD spectrum being represented by the dashed red lines. The spectral angle between the spectra from the two instrument was calculated for each leaf using Equation 3.15, and is displayed next to the graphs. The images next to each graph show an artificial true-colour image of the corresponding leaf that has been produced using the datacube constructed by the microslice spectrometer. The dashed box within each image shows the spatial area that was used to obtain the average microslice spectrometer spectrum.

The microslice spectrometer not only provides spectral information, but also provides spatial information. Figure 5.10 shows the reconstructed spatial images, and the spatial area that was averaged over to produce the microslice spectrum. In determining the microslice spectrometer performance it would be useful to assess the variation in spectral response across this apparently homogeneous spatial area in the microslice image.

Figure 5.7 showed that the relative reflectance of a true homogeneous target (a spectralon panel) varies across the FoV with a standard deviation of about 2% due to relative changes in the illumination across the FoV from the quartz-halogen lamp. Figure 5.11 shows the variation in spectra of a leaf across the apparently homogeneous spatial area of about 3 x 3 cm. This shows an intensity variation with a standard deviation of about 90% and the blue end of the spectrum, and 10% at the red end of the spectrum, with no discernible change in spectral shape. The spectral variations are therefore most likely to be a result of the geometry of the sample reflecting different amounts of light towards the sensor from different areas.

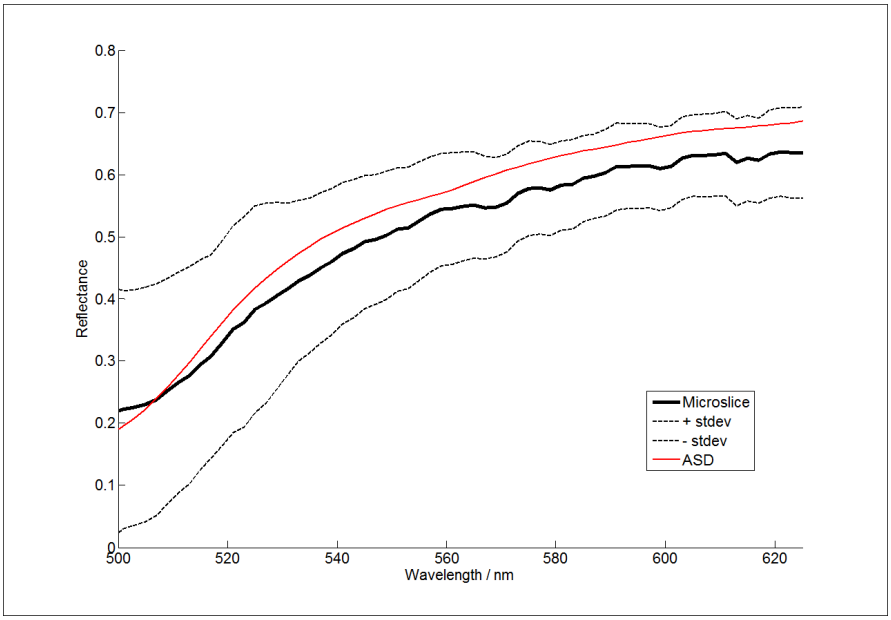

Figure 5.11: This plot shows the mean spectrum (solid black line) across a homogeneous spatial area in an image of a yellow leaf taken with the microslice spectrometer. The two dotted lines represent spectra one standard deviation either side of the mean spectrum, to show the spectral variation across the image. The red line represents the spectrum of the leaf as measured by an ASD FieldSpec 3 spectrometer.

This experiment shows the basic level of spectral classification performance of the microslice spectrometer. When deciding on a specific application for the microslice spectrometer, further tests would be required. A more rigerous laboratory test should be conducted with the aim of assesing specific microslice capabilities in controlled conditions. For example, for testing the capabilities of the instrument to distingush leaves in different stages of drying, the targets would need to be gathered from the same plant, and stored under the same conditions, with many repeat targets to ensure scientific rigour.

5.2.2 Imaging Minerals

Along with vegetation, minerals are also common natural targets imaged by hyperspectral remote sensing. Section 3.1.6 showed how dimensionality reduction algorithms can be used to map the mineralogy of an area using hyperspectral remote sensing data. This is made possible due to the distinct spectral signatures of different mineral types. Most spectral features that distinguish between different mineral types are in the near and short-wave infrared region, but some can be seen in the visible range, and so can theoretically be detected using the prototype microslice spectrometer [122].

5.2.2.1 Method

An experiment was conducted with the help of the British Geological Survey (BGS) to measure the accuracy with which the microslice spectrometer can image mineral reflectance spectra. BGS provided samples of ten different minerals that were either common remote sensing targets or thought to potentially contain notable spectral features in the 475-650 nm range. The minerals imaged were: hematite,

magnetite, goethite, halite, calcite, gypsum, kaolinite, malachite, fluorite, and langite. These minerals were chosen for different reasons. Hematite, magnetite, and goethite were chosen as they contain over 50% iron, an element that generally produces spectral features in the red part of the spectrum. Halite, calcite, and gypsum were chosen as they are *evaporite* minerals, and therefore commonly found in remote sensing target areas. Kaolinite was chosen as it is a pure clay, and is therefore has high natural abundance. Malachite, fluorite, and langite were chosen as the samples available displayed distinctive colours.

Multiple samples of some minerals were used (hematite (3), magnetite (3), calcite (3), gypsum (2)) giving a total of 17 mineral samples. The samples used were large unprocessed samples (about 5-10 cm in each dimension) with varying geometries (see Figure 5.12). The samples were illuminated with the same quartz-halogen lamp used in the previous experiment while being imaged with the microslice spectrometer, and then an ASD FieldSpec 3 spectrometer for reference. Each sample was imaged from different angles with both instruments to provide spectra from different parts of the sample and with different perspectives.

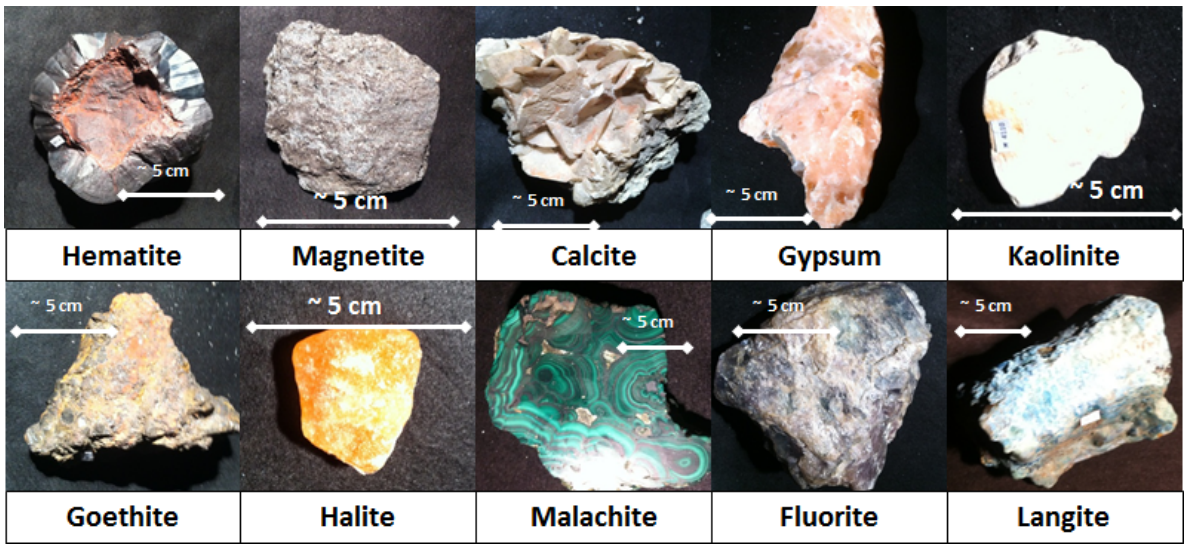

Figure 5.12: These photographs show samples of each of the different mineral types that were used in a test to assess the ability of the prototype microslice spectrometer to detect different mineral reflectance spectra. The samples were about 5-10 cm in size, and imaged with the ASD spectrometer, as well as the microslice spectrometer for comparison. The varying geometries meant that different imaging angles could give different reflectance results.

Unfortunately, just prior to this experiment the microslice spectrometer suffered some serious misalignment of the foreoptics, which probably occurred during transportation. This resulted in the spatial reconstruction of the microslice data being severely distorted, but in theory did not affect the spectral response of the instrument. It did appear to affect the spectral results from some of the samples, however, and so only results from four of the samples that produced notable results are presented here. These samples were of langite, goethite, malachite, and gypsum.

In order to assess the quality of the spectral data gathered from the microslice, it was compared to the

spectral results gathered using the ASD spectrometer. An area of 28 x 10 spatial pixels (about 3 x 3 cm on the physical target) was averaged in the microslice spectrometer image, as each sample contained a homogeneous area of this size, and this was this was the same sized area used in the previous vegetation study. The ASD spectrometer was used to image with a 1° field of view (FoV) from distances ranging from 40 cm to 5 cm, equating to target areas of $0.5\,cm^2$ and $0.03\,cm^2$ respectively. Multiple ASD spectrometer measurements from the same area consisting of 25 exposures of 272 ms were averaged for each mineral.

5.2.2.2 Results and Discussions

Figure 5.13 shows a plot of the spectra obtained from the mineral samples using the ASD spectrometer. The table in the figure provides a quantitative comparison of the spectra in terms of the spectral angle between each mineral sample.

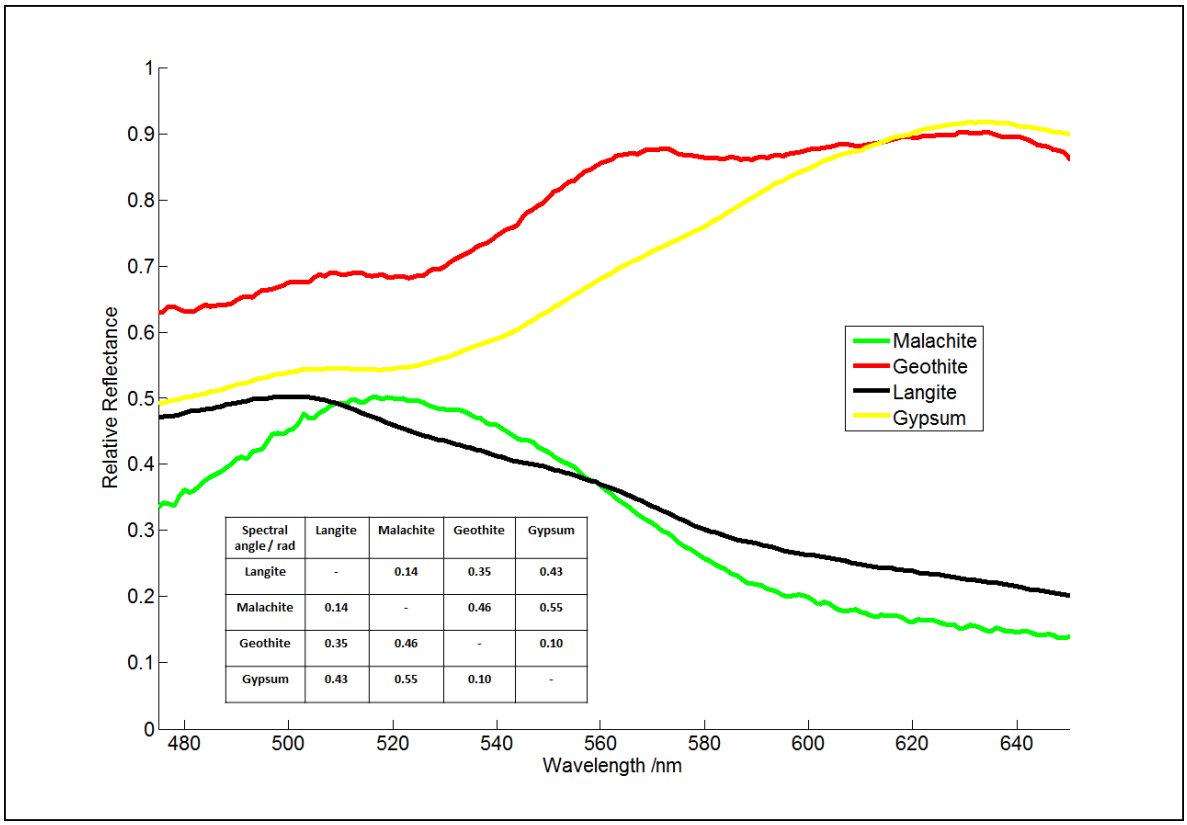

Figure 5.13: This graph shows the mean reflectance spectra obtained from imaging four different mineral samples using an ASD FieldSpec 3 spectrometer. Separate flat normalisation have been applied to these spectra for visualisation. It can be seen that these minerals display different spectral features in the visible wavelength range. The table shows the spectral angle between the reflectance spectra (calculated using Equation 3.15) over the 475-650 nm wavelength range.

Due to the variations in viewing distance of the ASD spectrometer, the absolute reflectance intensity was not significant. For a fair comparison, both the ASD and microslice spectra were therefore zero-to-one normalised (as in the previous study) using Equation 5.3. The spectral angle was calculated

between the spectra obtained from the two instruments for each mineral.

Figure 5.14 shows a visual and quantitative comparison between the spectra from the different instruments for each mineral. It can be seen that the microslice spectrometer is able to detect the spectra of mineral samples within an accuracy of 0.25 radians. The spectral angle between the instruments for each sample is lower than the spectral angle between the ASD spectrum for that mineral and any other (except for between goethite and langite). It can therefore be concluded that the microslice spectrometer is able to distinguish between certain spectrally distinct mineral samples, but not all.

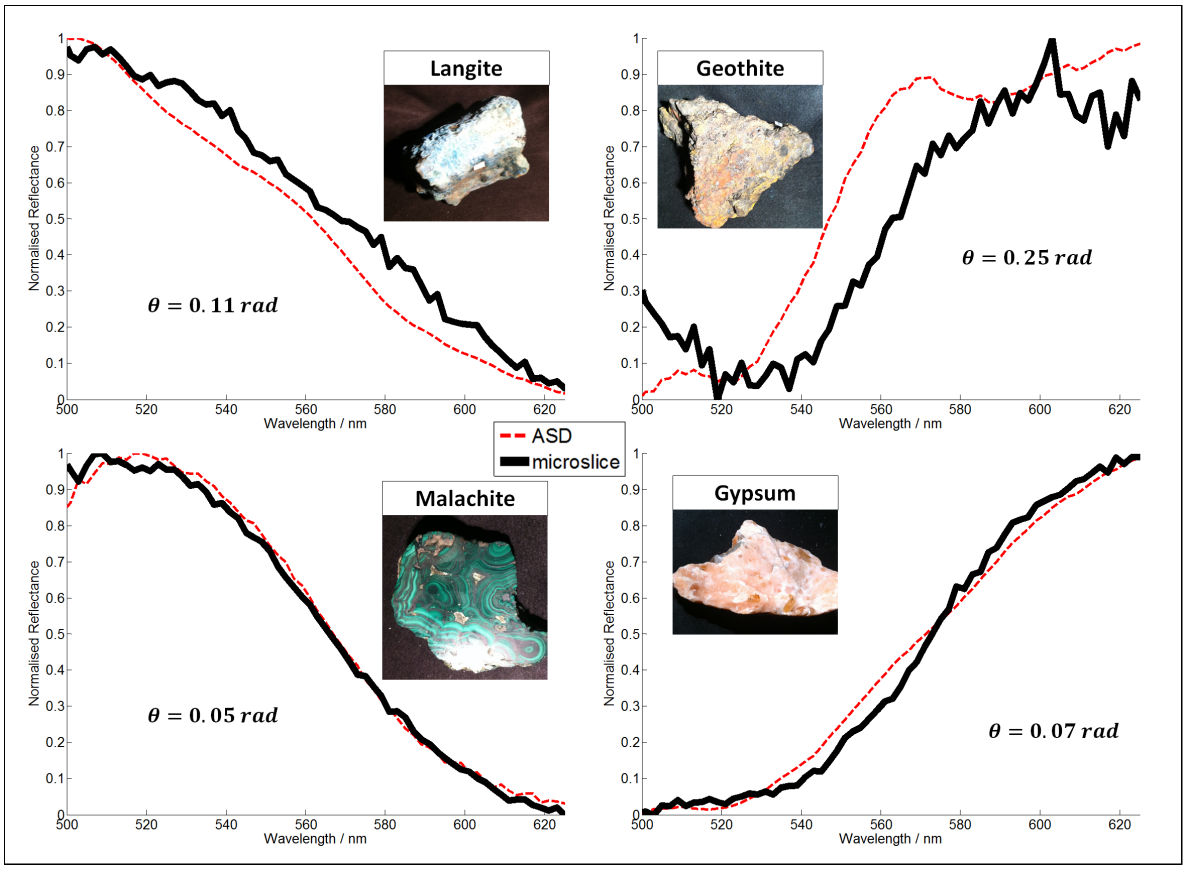

Figure 5.14: This figure compares the spectra obtained using the microslice spectrometer to those obtained using an ASD field spectrometer when imaging four different mineral samples. The spectra are plotted here after *zero-to-one* normalisation, with the microslice spectra being represented by the solid black lines, and the ASD spectrum being represented by the dashed red lines. The spectral angle between the spectra from the two instrument was calculated for each sample using Equation 3.15, and is displayed next to the graphs.

It would be useful (as it was with leaf spectra) to assess the variation in spectral response across an apparently homogeneous spatial area in the microslice image. Figure 5.15 shows that the variation in spectra of a mineral across a visually homogeneous spatial area of about 3 x 3 cm on the target. As was the case with the leaf results in Figure 5.11 this mainly shows an intensity variation, with no discernible change in spectral shape, suggesting that the variations are a result of the geometry of the sample reflecting different amounts of light towards the sensor from different areas.

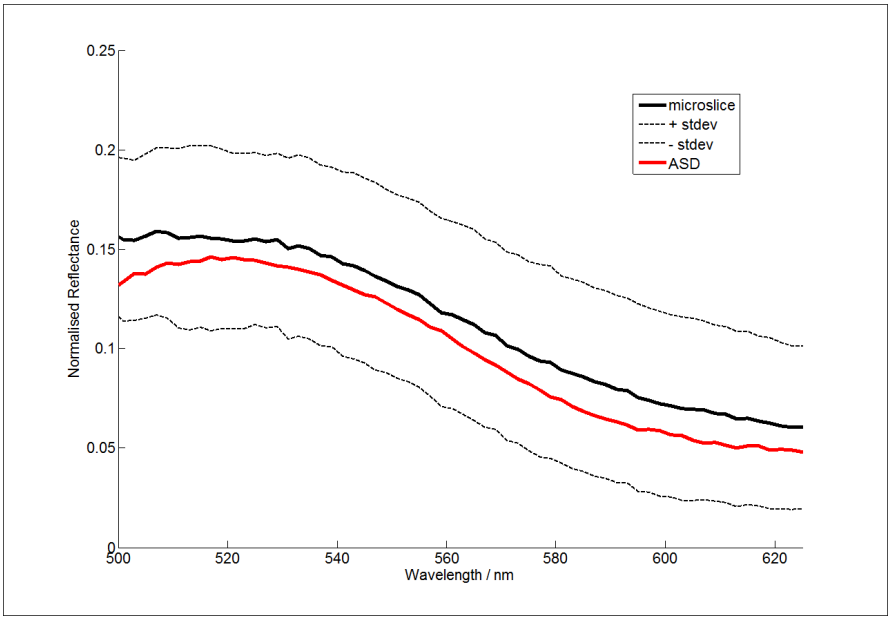

Figure 5.15: This plot shows the mean spectrum (solid black line) across a homogeneous spatial area in an image of a malachite mineral sample taken with the microslice spectrometer. The two dotted lines represent spectra one standard deviation either side of the mean spectrum, showing the spectral variation across the area. The red line shows a reference spectrum of the sample, as measured by an ASD FieldSpec 3 spectrometer.

The variations in the malachite spectrum have a standard deviation of about 25%, which is in general lower that that of the yellow leaf variation (see Figure 5.11). It can be seen from Figures 5.8 and 5.12 that the malachite sample appears to have a very physically flat surface (the same as the white reference panel), while the leaf has a relatively wavy surface. This may therefore be the cause of the differences in the percentage standard deviations over the two homogeneous areas. It is not clear, however, why the variation in the yellow leaf is wavelength dependent. This is most likely to be caused by the spectrometer system.

Another important comparison that can be made when testing an instrument's ability to determine the spectral reflectance of mineral samples, is to compare the results to those found in a *spectral library*. Spectral libraries are electronic databases that contain the reflectance spectra that have been gathered under very controlled conditions of many pure, ground mineral samples. The most detailed and widely used spectral libraries are the USGS spectral library [ ] and the JPL spectral library [ ], which detail the reflectance spectrum of hudereds on minerals tested in laboratory conditions.

Spectral libraries provide useful comparisons that would allow the ability of the microslice imager to distinguish the reflectance of pure mineral samples to be tested. There are shortcomings, however, of using spectral libraries when comparing them to data from instruments that are to be used for remote sensing. When a remote sensing instrument is used for mineral detection, it is required to image spectra from areas of ground that reflect multiple spectral signals. The data must be of sufficient quality that the desired spectra can be extracted.

5.3 Summary

This chapter has investigated the laboratory performance of the fully integrated prototype microslice spectrometer system. The spatial resolution was measured to be 1.8 x 2.6 mrad, and the spectral resolution was measured to be 7 nm over the 475-650 nm wavelength range.

The spectral performance of the system when imaging typical natural remote sensing targets in a controlled environment was also tested. The two types of targets used were leaves of different health, and minerals of different chemical compositions. The system was shown to produce spectra that lay within a spectral angle of 0.25 radians of the spectra gathered from a high precision ASD field spectrometer (using a spectral angle mapper (SAM) metric, see Equation 3.15). This was shown to be accurate enough to distinguish between almost all of the samples chosen in the experiments.

The results presented in this chapter give an indication of the performance of the current prototype microslice system, and provide an insight into its potential spectral classification capabilities. These experiments do not, however, test the capabilites of the microslice spectrometer for any specific imaging application. Once specific potential applications of the microslices specctrometer are identified, further laboratory tests would be required to determine the potential of the instrument within the specific appliactions.

The main drawbacks of these studies for assessing the capabilities of a remote sensing instrument lie in the imaging environment used. Although natural targets were imaged, they were not imaged in their natural environment (artificial illumination was used), and no consideration was given to how the performance would be affected by deployment on a remote sensing platform.

The next chapter addresses the first of these two drawbacks by investigating the performance of the microslice spectrometer in the field environment, which is more in line with remote sensing data collection. Chapter 7 partly addresses the second drawback, while also providing discussion about potential improvements to the microslice design for remote sensing applications.

Chapter 6

Field Performance Tests

This chapter is split in to two main parts. Firstly (following a brief description of the methods and purpose of field testing a remote sensing spectrometer in Section 6.1), Section 6.2 discusses ground based field testing that was carried out using the prototype microslice spectrometer. Secondly Section 6.3 details field and lab tests carried out to determine the potential of remote sensing, and specifically the microslice spectrometer to detect pollutants in river water. Although they are relatively distinct, these studies help provide a well rounded assessment of the capabilities of the microslice spectrometer in the field, and its potential for remote sensing.

6.1 Field Testing a Hyperspectral Remote Sensing System

A key part of developing a new hyperspectral imaging system is performing field tests, to get information about how it will perform in realistic remote sensing conditions. For a remote sensing system, a full field test would involve imaging test targets from an airborne platform using the appropriate scanning method. There are many reasons why imaging from an airborne platform would yield different results and require different data processing from imaging in a lab; for example, natural light would be used as opposed to artificial light, atmospheric absorption/scattering would affect the signal, and the scanning method used could cause spatial distortions.

For complete testing of a remote sensing instrument, three sets of measurements are typically obtained. These are: airborne spectral measurements taken using the instrument; ground truth spectral measurements taken with a field spectrometer; and physical ground truth data of the parameters being identified. The ground truth data, physical and spectral, provide validation for the test instrument data. These three sets of measurements therefore allow the spectral characteristics of different targets to be accurately identified, and the potential of the airborne instrument to detect these spectral characteristics to be assessed. The following case study shows the methods by which new remote sensing instruments are field tested and current capabilites are benchmarked.

The Cuprite area in Nevada, USA ($12\,km^2$) is a well known geological area that is used for testing

new spectral remote sensing instruments because of its high abundance of different minerals, and large areas of exposed rock faces [51]. Results from the first spectral mineral mapping of the area were published in 1980 [122]. This study mapped the distribution of limonite, kaolinite and alunite to a spatial resolution of 10 m using band ratio analysis on data from an aircraft based Bendix 24 channel multispectral scanner (MSDS) [123]. Lab test results from a 'high resolution reflectance spectrometer' were used to determine which band ratios that would optimally identify these minerals.

Cuprite area is a common area for instrument testing, and in 1990 ground truth data was gathered for AVIRIS mineral mapping [124]. The AVIRIS mineral mapping data has since been used as a 'ground truth' benchmark, with later remote sensing mappings simultaneously testing new instruments, as well as verifying, and improving on the quality of mapping in the Cuprite region [51].

In 1995 the first full hyperspectral survey of the Cuprite area was conducted using the airborne AVIRIS instrument (see Table 1.1) to map the mineralogy of the area [52]. The results were compared to the MSDS mapping for validity. Also in 1995 the HYDICE sensor (see Table 1.1) was used to map the mineralogy in the same area [64]. As part of the testing of the Hyperion remote sensing spectrometer (see Table 1.1), data taken from the Cuprite region in 2001 was used to map the mineral coverage, using data from AVIRIS as a comparison [51]. Figure 6.1 shows the progression of mineral mapping in the Cuprite area.

The Cuprite region provides a very useful geological testing area for new hyperspectral remote sensing imagers, as it provides an extensive area well mapped terrain with varying spectral refelectance. The size of homogeneous areas is also highly varied, allowing for an assesment of the instrument's spatial resolution and spectral unmixing capabilities (see Section 3.1.6).

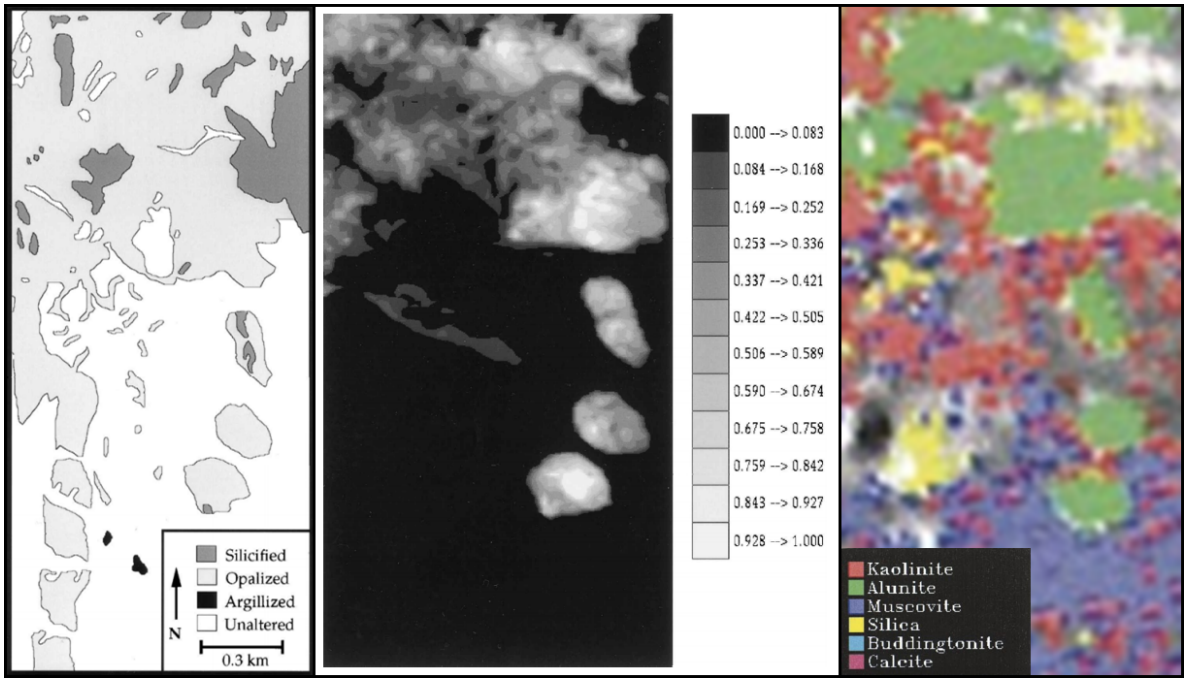

Figure 6.1: This figure shows the development of the mineral mapping in part of the Cuprite area in Nevada, USA over time. The area is a regular test site for airborne hyperspectral imaging systems, and whenever a new instrument is tested more data about the site is gathered. In particular, these figures show the abundance of alunite as mapped by three separate studies. The map on the left is reproduced from data taken using a Bendix 24 channel multispectral scanner (MSDS) in 1990, where alunite is part of the *opalized* category. The central figure shows the abundance on alunite, as mapped by the HYDICE spectral scanner in 1995, and the figure on the right shows a mineral map produced with data gathered using the Hyperion instrument in 2001. These images are taken from [51].

Analysis of data from the spaceborne CHRIS spectrometer (see Table 1.1) also provides a good example of hyperspectral remote sensing instrument testing. This is because CHRIS is an instrument that was developed to determine the capabilities of a particular instrument design, but is also a fully deployed hyperspectral imaging system. Data analysis of some of the first results obtained from the CHRIS instrument were presented by Guanter et al. in 2005 [125]. This analysis compared data obtained from two different CHRIS datasets with in-situ readings gathered using an ASD spectrometer. The purpose of these comparisons was to determine the quality of the processing techniques used to remove noise and perform atmospheric correction. Performing these airborne tests in conjunction with ground truth measurements was the only way of validating these corrections.

For testing the microslice spectrometer, the testing stage following laboratory testing, would be ground based field tests. This would determine more about the practical performance of the spectrometer, without having to perform airborne testing. There are many parameters that affect the results of an imaging spectrometer, which can change between lab and field tests. In field tests these parameters are closer to those encountered in airborne imaging, for example, targets are imaged in their natural environment, and natural light is used as illumination. These tests do not, however, take into account atmospheric interference, or the affect of platform vibrations ,or the scanning method on the

performance of the spectrometer.

The next section in this chapter details ground based field testing of the microslice spectrometer in an area containing a diverse array of natural remote sensing targets. The third section details a field and lab spectroscopy experiment that was carried out using the microslice to determine if pollution could be detected in the River Ganges.

6.2 Testing of the Microslice Spectrometer on The River Arrow

6.2.1 Background

Initial field testing of the microslice spectrometer system took place in August 2013 around part of the River Arrow near Studley in Warwickshire at GPS coordinates Lat: 52.26914, Long: -1.88223 (Global Mercator projection). This site was chosen as it displayed a wide variety of land cover types in a small area (see Figure 6.2), which were mapped by qualitative ground truth assessment. It was also a designated field test site used by The University of Worcester, and so gaining permission to conduct the fieldwork there was relatively straightforward.

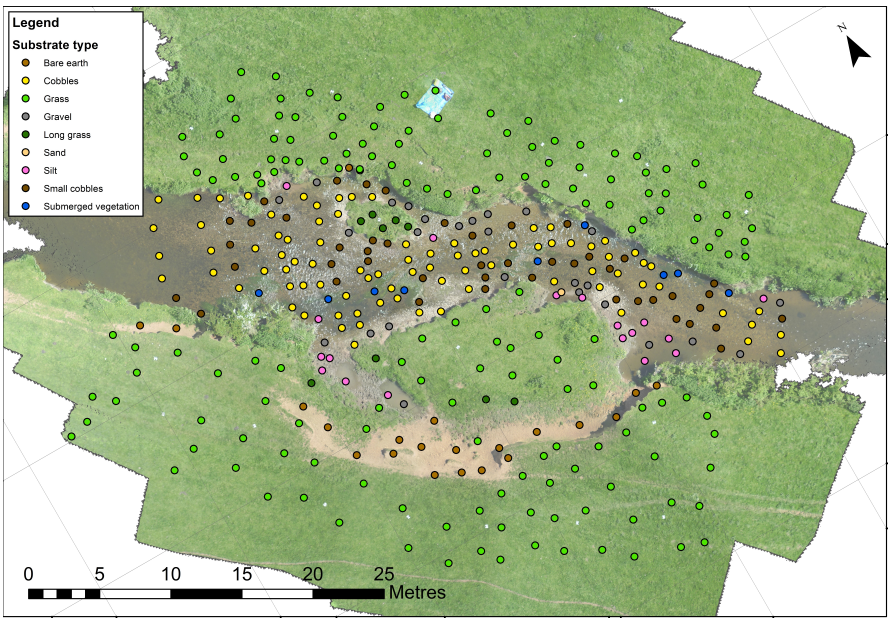

Figure 6.2: This image shows a plan view of the River Arrow test area, used to test the microslice spectrometer. The map indicates the wide array of different land types that are present over the relatively small area. The image was taken using UAV photography by Amy Woodget of The University of Worcester, and the land types were defined by qualitative ground truth assessment.

The tests involved imaging a variety of different natural targets around the river bank. They were designed to determine the ability of the microslice to identify spectral characters that could be used to classify different target types. An ASD FieldSpec 3 spectrometer (as used in the lab tests) was

also used to provide reference spectral spectral measurements of each target imaged by the microslice spectrometer. It was expected that field testing would provide a more realistic assessment of the remote sensing performance capabilities than the laboratory tests, as targets were imaged in their natural environment, with sunlight providing the illumination, and the instrument was exposed to outdoor conditions.

6.2.2 Method

6.2.2.1 Taking Measurements

Over the course of the two days of field testing, ten different land targets were imaged by both the microslice and the ASD spectrometers. The ten targets, which were defined based on appearance, were named: grass, dead grass, dry soil, lush grass (particularly green grass near the river), thistles, nettles, river plants (an assortment of vegetation found near the river bank), silt (river deposits), pebbles (dry on the river bank), and mud. These target types were qualitatively defined based on appearance and environemnt for the purposes of a general test of the classification cpabilities of the microslice spectrometer. No information was recorded about the grain size of the various sedement classes. Figure 6.3 shows photographs of the ten different target types imaged.

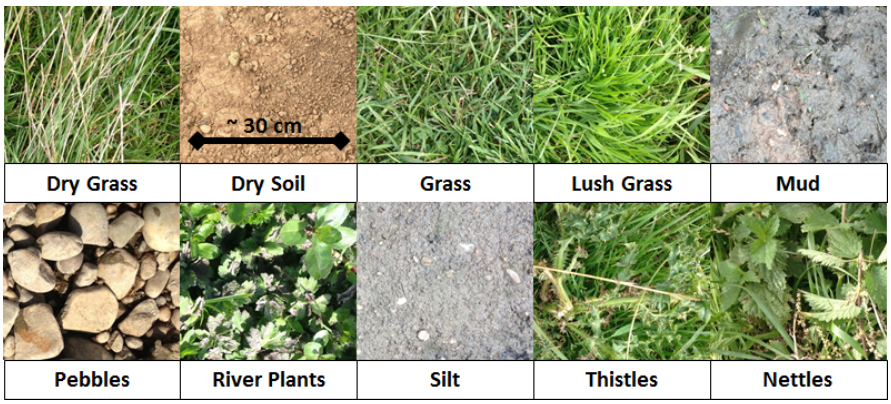

Figure 6.3: These are digital photographs of the ten different land target types that were imaged using the microslice spectrometer. The images show the rough target area used in the experiment, but are not exact representations of the target area imaged.

Images were also taken with the spectrometer in five different parts of the river. These images contained different river bed types, different flow types, and different water depths. These however are not used for analysis in this thesis. Figure 6.4 shows the location of each of the 15 imaging target areas.

Figure 6.4: This image shows a plan view of the River Arrow test area (Lat: 52.26914, Long: -1.88223), showing the positions of the different target areas that were imaged with the microslice and ASD spectrometers.

The set-up of the microslice spectrometer was similar to that used in the lab tests, with the instrument fixed to a tripod approximately 1.5 m above the ground, and connected with a USB connection cable to a laptop, which was running the image capture software. A Clarke Power 700 W generator was used to power the ATIK camera, the laptop, and the ASD spectrometer. This was not an ideal field set-up, as the generator was heavy and required electrical connections close to the water, but it was the best that could be provided at the time. Figure 6.5 shows the set-up of this field experiment.

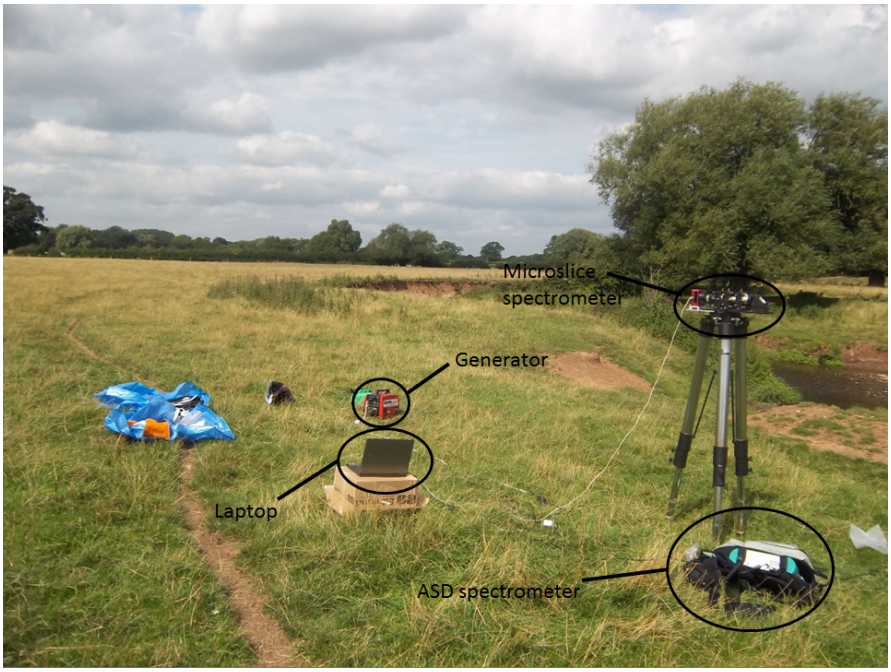

Figure 6.5: This photograph shows the field set-up used for testing the microslice spectrometer around the River Arrow. A Clarke Power 700 W generator was used to power the microslice detector, the laptop, and the ASD spectrometer. The laptop was used to control the capture settings of the microslice spectrometer, and download the images that it captured.

At each target location the microslice spectrometer was used to image a spectralon panel (three times) for white reference, as well as the target (three times). The ATIK 383L+ camera was set to 0.01s exposures, to minimise the chances of saturation, and a 0.0°C detector temperature was used for all images.

The ASD spectrometer was used immediately after the microslice for each target. A white reference was taken using the spectralon panel, followed by three measurements of the target. For each white reference, 10 x 36 ms exposures were averaged, and for each target measurement 25 x 36 ms exposures were averaged. An exposure time of 36 ms was chosen, as this was found to be the longest exposure time that did not lead to any saturation. All ASD spectrometer measurements were taken with a 1^{o} field of view (FoV) optic held approximately 30 cm above the target, giving a FoV of approximately $0.3\,cm^2$.

When conducting a field spectroscopy experiment it is important to ensure that all measurements are taken as close as possible to solar noon (1PM BST) and in direct sun, so that the best possible illumination conditions are used [126]. In this experiment all measurements were taken between the hours of 10:00 am and 16:00 pm (BST). Where possible, measurements were taken with illumination from direct sunlight, but there was a lot of cloud cover during both days of the experiment, so this was not always possible.

6.2.2.2 Data Processing

The data from the microslice was processed using the MATLAB software discussed in Chapter 4. An extra MATLAB module was specifically developed for this field test to produce a classification of the microslice images. This extra module used spectral angle mapper classification (as described in Chapter 3), with the ASD spectrometer data being used as the reference spectra. The SAM classification method is chosen as it is the only method investigated in Chapter 3 that can be used with the data available. The other two techniques (Mahalanobis distance and maximum likelihood) require multiple reference spectra to represent the full spectral variation of each target, which are not available in this experiment.

SAM_classification

The main purpose of this module is to classify the spatial pixels in each microslice image by land type with a SAM classification, using spectra gathered with the ASD spectrometer as reference spectra. This classification determines the ability of the microslice to distinguish between different target types. The reference spectrum of each target is compared to the spectrum of each spatial pixel in each target datacube by calculating the angle from Equation 3.15. The pixel is then defined as the target that had the reference spectra with the smallest angle. A threshold is also set, so if the smallest angle for a particular pixel is above the threshold, then the pixel is left unclassified. The results are used to create a *classification map* of each target area, which is plotted as a 2-dimensional colour image. The SAM method was chosen over other classification comparison methods discussed in Chapter 3, as other methods require multiple different reference spectra from different targets within a target type to define a class. The MATLAB code for this module can be found in Appendix A.7.

The *asd_comparison* MATLAB module (see Section 4.6.2) was also edited for the is experiment to assess the variation in the detected reflectance across the microslice imager FoV. The choice of spatial area to create the median microslice spectrometer spectrum for this module could significantly affect the spectral results due to spatial variations across the target area. Results using different areas were therefore obtained to assess the level of this variation. Nine different rectangular spatial areas of 20 x 6 pixels (about 2 x 2 cm on the target) within the datacube were chosen to obtain data from separately. The spatial areas chosen are shown overlayed on a spatial reconstructed image in Figure 6.6. The mean and standard deviation of the spectral angle between the ASD spectrometer spectrum and the microslice spectrometer spectrum from each spatial area was calculated.

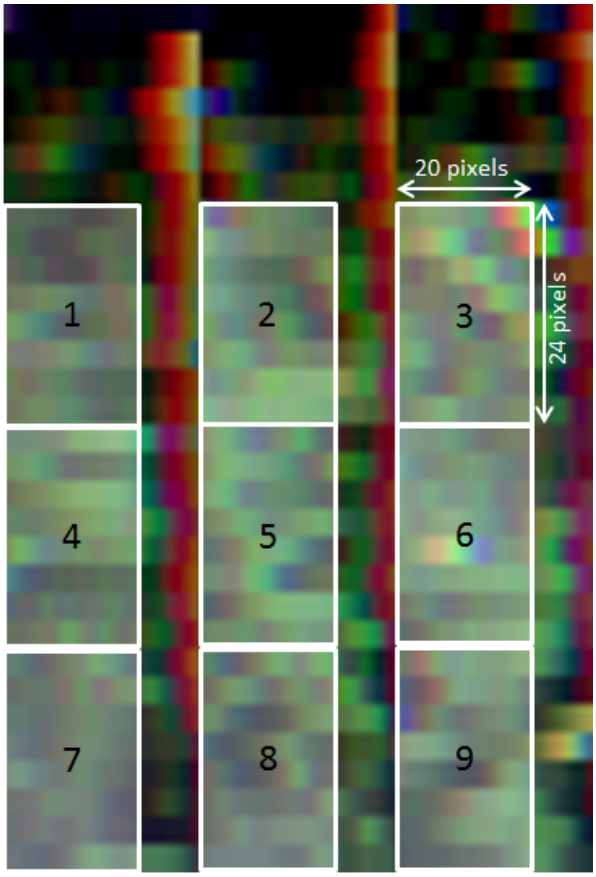

Figure 6.6: This figure shows the nine spatial areas in a spatially reconstructed microslice spectrometer image that were used to create separate median microslice spectra for each target in the field experiment. These were used to compare with spectra of the same targets gathered with an ASD field spectrometer, to not only test the variation of spectra between instruments, but also across the target field of view (FoV). Each spatial area is 20 x 24 pixels on the reconstructed datacube, which represents 20 x 6 pixels on the actual data before artificial magnification.

6.2.3 Results

Figure 6.7 shows the results of the field testing of the microslice spectrometer around the River Arrow. The results from imaging each target are represented by three panels: a photograph, a reconstructed datacube image, and a spectral comparison with the data from the ASD spectrometer. The ASD spectrometer was shown to produce very similar laboratory results to the microslice spectrometer in Chapter 5 (see Figure 5.11 and Figure 5.15).

There are various artifacts visible in the reconstructed datacube images that are not . These artifacts can be split into three types:

1. large white areas on the right of the reconstructed image
2. vertical lines that occur at the border between spectral boxes
3. small discoloured areas that occur allong spectral boxes.

The first set of artifacts occur due to missing white reference data caused by misalignment of the white reference panel. These areas are ignored for analysis purposes. The second set of artifacts occur due to slight imperfections in the spectral box placement (the technique of which is shown in Figure 4.22). The third set of artifacts occur due to off-set spectral callibration. The first set of artifact can easily be avoided in the future by using a larger white reference panel. The the second and third types artifacts, however, would require modifications to the data processing software, and modifications to the instrument set-up respectively. These are issues to be investigated when developing a second generation instrument.

The photographs do not show the exact FoV imaged by the microslice spectrometer, but give an indication of how homogeneous each target area was. The grass, lush grass dry soil, mud, and silt target areas can be seen to be very homogeneous; while the dead grass, nettles, thistles, pebbles, and river plant target areas are more varied. This means that for the latter targets it is important to choose an appropriate area to extract the median spectrum from. The spatially reconstructed images show which areas are appropriate to extract the median spectrum, as well as demonstrating the quality of spatial reconstruction.

The spectra of vegetation targets are imaged significantly more accurately with the microslice spectrometer than the non-vegetation targets; with the largest discrepancy in spectral angle between the two instruments for the vegetation targets being 0.13 rad for *nettle*, and the smallest discrepancy in spectral angle for non-vegetation targets being 0.26 for *silt* and *dry soil*. The microslice spectrometer appears to be able to detect the slight variations in reflectance spectra spectra for vegetation targets despite the inhomogeneous nature of some of the targets. The vegetation targets also have very small standard deviations on the spectral angle (≤ 0.02) compared to non-vegetation targets (≥ 0.3), which implies that non-homogeneity of the target does not significantly contribute to the spectral variation across the FoV of the microslice spectrometer.

Many of the white reference images for the microslice spectrometer measurements were saturated in some areas of the FoV, despite the camera being set to the minimum exposure setting (0.01 s). This not only means that some of these microslice spectrometer spectra were not normalised to the correct magnitude of reflectance, they were also not normalised to the correct spectral shape. Because of this saturation issue it became very important to take spectra from appropriate areas of the image. Varying illumination conditions also meant that the most important aspect of the spectra to be taken into account when comparing the two instruments was the spectral shape rather than the reflectance intensity.

The spectral angles in Figure 6.7 mostly seem relatively low (similar to those gather in lab testing in Chapter 5), indicating a strong correlation between the field measurements of the two instruments. To assess the variation of spectra across the microslice spectrometer FoV, the spectral angles between the spectra of each individual spatial pixel and the corresponding ASD spectrum were calculated for each

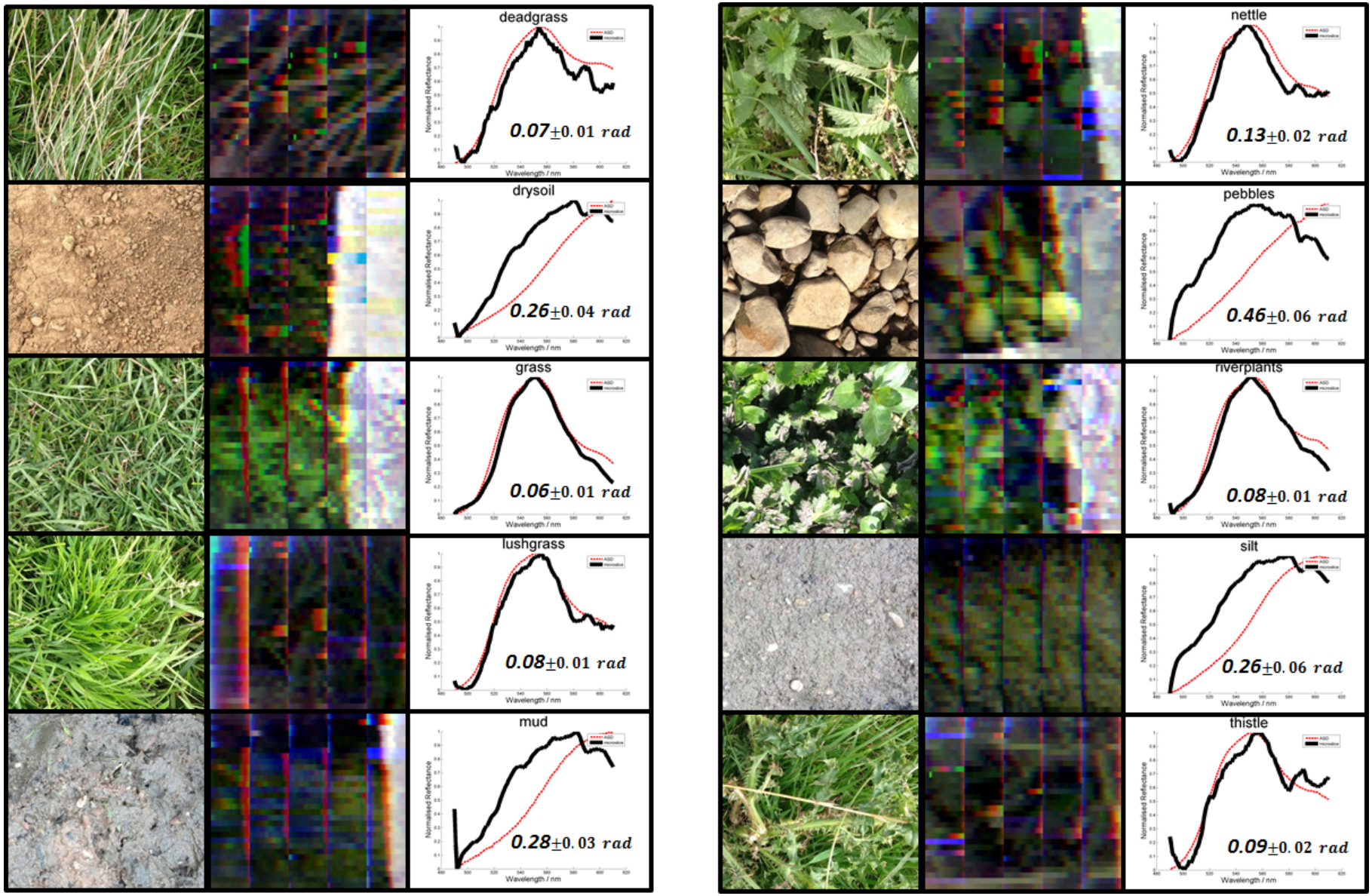

Figure 6.7: This figure shows the results from field testing the microslice spectrometer system around the River Arrow. The results from each target are represented in three panels. The left-hand panel shows a photograph of the approximate target area. The central panel shows a synthetic true-colour image generated from the reconstructed datacube. The right-hand panel shows a plot of the mean ASD spectrometer spectrum (in red) and the median microslice spectrometer spectrum (in black), as well giving the mean and standard deviation of the spectral angle (calculated using Equation 3.15) between the spectra of the two instruments for different spatial areas on the microslice spectrometer image.

microslice target datacube. The results of this are plotted for the grass target in Figure 6.8 to create a *similarity map* over the microslice field of view.

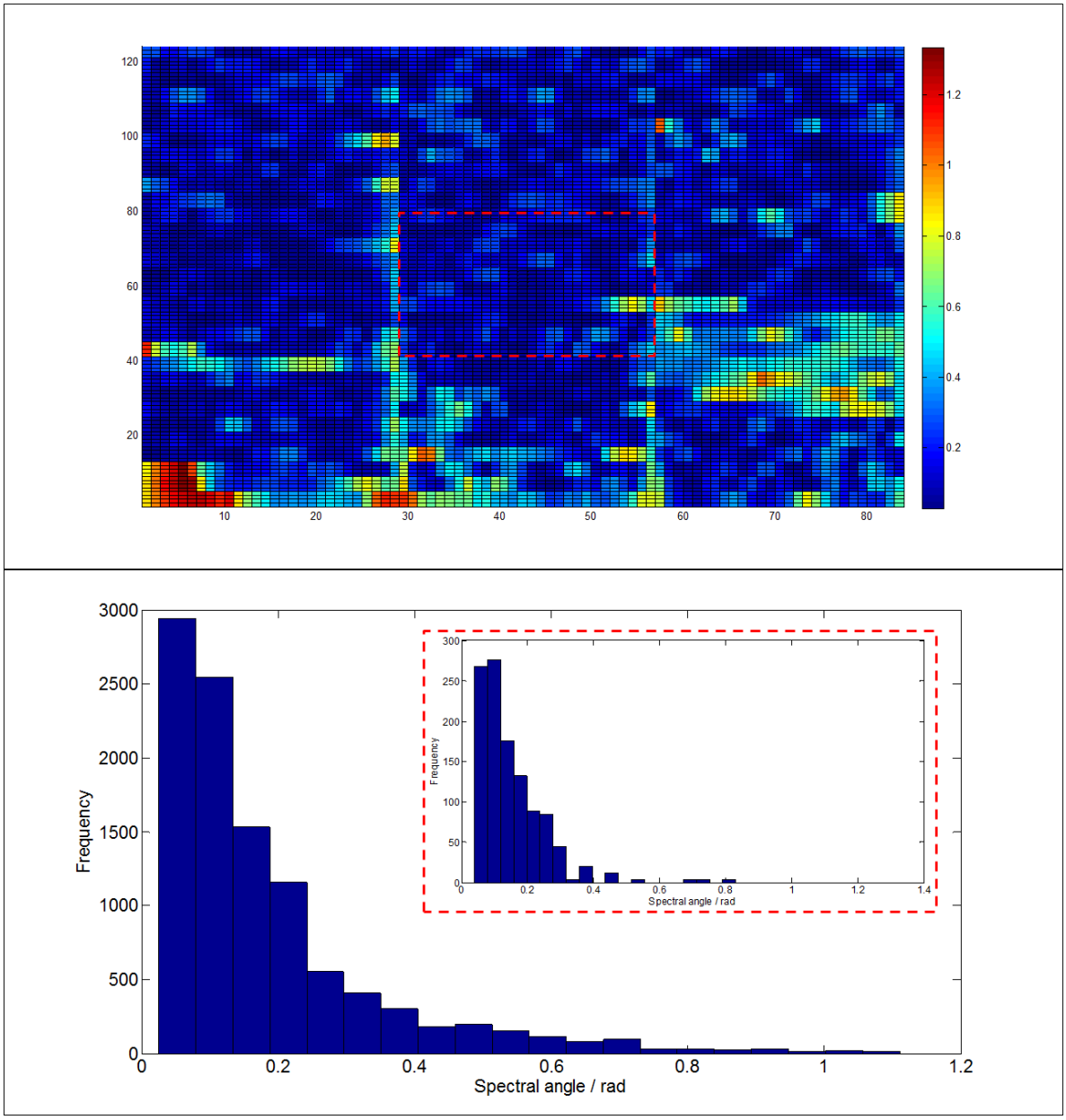

Figure 6.8: The map on the top shows the spectral angle between each spatial pixel in part of the microslice spectrometer field of view and the mean ASD spectrometer spectrum for a grass target. The histogram on the bottom shows the frequency of spectral angles within this FoV. The red dotted line in the surface plot shows the sub-area that was used to generate the results in Figure 6.7, and the histogram in the red dotted line shows the frequency of spectral angles within this sub-area.

In order to provide a more accurate measure of classification and hetrogeneity of the microslice spectrometer images, it would be useful to be able to ignore the atrifacts seen in th image. This would involve disregarding the spectra from pixels included as a result of spectral box mis-alignment, and pixels with clear mis-calibrations. It is possible to recalibrate the mis-calibrated pixels, but this is not be completely accurate, and for such large mis-calibrations a lot of the spectrum is lost. It would

therefore be prudent in the long term to address this issue at source in a second generation instument.

The appropriate pixels were disregarded using thresholding. It can be seen from Figure 6.8 that the majority of pixels have an angle lower than 0.1 radians, but there are some with much higher angles. These high angles can be put down to poor spectral box positioning, resulting in poor spectral calibration, or inhomogeneous areas within the FoV. Thresholding was used to create a map of the pixels in the grass target area that have a spectral angle of greater that 0.1 radians with the ASD spectrum, see Figure 6.9. This gives an indication of the areas of the FoV that potentially have poor spectral box positioning.

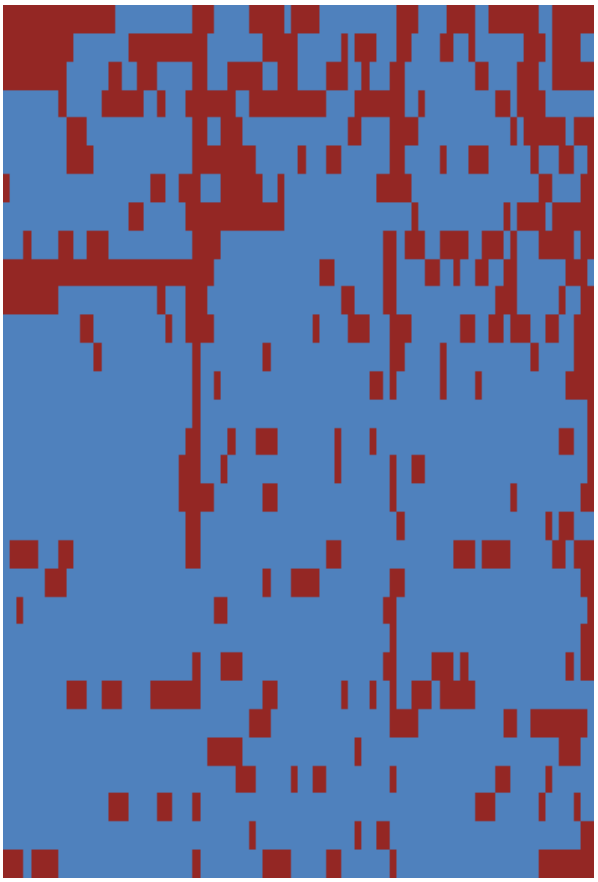

Figure 6.9: This image gives a different representation of the similarity map shown in Figure 6.8. This is a thresholded map of the pixels in the grass image taken by the microslice spectrometer. Those spectra with an angle less than 0.1 radians away from the ASD spectrum are shown in blue, with other pixels shown in red.

A spectral angle mapper (SAM) classification was applied using the *SAM_classification* MATLAB module (detailed in Section 6.2.2.2) to test the ability of the instrument to distinguish between spectra of different targets. The classification maps produced for the grass and mud targets are displayed in Figure 6.10. These maps show the results of classification with four different categories: grass, other vegetation, non-vegetation, and unclassified. Variations across the microslice spectrometer FoV can largely be put down to the inhomogeneity of the target area, or inaccurate datacube reconstruction.

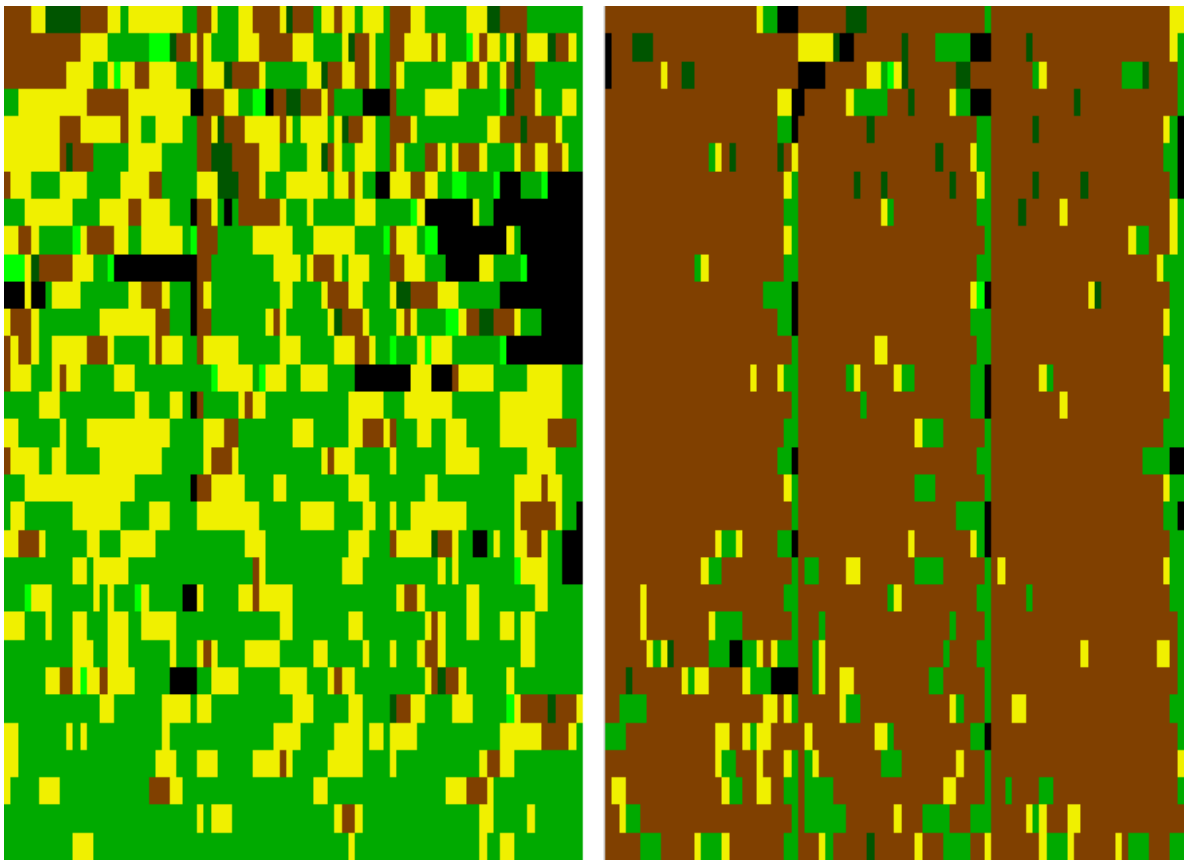

Figure 6.10: This image shows two maps of classifications of the grass target image (left) and the mud target image (right) taken by the microslice spectrometer near the River Arrow. A spectral angle mapper (SAM) classification was used with ASD spectrometer spectra of 10 different targets being used as the reference spectra. The colours in the map indicates how each pixel has been classified. Green indicates grass; yellow indicates other vegetation; brown indicates a non-vegetation target, and black indicates un-classified pixels.

For a more quantitative comparison, the percentage of correctly classified and incorrectly classified pixels within a 2604 pixel area in each target image were calculated. Initially the pixels were determined to be classified correctly if they were correctly determined to be vegetation, or non-vegetation. For the grass image the classification accuracy is 96.4%, with a false-positive recognition of 4.6%. Setting a classification threshold reduces the false-positive rate, but also decreases the classification accuracy. Classifications were performed using different threshold values to investigate how this affected the false-positive rate and accuracy. The results obtained for all target areas are shown in Table 6.1.

This classification test is similar to the experiment conducted in Section 3.2 on remote sensing data from the Eagle spectrometer. As with the Eagle results, it can be seen from Table 6.1 that as the threshold is decreased, the percentage of unclassified pixels increases, while the the accuracy and false-positive rate deceases. Adjusting the threshold also provides a trade-off in quality of results. A high threshold can be picked if one is mostly interested in correctly identifying the maximum number of pixels, while a low threshold can be picked if one is mostly interested in reducing the number of

Threshold:		**1.0**			**0.5**			**0.4**			**0.3**			**0.2**			**0.1**	
Target	**A**	**F-P**	**U**	**A**	**F-P**	**U**	**A**	**F-P**	**U**	**A**	**F-P**	**U**	**A**	**F-P**	**U**	**A**	**F-P**	**U**
Grass	96.0	3.6	0.4	92.4	2.2	5.4	90.0	2.0	8.0	86.5	1.8	11.7	74.6	1.0	24.4	37.2	0.3	62.5
Lush Grass	81.6	17.7	0.7	68.0	10.0	22.0	61.5	9.1	29.4	51.1	7.8	41.1	35.7	3.6	60.7	12.4	0.5	87.1
Dead Grass	58.1	41.3	0.6	47.9	36.6	15.5	44.6	35.1	20.3	39.6	32.9	27.5	29.2	24.1	46.7	9.7	7.9	82.4
Nettles	88.7	11.0	0.3	80.4	7.8	11.8	74.9	6.8	18.3	64.6	5.6	29.8	51.1	2.3	46.6	19.7	0.4	79.9
Thistles	78.7	20.5	0.8	64.9	14.0	21.1	59.7	12.8	27.5	51.9	11.2	36.9	38.2	6.6	55.2	12.3	1.0	86.7
River Plants	95.4	4.5	0.1	93.6	4.3	2.1	91.5	4.2	4.3	86.9	3.9	9.2	72.7	2.6	23.7	20.6	0.7	78.7
silt	44.9	55.0	0.1	44.2	53.1	2.7	43.8	52.1	5.0	43.3	48.5	8.2	31.0	2.1	37.9	9.0	1.9	89.1
Pebbles	34.1	64.3	1.6	32.8	55.9	11.3	32.3	51.7	16.0	31.2	46.4	22.4	22.9	31.6	45.5	6.9	1.3	91.8
Dry Soil	58.8	21.2	0.0	58.2	37.9	3.9	58.0	36.6	5.4	57.6	34.5	7.9	47.6	22.2	30.2	17.0	1.9	81.1
Mud	32.6	67.4	0.0	32.6	66.2	1.2	32.5	65.2	2.3	32.4	62.8	4.8	21.7	41.1	37.2	3.5	0.7	95.8

Table 6.1: This table show how the results of a spectral angle mapper (SAM) classification vary with the threshold value used for 10 different target types imaged using the microslice spectrometer around the River Arrow. Spectra taken using an ASD spectrometer were used as the reference spectra. '**A**' refers to the percentage of 2604 pixels that are correctly classified, '$\mathbf{F-P}$' refers to the percentage of the pixels that are incorrectly classified, and '**U**' refers to the percentage of the pixels that are left unclassified.

incorrect classifications. This trade-off is represented by plotting the results of the classification of the grass target in Figure 6.11.

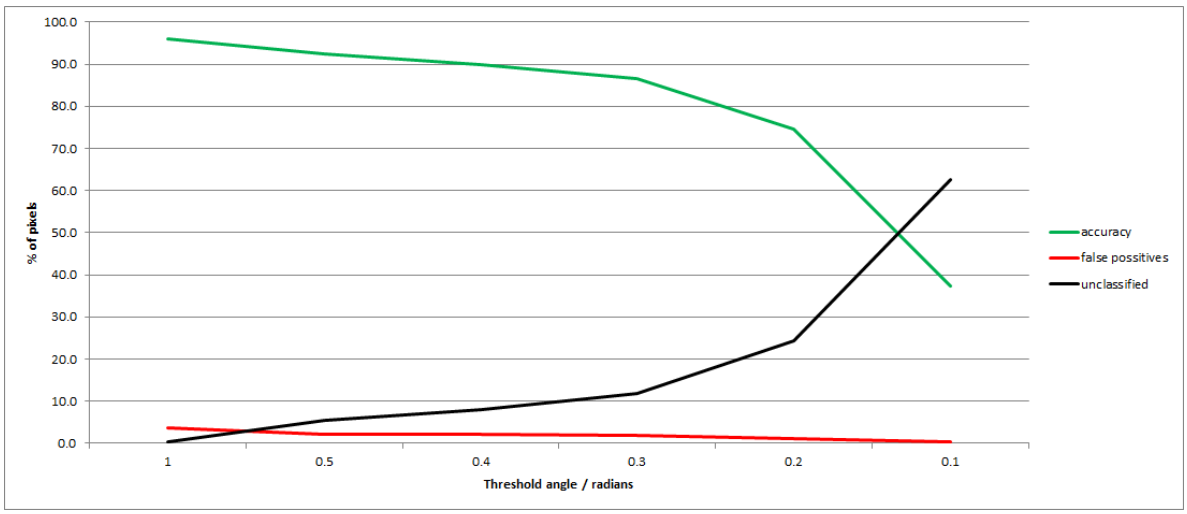

Figure 6.11: This graph show the trade-off effect on the quality of ground type classification produced by varying the threshold of a spectral angle mapper (SAM) classification. This data is taken from a grass target imaged with the microslice spectrometer, using spectra captured with an ASD spectrometer as reference spectra.

The most appropriate threshold to use is highly dependent on the purpose of the classification. One way to determine an objectively optimum threshold, is to redefine the 'accuracy' as the percentage of classified pixels that are correctly classified (i.e. ignore all unclassified pixels). This new definition give a measure of quality of the classification as single a percentage accuracy for each threshold. Figure 6.12 plots this accuracy to show how it varies with threshold. It can be seen that, in general, the accuracy increases as the threshold deceases. This is not surprising, as pixels classified incorrectly are more likely to have larger angles than those classified correctly. As the threshold decreases, however, fewer pixels are classified, so this creates a trade-off between classification accuracy, and number of pixels classified.

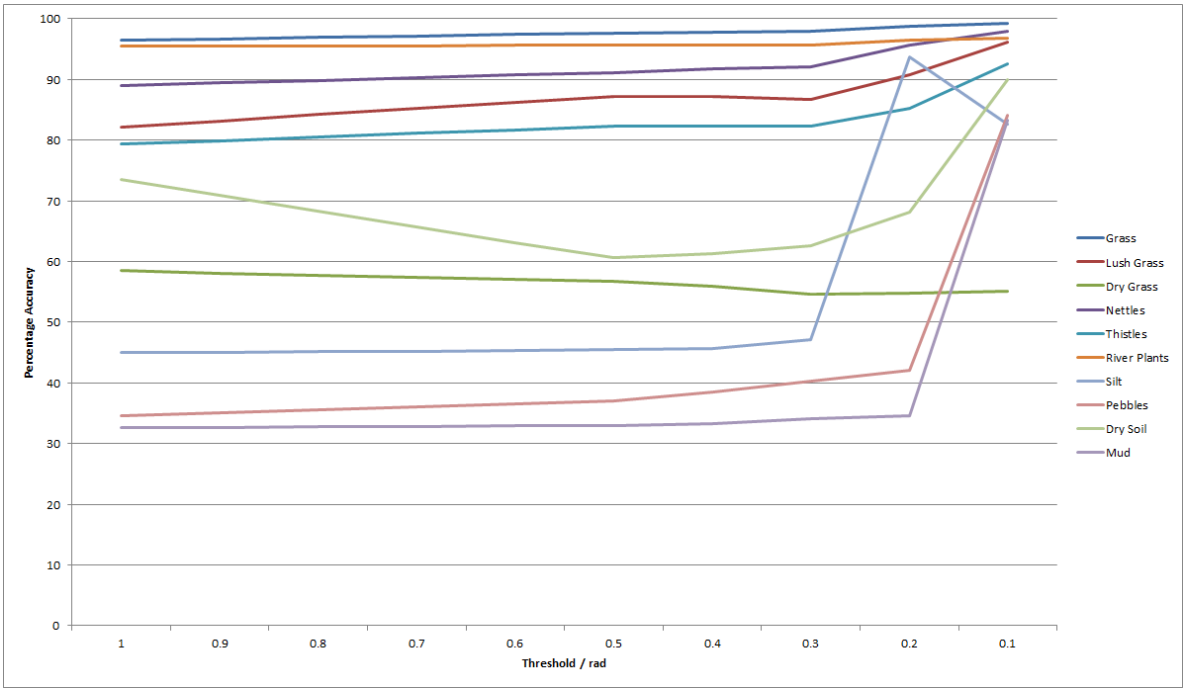

Figure 6.12: This graph plots the accuracy of spectral angle mapper (SAM) classification of images of different target types captured with the microslice spectrometer around the River Arrow. Spectra captured with an ASD spectrometer were used as reference spectra. For the purposes of this graph, the accuracy is defined as the percentage of classified pixels that are classified correctly (i.e. unclassified pixels are ignored).

One problem with this classification test is that, for some targets, the ASD spectrum is very different from the microslice spectrum, especially for the non-vegetation targets (see Figure 6.7). This leads to many non-vegetation targets being incorrectly classified. This issue could be averted by having different threshold values for different targets. If the threshold values are chosen as a multiple of the angles between the microslice and ASD spectrometer spectra, then the the effect of the difference in size of these angle should be negated. This is equivalent to normalising each spectral angle by the angle between the microslice and corresponding ASD spectrometer reference spectrum.

6.2.4 Discussions

The field experiment around the River Arrow, and subsequent classification tests provided useful information about the performance of the microslice spectrometer in a field environment. The results also highlighted some improvements that could be made to the data processing software, which were not as critical for the lab tests; for example, there are artificial spectral features at the edges of the slices due to offsets in the spectral box positioning along the slice, as well as missing bands in some slices due to offsets in the spectral box positioning across the slice. This experiment has also shown that the microslice spectrometer can be used to classify different ground types to reasonable degree of accuracy (96 % for grass).

The use of a spectral imaging instrument with a 2-dimensional FoV showed how the data that is

gathered from a point based imaging system (such as the ASD spectrometer) gives limited information, with the results from the microslice spectrometer highlighting the non-homogeneity of the spectral reflectance over a relatively small area of a specific target. The visble artifacts in the microslice spectrometer images are providing a significant hinderance to accurate classification and homogeneity assesment of the images. This needs to be addressed in the spectral box alignment software, and the alignment of the camera in a second generation instument. This is unlikely to completely irradicate all of the issues, and so post-processing re-callibaration and thresholding may still be required.

Using the microslice spectrometer for remote sensing applications, would require the assessment of several more performance capabilities. These are capabilities related to using the instrument on an airborne platform, specifically: the ability of the microslice to deal with vibrations from being mounted on an aircraft, and the ability to mosaic image captures taken using the step-and-stare scanning technique (see Figure 1.4). These issues are not dealt with in this thesis however, as they would require a test flight opportunity for full verification.

6.3 Detecting River Pollutants Using Spectral Imaging

6.3.1 Background

6.3.1.1 Pollution in the River Ganges

Water quality monitoring is one of the major applications of hyperspectral remote sensing, as was shown in Chapter 2. River pollution is a major challenge in India, particularly in the Ganges basin with 400 million inhabitants along its banks. The Ganges is used by leather tanneries, which produce large quantities of pollutants [127], and supports a heavy agriculture base which can be severely harmed by river pollution. Researchers from Kanpur Indian Institute of Technology (IITK) and Durham University collaborated to look at the potential for using hyperspectral remote sensing to detect the levels of pollutants in the River Ganges.

A previous study in 1996/7 investigated pollution upstream and downstream of the tanneries [128]. Almost all river parameters associated with pollution, such as Biochemical Oxygen Demand (BOD), Chemical Oxygen Demand (COD), and Chlorine (Cl) and Chromium (Cr) levels were found to have increased after the tanneries. High levels of heavy metal concentrations may influence plant growth in a negative way and, if these heavy metals end up in agricultural crops or in grazing lands, they pose a serious health threat, as they are toxic to humans and animals [129].

In-situ monitoring of the river water quality by taking samples does not give a complete picture of the pollution levels, as the water quality can vary significantly over a relatively small spatial area. In addition to this, in-situ monitoring is time consuming and expensive. Remote sensing technology has the capability to analyse river change over entire catchments [130, 131], and could be used to image the entire Ganges basin on a daily basis. If remote sensing data can accurately determine river

water quality, then a complete map of river pollution can be obtained, with a much higher temporal resolution than can realistically be achieved through ground measurements. Also, once deployment costs are incurred, then the expense and man hours required for collecting remote sensing data are minimal.

Continuous assessment of river characteristics is also useful for other applications, and as a result there is an increasing demand for remote sensing technology to improve the mapping of rivers and enable a more holistic analysis of the river system [132]. Using remote sensing to monitor pollution therefore also has the benefit that the data gathered could be of potential use in many other research areas.

Many chemical pollutants have their own unique spectral signature. If these spectral signatures can be detected from the reflectance of water that they are dissolved in, then remote sensing spectroscopy can be used, in theory, to detect river pollutants.

6.3.1.2 Detecting River Pollutants Using Satellite Imaging

In order to detect river pollutants using remote spectral imaging, there are two main requirements of the imaging spectrometer used. Firstly it must be able to spatially resolve the width of the river (smaller spatial resolution elements could be useful, but are not essential), and secondly it must be able to spectrally resolve the reflectance features of the pollutants. The width of the River Ganges varies from being about about 2 km in places to just 30m, both of which can be resolved by the majority of hyperspectral remote sensing instruments. Without knowing the exact spectral features that are to be detected, however, it cannot be determined which satellite based hyperspectral imagers are most suitable. The key specifications of some of the latest hyperspectral remote sensing instruments are shown in Table 6.2.

	Hyperion [28]	HYSI [30]	CHRIS [29]	Microslice
Spectral Range	400-2500 nm	400-950 nm	200-1050 nm	475-650 nm
Spectral Resolution	10 nm	15 nm	1.3-12 nm	7 nm
Spatial Resolution	30 m	80 m	17-20 m	1 km
Dwell Time	4.4 ms	11 ms	15 ms	5 s
IFoV	7.5 x 0.03 km	20 x 0.08 km	15 x 0.02 km	37 x 185 km
Altitude	705 km	N/A	670 km	670 km*
SNR (approximate)	50	100	100	$\sim 10^5$

Table 6.2: This table shows the key specifications of potential hyperspectral imaging instruments for detecting pollutants in the River Ganges. *The specifications of the microslice spectrometer are presented for the current instrument imaging at an altitude of 670 km (equal to that of CHRIS). This creates a set of fiducial specifications for the microslice; more realistic remote sensing specifications are presented in Chapter 7, which also shows the calculations used to estimate the SNR.

Hyperspectral instruments that have previously been used to monitor water quality remotely include AISA (monitoring lake water [47]) and Hyperion (monitoring coastal water [46]). There has been

very little use of hyperspectral instruments monitoring river water however. Table 6.2 shows that the spatial resolution of the microslice spectrometer will need to be improved (ideally by about a factor of about 100) if it is to monitor the River Ganges from a satellite. This can be achieved at the expense of the angular instantaneous field of view (IFoV) by alterations to the foreoptics design. The IFoV would still be significantly higher than that of the other instruments, allowing for a longer dwell time, and hence achieving a higher SNR. An alternative to lowering the angular IFoV of the microslice, would be to image from an aircraft, thus significantly reducing the imaging altitude (to around 1 km). The absolute IFoV would be reduced to about 50 x 260 m, causing the the spatial resolution to be reduced to about 2 m.

6.3.2 Field Spectroscopy on the River Ganges

6.3.2.1 Method

Fieldwork was carried along the path of the river Ganges with three main aims:

1. To determine what pollutants were present in the river, and in what concentrations.

2. To determine how these pollutant effect the spectral reflectance of the river.

3. To determine if these variations in spectral reflectance could be detected by a spaceborne remote sensing spectrometer.

The fieldwork was conducted in October 2013 at two different locations on the River Ganges in collaboration with IITK. Six test sites were analysed at the two different locations (see Figure 6.13). Location A was around the Haridwar area, which is upstream of the vast majority of urban areas. This means that a relatively low pollution level was expected. Two of the six test sites were in location A; one downstream of Haridwar (A1), and one upstream of Haridwar (A2).

Figure 6.13: This map shows the positions of two locations chosen for field testing (A and B) relative to the path of the Ganges through the Indian subcontinent. The map is edited from [133].

Location B was in the Kanpur area, which is downstream of many urban areas, so significantly higher levels of pollution were expected than in location A. Kanpur is home to a large tannery, which releases a lot of waste into the river. It is also just downstream from some major confluences; in particular the meeting of the Ganges and the Ramganga. Four of the six total test sites were in location B. Test site B1 was just downstream of Kanpur, site B2 was just upstream of Kanpur, site B3 was downstream of the confluence, and site B4 was upstream of the confluence. The higher the site number the higher further upstream the site was, as shown in Figure 6.14.

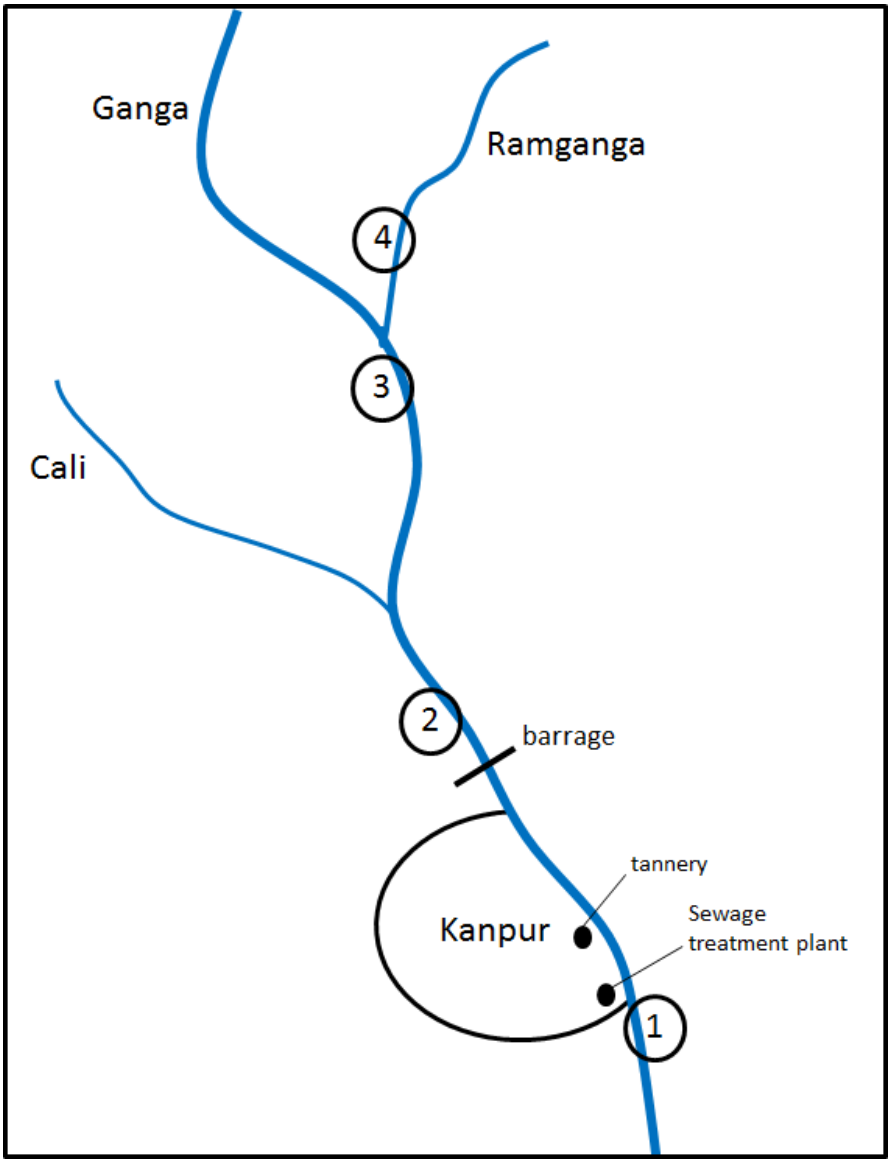

Figure 6.14: This map shows the four sites in field test Location B at which measurements were taken to determine the pollution level of the water. At each site, water samples were collected and spectral measurements of the water's reflectance were taken with a GER spectrometer. This map is not to scale.

At sites B1 and B3 analysis was done on both sides of the river, to see if there is any variation across the width of the river. This was specifically done at these sites as they were located just after where potential sources of pollution joined the river (the sewage treatment plant and tannery for site B1, and the Ramganga river for site B3), and since the flow could carry that pollution to one particular side of the river, it was ensured that the pollution was not missed.

At each site, two types of measurements were taken to satisfy aims 1 and 2 of the fieldwork. The first involved taking two samples of river water in bottles for analysis. One was to test for nitrogen and phosphorus, while the other was to test for heavy metals (chromium, cadmium, and lead). When there

were enough bottles available, backup samples were also taken. $H_2SO_4$and NHO_3 were added to the samples testing for the inorganic materials and metals respectively. These chemicals reduced the pH of the samples to below 2 so that they would be preserved for testing. The bottles were also packed with ice to help with preservation. Experimental protocol.....

The second type of measurements taken were spectral measurements. The initial aim of the fieldwork was to take these spectral measurements with an ASD field spectrometer (as used in the lab and field testing). It was also planned to carry out remote sensing spectral imaging at site B1 by using the microslice spectrometer mounted on a helicopter. In the event neither the ASD spectrometer nor the microslice spectrometer could be used, as they were not allowed through customs in India. A GER field spectrometer was used in place of the ASD spectrometer, which is a very similar type of instrument, but was much older and had not undergone any recent testing or calibration.

The GER spectrometer was used to take point based reflectance spectra from a distance of about 30 cm from the surface of the water. Multiple reflectance spectra were taken at each site for different depths of water. Spectra of the river bank were also taken, as an indication of the potential reflectance of the river bed, so they could potentially be used in distinguishing the water reflectance from the bed reflectance in river measurements. A white reference measurement was taken before each target measurement by imaging a spectralon panel. This allows a relative reflectance to be calculated for each target, hence negating variations in illumination.

Figure 6.15: This figure shows photographs of the Ganges river bank at all six locations at which water pollution measurements were taken. The river bank is an important indicator of what the river bed might be like, which helps interpret spectral reflectance of the river. It can be seen from the images that the river bank varies a lot along the river. The 'left' and 'right' labels refer to the left and right hand sides of the river when facing downstream.

6.3.2.2 Results and Discussions

The water samples gathered from the River Ganges were analysed at IITK. The levels of five chemical elements were measured, as indications of the levels of pollution in the river water. These elements

were nitrogen, phosphorus, chromium, cadmium, and lead. The results in Figure 6.16 show that the concentration of each pollutant element detected varies significantly throughout the course of the river. It can be seen that there are generally lower levels of pollutants in location A than location B. Aside from this loose correlation there are no clear conclusions that can be drawn from these results, which highlights the fact that the high spatial coverage that remote sensing data could provide would give a much clearer picture of how the levels of different pollutants vary along the river.

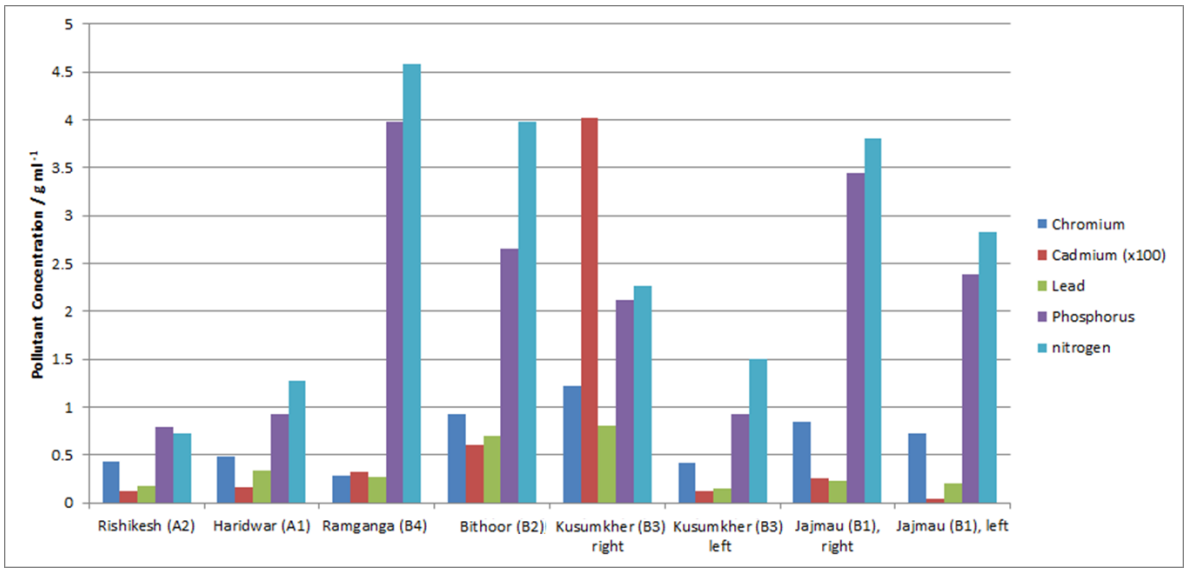

Figure 6.16: This bar chart show the concentrations of five different elements responsible for water pollution, in six different sites over two different locations along the River Ganges. The sites on the horizontal axis range from upstream (on the left) to down stream (on the right). The data were produced from water samples that were analysed by colleagues at IITK. At some sites samples were taken from both sides of the river ('right' and 'left' refer to the right hand side and left had side of the river when looking downstream). Note that the cadmium levels are multiplied by 100 for comparison.

The spectra from the GER spectrometer were processed at Durham University after the completion of the fieldwork, but appeared to give very inconsistent results. As the GER spectrometer was known to be an out-of-date instrument that had not been recently tested, and the ASD spectrometer was a relatively new well calibrated instrument, a subsequent test comparing the two spectrometers was conducted. This revealed that no useful spectral data had been gathered using the GER, meaning that no progress had been made towards satisfying fieldwork aim 2. In order to compensate for this, laboratory tests were designed, with the aim of imaging water containing the pollutant chemicals using the ASD spectrometer and the microslice spectrometer.

6.4 Laboratory Tests of Water Pollutants

Since the spectral data gathered from the fieldwork conducted on the Ganges were found to be of no use, it was decided to perform laboratory experiments on artificially created polluted water samples. An experiment was set up to determine how the spectral reflectance of water is affected by the presence

of certain chemicals containing the five elements recorded in Figure 6.16.

6.4.1 Method

The lab experiment that was conducted, involved using the ASD spectrometer and the microslice instrument to image water samples containing varying concentrations of six different chemicals. The six chemicals used were $Cr_2(SO_4)_3$, K_2CrO_4, $K_2Cr_2O_7$, Pb, NH_4, and P. These chemicals were chosen as they are potentially responsible for the levels of concentration of the elements in Figure 6.16. Each of the chemicals were mixed with untested tap water into separate 3 litre solutions and were imaged in a clear plastic bucket with a water depth of about 20 cm. Each sample was imaged with and without the presence of 37.5 g of sand mixed into the solution (~ 0.5 mm grain size), which was included to simulate turbidity. The concentrations of the chemicals used are displayed in Table 6.3. The spectral signature of the unaltered tap water was also imaged for comparison.

Compound	Pollutant element	Concentrations of element / $mg\,l^{-1}$			
$Cr_2(SO_4)_3$	***Cr***	8.8			
K_2CrO_4	***Cr***	0.89	4.5	8.9	45
$K_2Cr_2O_7$	***Cr***	1.2	9.0	12	90
Pb	***Pb***	33			
NH_4	***N***	26	130	260	1300
P	***P***	33			

Table 6.3: This table lists the concentrations of pollutant elements used to create solutions for spectral imaging. Each concentration of each chemical was created as a separate 3 litre sample, and imaged with the microslice imager and the ASD spectrometer. The solutions for each concentration of each compound were prepared independently (i.e. there were no mixtures of chemicals).

6.4.2 Results

Figure 6.17 displays the reflectance spectra of the highest concentrations of each of the six chemical solutions as measured by the ASD spectrometer. The magnitude of reflectance varies due to variations in illumination, but variations in the spectral shape of the reflectance spectra, reveal the effects of the chemicals present.

The graph shows that when some of the chemicals are dissolved in the water they cause clear changes to the spectral shape of the water reflectance. The K_2CrO_4 and $K_2Cr_2O_7$ solutions reflectance spectra differ from that of untested tap water in that they both give almost zero reflectance in the blue spectral region, up to around 460 and 490 nm respectively. The $Cr_2(SO_4)_3$ solution differs from the tap water reflectance by showing a peak at about 500 nm, where the water spectrum is much flatter.

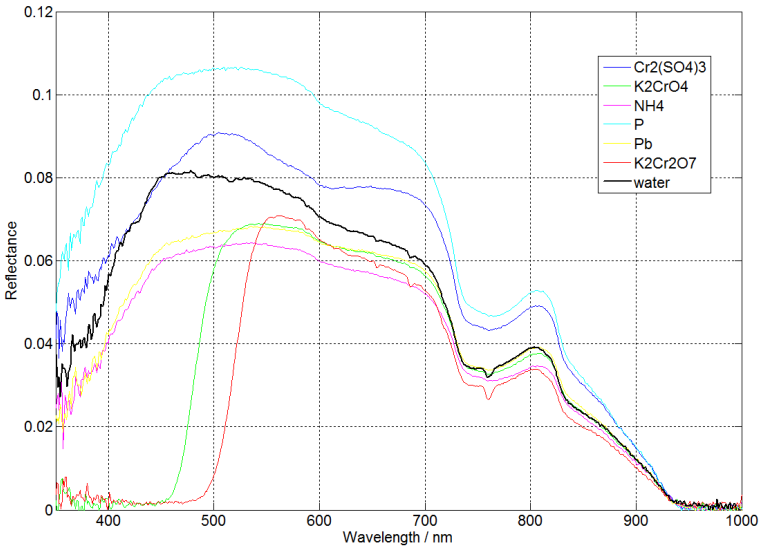

Figure 6.17: This graph shows the reflectance spectra of the highest concentrations produced for imaging of six different chemical solutions, as measured by an ASD spectrometer. The reflectance of pure water is also included for reference.

The other chemicals (Pb, NH_4, P) do not appear to affect the reflectance of the water significantly. This could be because these chemicals do not have any spectral features in the visible wavelength range, or because the concentrations are too small to have a noticeable difference. The maximum concentrations of Pb, N (in NH_4) and P used in this experiment were 33, 1300, and 33 $mg\,l^{-1}$ respectively, which are of the order of 100, 1000, and 20 higher than the concentrations found in the River Ganges respectively (see Figure 6.16). This suggests that river pollution in the Ganges due to lead, nitrogen or phosphorus is undetectable using spectral imaging.

The maximum concentrations of K_2CrO_4, $K_2Cr_2O_7$, and $Cr_2\,(SO_4)_3$ imaged were 45, 90, and 8.8 $mg\,l^{-1}$ of Chromium, which are of the order of 50 times higher than the concentrations found in the Ganges (see Figure 6.16). The lowest concentrations of chromium in K_2CrO_4 and $K_2Cr_2O_7$ imaged were 0.89 and 1.2 $mg\,l^{-1}$respectively. These are comparable concentrations to those found in the Ganges (see Figure 6.16). The spectral reflectance graphs of these concentrations are plotted in Figure 6.18. The other chromium compound ($Cr_2\,(SO_4)_3$) was not measured at a lower concentration, so it is not clear whether the spectral variations that it causes would be detectable at river concentration levels.

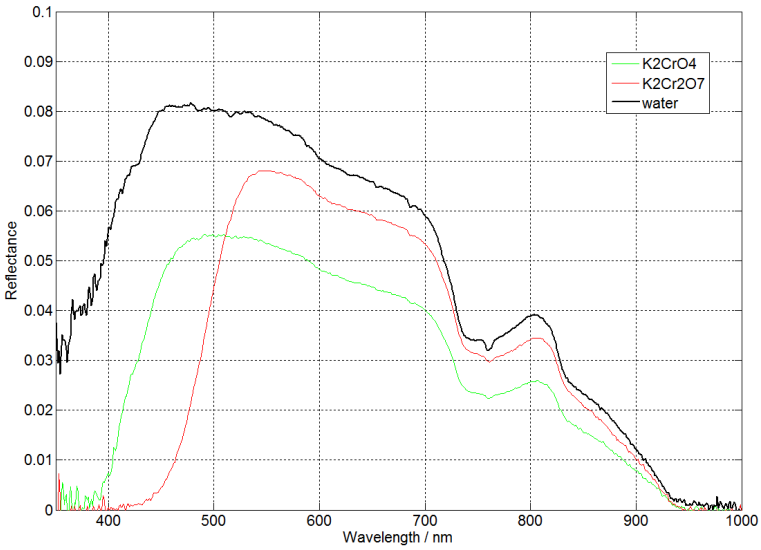

Figure 6.18: This graph shows the reflectance spectra of two chromium compound solutions as measured by the ASD spectrometer. The concentrations of chromium used to create these solutions were similar to the concentrations of chromium found in the River Ganges. The reflectance of pure water is also included for reference.

It can be seen from Figure 6.18 that, at similar concentrations to those found in the River Ganges, two chromium compounds (K_2CrO_4 and $K_2Cr_2O_7$) display practically zero reflectance at short wavelengths. The position where reflectance increases, however, has moved to shorter wavelengths (410 and 425 nm respectively) than for higher concentrations of the compounds. These results suggest that water pollution by Chromium can be detected with hyperspectral imaging in the visible wavelength range, if the chromium is in the form of K_2CrO_4 or $K_2Cr_2O_7$.

The microslice spectrometer was also used to image each water sample. The median microslice spectrum over the surface area of the water was calculated for each sample. Figure 6.19 provides a comparison between the spectra obtained with the microslice and ASD spectrometers when imaging K_2CrO_4 and $K_2Cr_2O_7$. This comparison shows that the microslice spectrometer is clearly able to detect the absorption feature of $K_2Cr_2O_7$, and can also detect the shoulder of the K_2CrO_4 absorption feature.

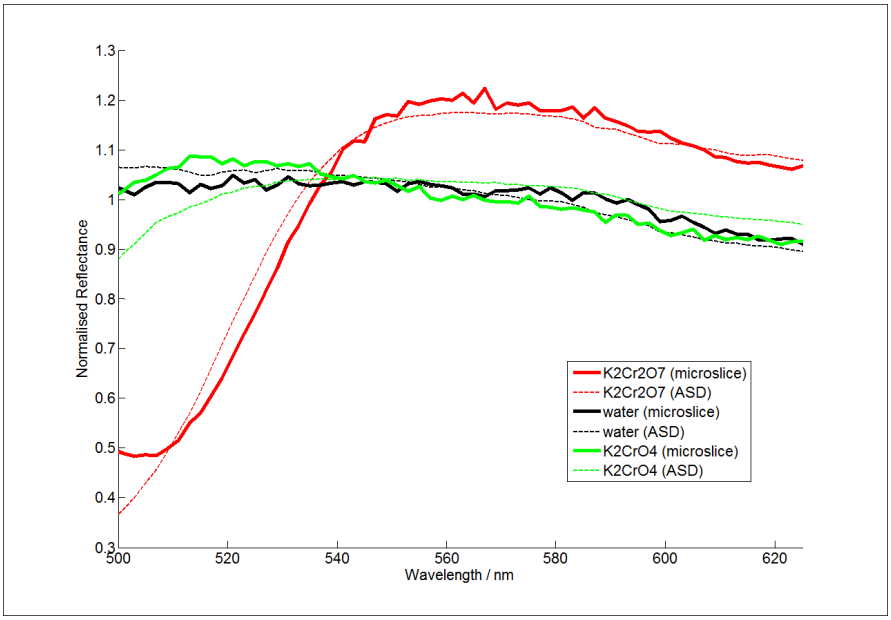

Figure 6.19: This graph compares the reflectance spectra of two chromium compound solutions when measured by the ASD spectrometer and the microslice spectrometer. Each spectrum has been normalised to give a mean value of 1. The concentrations of chromium used to create these solutions were similar to the concentrations of chromium found in the River Ganges.

This experiment has shown some water pollutants can be detected from their spectral signature using a field spectrometer. It has also shown that the prototype microslice spectrometer is capable of detecting K_2CrO_4 and $K_2Cr_2O_7$, when dissolved in water at comparable concentrations of chromium to those found in the River Ganges.

When assesing the ability of the microslice spectrometer to detect pollutants in different rivers, or under differnet conditions it is important to determine the concentration and noise limits of detection of these compounds. The concentration limit would be most accurately determined by repeating the above experiment with many different concentrations of each compound to see how this affects the accuracy of being able to distinguish the reflectance spectrum from that unpolluted water.

The noise detection limit can be determined by applying various levels of artificial noise to the reflectance spectra of both the polluted water and the tap water. This will allow the noise level at which the two sample can no longer be distinguished to be distingushed. A detection metric, ν, is defined in Equation X, where .....x is a parameter defined such that for un-polluted at the given noise level water a>=1 for all spectra.

$$\nu = p550 - p500 \tag{6.1}$$

Successful detection can occur at this level of noise if all spectra for $K_2Cr_2O_7$ polluted water give a value of a<1. Figure V shows the maxium value of a for different noise levels for $K_2Cr_2O_7$ polluted

water.

Figure 6.20: This graph shows the noise detection limit of $K_2Cr_2O_7$ using the microslice spectometer. Whene the detection metric, a, reaches 1 then the polluted and non-polluted sollutions cannot be distinguished at that noise level. Here it can be seen that the noise detection limit is ...

The noise detection limit could also be assesed in parallel with the concentration detection limit.

6.4.3 Discussions

This experiment has shown that the some pollutants in water (K_2CrO_4 or $K_2Cr_2O_7$) can be convincingly detected with hyperspectral measurements. The spectral range that the distinguishing spectral features occur in is 400-600 nm (depending on the concentrations). Above 600 nm the spectral shapes of all the dissolved pollutants are very similar to that of the pure water (see Figure 6.17). There is no particularly tight requirement on the spectral resolution of the instrument, as the spectral features are of the order of 50 nm wide.

These results could lead to further experiments to determine if it is possible to detect these pollutant in the field. When extending this experiment to field tests there are many extra factors that would affect the instrument capabilities. For example, only some of the chromium in the river may be in the form of K_2CrO_4 or $K_2Cr_2O_7$, meaning that lower concentrations of the substances would need to be detected. Also, in actual river samples, there are many different chemicals present, each with a different spectral signature. The spectral data gathered will therefore require spectral unmixing (see Section 3.1.6). This means that it is important that the spectral signatures of the other major chemicals present in the water are known (see Section 3.1.4). There is also the factor of differing illumination conditions that are experienced in the field but not the laboratory. It was shown in Section 6.2, however, that the prototype microslice spectrometer is able to cope better with outdoor illumination conditions than many conventional instruments.

6.5 Summary of Field Testing

This chapter has demonstrated the field performance of the prototype microslice spectrometer from a ground based platform. It was shown that vegetation spectra imaged by the spectrometer matched those taken using an ASD field spectrometer to within 0.13 rad, when compared using spectral angles. Classification using the spectral angle mapper technique gave classification accuracies of 96% when classifying grass targets.

The potential of microslice spectrometer for detecting pollutants in river water was also assessed. Physical ground truth data was used in conjunction with laboratory tests to find that K_2CrO_4 and

$K_2Cr_2O_7$ could be detected using the prototype microslice spectrometer when dissolved in water at the same concentrations as may be found in the River Ganges.

After successful ground based field testing, the next step is to relate the results to the potential performance from a spaceborne platform. This could be done with the help of atmospheric modelling, which is discussed in the next chapter. modelling helps assess the potential remote sensing performance of an instrument, without the expense and time required for a re-design and satellite deployment. The key to determining the potential of microslice technology for detecting river pollutants, lies in determining whether the fiducial specifications set out in Table 6.2 can be adjusted to give appropriate spatial resolution, spectral resolution, and SNR. This is explored in the next two chapters.

Chapter 7

Modelling the Performance of aRemote Sensing Microslice Hyperspectral Imager

Before attempting to develop a fully operational microslice remote sensing system, it is imperative that as much data as possible is gathered to determine the expected performance of the instrument as a remote sensing spectrometer. This thesis has so far tested the spectral and spatial capabilities of a prototype microslice instrument in the lab and in the field. Another key part of the development and assessment of any remote sensing hyperspectral imager is modelling its performance from an airborne platform. There are many factors that would affect the performance of such an instrument when using it for aerial imaging that are not present in ground based testing, in particular the effects of the Earth's atmosphere on the detected light. There are also many technological, administrative, and funding issues associated with deploying an imaging instrument on an airborne platform. A way to assess the aerial performance of an instrument without having to deal with these issues is to use atmospheric modelling.

The interference of the atmosphere on reflected light can have a significant impact on the signal strength, and hence the signal to noise ratio (SNR), received by a remote sensing instrument. The SNR is an important aspect of the performance of a hyperspectral remote sensing instrument, as a high SNR allows spectral features to be more easily identified, and can improve the accuracy of classification algorithms. It was shown in Chapter 2 that many remote sensing applications require a certain level of SNR to be successful (see Table 2.1). An instrument that can image with a high SNR is therefore more suited to such applications, particularly when imaging in poor light conditions.

One of the main features of the microslice spectrometer is that it is expected to be able to achieve a higher SNR than other remote sensing spectrometers. This chapter uses atmospheric modelling to investigate the potential SNR that is achievable for the spectrometer imaging from a low Earth orbit

(LEO) satellite, and compares it to results from the same model applied to the CHRIS spectrometer (which images using a relatively conventional pushbroom scanning method from an LEO satellite) [29]. The CHRIS instrument is used for comparison, as it is also a proof-of-concept instrument that utilises some of the latest technologies. Typically a remote sensing spectromeret will initially be tested as an airborne system, so since CHRIS is a spacebourne instrument, the performance of the microslice system is also modelled from an airborne platform towards the end of this Chapter. The modeled SNR for both instruments are compared for different atmospheric parameters and conditions to determine under what circumstances, and for what purposes the microslice spectrometer would provide more useful data than a conventional hyperspectral instrument.

7.1 modelling the SNR of a Remote Sensing Spectrometer

For a complete understanding of the achievable SNR of a remote sensing instrument, it is important to model results under a range of different conditions (solar illumination, atmospheric conditions, etc.). When modelling the SNR of an airborne or satellite based remote sensing spectrometer, there are five factors to be considered:

1. The amount of solar radiance.
2. The effects of atmospheric interference on the light.
3. The reflectance properties of the target.
4. The response of the instrument.
5. The level of noise.

Factors 1-3 are used to determine the total amount of radiance at the entrance to the instrument (the *at-sensor radiance*), and are independent of the instrument used. Factor 4 defines the amount of signal detected by the instrument per spatial element, per integration time, per at-sensor radiance, and is a product of the instrument design. Factor 5 gives the amount of noise per spatial element per integration time, and is dependent on the signal level and the properties of detector used. These five factors are functions of wavelength, and can be used to determine the SNR as shown by Equation 7.1.

$$SNR(\lambda) = \frac{radiance(\lambda) \times response(\lambda)}{noise(\lambda)} \tag{7.1}$$

Factors 1 and 2 are the most difficult to determine as quantitative measurements cannot be obtained directly, as the effect of the atmosphere on electromagnetic radiation is dependent on many different parameters [134]. These effects can, however, be modeled by using a *radiative transfer* modelling software package. There are several such packages available for spectral data, the main ones being MODTRAN [135], FASCODE-2 [136], and 6S [137]. Factor 3 is dependent on the target, and can be taken from a spectral library, and incorporated into the model. Factor 4 is calculated using the

properties of the instrument design. When calculating the response of a prototype instrument (such as the microslice spectrometer), it is important to recognise which properties of the instrument are fundamental to the design concept, and which are merely limited by the currently used components. Factor 5 is calculated by summing all of the sources of random noise in quadrature.

This chapter models and compares the SNR for the prototype microslice spectrometer and the CHRIS spectrometer by calculating the five factors for each instrument. The following subsections detail how the radiance, instrument response, and noise levels are calculated, so that they can be applied to Equation 7.1.

7.1.1 Using MODTRAN to Model Radiance

MODTRAN (the MODerate resolution atmospheric TRANsmission model) was the software chosen to perform atmospheric modelling in this study, mainly because it is the most commonly used and regularly updated package with a graphical user interface (GUI). The MODTRAN 4 version of the software was used as it was cheaper than the latest version (MODTRAN 5), and contained all of the required capabilities. MODO is the GUI for MODTRAN, which was developed by ReSe Applications Schläpfer [138].

MODO is utilised by creating a *tape5* file in which the user defines all of the atmospheric parameters. The major parameters include:

1. The solar (azimuth) angle. This is the angle between the direction of incoming illumination and the direction of the reflected radiation that travels towards the sensor.(see Figure 7.1). This affects the at-sensor radiance, as it affects the amount of scattering required on the reflected rays.

2. The solar/sensor zenith angle. This is the angle between the zenith (the direction perpendicularly upwards to the Earth's surface) and the light path from the target to the sun/sensor (see Figure 7.1). This affects the amount of light that is absorbed and scattered by the atmosphere, as the higher this angle is, the further the rays have travelled though the atmospherebefore they reach the sensor. In MODO, and hence for the modelling in this chapter, the zenith angle is defined as $180 - zenith\,angle$.

3. The sensor altitude. The level of atmospheric interference is affected by the sensor altitude, as not only will a higher altitude lead to a greater path length, it will also lead to interference from different levels of the atmosphere which have different chemical compositions. Spaceborne imagers will not be affected by slight changes in altitude as they operate well above the Earth's atmosphere.

4. The target. Different targets can have vastly different spectral reflectance spectra, and so the target reflectance has a major impact on the at-sensor radiance. The target reflectance is generally what the remote sensing spectrometer is trying to measure.

5. The atmospheric concentration of water vapour. Water vapour absorbs many different wavelengths of light, and therefore high levels of water vapour can affect the radiance levels. Water vapour comprises 0-4% of the atmosphere depending on time and location [139]. This level of variation makes it important to model the radiance for different water vapour concentrations.

6. The atmospheric concentration of aerosols. The presence of aerosols limits the amount of light that passes through the atmosphere, and therefore affects the at-sensor radiance. The level to which aerosols affect the transmittance of the air in know as the aerosol optical thickness (AOT) [140].

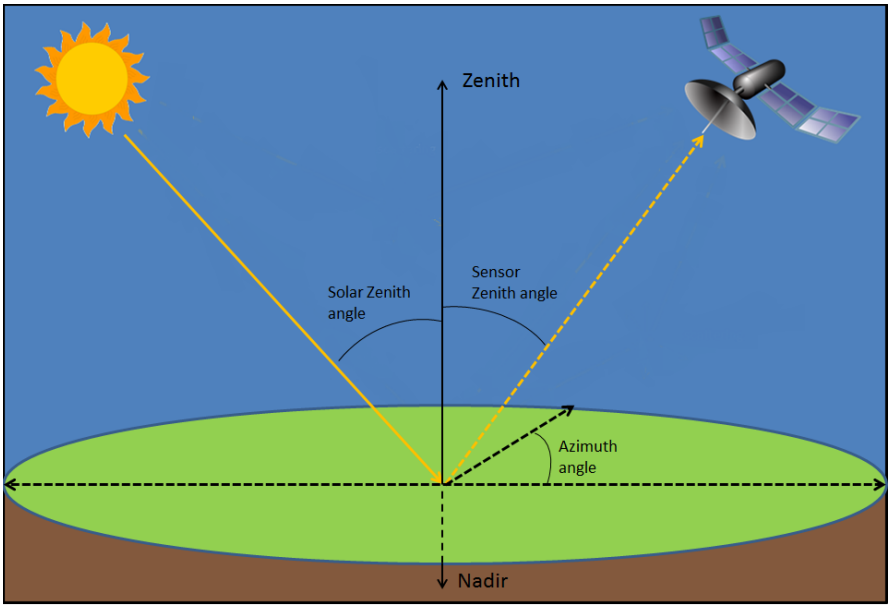

Figure 7.1: This diagram shows the definitions of the azimuth???? and zenith angles, demonstrating how they are used to define the path of reflected light.

Figure 7.2 shows how the six major parameters are defined using the MODO interface.

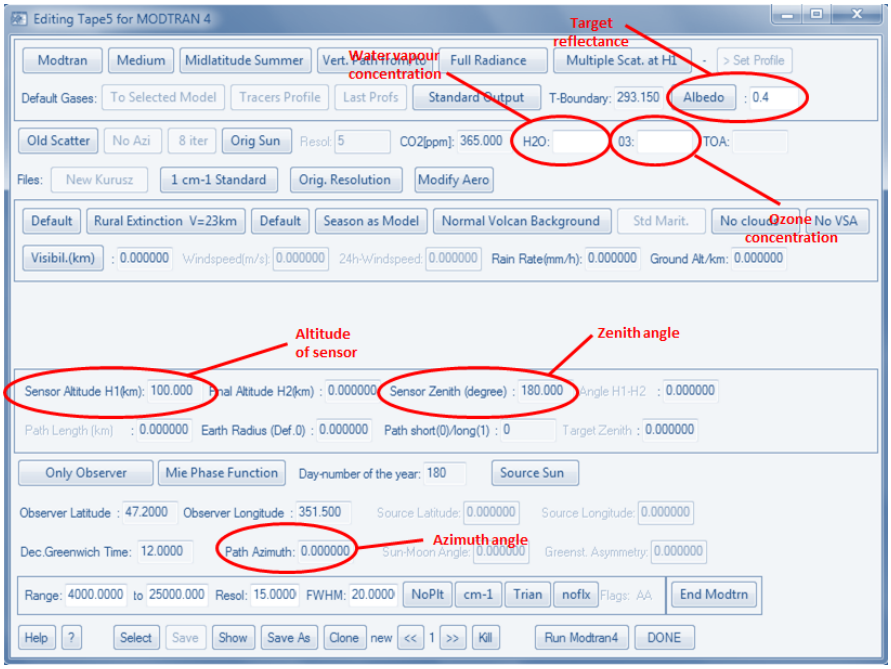

Figure 7.2: This screenshot shows the MODO interface that is used for creating and editing tape5 files. The key parameters that determine the radiance are highlighted. This file is run with MODTRAN software to model the at-sensor radiance across the spectrum. Note that in MODO the zenith angle is defined as $180 - zenith\,angle$.

Once a tape5 file has been created by the user, the MODTRAN 4 code is run, generating a tape6, tape7, tape8, and 7sc file. MODTRAN determines twelve different wavelength dependent radiance measures associated with the atmospheric propagation of the light. The tape7 file contains all of this modeled data, which can be extracted into a text file. The key outputs (which are modeled across the spectrum) are: the ground reflectance (i.e. the radiance that has been reflected from the ground to the sensor altitude), the path scatter (i.e. the amount of light scattered by the atmosphere to the sensor altitude), and the total radiance (i.e. the sum of the ground reflectance and the path scatter). Figure 7.3 shows plots of these three radiance spectra for four different ground targets when observed from an altitude of 670 km (the altitude of the CHRIS spectrometer), with optimal atmospheric parameters. It can be noted that the scatter is the dominant source of radiance below a certain wavelength (which is dependent on the target), and above this wavelength the reflectance becomes the dominant source.

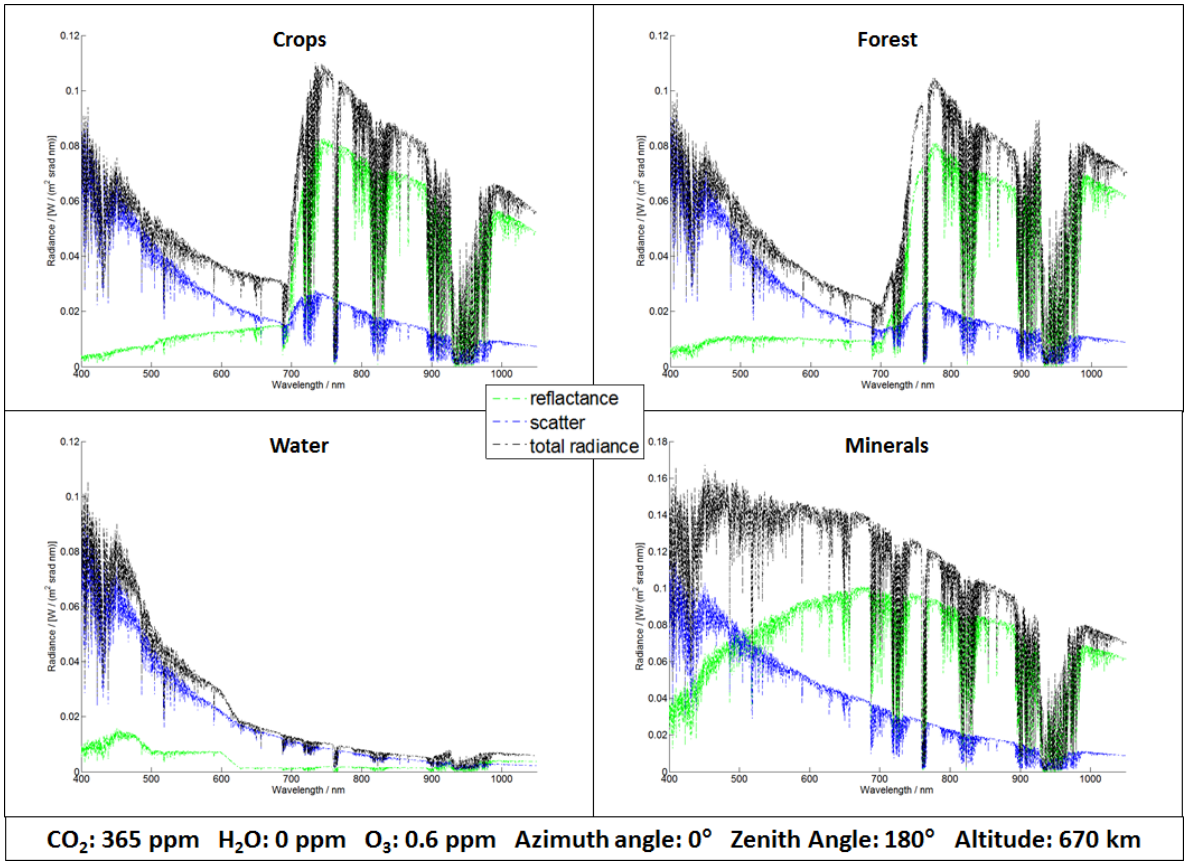

Figure 7.3: These graphs show the modeled at-sensor radiance calculated by MODTRAN 4 for various targets, and with optimal atmospheric parameters (given below the graphs). An altitude of 670 km was chosen as that is the altitude of the CHRIS spectrometer. The graphs show the ground reflectance in green, the path scatter in blue, and the total radiance in black.

The graphs in Figure 7.3 show the radiance in ideal atmospheric conditions, i.e. with minimal concentrations of CO_2, H_2O and O_3, as well as nadir solar illumination. A spaceborne hyperspectral remote sensing instrument needs to be able to capture data for a variety of solar angles and atmospheric conditions. It is therefore important to model the radiance for less optimal conditions. The water vapour concentration in the atmosphere varies in the range 0-4% (0-40000 ppm), while the ozone concentration in the atmosphere is fairly stable at 0.6% [139]. These concentrations have slight effects on the at-sensor radiance, but a more significant impact is made by varying the zenith and azimuth angles. The zenith and azimuth angles increase the path length, and hence the amount of atmospheric absorption and scattering. Figure 7.4 shows how zenith and azimuth angles of 60° give lower ground reflectance and higher the path scatter compared to the results modeled for nadir imaging, particularly in the visible wavelength range.

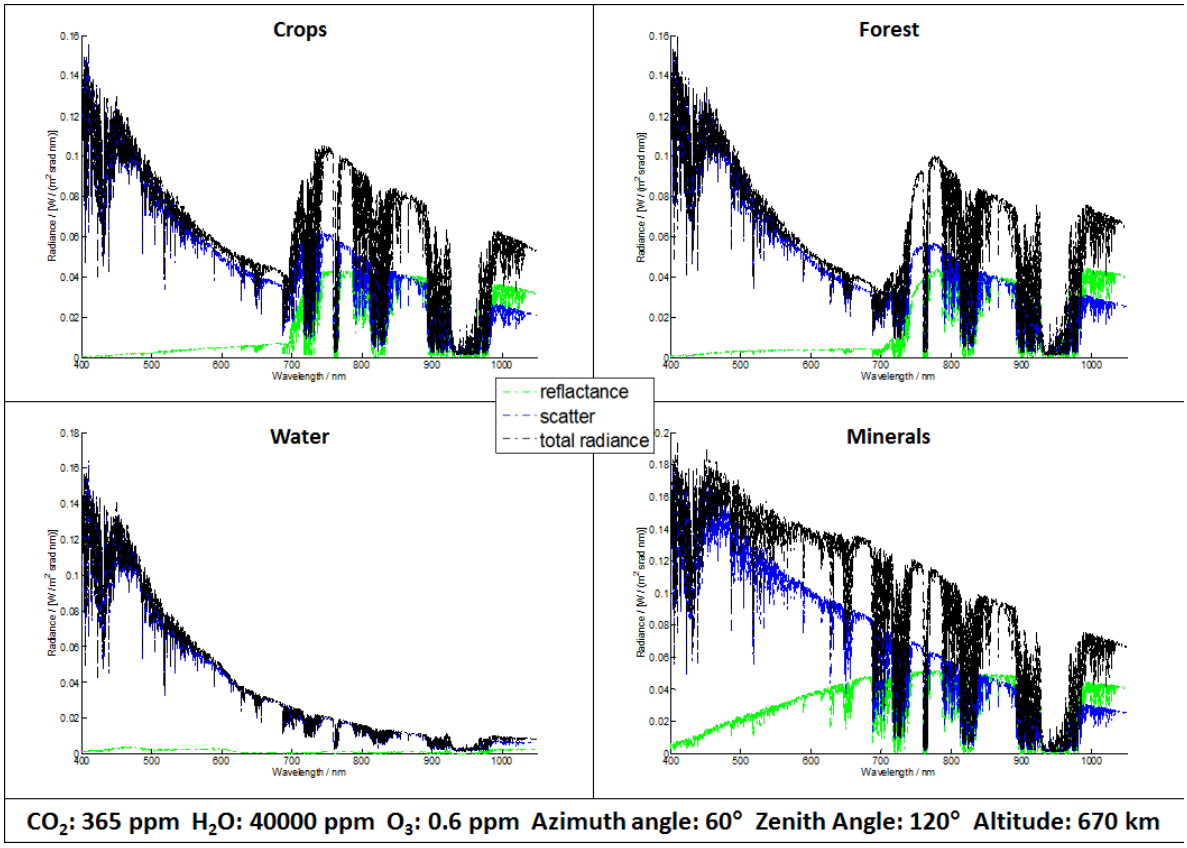

Figure 7.4: These graphs show the modeled at-sensor radiance calculated by MODTRAN 4 for various targets, and with sub-optimal atmospheric parameters (given below the graphs). The graphs show the ground reflectance in green, the path scatter in blue, and the total radiance in black.

The radiance function calculated using radiative transfer modelling can be used in Equation 7.1 with the instrument response and noise levels to calculate the SNR. It is important to note that in order to calculate the signal (the numerator in Equation 7.1), the ground reflected radiance (the green lines in Figures 7.3 and 7.4) should be used. This is because detecting the ground reflectance is the purpose of the spectrometer, and so any additional at-sensor radiance (e.g. caused by scatter) must be removed by *atmospheric correction*, which will be discussed in Section 7.1.4. The total at-sensor radiance (the black lines in Figures 7.3 and 7.4) will still affect the noise levels however (the denominator in Equation 7.1).

7.1.2 Estimating the Response of an Instrument

The instrument response is the factor that converts the level of at-sensor radiance calculated by MODTRAN into the amount of signal detected by the instrument. The spectral radiance is in units of $W\,m^{-2}sr^{-1}nm^{-1}$, while the detected signal is in units of $electrons\,nm^{-1}sp^{-1}$, where sp represents a spatial element. In order to calculate the factor that performs this conversion, six parameters must be known:

1. The area of the entrance pupil (A). This is a multiplier that converts the radiance units to

$W\,sr^{-1}nm^{-1}$ (or $J\,sr^{-1}nm^{-1}s^{-1}$).

2. The solid angle per spatial element (φ). This is calculated from the field of view (FoV) of the instrument and the number of spatial elements. This is a multiplier that converts the units to $J\,sp^{-1}nm^{-1}s^{-1}$.

3. The energy of the photons at each wavelength ($E(\lambda)$). This is a divisor that is converts the units to $photons\,sp^{-1}nm^{-1}s^{-1}$.

4. The efficiency of the instruments optics/detector ($\eta(\lambda)$). This is a multiplier that converts the units to $electrons\,sp^{-1}nm^{-1}s^{-1}$.

5. The dwell time of each spatial pixel (t). This is a multiplier that converts the units to $electrons\,nm^{-1}sp^{-1}$.

These parameters can be used to calculate the instrument response as a function of wavelength using Equation 7.2. The instrument response is a function of wavelength, because the photon energy and the optics/detector efficiency are functions of wavelength.

$$Response(\lambda) = \frac{A\varphi\eta(\lambda)t}{E(\lambda)} \tag{7.2}$$

The properties of the microslice spectrometer that affect these parameters, and therefore have a bearing on the instrument response are: the area of the entrance pupil, the instantaneous field of view (IFoV), the number of spatial elements, the transmittance of the optics (lenses, microlenses, dispersion element, and filter), and the response of the detector.

When comparing the response of two different instruments it is important to bear in mind that some of these properties are defined fundamentally by the instrument design concept, and others are merely a product of the components or set-up chosen for the current model. For example, in the prototype microslice spectrometer, five microlens arrays were used so that it could be made with off-the-shelf components to reduce costs. In a custom design however, a maximum of four microlens arrays would be needed, which would increase the throughput of the instrument without changing the design concept.

7.1.3 Calculating the Noise

There are three sources of noise associated with photon detection:

1. Signal noise (or Poisson noise). This is the statistical noise associated with detecting photon counts, and follows a Poisson distribution. The standard deviation of this noise is given by $N_s = \sqrt{S}$, where S is the total at-sensor radiance (the black lines in Figures 7.3 and 7.4) multiplied by the instrument response (Equation 7.2). The signal noise is generally the dominant noise source in remote sensing.

2. Dark noise (or thermal noise). This is caused by thermal excitation of electrons in the detector, which create counts when there is no incident signal. For a given instrument, and a fixed temperature this occurs randomly at a constant rate with a uniform variance, known as the dark current. The dark noise standard deviation is therefore given by $N_d = \sqrt{dark\,current \times t}$. The dark noise becomes a more significant source of noise when there are low light levels. The dark noise is also a more significant source of noise when imaging in the infrared wavelength range.

3. Read noise (or detector noise). This is an additive noise associated with digitising the signal on the detector. This has a fixed standard deviation for each detector, denoted as N_r. The read noise is generally negligible, but can have significance if exceptionally short exposure times are being used.

When calculating the total noise level in the detected signal, the three separate sources of noise should be added in quadrature because they are standard deviation values of random noise sources. The total noise recorded by the instrument is therefore given by Equation 7.3.

$$N_{total} = \sqrt{N_s^2 + N_d^2 + N_r^2} \tag{7.3}$$

7.1.4 Atmospheric Correction

As well as being used for performance modelling, radiative transfer models are used to perform atmospheric correction. When decoding real remote sensing data to determine the reflectance of a target, the atmospheric propagation of the light must be taken into account. The radiance received by the instrument is a combination of the ground reflectance, as well as atmospheric scatter and absorption. The spectral signal received from remote sensing data can be processed into a ground reflectance spectrum by using atmospheric modelling in two steps:

1. Use the instrument response to determine what the at-sensor radiance would have been. This is the real equivalent of what is modeled by MODTRAN to create the black lines in Figures 7.3 and 7.4.

2. Subtract the expected path scatter to obtain an estimate of the ground reflectance. The path scatter is estimated using a radiative transfer model such as MODTRAN, and is therefore equivalent to the blue lines in Figures 7.3 and 7.4.

The application of these two steps is known as atmospheric correction, and the concept of how this can be used to obtain an estimate of the true ground reflectance from remote sensing data is demonstrated in Figure 7.5. In this figure it can be seen that the estimated spectral reflectance (bottom right) has gaps around 1400 nm and 1900 nm. This is because these are the centers of two water absorption bands, meaning that there is no radiance at those wavelengths (see top right graph) making it impossible to perform atmospheric correction.

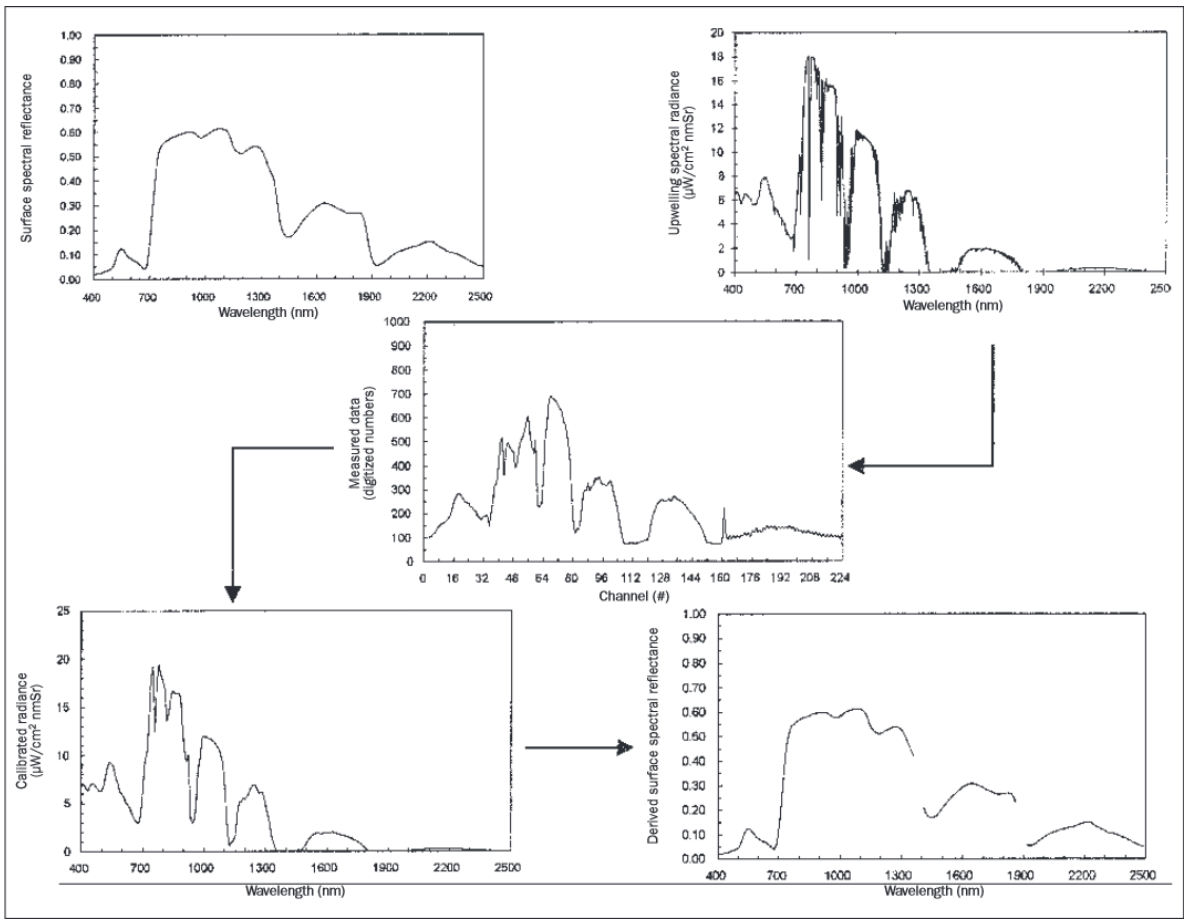

Figure 7.5: This image shows how the spectral signal on a hyperspectral remote sensing detector is generated from the ground reflectance, and how the ground reflectance can therefore be estimated using the instrument response and radiative transfer models of the light propagation. This second process is known as atmospheric correction. The top left panel shows the true spectral reflectance of the target being imaged. The top right panel shows the the true spectral at-sensor radiance generated, which is a product of the reflectance and atmospheric scattering. The central panel shows the spectral signal that is generated on the detector, which is a product of the radiance and the spectral response of the instrument. The bottom left panel shows the estimated radiance that is calculated using the signal and the estimated response of the detector. The bottom right panel shows the estimated spectral reflectance of the target that is calculated using the estimated radiance and the modeled path scatter.

7.2 Comparison of the SNR of the Microslice Spectrometer to that of the CHRIS Spectrometer

This section applies the calculations outlined in the previous section to generate a model of the remote sensing SNR capabilities of a microslice spectrometer under different imaging conditions. In order to provide a benchmark for these results, a comparison is provided by also modelling the SNR of a conventional pushbroom spectrometer(CHRIS) [29].

7.2.1 CHRIS

CHRIS (the Compact High Resolution Imaging Spectrometer) is a spectrometer that was developed and deployed by the European Space Agency (ESA) as a proof of concept mission. It was the most advanced instrument deployed on ESA's PROBA (PRoject for On-Board Autonomy) satellite, the primary purpose of which was to provide a platform for novel spaceborne proof-of-concept technology. The CHRIS instrument has three important similarities to the microslice spectrometer that make it a suitable instrument for comparison:

1. It images hyperspectrally over the visible wavelength range (CHRIS also operates in the near infra-red).

2. It is a proof-of-concept instrument to test the viability of a spectrometer design.

3. It uses a slightly unconventional scanning method to effectively increase the dwell time of a particular area.

To provide a suitable comparison, calculations were initially performed assuming that the microslice spectrometer was also being used on the PROBA platform (i.e. at an altitude of 670 km), with the same foreoptics as the CHRIS instrument. The instruments are compared using the properties of the CHRIS spectrometer in its current state, and properties of the microslice spectrometer as if it were using optimal components and optimal datacube reconstruction. This is deemed to be a fair comparison as CHRIS is a fully operational instrument, while the microslice spectrometer was built as a prototype to inform a fully operational design. The microslice prototype spectrometer cost around £20k to develop (excluding staff time), and although CHRIS was part of a 'low-cost' mission its cost will still have been an order of magnitude greater.

Calculations of the response of each instrument and their associated noise levels to were applied to the radiance spectra modeled by MODTRAN to determine the SNR for each instrument using Equation 7.1. This was done for various different targets, and for various different atmospheric parameters to determine under what conditions, and for what purposes each instrument would perform better.

7.2.2 Comparing the Instrument Responses

The instrument response and dwell time are the underlying factors that causes different instruments to be able to achieve different levels of SNR. The properties that determine the response of an instrument were outlined in Section 7.1.2. These properties were calculated for both the microslice and CHRIS spectrometers, and are shown in Table 7.1. Initial comparisons are made for using a microslice system on the back of the CHRIS foreoptics at the same altitude (670 km) so that the instruments are being compared with appropriately comparable properties.

Property	Microslice	CHRIS	Notes
area of the entrance pupil (A)	$0.011\,m^2$	$0.011\,m^2$	CHRIS has a pupil diameter of 120 mm, so the microslice spectrometer is said to have the same.
solid angle per spatial element (S)	$3.0 \times 10^{-8}\,strad\,sp^{-1}$	$8.7 \times 10^{-10}\,strad\,sp^{-1}$	This is dependent on the number of spatial elements and the angular instantaneous field of view (IFoV). The microslice spectrometer has more spatial elements, but it also has a much larger IFoV
transmittance of the optics (T)	82 %	82 %	This is dependent on the number of optical elements, and the materials used. It is difficult to predict exactly, but is estimated for ten optical components with a transmittance of 98% for both instruments.
Quantum efficiency (QE) of the detector (D)	$55 - \left(\frac{\sqrt{20}}{150}\left(\lambda - 550\right)\right)^2$	$\frac{1}{3}\left(86 - \frac{13\lambda}{200}\right)$	These QE spectra are calculated by fitting simple polynomials to the published QE. The response of the current microslice detector is slightly higher than that of the CHRIS instrument, but the detector chosen is not fundamental to the design of either instrument.
energy of the photons (E)	$E = {}^{hc}/_{\lambda}$	$E = {}^{hc}/_{\lambda}$	This is required to calculate the response, but is clearly independent of the instrument used.
dwell time (t)	1300 ms	15 ms	Due to the increased IFoV of the microslice spectrometer in the along track direction, it is able to achieve a much higher dwell time for each spatial element. The PROBA satellite travels at $7.5\,kms^{-1}$, but CHRIS uses a scanning technique that allows the dwell time to be extended by a multiple of 5. The CHRIS value is therefore calculated for a groundtrack speed of $1.4\,kms^{-1}$ and the microslice value for a groundtrack speed of $7\,kms^{-1}$.

Table 7.1: This table shows the properties of the microslice and CHRIS spectrometer designs that are used to calculate the response of each instrument. The properties of the microslice spectrometer have been calculated as if it were using the CHRIS foreoptics so that an appropriate comparison is provided. The instrument response enables the detected signal to be determined based on the at-sensor radiance.

The properties in Table 7.1 were used to calculate the response of each instrument as a function of wavelength using Equation 7.2, and the results are plotted in Figure 7.6. The response of the microslice spectrometer is more than a factor of 10^4 larger than that of CHRIS, which due to the its larger IFoV in the along track direction giving a larger solid angle per spatial element as well as a significantly increased dwell time.

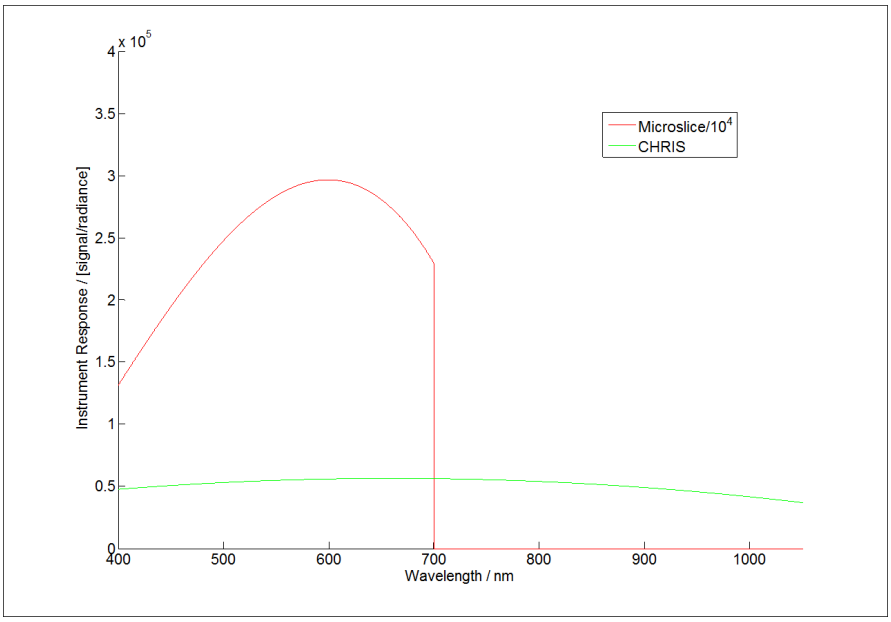

Figure 7.6: This graph compares the response factors of the the CHRIS spectrometer with the microslice spectrometer, when both instruments are imaging at 670 km altitude and using CHRIS foreoptics. These factors allow the signal received by each instrument to be calculated for a given at-sensor radiance. The microslice spectrometer response is only shown below 700 nm as the current spectral range of the instrument is 475-650 nm. Note that the microslice spectrometer response has been divided by 10^4 for comparison.

The radiance was modeled, and the noise levels were calculated as a function of wavelength for each instrument as outlined in Section 7.1. These were used to calculate the SNR of each instrument as a function of wavelength by applying Equation 7.1.

7.2.3 Instrument Comparison Results

Using the CHRIS foreoptics gives the microslice instrument an instantaneous field of view (IFoV) of 9 x 9 km, and a spatial resolution of 270 x 50 m. The uneven spatial resolution and square IFoV are a result of the foreoptics lenses in the CHRIS instrument not being anamorphic.

Figure 7.7 shows the modeled SNR spectrum for each instrument using the CHRIS foreoptics when imaging a spectrally flat target of albedo 0.5 (50% reflectance) from 670 km altitude, with optimal atmospheric conditions. It can be seen that modelling the SNR of CHRIS gives results of a similar magnitude and spectral shape to those obtained empirically. This evidence is taken to support the accuracy of the modelling method used. The CHRIS spectrometer is shown to obtain an SNR of about 50, while the microslice spectrometer obtains an SNR over 100 times larger.

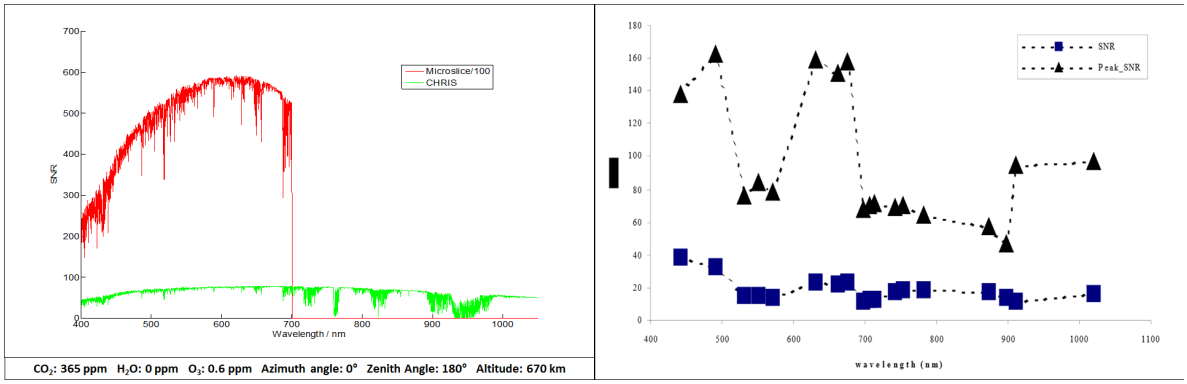

Figure 7.7: The graph on the left compares the modeled SNR of the microslice and CHRIS spectrometers when imaging a flat 50% reflectance target at 670 km altitude. The data is modeled for both instruments using the foreoptics of the CHRIS instrument, but with different spatial resolutions (270 x 50 m for the microslice spectrometer, and 20 m for the CHRIS spectrometer). Optimal atmospheric conditions are used (given below the graph). Note that the microslice spectrometer SNR is has been divided by 100 for comparison. The graph on the right shows the SNR of the CHRIS spectrometer as determined using empirical data from the brightest pixels in an image of urban targets, taken from [141].

For a meaningful comparison of how the SNR of the instruments affects their capabilities, it is important to relate the SNR values to those required for different remote sensing applications (see Table 2.1). A SNR over 100 can be seen to be good enough for many applications, and a SNR of 1000 or more is suitable for any current application, though instruments with higher SNR values could lead to new applications. For any meaningful data to be recorded the signal should be an order of magnitude higher than the noise, meaning that data with a SNR of lower than 10 is too noisy to be useful. Taking these requirements into account, the SNR of the CHRIS instrument can be said to be suitable for many applications, such as red edge detection, but not be good enough for others, such as detection of hydrocarbon pollution, even under optimal atmospheric conditions.

In order to compare the relative performance of the two instruments fairly in the following models, the SNR of the CHRIS instrument was calculated for data that is re-sampled at the same spatial resolution as the microslice instrument (270 x 50 m). Figure 7.8 plots the SNR of both spectrometers when imaging various targets. These graphs show that the SNR of CHRIS barely gets above 100 in the visible wavelength range when imaging water, crops and forest targets, while fairing slightly better for minerals. The SNR of the microslice spectrometer is over 10 times greater than that of CHRIS, and is generally around 1000 or more in the 475-650 nm wavelength range.

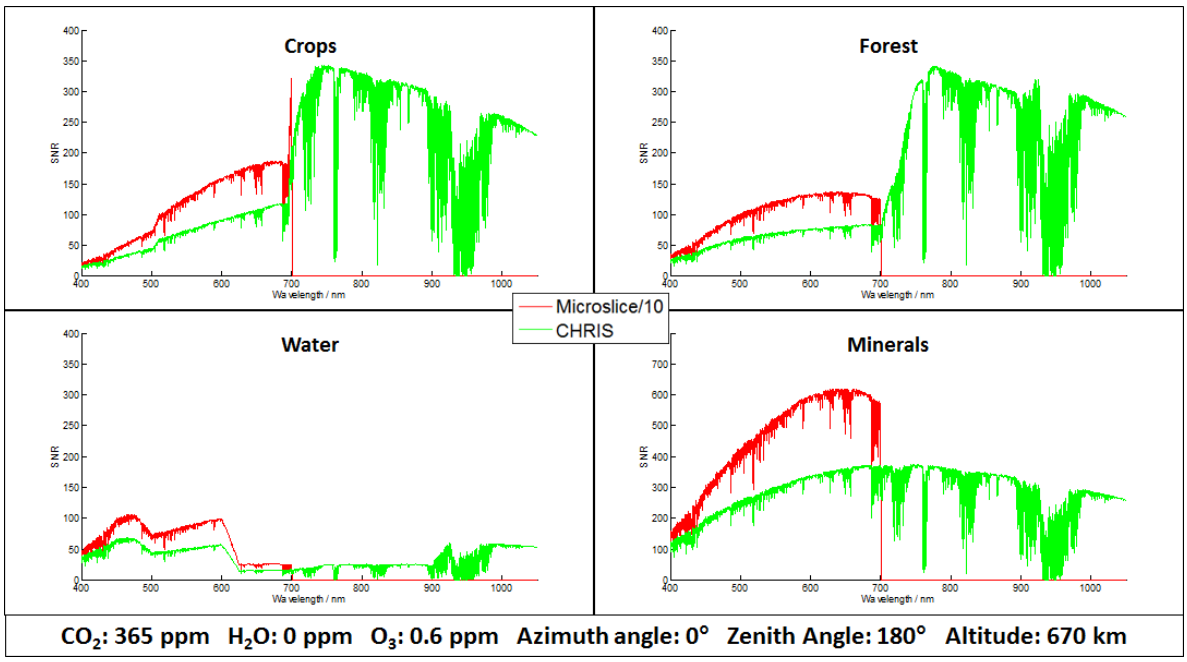

Figure 7.8: These graphs compare the SNR modeled for the microslice (red) and CHRIS (green) spectrometers when imaging four different natural remote sensing targets at 670 km altitude. These results are for both instruments imaging with the CHRIS foreoptics, and for data at a spatial resolution of 50 x 270 m. Optimal atmospheric conditions are used (given below the graphs). Note that the microslice spectrometer SNR is has been divided by 10 for comparison.

In the comparisons so far, the SNR of both instruments have been modeled for optimal atmospheric conditions. If the same targets from Figure 7.8 are modeled using sub-optimal atmospheric parameters, then the lower at-sensor radiance causes the SNR values to decrease for both instruments (see Figure 7.9). For these parameters the SNR of both instruments is reduced significantly, but the microslice spectrometer SNR remains over 10 times greater than that of CHRIS. The effect of these atmospheric parameters on the SNR is dependent on wavelength, with a reduction of a factor of about 2 in the near-infrared, and a factor of about 10 in the ultraviolet when compared to optimal conditions.

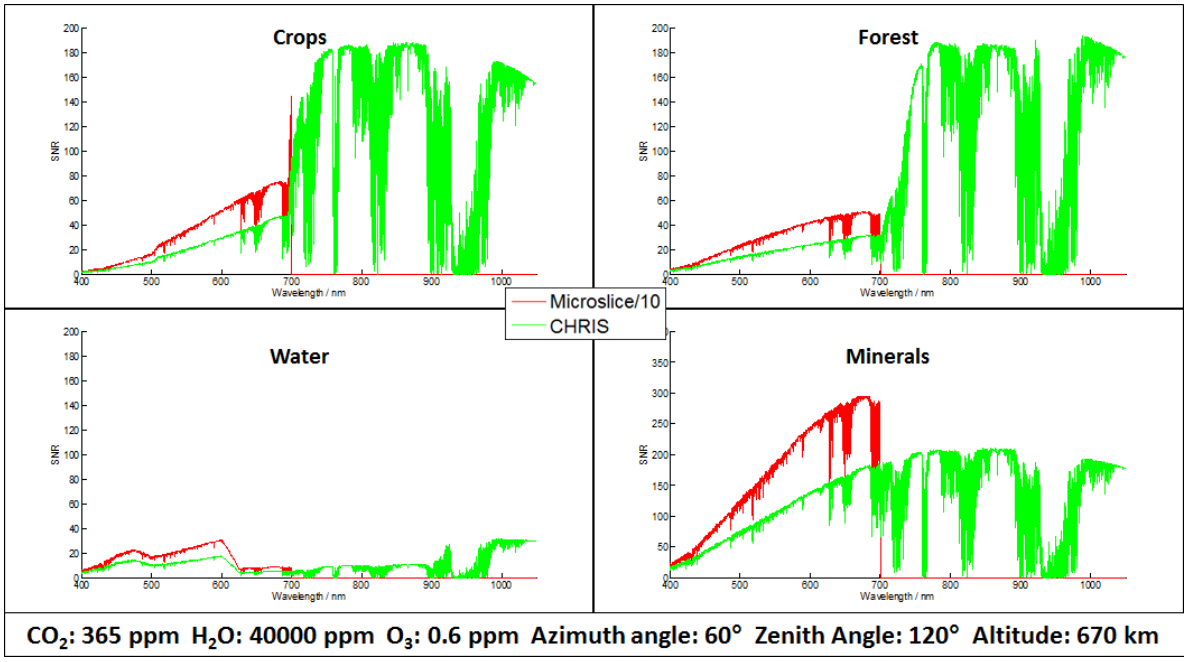

Figure 7.9: These graphs compare the SNR modeled for the microslice (red) and CHRIS (green) spectrometers when imaging four different natural remote sensing targets at 670 km altitude. These results are for both instruments imaging with the CHRIS foreoptics, and for data at a spatial resolution of 50 x 270 m. Sub-optimal atmospheric parameters (given below the graphs) are used to create these plots. Note that the microslice spectrometer SNR has been divided by 10 for comparison.

The significantly greater SNR values obtained by the microslice spectrometer compared to CHRIS are largely as a result of the greater along track IFoV. The microslice spectrometer does, however, have a smaller swath width (9 km compared to 15 km), when using the same foreoptics. If the microslice spectrometer were to be able to obtain the same swath width as CHRIS, then the size of the microlens arrays, and hence the size of the detector would need to increase. A 67% increase in the number of spatial elements would be required in the across swath direction , increasing the size of the microlens arrays and the number of detector pixels required by the same factor. Currently about 2000 detector pixels are being used in that direction, so about 3400 pixels would be required on the detector, which is quite feasible with modern CCD detectors. This assumes that spectral slices of the same width are used, with the same amount of *dead space* between slices.

In the along swath direction, the microslice spectrometer has fewer spatial elements, which leads to different spatial resolutions in the two directions when using the CHRIS foreoptics. This is a deliberate part of the instrument design that was incorporated because of the way that the spectra are dispersed, which means that more spatial elements fit in the same amount of detector space in the across track direction than the along track direction. In the prototype microslice spectrometer this is corrected for by having anamorphic foreoptics, which re-image a non-square IFoV onto the square microlens arrays.

In order to image at the 20 m spatial resolution that CHRIS can achieve, it is not feasible to simply

increase the number of spatial elements, as this would require an increase in detector size by an approximate factor of 14 in the along swath direction (to about 35000 pixels). A 20 m spatial resolution can still be achieved however through decreasing the IFoV along the swath by a factor of 14. Increasing the number of spatial elements along the swath from 33 to 50, allows for a decease in IFoV in this direction of only a factor of 9 (from 9 km to 1 km). This increase in the number of spatial elements would require an equivalent increase in the microlens arrays, and an increase in detector space required from about 2500 to about 3800. The swath width would also need to decrease by a factor of 2.5 (from the new 15 km to 6 km) to allow all of the spatial elements to fit on the detector.

These hypothetical adjustments to the microslice spectrometer design have shown that it is able to achieve the same spatial resolution as CHRIS, with comparable spatial coverage. This design would require a 3800 x 3400 pixel detector and 17 x 17 mm microlens arrays. CDD arrays of 4000 x 4000 pixels are readily available [142], and SUSS MicroOptics claim to be able to manufacture microlens arrays up to 100 x 100 mm. Since this design still images multiple (50) spatial elements along the swath, it will still be able to achieve a larger dwell time than CHRIS, meaning that it should still be able to achieve a higher SNR.

In order to perform a comparison that highlights the fundamental design differences of the two instruments, the microslice spectrometer SNR was modeled for this hypothetical design that can image at the same spatial resolution as CHRIS (20 m), with a comparable swath width (6 km compared to 15 km). The results of modelling the SNR of both instruments with the same spatial resolution and comparable swath widths are shown in Figure 7.10. This shows that the SNR of the microslice spectrometer can still be about a factor of 10 higher than that of CHRIS.

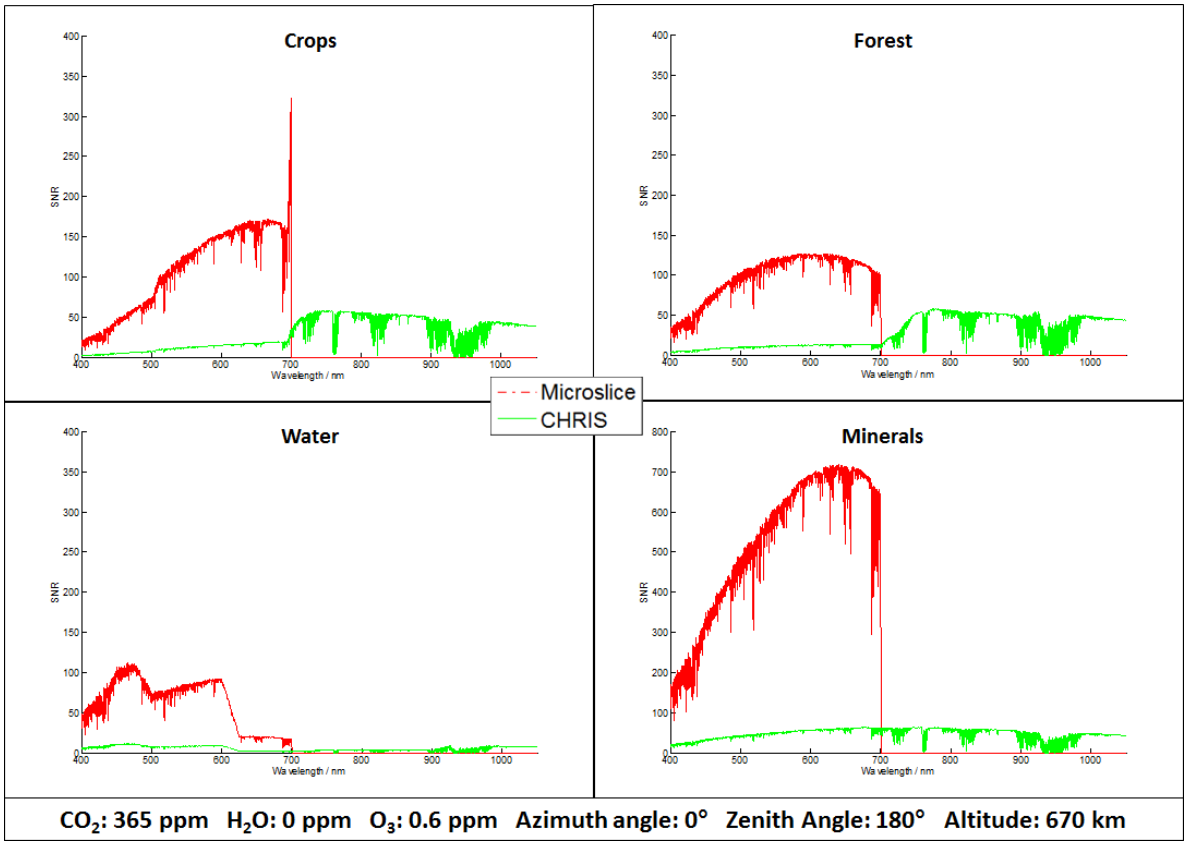

Figure 7.10: These graphs compare the SNR modeled for the microslice (red) and CHRIS (green) spectrometers when imaging four different targets at an altitude of 670 km. This model is for an adjusted design of the microslice spectrometer whereby it images at the same spatial resolution (20 m), and with a comparable swath width to the CHRIS instrument (6 km compared to 15 km). Optimal atmospheric conditions are used (given below the graphs).

These comparisons essentially highlight the flexibility given by the 2-dimensional IFoV of the microslice spectrometer; i.e. the ability to image with a larger dwell time (700 ms compared to 15 ms) at the expense of the swath width (6 km compared to 15 km). This 700 ms dwell time is also enhanced by the larger number of detector pixels and smaller wavelength range used by the microslice spectrometer design.

A way to achieve a good spatial resolution with the microslice spectrometer without reducing the SNR so significantly would be to image from an airborne platform (i.e. using a small aircraft or UAV at $\leq 5\,km$ altitude). If the microslice spectrometer were to be used on a aircraft, one would expect different results, as the lower altitude would decrease the amount of atmospheric scattering, meaning that the radiance would be dominated by reflectance rather than scatter. Using the microslice spectrometer with its current foreoptics would give spatial resolutions of about 1.5 m and 7.5 m, with swath widths of 0.26 km and 1.3 km, at 1 km and 5 km altitudes respectively. The SNR of the microslice spectrometer was therefore modeled as if it were imaging from an airborne platform at 5 km and 1 km altitude traveling at $100\,ms^{-1}$. The results are plotted in Figure 7.11. The velocity

of $100\,ms^{-1}$ was chosen, as this is about the speed of a typical remote sensing aircraft, such as the Dornier 228: G-ENVR, which is used to fly the Eagle spectrometer [11].

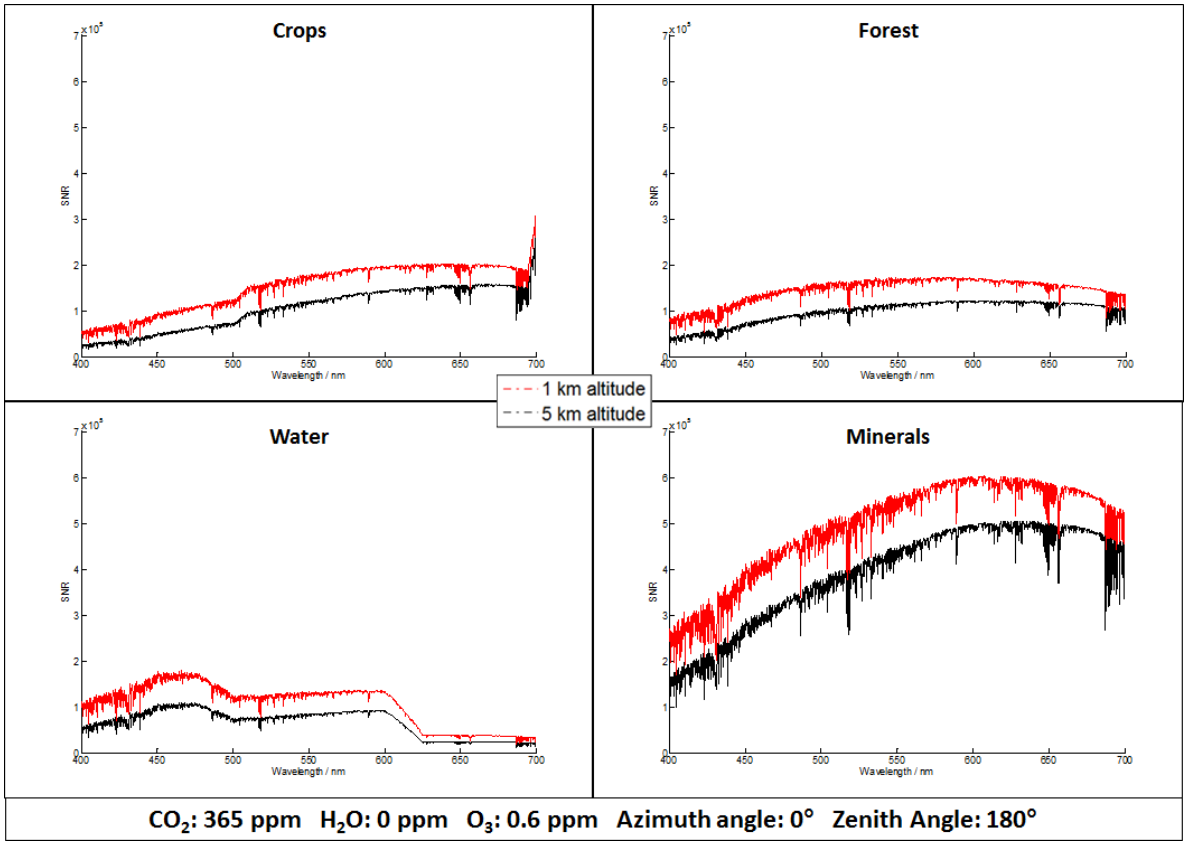

Figure 7.11: These graphs show the modeled SNR that would be achieved by the microslice spectrometer for imaging four different targets at altitudes of 1 km (red) and 5 km (black). Optimal atmospheric conditions are used (given below the graphs).

The modeled SNR values of $\sim 10^5$ for airborne imaging show the potential achievable by the scanning technique, but they are likely to be limited to lower values by systematic factors. The SNR, however, is still likely to be more than an order of magnitude higher those obtained from a LEO satellite. This is due to the fact that the higher reflected radiance received at lower altitudes outweighs the shorter integration time. The main advantage of airborne imaging, however, is that a much greater spatial resolution is achieved without having to increase the number of spatial elements. Imaging from an airborne platform also has greater flexibility in the timing of a survey of a particular area, meaning that an imaging survey could be conducted under the most appropriate conditions. The spatial coverage that can be imaged from an airborne platform is, however, much lower than is achievable from a satellite.

7.3 Summary

The modelling calculations performed in this chapter have shown that the current design of the microslice spectrometer would allow it to be able to achieve a SNR over 10 times greater than the CHRIS spectrometer when imaging from the same platform, using the same foreoptics. This would be for data sampled at the same spatial resolution (50 x 270 m), but a slightly smaller swath width for the microslice spectrometer (9 km compared to 15 km for CHRIS).

If the design of the microslice spectrometer were to be changed to give the same spatial resolution as CHRIS can achieve (20 m), and a 6 km swath width, then it would still have a SNR about 10 times larger. This significant difference is achievable for a relatively small difference in swath width due to the small wavelength range of the microslice spectrometer, and the fact that a larger CCD can be used (4000 x 4000 pixels). Attaining the same swath width would not be feasible with the current design without reducing the spatial resolution, due to detector size limitations.

If the microslice spectrometer were to be used to image from an aircraft with the prototype design at 1 km altitude, it could maintain a SNR over an order of magnitude greater than that of CHRIS while improving the spatial resolution to 1.5 m.

These comparisons have shown that the 2-dimensional IFoV of the microslice spectrometer allows greater flexibility in trading-off the IFoV for the dwell time than the CHRIS instrument, and can hence optimise the SNR for the particular application. It should also be noted that these improved SNR performances are achieved in spite of the fact that the CHRIS instrument scanning technique increases its dwell time by a factor of five at the cost of reducing the spatial coverage along the swath by a factor of five.

Table 7.2 summarises the potential specifications of a microslice instrument based on the trade-offs that have been discussed in this chapter. The wide variety of specifications are possible as a result of the trade-offs allowed by the 2-dimensional instantaneous field of view (IFoV) of the instrument. If these specifications are compared to those in Table 1.1, it can be seen that the SNR is typically much higher for the microslice spectrometer in spite of the fact that the other specifications are, in general, typical for remote sensing hyperspectral imagers. These very large SNR values are, however, likely to be limited to lower values by systematic factors, but they should still be significantly higher than for other remote sensing hyperspectral imagers.

	original	CHRIS foreoptics	same spatial res	aircraft 5km	aircraft 1km
Spectral Range	475-650 nm	475-650 nm	475-650 nm	475-650 nm	475-650 nm
Spectral Resolution	7 nm	7 nm	7 nm	7 nm	7 nm
Spatial Resolution	1 km	270 x 50 m	20 m	7.5 m	1.5 m
No. of Spatial Elements	33 x 180	33 x 180	50 x 180	33 x 180	33 x 180
Dwell Time	5 s	1.3 s	0.1 s	2.5 s	0.5 s
IFoV	37 x 85 km	9 x 9 km	0.7 x 3.6 km	0.26 x 1.3 km	50 x 250 m
Altitude	670 km	670 km	670 km	5 km	1 km
SNR	$\sim 10^5$	$\sim 10^4$	~ 100	$\sim 10^5$	$\sim 10^5$

Table 7.2: This table shows a summary some of the potential specifications that could theoretically be achieved for a microslice spectrometer, by trade-offs that have been discussed in this chapter. The very large SNR values are likely to be limited to lower values by systematic factors.

Although the affects of the atmosphere provide the biggest difference between ground based and remote sensing imaging spectroscopy, there are other factors to be taken into account. For example, the scanning technique used, and the vibrations caused by the airborne platform are likely to have a negative effect on the performance of the instrument. To test these effects reliably, however, would require more advanced testing from an airborne platform.

Another potential advantage of the microslice spectrometer design over conventional pushbroom remote sensing spectrometers lies in the size and weight of the instrument. The CHRIS instrument is one of the smallest and lightest hyperspectral remote sensing instruments (see Table 1.1), being 79 x 20 x 26 cm in size and weighing 14kg. The prototype microslice spectrometer, however, measures 54 x 17 x 17 cm and weighs 10 kg.

The design of the prototype microslice spectrometer can potentially be developed to provide an even more compact and lighter instrument. Half of the current spectrometer weight is from the base plate with most of the rest contributed by mechanical fittings used to hold the components in place, with the actual components of the spectrometer contributing less than 1 kg of the weight. Also, a lot of the space occupied by the instrument is due to the mechanical fittings (see Figure 4.16), as well as the off-the-shelf camera/detector system which could be made a lot smaller with custom parts.

The optical components of the instrument (excluding the camera) can fit in a cylinder 32 mm in diameter and 200 mm long. The microslice spectrometer could therefore potentially be designed to be around 5 x 5 x 30 cm, and weigh around 2 kg. If this could be achieved, this design could potentially be deployed on a 3U cubesat, which is a miniturised 10 x 10 x 30 cm satellite generally used for testing satellite technologies [143]. Cubesat deployment is a relatively easy and cheap way to deploy an instrument in space, as they can *piggyback* on a primary satellite deployment.

Chapter 8

Discussions and Conclusions

This thesis has presented some of the current applications of hyperspectral remote sensing, as well as investigating the latest instruments and data analysis techniques used. One particular instrument driving requirement identified for certain applications was the signal to noise ratio (SNR). A prototype novel spectrometer has been developed that uses microslice technology to achieve simultaneous spectral and 2-dimensional spatial multiplexing, giving it the potential to achieve an improved SNR compared to conventional remote sensing spectrometers at the expense of other parameters. Laboratory and field tests of this instrument demonstrated that it was able to achieve 7.0 nm spectral resolution over the 475-650 nm wavelength range, and a 1.8 x 2.6 mrad spatial resolution. Atmospheric modelling was used to estimate the potential performance of such an instrument from a remote sensing platform, demonstrating that it could indeed achieve a significantly higher SNR than a conventional remote sensing spectrometer at the expense of other parameters.

8.1 Relative Capabilities of the Microslice Spectrometer

The instrument presented in this thesis represents a novel approach to hyperspectral remote sensing in its use of microslice technology to image a wide 2-dimentional instantaneous field of view (IFoV) and simultaneously achieve full spectral coverage over the 475-650 nm wavelength range. As with other hyperspectral remote sensors, it uses a standard imaging spectrograph (see Figure 1.5) to generate spectral data. The uniqueness of the instrument design lies in the novel imaging optics used to feed the spectrograph. In a standard hyperspectral imager, light at the entrance pupil is collimated and then focused onto a slit, which serves as the entrance to the spectrograph. In the microslice design, however, the collimated light is focused onto a set of a lenslet arrays that slice the image up into an array of small slits (slitlets), which feed into the spectrograph. The fact that multiple slitlets are imaged simultaneously allows for the 2-dimensional IFoV provided by this instrument. The current specifications of the prototype microslice hyperspectral imaging system are presented in Table 8.1. Additional performance parameters such as signal to noise ratio (SNR) are dependent on the

implementation of the instrument.

Spectral Range	475 - 650 nm
Spectral Resolution	7.0 nm
Field of View	52 x 260 mrad
Spatial Resolution	1.8 x 2.6 mrad
Size	17 x 17 x 54 cm
Weight	10 kg

Table 8.1: This table shows the latest specifications of the prototype microslice hyperspectral imager.

As with any imaging spectrometer, the amount of information that can be gathered is ultimately limited by the number of detector pixels available. The minimum number of detector pixels required by a hyperspectral system can be determined using Equation 8.1, where *sp* represents the size of a spatial element. For resolution elements that are spatially contiguous on the detector, at least two pixels are required per element for optimal sampling. This applies to the spectral resolution, and the spatial resolution along the slice in the microslice spectrometer. Since no spatial information is retained across a slice the spatial sampling in this direction is determined directly by the slice width.

$$number\,of\,detector\,pixels = \left(\frac{2 \times spectral\,range}{spectral\,resolution\,size}\right) \times \left(\frac{2 \times IFoV}{vertical\,sp \times horizontal\,sp}\right) \tag{8.1}$$

This equation shows that for a fixed size of detector, improving the quality of one parameter requires a compromise in the quality of another. For example, increasing the IFoV can be achieved by changing the focal length of the foreoptics, but this leads to a reduction in the spatial resolution for the same spatial sampling. Alternatively the same spatial resolution could be maintained with a trade-off in the spectral performance. To fit the spectral slices on the same number of detector pixels, however, either the spectral range must decrease, or spectral resolution must decrease. (Note: a 'decrease' in spectral or spatial resolution results in an increase in the value of the resolution element size to fit with Equation 8.1). This compromise can be understood using the flowchart in Figure 8.1. The effects of changing other parameters can be derived in the same way. Altering any instrument parameter requires an appropriate change in instrument design, but the spatial and spectral resolutions are also fundamentally limited by the quality of the optical system.

The spectral range of the instrument can be increased in two ways. One way would be to increase the length of the dispersed slices by increasing the spectral range of the bandpass filter; this would require the microslicer to be altered to avoid overlap of slices on the detector. This would also require the anamorphic magnification of the foreoptics to change, so that regular spatial sampling of the ground is retained. The second way of increasing the spectral range would be to decrease the line density on the dispersion element (grism), thus lowering the angular dispersion, which would lead to a lower spectral resolution.

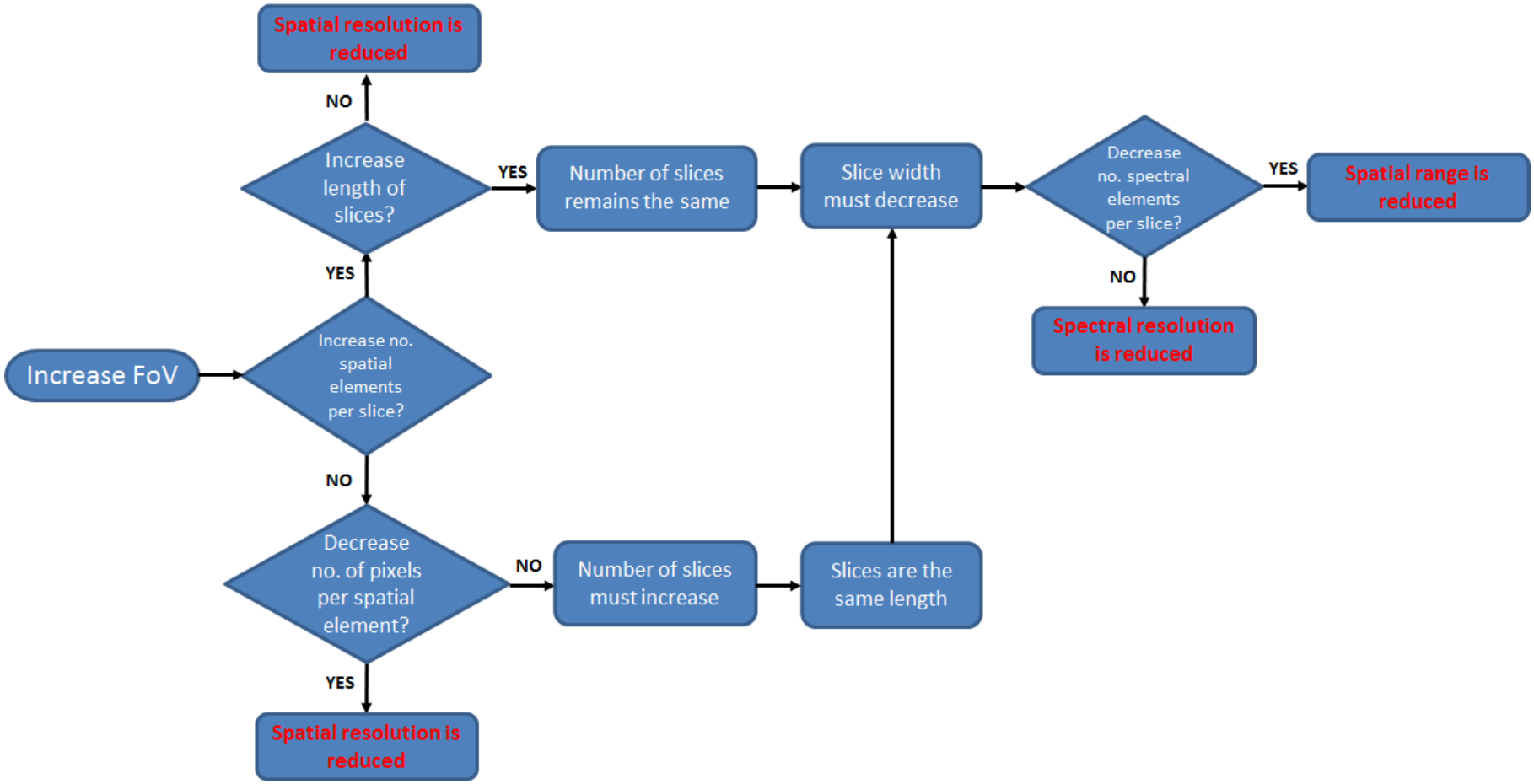

Figure 8.1: This flowchart shows that, for a fixed number of detector pixels, increasing the field of view of an imaging spectrometer inevitably leads to a compromise in another instrument parameter. The same is true for altering any of the other parameters.

Conversely the spectral resolution can be increased by increasing the line density on the dispersion element, thus increasing the dispersion angle. This would require either the spectral range to decrease, or the detector to be larger, or the number of slices in the slice width direction to decrease. Decreasing the number of slices would be done by changing the number and focal lengths of microlenses in the arrays, to match the number of slices required.

To increase the potential spatial resolution of the instrument, the number of pixels per spatial target area must increase. This can be done by either increasing the number of spatial pixels, or decreasing the IFoV. Increasing the number of spatial pixels would require longer slices and/or and more slices in the appropriate direction, which can be achieved by changing the microlens arrays, and would require a larger detector. Decreasing the IFoV would involve changing the focal length of the foreoptics

The microslice spectrometer (like other spectrometers) is constrained by Equation 8.1, but it has the advantage of also being able to trade off between the two spatial dimensions of the IFoV. This provides more flexibility in the ability to trade off swath width for additional dwell time, allowing a greater signal to noise ratio (SNR) to be achieved at the expense of the spatial coverage of each flightline.

One disadvantage of the microslice design, is that using multiple slitlets at the entrance to the spectrograph to provide the 2-dimensional IFoV requires gaps (*dead space*) to be left on the detector between dispersed slices. This means that the size of the detector used needs to be larger than the number of pixels required to gather the spectral and spatial information. A traditional pushbroom spectrometer only images a single dispersed slit, and hence, aside from leaving a few unused pixels at the edge of the detector, no detector space is wasted. Figure 8.2 illustrates this concept.

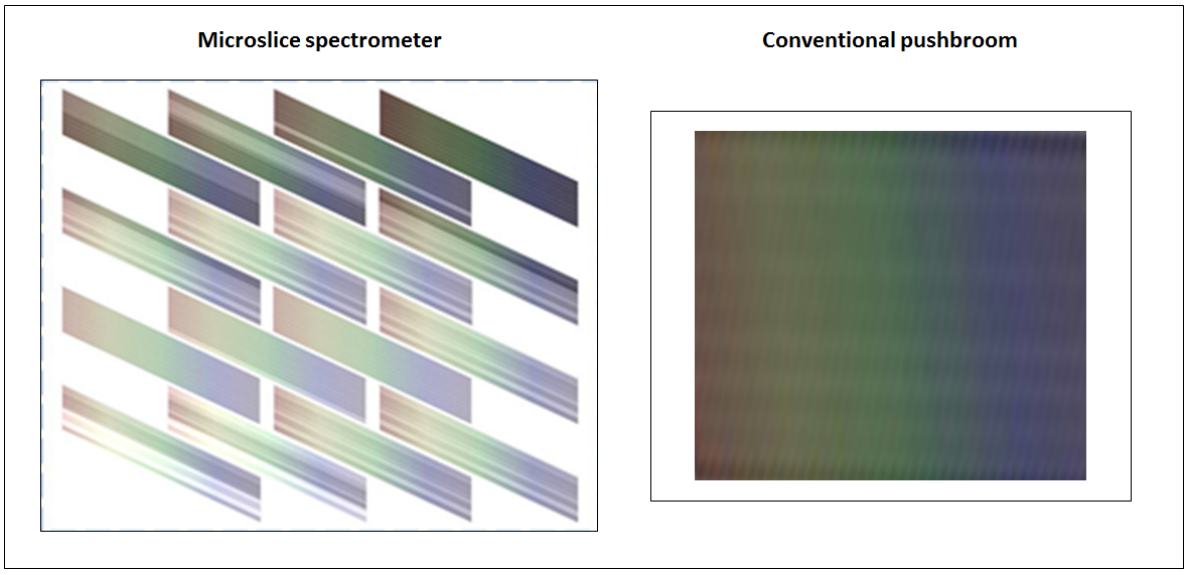

Figure 8.2: This figure shows why the microslice spectrometer design requires a larger detector than a standard spectrometer to image the same amount of hyperspectral information. The image on the left shows dispersed spectra, as they would appear on the microslice spectrometer detector. The image on the right shows how the same amount of information uses a smaller area when dispersed on a standard pushbroom spectrometer detector.

The number wasted pixels on the microslice spectrometer detector can be reduced by dispersing a single rectangular spectral slice for all of the spatial pixels in one dimension (see Figure 8.3). Although this method would provide better coverage of the detector, it would also mean that for a given spectral range/resolution, trading off the the spatial dimensions of the IFoV would require a more dramatic change in the shape of the detector. This is because all the spectral information is only using pixel space in one dimension on the detector. The tilt of the spectra into parallelograms, can therefore be seen to share the space being taken up by spectral information between both detector dimensions, therefore allowing the shape of the detector area used to more closely resemble the shape of the IFoV. The current design is therefore better suited to trade-offs between swath width and dwell time (i.e. a more square IFoV), while rectangular slices, would be preferable for a long and thin (or short and wide) IFoV.

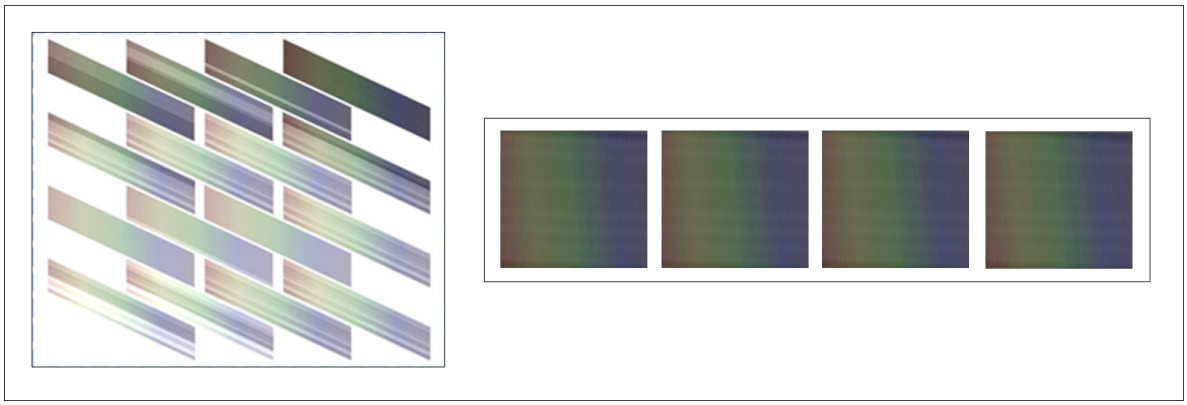

Figure 8.3: This figure shows how a change in instrument design of the microslice spectrometer could allow the detector pixels to be used more efficiently, but would also alter the required dimensions of the detector. The image on the left shows dispersed spectra, as they would appear on the current microslice spectrometer design. The image on the right shows the same information represented by a single row of rectangular dispersed spectra.

As well as the capabilities of an imaging spectrometer being limited by the number of detector pixels, some of the specifications are governed by the limits of various physical parameters. The limit to the spectral resolution is governed by the maximum line density that can be achieved on the dispersion element. A higher line density creates a higher angular dispersion, which therefore creates a larger number of pixels per nm, equating to a higher spectral resolution. The maximum line density achievable in commercially available plane ruled gratings is about 3600 lines/mm [144]. The grating line density also affects the spectral range, as the amount of dispersion determines the detector area that a given spectral range requires. The spectral and spatial resolutions are also limited by aberrations in the optics, which provide a limit to the size of a resolvable spectral or spatial element.

In theory, the instrument specifications could be improved by increasing the detector size, as this does not involve any compromise of other specifications, except for possibly instrument size. The maximum number of detector pixels is limited by the maximum size of the CCD. The largest CCD sensor currently available is the e2v CCD231-C6 detector, which has 6160 x 6144 pixels [142] (although

CMOS sensors are available up to 120 megapixels [145]). This CCD detector, however, has a pixel size of 15 μm, which is too large to resolve each spatial element with the current microslice spectrometer design. CCD chips are available with smaller pixels that are about 4000 x 4000 pixels. It is also possible to mosaic multiple CCD chips together to form a larger detector, but this may lead to issues with cross-calibration and reading out the data.

8.2 Future Potential Applications for Microslice Technology in Remote Sensing

The use of microslice technology in hyperspectral remote sensing is best suited to imaging a short wavelength range at moderate spatial and spectral resolution, while allowing for a large 2-dimensional IFoV. The unique 2-dimensional IFoV imaged using this design allows a trade-off between the two spatial dimensions meaning that a high dwell time, and hence SNR, is achievable from a moving platform, at the expense of the swath width.

The prototype microslice spectrometer obtains spatially resolved spectra from 475-650 nm at 7.0 nm resolution. In Section 6.4 it was determined that in order to detect certain river pollutant compounds dissolved in water, spectral measurements in the 400-600 nm range are required. In order to make this adjustment not only must the wavelength range increase slightly, it must also undergo a small shift in position. These changes can be achieved by changing the ruling and the angle of the grism. The purpose of the grism angle is to keep the light on axis after it is dispersed by the ruled surface. The angle of the prism therefore determines which wavelength (the central wavelength of the range) is kept on axis.

As discussed earlier, increasing the wavelength range can be done in three different ways, but the best method is to increase the detector size to accommodate for the longer spectra. The current detector is 3362 pixels across, but only uses about 2500 in the slice width direction. This means that an increase in spectral range of around 14% (475-650 nm to 400-600 nm), would not require an increase in detector size.

In Section 6.3 it was also determined that in order to monitor useful spatial variations of pollutants across the Ganges river from an altitude of 670 km, an increase in spatial resolution of around 100 times (from about 1 km) would be required for the microslice spectrometer. In this case an increase in the detector size is not a feasible solution due to the magnitude of the change. Therefore the IFoV must decrease, either by reducing the angular IFoV at a fixed altitude, which is done by changing the foreoptics magnification, or by reducing the altitude for a fixed angular IFoV (for example, imaging from an aircraft at 5 km also gives a spatial resolution of 7.5 m for an IFoV of 1.3 x 0.25 km). In Section 7.2 it was shown that imaging from an aircraft has the benefit of maintaining a high SNR, while satellite imaging has the advantage of providing greater spatial coverage at a high temporal resolution.

In Chapter 2, a sudy that used the HyMap airborne scanner showed that mapping hydrocarbon contamination on the ground is possible using hyperspectral imaging. This requires short-wave infrared imaging, and so a new dispersion element would be needed for the microslice spectrometer. Also, a new detector would be required as silicon CCD detectors cannot detect above 1200 nm. To detect in the 1700-1750 nm wavelength range an InGaAs or HgCdTe detector would be needed [146]. These detectors have different properties than standard CCDs, meaning that a change in detector could affect the instrument design and/or capabilities. The quantum efficiency (QE) of both materials is higher than that of a silicon CCD, but both detector types would also lead to a significant increase in the instrument cost, as infra-red detectors cost of the order of 10 times more per pixel. InGaAs detectors are only available up to about 1 megapixel in size, where as HgCdTe detectors are currently available up to 4 megapixels, with 16 megapixel detectors being developed [147]. The detector size is very important, as a larger detector is essential for recording a larger amount of information, which improves the capabilities of the instrument.

The grism would have to be blazed for optimal dispersion around 1725 nm, and a new grism angle would be needed to ensure that the linear design of the instrument is maintained. Also, the level of dispersion could be increased, which would lead to an increase in the spectral resolution achievable by the system. To increase the dispersion by a factor of 3.5 (dispersing a 50 nm wavelength range over the same detector area as the 175 nm wavelength range was dispersed) the ruling on the grating would need to be increased by a factor of 3.5 (from 200 lines/mm to 700 lines/mm). 600 lines/mm is the limit that can currently be achieved for plane transmission gratings/grisms without a significant reduction in efficiency This would give a spectral coverage of about 60 nm instead of 50 nm over the same detector area. Plane reflection gratings can be used if higher line densities are required, up to 3600 lines/mm [144].

Figure 7.11 showed that if the microslice spectrometer were to be used on an airborne platform at 5 km altitude, it could theoretically achieve an SNR of up to $\sim 10^5$ for an integration time of about 1 s, although an SNR of this magnitude is likely to be limited by other factors. A spatial resolution of 7.5 m would also be achieved (compared to the 10 m resolution of HyMap), and the instrument would image a swath width of 1.3 km. Using airborne imaging would therefore provide a suitable SNR and spatial resolution for hydrocarbon detection. It would, however lead to a much lower spatial coverage than from a satellite, and observations would require continual financial investment to achieve any level of temporal resolution. These downsides to airborne imagery are not relevant however if a one-off survey of a particular area is required to detect hydrocarbon contamination. It would be easy to trade off the spatial resolution with the swath width by altering the imaging altitude.

Many hyperspectral remote sensing systems utilise multiple instruments in order to provide wider spectral coverage, for example the Eagle/Hawk imaging system described in Chapter 3. Another example of such a hybrid remote sensing system uses a *CASI-1500* (350-1050 nm) and a *SASI-600*

(950-2450 nm) for mineral mapping in Antarctica [148]. Despite the use of multiple instruments the SNR in the short-wave infrared (SWIR) is sub-optimal (< 15) in low reflectance areas for most effective mineral mapping. An altered microslice spectrometer design could provide a high SNR over a relatively short SWIR wavelength range, increasing the potential of hyperspectral imaging in remote sensing of Antarctic minerals.

In order to take this work further the potential of each of these three applications should be assessed in terms of:

1. The extent to which they required the unique design of the microslice spectrometer
2. The feasibility of making the appropriate design changes
3. The continued demand for the application.

8.3 The Next Steps for Microslice Technology

This thesis has determined several potential applications for microslice technology. It has also shown improvements that must be made to the current microslice system in order to obtain more reliable data. Some of these improvement relate to the current instrument, but most relate to the data processing software and data interpretation. The most pressing concern are the spatial and spectral aretifacts that often arise in the data, as seen in Figure 6.7. These aretifacts area a result of the spectral box positioning being slightly misaligned.

Another software issue is the spatial resolution, which currently does not reach the resolution limit of the instrument. This is also due to imperfections in the spectral box positioning. A more accurate way of defining the spectral box positions would therefore lead to fewer spectral artifacts, as well as more accurate spatial data. This would also lead to higher classification accuracies.

For a fully functional hyperspectral imaging system, The software and instrument should be more integreated. This would not only facilitate ease of use, but could also improve the instrument capabilities. A large part of this would be to integrate the capture software and image processing software, which would require one or both pieces of software to be rewritten in compatible languages. This would allow captured images to be automatically stored and processed, including spectral callibration and potenially classification.

In order to develop a second generation microslice system for a specific application, appropriate design alterations would need to be made, and further proof-of-concept laboratory tests would need to be conducted to test the practical capabilities of the re-designed instrument. A second generation microslice spectrometer should also include the capability to gather data from a remote sensing platform.

In Chapter 6 the potential for the microslice spectrometer to be used as a remote sensing instrument were assessed by performing ground based field tests. This experiment also demonstrated the capabilities of the microslice spectrometer as a ground based imaging field spectrometer. The test highlighted the potential advantages of imaging a 2-dimensional spatial area, instead of just recording a point based spectrum, such as being able to determine the local spectral reflectance variation of a target, and being able to reference a spectral reading to a spatial point.

The biggest potential for microslice technology, however, lies in remote sensing. For detection of hydrocarbon contamination in the ground, a very similar design concept to the initial prototype could be used, but with alterations to some of the components. Each of the design adjustments required can affect the performance of the instrument, and therefore the new components would require laboratory performance testing before integration. Further thought should also be put into the mechanical design to make the fittings for the optical components smaller, lighter, and less prone to miss-alignment.

Hydrocarbon detection was found to require a new detector, which could image in the short-wave infrared spectral region (specifically 1700-1760 nm). Using an infrared detector would significantly increase the cost of the detector from about £1.5k to over £100k. The instrument response will be improved, however, due to a higher QE. Infrared detectors are much more sensitive to thermal noise than visible detectors, and so more cooling would be required. The entire system would have to be cooled to around -50^{o}C, and the detector would have to be cooled to around -150^{o}C, depending on the specific wavelength range used. This would increase the size, weight and cost of the system.

A HgCdTe detector is expected to be the best choice, as they will soon be available up to 16 megapixels in size [147]. These detectors are monochromatic detectors, which are generally designed as independent detector chips that not integrated into a camera system. This allows a custom camera and software interface to be developed that best suits the requirements of the instrument. The throughput of the camera, and the efficiency of the detector would need to be tested before integration. The performance of the integrated camera, detector and capture system should also be tested to determine if all of the capture capability requirements of the instrument are met.

Although the HyMap spectrometer that was used for the study in Chapter 2 has a spatial resolution of 10 m, there is no specific restriction on the spatial resolution for hydrocarbon contamination detection, as the required resolution is dependent on the contaminated area. Since the price of a 16 megapixel HgCdTe detector is likely to be over £100k, it would probaly be more cost-effective to use a smaller detector (4 megapixels), at the expense of having a worse spatial resolution (15 m). The detector would be a quarter of the area, meaning that 75% of the detector cost would be saved ($\sim$ £100k) without having a significant impact on the performance of the instrument for hydrocarbon detection.

Using a smaller detector would have particularly little impact on the instrument performance when it is considered that it is easy to obtain a better spatial resolution at the expense of the IFoV for airborne imaging, by lowering the imaging altitude. The smaller detector would also mean that the microlens arrays and equivalent collimating optics would also be smaller. This could lead to less optical

abberations, so the quality of the slitlet images produced by the foreoptics and microslice system could increase. A detailed re-design of the instrument should be produced that not only highlights the capabilities of the new system, but also the size, weight, and cost of the instrument, to see if its development as a airborne imager is feasible.

For hydrocarbon detection the grating ruling would also need to increase to about 600 lines/mm to provide an appropriate spectral range, so the performance of the grating should be tested before integration. If a grism were still to be used, it would need to be blazed for dispersion of 1730 nm light, and the angle would need to be increased for the appropriate optical axis adjustment. A volume phase holographic (VPH) grating (as described in Section 1.4.1) could be used as an alternative to the ruled surface of the grism. This would have the advantage of having higher throughput and allowing for a more customisable design, at a slightly higher expense.

It has been shown that slight alterations to the microslice spectrometer design could lead to improved detection of hydrocarbon contamination when imaging from an airborne platform. This would mainly be as a result of the instrument being able to image with a SNR that is an order of magnitude higher than is currently achievable by remote sensing hyperspectral imaging, when other parameters are compromised. It is also likely to be able to achieve improved spectral and spatial resolutions. The new design could theoretically use a 2000 x 2000 pixel detector to simultaneously image an area of 1.3 x 0.25 km from an airborne platform at a spatial resolution of about 15 m, in the 1700-1760 nm spectral range at a spectral resolution of about 2 nm, and with an SNR an order of magnitude higher than is currently achievable.

Hydrocarbon contamination of the ground can be a serious problem for the health of ecosystems. Early detection of such contamination can lead to swift remediation, which would minimise the damaged caused. The detection of hydrocarbon contamination using remote sensing has previously been limited by the spectral resolution and SNR that can be achieved. Microslice technology has been shown to theoretically allow a hyperspectral imaging system to image in the spectral region for detecting hydrocarbon contamination with a higher spectral resolution and SNR than has previously been possible.

Bibliography

[1] M. A. Lefsky, W. B. Cohen, G. G. Parker, and D. J. Harding, "Lidar remote sensing for ecosystem studies," *Bioscience*, vol. 52, no. 1, pp. 19–30, 2002.

[2] Z. P. Lee, K. L. Carder, C. D. Mobley, R. G. Steward, and J. S. Patch, "Hyperspectral remote sensing for shallow waters: 2. deriving bottom depths and water properties by optimization," *Applied Optics*, vol. 38, no. 18, pp. 3831–3843, 1999.

[3] R. V. Martin, "Satellite remote sensing of surface air quality," *Atmospheric Environment*, vol. 442, no. 34, pp. 7823–7843, 2008.

[4] A. M. Dewan and Y. Yamaguchi, "Land use and land cover change in greater dhaka and bangladesh: Using remote sensing to promote sustainable urbanization," *Applied Geography*, vol. 29, no. 3, pp. 390–401, 2009.

[5] History of aerial photography. PAPA International. [Online]. Available: http://www.papainternational.org/history.asp

[6] G. Nagy and J. Tolaba, "Nonsupervised crop classification through airborne multispectral observations," *IBM Journal of Research and Development*, vol. 16, no. 2, p. 138, 1972.

[7] G. Vane, A. Goetz, and J. Wellman, "Airborne imaging spectrometer: A new tool for remote sensing," *Geoscience and Remote Sensing*, vol. GE-22, no. 6, pp. 546–549, 1984.

[8] G. Vane, R. Green, T. G. Chrien, H. T. Enmark, E. Hansen, and W. M. Porter, "The airborne visible infrared imaging spectrometer (aviris)," *Remote Sensing of Environment*, vol. 44, no. 2-3, pp. 127–143, 1993.

[9] D. Bannon, "Hyperspectral imaging: Cubes and slices," *Nature Photonics*, vol. 3, no. 11, pp. 627–629, 2009.

[10] S. L. Ustin, D. A. Roberts, J. A. Gamon, G. P. Asner, and R. O. Green, "Using imaging spectroscopy to study ecosystem processes and properties," *Bioscience*, vol. 54, no. 6, pp. 523–534, 2004.

[11] The dornier 228: G-envr. Airborne Research & Survey Facility. [Online]. Available: http://arsf.nerc.ac.uk/aircraft/

[12] R. R. Navalgund and S. S. Ray, *Hyperspectral Data, Analysis Techniques and Applications*. Bishen Singh Mahendra Pal Singh, 2011.

[13] Diffraction grating selection guide. Newport Gratings. [Online]. Available: http://www.newport.com/Diffraction-Grating-Selection-Guide/421120/1033/content.aspx

[14] K. Kaufman. (2010, July) Cmos technology for scientific imaging. Spectroscopy. [Online]. Available: http://www.spectroscopyonline.com/spectroscopy/Column%3A+Laser+and+Optics+Interface/CMOS-Technology-for-Scientific-Imaging/ArticleStandard/Article/detail/680766

[15] Fourier transform spectrometer. Wolfram Research. [Online]. Available: http://scienceworld.wolfram.com/physics/FourierTransformSpectrometer.html

[16] Y. Ferrec and J. Primot, "Speceborne hyperspectral imaging with a static fourier transform spectrometer," *SPIE Newsroom*, 2013.

[17] Landsat missions timeline. U.S. Geological Survey. [Online]. Available: http://landsat.usgs.gov/about_mission_history.php

[18] G. Vane, F. Billingsley, and J. Dunne, "Observational parameters for remote sensing in the next decade," *Proceedings SPIE*, 1982.

[19] P. Goel, S. Prasher, J. Landry, R. Patel, R. Bonnell, A. Viau, and J. Miller, "Potential of airborne hyperspectral remote sensing to detect nitrogen deficiency and weed infestation in corn," *Computers and Electronics in Agriculture*, vol. 38, no. 2, pp. 99–124, 2003.

[20] K. Makisara, M. Meinander, and M. Rantasuo, "Airborne imaging spectrometer for applications (aisa)," *IGARSS'93: Better understanding of Earth Environment*, vol. 1-4, pp. 479–481, 1993.

[21] R. W. Basedow, D. C. Carmer, and M. E. Anderson, "Hydice system: Implementation and performance," *Proceedings SPIE*, vol. 2480, pp. 258–267, 1995.

[22] R. Lawrence and M. Labus, "Early detection of douglas-fir beetle infestation with subcanopy resolution hyperspectral imagery," *Western Journal of Applied Forestry*, vol. 18, no. 3, pp. 202–206, 2003.

[23] W. Barnes, T. Pagano, and V. Salomonson, "Prelanuch characteristics of the moderate resolution imaging spectrometer (modis) on eos-am1," *IEEE Transactions on Geoscience and Remote Sensing*, vol. 36, no. 4, pp. 1088–1100, 1998.

[24] Y. Yamaguchi, A. Kahle, H. Tsu, T. Kawakami, and M. Pniel, "Overview of advanced spaceborne thermal emission and reflection radiometer (aster)," *IEEE Transactions on Geoscience and Remote Sensing*, vol. 36, no. 4, pp. 1062–1071, 1998.

[25] N. Oppelt and W. Mauser, "Airborne visible / infrared imaging spectrometer avis: Design, characterization and calibration," *Sensors*, vol. 7, no. 9, pp. 1934–1953, 2007.

[26] T. Cocks, R. Jenssen, A. Stewart, I. Wilson, and T. Shield, "The hymap airbore hyperspectral sensor: The system calibration and performance," *Presented at 1st EARSEL Workshop on Imaging Spectroscopy*, 1998.

[27] M. Rast, J. Bezy, and S. Bruzzi, "The esa medium resolution imaging spectrometer meris a review of the instrument and its mission," *International Journal of Remote Sensing*, vol. 20, no. 9, pp. 1681–1702, 1999.

[28] J. Pearlman, P. Barry, C. Segal, J. Shepanski, D. Beiso, and S. Carman, "Hyperion and a space-based imaging spectrometer," *IEEE Transactions on Geoscience and Remote Sensing*, vol. 41, no. 6, 2003.

[29] M. Barnsley, J. Settle, M. Cutter, D. Lobb, and F.Teston, "The proba/chris mission: A low-cost smallsat for hyperspectral and multi-angle and observations of the earth surface and atmosphere," *IEEE Transactions on Geoscience and Remote Sensing*, vol. 42, no. 7, pp. 1512–1520, 2004.

[30] A. S. K. Kumar and A. Chowdhury, "Hyper-spectral imager for lunar mineral mapping in visible and near infrared band," *Current Science*, vol. 96, no. 4, 2009.

[31] R. L. Lucke, M. Corson, N. R. McGlothlin, S. D. Butcher, D. L. Wood, D. R. Korwan, R. R. Li, W. A. Snyder, C. O. Davis, , and D. T. Chen, "Hyperspectral imager for the coastal ocean: instrument description and first image," *Applied Optics*, vol. 50, no. 11, pp. 1501–1516, 2011.

[32] Airborne - specim. Specim. [Online]. Available: http://www.specim.fi/index.php/products/airborne

[33] P. M. Mehl, Y. R. Chen, K. M. Kim, and D. E. Chan, "Development of hyperspectral imaging technique for the detection of apple surface defects and contaminations," *Journal of Food Engineering*, vol. 61, no. 1, pp. 67–81, 2004.

[34] A. A. Gowen, C. P. O'Donnell, P. J. Cullen, G. Downey, and J. M. Frias, "Hyperspectral imaging - an emerging process analytical tool for food quality and safety control," *Trends in Food Science and Technology*, vol. 18, no. 12, pp. 590–598, 2007.

[35] Z. H. Pan, G. Healey, M. Prasad, and B. Tromberg, "Face recognition in hyperspectral images," *IEEE Transactions on Pattern Analysis and Machine Intelligence*, vol. 25, no. 12, pp. 1552–1560, 2003.

[36] Y. Roggo, A. Edmond, P. Chalus, and M. Ulmschneider, "Infrared hyperspectral imaging for qualitative analysis of pharmaceutical solid forms," *Analytica Chimica Acta*, vol. 535, no. 1-2, pp. 79–87, 2005.

[37] T. Vo-Dinh, F. Yan, and M. B. Wabuyele, "Surface-enhanced raman scattering for medical diagnostics and biological imaging," *Journal of Raman Spectroscopy*, vol. 36, no. 6-7, pp. 640–647, 2005.

[38] M. T. Eismann, C. R. Schwartz, J. N. Cederquist, J. A. Hackwell, and R. J. Huppi, "Comparison of infrared imaging hyperspectral sensors for military target detection applications," *Proceedings of the Society of Photo-Optical Instrumentation Engineers (SPIE)*, vol. 2819, pp. 91–101, 1996.

[39] J. P. Ardouin, J. Levesque, and T. A. Rea, "A demonstration of hyperspectral image exploitation for military applications," *Proceedings of the 10th International Conference on Information Fusion*, vol. 1-4, pp. 1632–1639, 2007.

[40] S. G. Bajwa and L. F. Tian, "Soil fertility characterization in agricultural fields using hyperspectral remote sensing," *Transactions of the American Society of Agricultural Engineers*, vol. 48, no. 6, pp. 2399–2406, 2005.

[41] N. K. Patel, C. Patnaik, S. Dutta, A. M. Shekh, and A. J. Dave, "Study of crop growth parameters using airborne imaging spectrometer data," *International Journal of Remote Sensing*, vol. 22, no. 12, pp. 2401–2411, 2001.

[42] G. Guyot, F. Baret, and S. Jacuemoud, *Imaging spectroscopy: Fundamentals and Prospective Appplications*, S. S. . B. Media, Ed. Springer Science & Business MediaSpringer Science & Business Media, 1992.

[43] J. B. Guo, C. Huang, H. G. Wang, Z. Y. Sun, and Z. H. Ma, "Disease index inversion of wheat stripe rust on different wheat varieties with hyperspectral remote sensing," *Spectroscopy and Spectral Analysis*, vol. 29, no. 12, pp. 3353–3357, 2009.

[44] J. B. Jiang, Y. H. Chen, and W. J. Huang, "Using hyperspectral remote sensing to estimate canopy chlorophyll density of wheat under yellow rust stress," *Spectroscopy and Spectral Analysis*, vol. 30, no. 8, pp. 2243–2247, 2010.

[45] W. Feng, X. Yao, Y. Tian, W. Cao, and Y. Zhu, "Monitoring leaf pigment status with hyperspectral remote sensing in wheat," *Australian Journal of Agricultural Research*, vol. 59, no. 8, pp. 748–760, 2008.

[46] V. E. Brando and A. G. Dekker, "Satellite hyperspectral remote sensing for estimating estuarine and coastal water quality," *IEEE Transactions on Geoscience and Remote Sensing*, vol. 41, no. 6, pp. 1378–1387, 2003.

[47] S. Koponen, J. Pulliainen, K. Kallio, and M. Hallikainen, "Lake water quality classification with airbourne hyperspectral spectrometer and simulated meris data," *Remote Sensing of Environment*, vol. 79, no. 1, pp. 51–59, 2002.

[48] M. L. Smith, S. V. Ollinger, M. E. Martin, J. D. Aber, R. A. Hallett, and C. L. Goodale, "Direct estimation of aboveground forest productivity through hyperspectral remote sensing of canopy nitrogen," *Ecological Applications*, vol. 12, no. 5, pp. 1286–1302, 2002.

[49] P. M. Treitz and P. J. Howarth, "Hyperspectral remote sensing for estimating biophysical parameters of forest ecosystems," *Progress in Physical Geography*, vol. 23, no. 3, pp. 359–390, 1999.

[50] A. Held, C. Ticehurst, L. Lymburner, and N. Williams, "High resolution mapping of tropical mangrove ecosystems using hyperspectral and radar remote sensing," *International Journal of Remote Sensing*, vol. 24, no. 13, pp. 2739–2759, 2003.

[51] F. Kruse, J. Boardman, and J. Huntington, "Comparison of airborne hyperspectral data and eo-1 hyperion for mineral mapping," *IEEE Transactions on Geoscience and Remote Sensing*, vol. 41, no. 6, 2003.

[52] F. Kruse, L. Richardson, and V. Ambrosia, "Techniques developed for geologic analysis of hyperspectral data applied to near-shore hyperspectral ocean data," *Presented at the Fourth International Conference on Remote Sensing for Marine and Coastal Environments*, 1997.

[53] B. Horig, F. Kuhn, F. Oschutz, and F. Lehmann, "Hymap hyperspectral remote sensing to detect hydrocarbons," *International Journal of Remote Sensing*, vol. 22, no. 8, pp. 1413–1422, 2001.

[54] D. N. H. Horler, M. Dockray, and J. Barber, "The red edge of plant leaf reflectance," *International Journal of Remote Sensing*, vol. 4, no. 2, pp. 273–288, 1983.

[55] T. P. Dawson and P. J. Curran, "A new technique for interpolating the reflectance red edge position," *International Journal of Remote Sensing*, vol. 19, no. 11, pp. 2133–2139, 1998.

[56] D. W. Lamb, M. Steyn-Ross, P. Schaare, M. M. Hanna, W. Silvester, and A. Steyn-Ross, "Estimating leaf nitrogen concentration in ryegrass (lolium spp.) pasture using the chlorophyll red-edge: Theoretical modelling and experimental observation," *International Journal of Remote Sensing*, vol. 23, no. 18, pp. 3619–3648, 2002.

[57] G. I. Metternicht and J. A. Znick, "Remote sensing of soil salinity: Potentials and constraints," *Remote Sensing of Environment*, vol. 85, no. 1, pp. 1–20, 2003.

[58] R. L. Dehaan and G. R. Taylor, "Field-derived spectra of salinized soils and vegetaiton as indicators of irrigation-induced soil salinization," *Remote Sensing of Environment*, vol. 80, no. 3, pp. 406–417, 2002.

[59] A. Morel and L. Prieur, "Analysis of variations in ocean color," *Liminology and Oceanogrophy*, vol. 22, no. 4, pp. 709–722, 1977.

[60] Global forest cover in 1990, listed by country. [Online]. Available: http://rainforests.mongabay.com/deforestation_1990.html

[61] C. B. Field and H. A. Mooney, *The Economy of Plant Form and Function*, T. Givnish, Ed. Cambridge University Press, 1986.

[62] A. Lugo and S. Sndaker, "The ecology of mangroves," *Annual Review of Ecology and Systematics*, vol. 5, pp. 39–64, 1974.

[63] Douglas-fir beetle, dendroctonus pseudotsugae. Ministry for Forsets and Range, British Colombia. [Online]. Available: http://www.for.gov.bc.ca/hfp/publications/00198/douglas-fir_beetle.htm

[64] R. G. Resmini, M. E. Kappus, W. S. Aldrich, J. C. Harsanyi, and M. Anderson, "Mineral mapping with hyperspectral digital imagery collection experiment (hydice) sensor data at cuprite and nevada and u.s.a." *International Journal of Remote Sensing*, vol. 18, no. 7, pp. 1553–1570, 1997.

[65] K. E. White, "Bioavailability of polycyclic aromatic hydrocarbons in the aquatic environment," Ph.D. dissertation, NC State University, 2006. [Online]. Available: http://repository.lib.ncsu.edu/ir/handle/1840.16/3855

[66] E. A. Cloutis, "Spectral reflectance properties of hydrocarbons: Remote-sensing implications," *Science*, vol. 245, pp. 165–168, 1989.

[67] K. Katsouyanni, G. Touloumi, C. Spix, J. Schwartz, F. Balducci, S. Medina, G. Rossi, B. Wojtyniak, J. Sunyer, L. Bacharova, J. Schouten, A. Ponka, and H. Anderson, "Short term effects of ambient sulphur dioxide and particulate matter on mortality in 12 european cities: Results from time series data from the aphea project," *British Medical Journal*, vol. 314, no. 7095, pp. 1658–1663, 1997.

[68] R. Symonds, W. Rose, G. Bluth, and T. Gerlach, "Volcanic gas studies - methods and results and and applications," *Reviews in Mineralogy and Geochemistry*, vol. 30, pp. 1–66, 1994.

[69] A. J. Moffat and M. M. Millan, "The application of optical correlation techniques to the remote sensing of so2 plumes using skylight," *Atmospheric Environment*, vol. 5, pp. 677–690, 1971.

[70] R. E. Stoiber and A. Jepsen, "Sulfur dioxide contribution to the atmosphere by volcanoes," *Science*, vol. 182, no. 4112, pp. 577–578, 1973.

[71] A. Sutton, T. Elias, T. Gerlach, and J. Stokes, "Implications for eruptive processes as indicated by sulfur dioxide emissions from kilauea volcano and hawaii and 1979-1997," *Journal of Volcanology and Geothermal Research*, vol. 108, no. 1-4, pp. 283–302, 2001.

[72] T. Casadevall, W. Rose, T. Gerlach, L. Greenland, J. Ewert, R. Wunderman, and R. Symonds, "Gas emissions and the eruption of mt. st. helens through 1982," *Science*, vol. 221, no. 4618, pp. 1383–1385, 1983.

[73] S. Young, P. Francis, J. Barclay, T. Casadevall, C. Gardner, B. Darroux, M. Davies, P. Delmelle, G. Norton, A. Maciejewski, C. Oppenheimer, J. Stix, and I. Watson, "Monitoring so2 emission at the soufrière hills volcano: implications for changes in eruptive conditions," *Geophysical Research Letters*, vol. 25, no. 19, pp. 3681–3684, 1998.

[74] B. Galle, C. Oppenheimer, A. Geyer, A. J. S. McGonigle, M. Edmonds, and L. Horrocks, "A miniaturised ultraviolet spectrometer for remote sensing of so2 fluxes: A new tool for volcano surveillance," *Journal of Volcanology and Geothermal Research*, vol. 119, no. 1-4, pp. 241–254, 2003.

[75] M. Wang, "Remote sensing of the ocean contributions from ultraviolet to near-infrared using the shortwave infrared bands: simulations," *Applied Optics*, vol. 46, no. 9, pp. 1535–1547, 2007.

[76] C. Lavigne, G. Durand, and A. Roblin, "Ultraviolet light propagation under low visibility atmospheric conditions and its application to aircraft landing aid." *Applied Optics*, vol. 35, no. 46, pp. 9140–9150, 2006.

[77] G. Guyot and F. Baret, "Utilisation de la haute résolution spectrale pour suivre l'état des couverts végétaux," *Proceedings of the 4th International colloquium on spectral signatures of objects in remote sensing*, pp. 279–286, 1988.

[78] J. Miller, E. Hare, and J. Wu, "Quantitative characterization of the vegetation red edge reflectance 1. an inverted-gaussian reflectance model," *International Journal of Remote Sensing*, vol. 11, no. 10, pp. 1755–1773, 1990.

[79] R. Pu, P. Gong, G. Biging, and M. Larrieu, "Extraction of red edge optical parameters from hyperion data for estimation of forest leaf area index," *IEEE Transactions on Geoscience and Remote Sensing*, vol. 41, no. 4, pp. 916–921, 2003.

[80] M. A. Cho and A. K. Skidmore, "A new technique for extracting the red edge position from hyperspectral data: The linear extrapolation method," *Remote Sensing of Environment*, vol. 101, no. 2, pp. 181–193, 2006.

[81] S. E. Franklin, M. B. Lavigne, M. J. Deuling, M. A. Wulder, and E. R. H. Jr, "Estimation of forest leaf area index using remote sensing and gis data for modelling net primary production," *International Journal of Remote Sensing*, vol. 18, no. 16, pp. 3459–3471, 1997.

[82] G. P. Asner, J. M. O. Scurlock, and J. A. Hicke, "Global synthesis of leaf area index observations: Implications for ecological and remote sensing studies," *Global Ecology and Biogeography*, vol. 12, no. 3, pp. 191–205, 2003.

[83] T. N. Carlson and D. A. Ripley, "On the relation between ndvi and fractional vegetation cover and and leaf area index," *Remote Sensing of Environment*, vol. 62, no. 3, pp. 241–252, 1997.

[84] W. R. Stern and C. M. Donald, "Relationship of radiation and leaf area index and crop growth-rate," *Nature*, vol. 189, no. 476, pp. 597–598, 1961.

[85] J. L. Monteith and M. H. Unsworth, *Principles of Environmental Physics*. Academic Press, 1990.

[86] N. Breda, "Ground-based measurements of leaf area index: A review of methods and instruments and current controversies," *Journal of Experimental Botany*, vol. 54, no. 392, pp. 2403–2417, 2003.

[87] J. R. Jensen, *Remote sensing of the environment: an earth resource perspective.* Prentice Hall, 2000.

[88] N. Pettorelli, J. O. Vik, A. Mysterud, J. Galliard, C. J. Tucker, and N. C. Stenseth, "Using the satellite-derived ndvi to assess ecological response to environmental change," *Trends in Ecology and Evolution*, vol. 20, no. 9, pp. 503–510, 2005.

[89] R. Clark and T. Roush, "Reflectance spectroscopy: Quantatative analysis techniquesfor remote sensing applications," *Journal of Geophysical Research*, vol. 87, no. B7, pp. 6329–6340, 1984.

[90] Z. Huang, B. Turnera, S. Durya, I. Wallisb, and W. Foleyb, "Estimating foliage nitrogen concentration from hymap data using continuum removal analysis," *Remote Sensing of Environment*, vol. 93, no. 1-2, pp. 18–29, 2004.

[91] Z. I. Kalantan, "Methods for estimation of intrinsic dimensionality," Ph.D. dissertation, Durham University, 2014. [Online]. Available: http://etheses.dur.ac.uk/9500/

[92] A. L. Price, N. J. Patterson, R. M. Plenge, M. E. Weinblatt, N. A. Shadick, and D. Reich, "Principal components analysis corrects for stratification in genome-wide association studies," *Nature Genetics*, vol. 38, no. 8, pp. 904–909, 2006.

[93] S. Vyas and L. Kumaranayake, "Constructing socio-economic status indices: How to use principal components analysis," *Health Policy and Planning*, vol. 21, no. 6, pp. 459–468, 2006.

[94] C. W. Chang, D. A. Laird, M. J. Mausbach, and C. R. Hurburgh, "Near-infrared reflectance spectroscopy - principal components regression analyses of soil properties," *Soil Science Scociety of America Journal*, vol. 65, no. 2, pp. 480–490, 2001.

[95] Y. Pan, J. Wu, H. Huang, and J. Liu, "Spectral regression discriminant analysis for hyperspectral image classification; international archives of the photogrammetry," *Remote Sensing and Spatial Information Sciences*, vol. 39, no. B3, 2012.

[96] Envi software - image analysis software. [Online]. Available: http://www.exelisvis.com/ProductsServices/ENVI/ENVI.aspx

[97] J. Krishnaswamy, S. Kamaljit, S. Bawa, K. Ganeshaiah, and M. Kiran, "Quantifying and mapping biodiversity and ecosystem services: Utility of a multi-season ndvi based mahalanobis distance surrogate," *Remote Sensing of Environment*, vol. 113, no. 4, pp. 857–867, 2009.

[98] Mahalanobis description. Jenness Enterprises. [Online]. Available: http://www.jennessent.com/arcview/mahalanobis_description.htm

[99] M. Cho, P. Debba, R. Mathieu, L. Naidoo, J. V. Aardt, and G. Asner, "Improving discrimination of savanna tree species through a multiple-endmember spectral angle mapper approach: Canopy-level analysis," *IEEE Transactions on Geoscience and Remote Sensing*, vol. 48, no. 11, pp. 4233–4142, 2010.

[100] A. H. Strahler, "The use of prior probabilities in maximum likelihood classification of remotely sensed data," *Remote Sensing of Environment*, vol. 10, no. 2, pp. 135–163, 1980.

[101] N. Keshava and J. F. Mustard, "Spectral unmixing," *IEEE Signal Processing Magazine*, vol. 19, no. 1, pp. 44–57, 2002.

[102] M. A. Friedl and C. E. Brodley, "Decision tree classification of land cover from remotely sensed data," *Remote Sensing of Environment*, vol. 61, no. 3, pp. 399–409, 1997.

[103] M. Xu, P. Watanachaturaporn, P. Varshney, and M. K. Arora, "Decision tree regression for soft classification of remote sensing data;," *Remote Sensing of Environment*, vol. 97, no. 3, pp. 322–336, 2005.

[104] R. R. Navalgund and S. S. Ray, *Hyperspectral Data and Analysis Techniques and Applications*, 2011.

[105] A. Lausch, M. Pause, I. Merbach, S. Gwillym-Margianto, K. Schulz, S. Zacharias, and R. Seppelt, "Scale-specific hyperspectral remote sensing approach in environmental research," *Photogrammetrie Fernerkundung Geoinformation*, no. 5, pp. 589–601, 2010.

[106] B. A. Woodcock, J. Redheada, A. J. Vanbergenb, L. Hulmesa, S. Hulmesa, J. Peytona, M. Nowakowskic, R. F. Pywella, and M. S. Hearda, "Impact of habitat type and landscape structure on biomass and species richness and functional diversity of ground beetles," *Agriculture and Ecosystems & Environment*, vol. 139, no. 1-2, pp. 181–186, 2010.

[107] Aisaeagle - description. Universitat Leipzig, Faculty of Physics and Earth Science, Atmospheric Radiation Group. [Online]. Available: http://www.uni-leipzig.de/~strahlen/web/research/en_index.php?goto=eagle

[108] M. Dubbeldam, R. Content, J. Allington-Smith, S. Pokrovsky, and D. Robertson, "An integral field unit for the gemini near-infrared spectrograph," *SPIE Proceedings*, vol. 4008, pp. 1181–1192, 2000.

[109] R. Content, S. Blake, C. Dunlop, D. Nandi, R. Sharples, G. Talbot, T. Shanks, D. Donoghue, N. Galiatsatos, and P. Luke, "New microslice technology for hyperspectral imaging," *Remote Sensing*, no. 5, pp. 1204–1219, 2013.

[110] Fundamentos de la espectroscopia. [Online]. Available: http://pendientedemigracion.ucm.es/info/Astrof/users/jaz/TRABAJOS/UGARTE/3.htm

[111] (2007, March) Sigma sd14. Photo Review. [Online]. Available: http://www.photoreview.com.au/reviews/advanced-compact-cameras/sigma-sd14

[112] Aviris instrument. NASA (JPL). [Online]. Available: aviris.jpl.nasa.gov/html/aviris.instrument.html

[113] D. Coffin. Decoding raw digital photos in linux. [Online]. Available: http://www.cybercom.net/~dcoffin/dcraw

[114] (2000) The effect of temperature on ccd's. DP Review. [Online]. Available: http://www.dpreview.com/news/2000/5/3/ccdtemperature

[115] P. K. Varshney and M. K. Arora, *Advanced Image Processing Techniques for Remotely Sensed Data*, 2004.

[116] Atomic spectra. [Online]. Available: http://hyperphysics.phy-astr.gsu.edu/hbase/quantum/atspect2.html

[117] R. D. Fiete and T. Tantalo, "Comparison of snr image quality metrics for remote sensing systems," *Optical Engineering*, vol. 40, no. 4, 2000.

[118] H. J. Landau, "Sampling, data transmission, and the nyquist rate," *Proceedings of the IEEE*, vol. 55, no. 10, pp. 1701–1706, 1967.

[119] B. Atkins. (2007, April) Modulation transfer function - what is it and why does it matter? photo.net. [Online]. Available: http://photo.net/learn/optics/mtf/

[120] R. Betancourt-Benitez, R. Ning, D. Conover, and S. Liu, "Composite modulation transfer function evaluation of a cone beam computed tomography breast imaging system," *Optical Engineering*, vol. 48, no. 11, 2009.

[121] Fieldspec 3 series. Sphere Optics. [Online]. Available: http://www.sphereoptics.de/en/spectrometers/fieldspec-3-asdi-spectrometer.php

[122] R. Ashley and M. Abrams, "Alteration mapping using multispectral images - cuprite mining district and esmeralda county and nevada," *U.S. Geological Survey and Open File Report*, pp. 80–367, 1980.

[123] E. Zaitzeff, C. Korb, and C. Wilson, "Msds: An experimental 24-channel multi-spectral scanner system," *IEEE Transactions on Geoscience Electronics*, vol. 9, no. 3, 1971.

[124] G. Swayze, R. N. Clark, F. Kruse, S. Sutley, and A. Gallagher, "Ground-truthing aviris mineral mapping at cuprite, nevada," *NASA Technical Reports Server (NTRS)*, 1992.

[125] L. Guanter, L. Alonso, and J. Moreno, "First results from the chris/proba hyperspectral/multiangle satallite system over land and water targets," *IEEE Geoscience and Remote Sensing Letters*, vol. 2, no. 3, 2005.

[126] A. M. Arthur. (2007) Field guide for the asd fieldspec pro - white reference mode. Field Spectroscopy Facility. [Online]. Available: http://fsf.nerc.ac.uk/resources/guides/pdf_guides/asd_guide_v2_wr.pdf

[127] M. G. Rao and N. V. N. Kumar, "The tannery industrial effluent effect on succinate dehydrogenase activity pattern in a freshwater snail and pila globosa," *Proceedings of the Indian Acadamy of Sciences - Animal Science*, vol. 91, no. 5, pp. 427–431, 1982.

[128] A. R. Khwaja, R. Singh, and S. N. Tandon, "Monitoring of ganga water and sediments vis-a-vis tannery pollution at kanpur (india): A case study," *Environmental Monitoring and Assessment*, vol. 89, pp. 19–35, 2001.

[129] Water pollution guide - health. Guides Network. [Online]. Available: http://www.water-pollution.org.uk/health.html

[130] L. A. K. Mertes, "Remote sensing of riverine landscapes," *Freshwater Biology*, vol. 47, no. 4, pp. 799–816, 2002.

[131] W. A. Marcus and M. A. Fonstad, "Remote sensing of rivers: the emergence of a subdiscipline in the river sciences," *Earth Surface Processes and Landforms*, vol. 35, no. 15, pp. 1867–1872, 2010.

[132] K. D. Fausch, C. E. Torgersen, C. V. Baxter, and H. W. Li, "Landscapes to riverscapes: Bridging the gap between research and conservation of stream fishes," *Bioscience*, vol. 52, pp. 483–498, 2002.

[133] N. Milton. (2012, September) Building bridges between britain and bangladesh. Practical Action. [Online]. Available: http://practicalaction.org/blog/climate_change/building-bridges-between-britain-and-bangladesh

[134] S. Chandrasekhar, *Radiative Transfer*. Dover Publications, 1960.

[135] A. Berk, G. P. Anderson, P. K. Acharya, L. S. Bernstein, L. Muratov, J. Lee, M. Fox, S. M. Adler-Golden, J. H. Chetwynd, M. L. Hoke, R. B. Lockwood, J. A. Gardner, T. W. Cooley, C. C. Borel, P. E. Lewis, and E. P. Shettle, "Modtran (tm) 5: 2006 update; algorithms and technologies for multispectral and hyperspectral and and ultraspectral imagery xii pts 1 and 2," *Proceedings of SPIE*, vol. 6233, p. F2331, 2006.

[136] H. Smith, D. Dube, M. Gardner, S. Clough, F. Kneizys, and L. Rothman, "Fascode: Fast atmospheric signature code (spectral transmittance and radiance)," *Scientific Report 2 and Air Force Geophysics Laboratory and Hanscom AFB and Massachusetts*, 1978.

[137] E. F. Vermote, D. Tanre, J. L. Deuze, M. Herman, and J. J. Morcrette, "Second simulation of the satellite signal in the solar spectrum and 6s: An overview," *IEEE Transactions on Geoscience and Remote Sensing*, vol. 35, no. 3, pp. 675–696, 1997.

[138] Modo. Re Se Applications Schlapfer. [Online]. Available: http://www.rese.ch/products/modo/index.html

[139] J. M. Wallace and P. V. Hobbs, *Atmospheric Science; An Introductory Survey.* Academic Press, 2006.

[140] Aerosol optical thickness. NASA. [Online]. Available: http://disc.sci.gsfc.nasa.gov/data-holdings/PIP/aerosol_optical_thickness_or_depth.shtml

[141] A. Barducci, D. Guzzi, P. Marcoionni, , and I. Pippi, "Chris-proba performance evaluation: signal-to-noise ratio and instrument efficiency and data quality from acquisitions over san rossore (italy) test site," *Proceedings of Third CHRIS/Proba Workshop*, vol. ESA-SP-593, 2005.

[142] Imaging sensors (cmos, ccd, emccd) resources. e2v. [Online]. Available: http://www.e2v.com/products/high-performance-imaging-solutions/imaging-sensors-cmos-ccd-emccd/?resources

[143] K. Woellerta, P. Ehrenfreunda, A. J. Riccob, and H. Hertzfelda, "Cubesats: Cost-effective science and technology platforms for emerging and developing nations," *Advances in Space Research*, vol. 47, no. 4, pp. 663–684, 2011.

[144] Holographic vs ruled grating - which to use. McPherson. [Online]. Available: http://www.mcphersoninc.com/howtoselectagrating.htm

[145] (2010) Canon announces 120 megapixel aps-h format cmos sensor. Canon. [Online]. Available: cpn.canon-europe.com/content/news/120_megapixel_apsh_format_cmos_sensor.do

[146] H. Yoon, M. Dopkiss, and G. Eppeldauer, "Performance comparisons of ingaas, extended ingaas, and short-wave hgcdte detectors between 1 mu m and 2.5 mu m," *Proceedings of SPIE*, vol. 6297, no. 3, p. 29703, 2006.

[147] T. Sprafke and J. W. Beletic. (2008) High-performance infrared focal plane arrays for space applications. The Optical Society. [Online]. Available: http://www.osa-opn.org/home/articles/volume_19/issue_6/features/high-performance_infrared_focal_plane_arrays_for_s/

[148] M. Black, A. Fleming, T. Riley, G. Ferrier, P. Fretwell, J. McFee, S. Achal, and A. U. Diaz, "On the atmospheric correction of antarctic airborne hyperspectral data," *Remote Sensing*, vol. 6, no. 5, pp. 4498–4514, 2014.

[149] M. L. A.S. Mazer, M. Martin and J. Solomon, "Image processing software for imaging spectrometry data analysis," *Remote Sensing of Environment*, vol. 24, pp. 201–210, 1988.

[150] P. Acharya, A. Berka, G. Anderson, N. Larsenc, S. Tsay, and K. Stamnes, "Modtran4: Multiple scattering and bi-directional reflectance distribution function (brdf) upgrades to modtran," *Proceeding SPIE*, vol. 3756, 1999.

[151] G. P. Asner, D. Nepstad, G. Cardinot, and D. Ray, "Drought stress and carbon uptake in an amazon forest measured with spaceborne imaging spectroscopy," *Proceedings of the National Academy of Sciences of the United States of America*, vol. 101, no. 16, pp. 6039–6044, 2004.

[152] E. Ben-Dor, S. Chabrillat, J. A. M. Dematte, G. R. Taylor, J. Hill, M. L. Whiting, and S. Sommer, "Using imaging spectroscopy to study soil properties," *Remote Sensing of Environment*, vol. 113, pp. S38–S55, 2009.

[153] Y. Chen, N. M. Nasrabadi, and T. D. Tran, "Hyperspectral image classification using dictionary-based sparse representation," *IEEE Transactions on Geoscience and Remote Sensing*, vol. 49, no. 10, pp. 3973–3985, 2001.

[154] M. L. Clark, D. A. Roberts, and D. B. Clark, "Hyperspectral discrimination of tropical rain forest tree species at leaf to crown scales," *Remote Sensing of Environment*, vol. 96, no. 3-4, pp. 375–398, 2005.

[155] J. Clevers, L. Kooistra, and E. Salas, "Study of heavy metal contamination in river floodplains using the red-edge position in spectroscopic data," *International Journal of Remote Sensing*, vol. 25, pp. 3883–3895, 2004.

[156] T. Elias, A. J. Sutton, C. Oppenheimer, K. A. Horton, H. Garbeil, V. Tsanev, A. J. S. McGoniglea, and G. Williams-Jones, "Comparison of cospec and two miniature ultraviolet spectrometer systems for so2 measurements using scattered sunlight," *Bulletin of Volcanology*, vol. 68, no. 4, pp. 313–322, 2006.

[157] C. Giardino, A. D. V. E. Brando, N. Strombeck, and G. Candiani, "Assessment of water quality in lake garda (italy) using hyperion," *Remote Sensing of Environment*, vol. 109, no. 2, pp. 183–195, 2007.

[158] A. F. H. Goetz, B. N. Rock, and L. C. Rowan, "Remote sensing for exploration; an overview," *Economic Geology*, vol. 78, no. 4, pp. 573–590, 1983.

[159] P. Gupta, S. A. Christopher, J. Wang, R. Gehrig, Y. Lee, and N. Kumar, "Satellite remote sensing of particulate matter and air quality assessment over global cities," *Atmospheric Environment*, vol. 40, no. 30, pp. 5880–5892, 2006.

[160] D. Haboudane, J. R. Miller, E. Pattey, P. J. Zarco-Tejada, and I. B. Strachan, "Hyperspectral vegetation indices and novel algorithms for predicting green lai of crop canopies: Modeling and validation in the context of precision agriculture," *Remote Sensing of Environment*, vol. 90, no. 3, pp. 337–352, 2004.

[161] P. T. Janos and P. F. Tunde. (2008) Geoinformatics. Digitalis Tankonyvtar. [Online]. Available: http://www.tankonyvtar.hu/en/tartalom/tamop425/0032_terinformatika/ch05.html

[162] S. K. Jenson and J. O. Domingue, "Extracting topographic structure from digital elevation data for geographic information-systems analysis," *Photogrammetric Engineering and Remote Sensing*, vol. 54, no. 11, pp. 1593–1600, 1988.

[163] K. Kallio, T. Kutser, T. Hannonen, S. Koponen, J. Pulliainen, J. Vepsalainen, and T. Pyhalahti, "Retrieval of water quality from airborne imaging spectrometry of various lake types in different seasons," *Science of the Total Environment*, vol. 268, no. 1-3, pp. 59–77, 2001.

[164] F. Kuhna, K. Oppermann, and B. Horig, "Hydrocarbon index - an algorithm for hyperspectral detection of hydrocarbons," *International Journal of Remote Sensing*, vol. 25, no. 12, pp. 2467–2473, 2004.

[165] M. A. Lefsky, W. B. Cohen, G. G. Parker, and D. J. Harding, "Lidar remote sensing for ecosystem studies," *Bioscience*, vol. 52, no. 1, pp. 19–30, 2002.

[166] R. J. Leigh, C. Whyte, D. Lobb, M. Cutter, and P. Monks, "Compaqs - a novel spectrometer for small air quality and climate monitoring missions in the uv and visible," *Geophysical Research Abstracts, EGU General Assembly*, vol. 10, 2008.

[167] R. C. Levy, L. A. Remer, J. V. Martins, Y. J. Kaufman, A. Plana-Fattori, J. Redemann, and B. Wenny, "Evaluation of the modis aerosol retrievals over ocean and land during clams," *Journal of Atmospheric Sciences*, vol. 62, no. 4, pp. 974–992, 2005.

[168] D. R. Lyzenga, "Passive remote sensing techniques for mapping water depth and bottom features," *Applied Optics*, vol. 17, no. 3, pp. 379–383, 1978.

[169] M. E. Martin, S. D. Newmana, J. D. Aber, and R. G. Congalton, "Determining forest species composition using high spectral resolution remote sensing data," *Remote Sensing of Environment*, vol. 65, no. 3, pp. 249–254, 1998.

[170] M. E. Martin, L. C. Plourde, S. V. Ollinger, M. L. Smith, and B. E. McNeil, "A generalizable method for remote sensing of canopy nitrogen across a wide range of forest ecosystems," *Remote Sensing of Environment*, vol. 112, no. 9, pp. 3511–3519, 2008.

[171] R. Meier, "Ultraviolet spectroscopy and remote sensing of the upper atmosphere," *Space Science Reviews*, vol. 58, no. 1, pp. 1–185, 1991.

[172] R. Nave. Rayleigh and mie scattering. [Online]. Available: http://hyperphysics.phy-astr.gsu.edu/hbase/atmos/blusky.html

[173] M. Quemada, J. L. Gabriel, and P. Zarco-Tejada, "Airborne hyperspectral images and ground-level optical sensors as assessment tools for maize nitrogen fertilization," *Remote Sensing*, vol. 6, no. 4, pp. 2940–2962, 2014.

[174] R. Richter, "Model sensat: A tool for evaluating the system performance of optical systems," *Proceedings SPIE*, vol. 1312, 1990.

[175] Agriculture. Satellite Imaging Corporation. [Online]. Available: http://www.satimagingcorp.com/svc/agriculture.html

[176] Population of the entire world, yearly, 1950 - 2100. Geohive. [Online]. Available: http://www.geohive.com/earth/his_history3.aspx

[177] Years of fossil fuels remaining. Energy Realities. [Online]. Available: http://www.energyrealities.org/chapter/energys-future/item/years-of-fossil-fuels-remaining/erp6D28994FAAEECC86A

[178] Ganges. The Free Dictionary. [Online]. Available: http://encyclopedia2.thefreedictionary.com/Ganges+River+Valley

[179] Jpl spectral library. NASA. [Online]. Available: http://speclib.jpl.nasa.gov/documents/jpl_desc

[180] Usgs digital spectral library. The U.S. Geological Survey. [Online]. Available: http://speclab.cr.usgs.gov/spectral-lib.html

Appendix A

Data Processing MATLAB code

A.1 spectrum_posx

```
clearvars -except file whitespectra repeat repeats t target targets tlen wh wbands


% read and flip CCD image

CCDinv = fitsread('test.fit');
CCD = ones(2537,3362);
for x = 1:2537;
    for y = 1:3362;
        CCD(2538-x,y) = CCDinv(x,y);
    end
end

% define data parameters

nspec = 31; nspac = 16;
theta = 61;
l = 165; w = 28; h = 90;
leaway = 15;


% threshold CCD to find spectral positions

threshold = 30000; threshold = threshold/(2^16);
```

```
CCD = CCD/65535;
CCD = im2bw(CCD,threshold);


% importexpected x and y coordiantes of spectral box positions

posx = load(['posx.mat']);
posy = load(['posy.mat']);


% find bottom right corner of each spectrum

posx2 = posx+l;
posy2 = posy+h+w;

for yspec = 1:nspac;
    for xspec = 1:nspec;
        y = posy2(yspec,xspec)-(w/2);
        for x = (posx2(yspec,xspec)-leaway):(posx2(yspec,xspec)+leaway);
            if CCD(y,x) == 0
                if CCD(y,x+1) ==0
                    posx2(yspec,xspec) = (x-1); break
                end
            end
        end

        x = posx2(yspec,xspec)-(leaway/3);
        for y = (posy2(yspec,xspec)-leaway):(posy2(yspec,xspec)+leaway);
            if CCD(y,x) == 0
                if CCD(y+1,x) == 0
                    posy2(yspec,xspec) = (y-1); break
                end
            end
        end
    end
end
```

```
% find top left corner of each spectrum

for yspec = 1:nspac
    for xspec = 1:nspec;
        y = posy(yspec,xspec)+(w/2);
        for x = (posx(yspec,xspec)-(2*leaway/3)):(posx(yspec,xspec)+(2*leaway/3));
            if CCD(y,x) == 1
                if CCD(y,x+1) == 1
                    posx(yspec,xspec) = x; break
                end
            end
        end
        x = posx(yspec,xspec)+(leaway/5);
        for y = (posy(yspec,xspec)-(0*leaway/3)):(posy(yspec,xspec)+(2*leaway/3));
            if CCD(y,x) == 1
                if CCD(y+1,x) == 1
                    posy(yspec,xspec) = y; break
                end
            end
        end
    end
end

posx2 = posx2-posx;
posy2 = posy2-posy;


% define position of the first spectrum for reference

startx = min(min(posx)); starty = min(min(posy));
posx = posx-startx+1;
posy = posy-starty+1;

imwrite(CCD,'threshold','TIF')
```

A.2 untransform_boxes

```
clearvars -except W wh asdwhite leaf1 whitedatacube posx posy posx2 posy2 startx starty
whitespectra spectra specbandshg file repeat repeats t target targets tlen wbands

% define data parameters
theta = 61;
l = 165; w = 28; h = 90;
nspec = 31; nspac = 16;
lea = 0; % amount cut off of each spectrum

% x and y position of each corner of the first spectrum
ax = startx + lea;
bx = startx + lea;
cx = startx + l - lea;
dx = startx + l - lea;
ay = starty + lea;
by = starty + w - 1 - lea;
cy = starty + l + lea;
dy = starty + l + w - 1 - lea;

% read and flip CCD image

CCDinv = fitsread(file);
CCD = flipud(CCDinv);
CCDi = CCD/65535;
imwrite(CCDi,'spectra','TIF')

% transform spectra from parallelograms to rectangles

pin = zeros(2,4);
pout = zeros(2,4);
specs = zeros((by-ay+1),(cx-ax+1),nspec*nspac);

for x = 1:nspec;
    for y = 1:nspac;
        cx = ax + posx2(y,x); dx = bx + posx2(y,x);
        cy = ay + posy2(y,x)-w; dy = by + posy2(y,x)-w;
```

```
        pin(1,:) = [ax bx cx dx];
        pin(2,:) = [ay by cy dy];
        pout(1,:) = [ax bx cx dx];
        pout(2,:) = [ay by ay by];
        pint = pin';
        poutt = pout';
        tform = cp2tform(pint,poutt,'affine');
        CCDt = imtransform(CCD((ay-lea+posy(y,x)):(dy+lea+posy(y,x)),
               (ax-lea+posx(y,x)):(dx+lea+posx(y,x))),tform);
        specs(:,1:(cx-ax+1),((y-1)*nspec)+x) = CCDt((cy-starty+1):(dy-starty+1),
                                               (ax-startx+1):(cx-startx+1));
        for a = (ax-lea+posx(y,x)):(dx+lea+posx(y,x));
            b = (cy-ay+1) *( (a-(ax-lea+posx(y,x))) / ((dx+lea+posx(y,x))-(ax-lea+posx(y,x))) );
            c = round(b+posy(y,x)+starty);
            d = round(b+w-1+posy(y,x)+starty);
            CCD(c,a,1) = (2^16)-1; CCD(d,a,1) = (2^16)-1;
        end
        CCD((ay-lea+posy(y,x)):(ay-lea+posy(y,x))+w-1,(ax-lea+posx(y,x)),1) = (2^16)-1;
        CCD((dy+lea+posy(y,x))-w+1:(dy+lea+posy(y,x)),(dx+lea+posx(y,x)),1) = (2^16)-1;
    end
end

% stack spectral slices into appropriately orientated array

specsnew = zeros(l,(by-ay+1),nspec*nspac);
for x = 1:l;
    for y = 1:(by-ay+1);
        for z = 1:nspec*nspac;
            specsnew(x,y,z) = specs(y,x,z);
        end
    end
end

specbands = specsnew;
for i = 1:(w-(2*lea));
    specbands(:,i,:) = specsnew(:,(w-(2*lea))+1-i,:);
end
```

A.3 untransform_speccal

```
% read, combine and correctly orientate calibration images

CCDinv = fitsread('Hg_001.fit');
CCD1 = flipud(CCDinv);
CCDinv = fitsread('Hg_004.fit');
CCD2 = flipud(CCDinv);
CCD(1:1400,:) = CCD1(1:1400,:);
CCD(1401:2537,:) = CCD2(1401:2537,:);

CCDi = CCD/65535;
imwrite(CCDi,'spectra','TIF')
```

A.4 interpolate

```
% spectrally calibrate each slice

spec = zeros(l,nspec*nspac);
hgi = 546; hgii = 577;
low = 470; high = 659;
wavebands = zeros(wbands,w,nspec*nspac);
dd=zeros(nspec*nspac,1);
for slice = 1:(nspec*9);
    spec(:,slice) = mean(specbandshg(:,:,slice),2);
    [qq,I] = max(spec(45:80,slice)); [ww,II] = max(spec(85:125,slice));
    I = I+44;
    II = II+84;
    I = ((I-3)*spec(I-3,slice) + (I-2)*spec(I-2,slice) + (I-1)*spec(I-1,slice)
        + (I)*spec(I,slice) + (I+1)*spec(I+1,slice) + (I+2)*spec(I+2,slice)
        + (I+3)*spec(I+3,slice)) / (spec(I-3,slice) + spec(I-2,slice) + spec(I-1,slice)
        + spec(I,slice) + spec(I+1,slice) + spec(I+2,slice) + spec(I+3,slice));
    II = ((II-3)*spec(II-3,slice) + (II-2)*spec(II-2,slice) + (II-1)*spec(II-1,slice)
        + (II)*spec(II,slice) + (II+1)*spec(II+1,slice) + (II+2)*spec(II+2,slice)
        + (II+3)*spec(II+3,slice)) / (spec(II-3,slice) + spec(II-2,slice) + spec(II-1,slice)
        + spec(II,slice) + spec(II+1,slice) + spec(II+2,slice) + spec(II+3,slice));
    dldx = (hgii-hgi)/(II-I);
    dd(slice) = dldx;
    l1 = hgi-((I-1)*dldx);
    l2 = l1+((l-1)*dldx);
    for line  = 1:w;
  wavebands(:,line,slice) =
  interp1(l1:dldx:l2,specbands(:,line,slice),low:(190/wbands):high,'linear');
    end
end


% write values into datacube

depth = wbands; width = nspec; length = (by-ay+1)*nspac;
datacube = zeros(depth,width,length);
for x = 0:(nspac-1);
```

```
    for y = 1:nspec;
        datacube(:,y,((x*(by-ay+1))+1):((x+1)*(by-ay+1))) = wavebands(:,:,y+(x*nspec));
    end
end


% rearange dimentions and re-bin

newdatacube = zeros(nspec*4,length,wbands);
for x = 1:length;
    for y = 1:nspec*4;
        for z = 1:wbands;
            newdatacube(y,x,z) = datacube(z,ceil(y/4),x);
        end
    end
end
datacube = newdatacube*1;


% export datacube

whitedatacube = datacube+1;
multibandwrite (whitedatacube,'datacubebsq','bsq')
```

A.5 asd_comparison

```
% import and average asd data

asd1 = importdata([target '00001.txt']);
asd2 = importdata([target '00002.txt']);
asd3 = importdata([target '00003.txt']);
asdspectrum = (asd1+asd2+asd3)/3;
wavelength = asdspectrum(121:311,1);
asdspectrum = asdspectrum(121:311,2);

% define spectral cut-off

lcut = 15; upcut = 80;
asdspectrum = asdspectrum(lcut*(190/wbands):(190/wbands):upcut*(190/wbands));
spectrum = spectrum(lcut:upcut);

% normalise to minimum=0 and maximum=1 and plot

asdspectrumnorm = (asdspectrum-min(asdspectrum));
asdspectrumnorm = asdspectrumnorm/max(asdspectrumnorm);
spectrumnorm = (spectrum-min(spectrum)); spectrumnorm = spectrumnorm/max(spectrumnorm);
figure (6); hold on; axis([500,625,0,1]);
plot(wavelength(lcut*(190/wbands):(190/wbands):upcut*(190/wbands)),asdspectrumnorm,
     'r--','LineWidth',4)
plot(wavelength(lcut*(190/wbands):(190/wbands):upcut*(190/wbands)),spectrumnorm,
     'k','LineWidth',6)
xlabel('\fontsize{20}Wavelength / nm');
ylabel('\fontsize{20}Normalised Reflectance');
legend('ASD','microslice'));
saveas(figure(6),['zerotoone' target],'png')

%calculate angle between spectra

A = asdspectrumnorm'*spectrumnorm;
B = sqrt(spectrumnorm'*spectrumnorm);
C = sqrt(asdspectrumnorm'*asdspectrumnorm);
angle = acos(A/(B*C));
```

A.6 run

```
close all; clear all

target = 'grass'; % define target image
wbands = 95; % defines spectral sampling


% calculateand average microslice white references

repeats = 3;
whitespectra = zeros(wbands,repeats);

file = [target 'white_001.fit'];
run('ATIK_spectra_posxy')
run('ATIK_untransform_speccal')

for repeat = 1:repeats;
    file = [target 'white_00' num2str(repeat) '.fit'];
    run('ATIK_untransform_boxes')
    run('ATIK_interpolate_boxes')
end

whitespectrum = mean(whitespectra,2);

% calculate and avereage corrected target spectra for microslice

repeats = 3;
spectra = zeros(wbands,repeats);

for repeat = 1:repeats;
    file = [target '_00' num2str(repeat) '.fit'];
    run('ATIK_untransform_boxes')
    run('ATIK_interpolate_spectra')
end

spectra(isnan(spectra)) = 0;
spectrum = mean(spectra,2);
```

A.7 SAM_classification

```
% define class map area

swathx = 124; swathy = 84;
class = zeros(swathx,swathy);
classmap = zeros(swathx,swathy,3);

% define colors of each target

red = [0,0,0,240,240,240,128,128,128,128,0];
green = [170,255,85,240,240,240,64,64,64,64,0];
blue = [0,0,0,0,0,0,0,0,0,0,0];

% define target classes and thresholds

targets = ['grass      '; 'lushgrass  '; 'deadgrass  '; 'nettle     '; 'thistle    ';
'riverplants'; 'silt       '; 'pebbles    '; 'drysoil    '; 'mud        '];
tlen = [5,9,9,6,7,11,4,7,7,3];
threshold = [0.0603;0.0810;0.0671;0.1265;0.0897;0.0769;0.2586;0.4614;0.2593;0.2828];


% run SAM classification

accuracy = 0; unclassified = 0;
for x = 1:swathx; % for all pixels in the image
    for y = 1:swathy;
        targetangle = zeros(10,1);
        for T = 1:10; % for each target
            %calculate angle between pixel and target
            classtarget = targets(T,1:tlen(T));
            load(['asd' classtarget '.mat']); classspectrum = asdspectrumnorm;
            spectrum = datacube(x,y,lcut:upcut);
            spectrum = reshape(spectrum,(upcut-lcut+1),1);
            respectrum = zeros(58,1);
            reclassspectrum = zeros(58,1);
            for n = 1:58
                respectrum(n) = sum(spectrum(((n*2)-1):(n*2)));
```

```
                reclassspectrum(n) = sum(classspectrum(((n*2)-1):(n*2)));
            end
            spectrumnorm = (respectrum-min(respectrum));
            spectrumnorm = spectrumnorm/max(spectrumnorm);
            classspectrumnorm = (reclassspectrum-min(reclassspectrum));
            classspectrumnorm = classspectrumnorm/max(classspectrumnorm);
            spectrum1 = spectrumnorm; spectrum2 = classspectrumnorm;
            A = spectrum1'*spectrum2;
            B = sqrt(spectrum1'*spectrum1);
            C = sqrt(spectrum2'*spectrum2);
            targetangle(T) = acos(A/(B*C));
        end
        % find smallest angle, and classify as class of that target
        [u,v] = min(targetangle);
        if u < 1;
            class(x,y) = v;
        else class(x,y) = 11;
        end
        if class(x,y) < 7;
            accuracy = accuracy+1;
        elseif class(x,y) == 11;
            unclassified = unclassified + 1;
        end
        % write data to coulour class map
        classmap(x,y,1) = red(class(x,y));
        classmap(x,y,2) = green(class(x,y));
        classmap(x,y,3) = blue(class(x,y));
    end
end
classmap = classmap/255;

% output results

accuracy = accuracy/(swathx*swathy)
unclassified = unclassified/(swathx*swathy)
falsepossitive = (1-accuracy-unclassified)
save(['classification' target],'class')
save(['classificationmap' target],'classmap')
```